

Universiteit
Antwerpen

Faculteit Wetenschappen

Departement Fysica

**In-situ Transmission Electron Microscopic Nanomechanical
Investigations of Ni**

**In-situ Transmissie-Elektronenmicroscopisch Nanomechanisch
Onderzoek van Ni**

Proefschrift voorgelegd tot het behalen van de graad van

Doctor in de Wetenschappen

aan de Universiteit Antwerpen, te verdedigen door

Vahid Samaee

Promotoren:

Prof. Dr. D. Schryvers

Prof. Dr. H. Idrissi

Antwerpen

2018

Members of the Jury

Chairman

Prof. Dr. B. Partoens, University of Antwerp, Belgium

Promotors

Prof. Dr. D. Schryvers, University of Antwerp, Belgium

Prof. Dr. H. Idrissi, Université catholique de Louvain, and University of Antwerp, Belgium

Members

Prof. Dr. R. Schwaiger, Karlsruhe Institute of Technology, Germany

Prof. Dr. T. Pardoen, Université catholique de Louvain, Belgium

Prof. Dr. J. Hadermann, University of Antwerp, Belgium

Contact information



Vahid Samaee

EMAT - Electron Microscopy for Materials Science

University of Antwerp - Department of Physics

Groenenborgerlaan 171, B-2020 Antwerpen

Belgium

Vahid.samaee@uantwerpen.be

To my dear Mother

Preface

Nano- and micro-scale materials are used in various technologies such as microelectronics and micro-electro-mechanical systems. In these applications, small sized materials are subjected to external and internal stresses that can affect their integrity. However, although nanomechanical testing now has enabled the investigation of mechanical properties of these systems, the interpretation of the results and proposed mechanisms at small-scales are still under discussion. For instance, both steady and intermittent plastic flow has been observed in single crystals micro-scale samples, and the exact nature of the mechanisms underlying the mechanical properties is still unclear. Furthermore, nanomechanical testing gives the chance to tackle old questions such as the role of interfaces in the mechanical properties. In the present thesis, advanced scanning and transmission electron microscopy including in-situ micro/nanomechanical testing techniques have been used to unravel the elementary deformation mechanisms in micron sized single and bi-crystal Ni samples. Focused ion beam preparation of micropillars followed by in-situ scanning electron microscopy cyclic deformation has been performed at Karlsruhe Institute of Technology (KIT) while DD simulations of the activation of single arm sources were performed in the Laboratoire d'Etude des Microstructures (LEM), CNRS-ONERA. Finite element modelling of the image force of grain boundaries was performed at the Technical University Bergakademie Freiberg.

Organization of the thesis:

Chapter 1 gives a general introduction to the basics of dislocation theory, interfaces, and mechanical testing. Also, different nanomechanical testing techniques including in-situ TEM techniques are briefly described.

Chapter 2 provides a review on the materials as well as the techniques and instruments used in this thesis including the basic TEM characterization techniques, the in-situ nanomechanical testing instrument, the digital image cross correlation and the basic sample preparation techniques.

Chapter 3 introduces a novel sample preparation method for quantitative in-situ TEM nanotensile testing and presents the analysis of the quality and the mechanical properties of the prepared single crystal nickel sample.

Chapter 4 presents the improved sample preparation introduced in Chapter 3 including an extra in-situ TEM step as well as the in-situ TEM nanotensile test results of a single crystal nickel sample containing very few single arm sources. The results provide a new insight to the role of the surface and the single arm dislocation sources on the mechanical properties of nanoscale single crystal samples.

Chapter 5 presents the results of an in-situ TEM nanotensile test on a bi-crystal tensile sample containing a coherent twin boundary which was prepared by the method explained in chapter 4. It reveals new quantitative information on the interaction of the screw and non-screw dislocations with the coherent twin boundary.

Chapter 6 presents the TEM microstructural investigation of single and bi-crystal nickel micropillars cyclically deformed in a SEM. Conventional and advanced TEM techniques are used to reveal various aspects of dislocation structures in those micro samples.

| | |
|---|----|
| Preface..... | iv |
| Contents | vi |
| 1 Introduction | 1 |
| 1.1 Fundamental Concepts | 4 |
| 1.1.1 Dislocations..... | 4 |
| 1.1.2 Interfaces..... | 8 |
| 1.1.3 Interaction of Dislocations with Grain Boundaries | 11 |
| 1.1.4 Size Effect..... | 13 |
| 1.2 Mechanical Testing, | 16 |
| 1.2.1 Tensile Test..... | 16 |
| 1.2.2 Compression Test..... | 17 |
| 1.2.3 Fatigue Test..... | 17 |
| 1.2.4 Schmid's Law | 18 |
| 1.2.5 Microstructural Investigation..... | 19 |
| 1.3 Overview on Micro- and Nanomechanical Testing | 22 |
| 1.3.1 Miniaturized Deformation Methods | 25 |
| 1.3.2 Micro- and Nanomechanical Testing Methods..... | 26 |
| 1.4 In-situ Approaches in Micro- and Nanomechanical Testing | 27 |
| 1.5 In-situ Testing in Transmission Electron Microscopes..... | 28 |
| 1.5.1 Mechanical Straining Holders..... | 28 |
| 1.5.2 Micro Electro-Mechanical Systems..... | 31 |
| 2 Materials and Methods | 34 |
| 2.1 Materials..... | 35 |
| 2.2 Transmission Electron Microscopy (TEM) | 35 |
| 2.2.1 Introduction..... | 35 |
| 2.2.2 Diffraction Mode | 38 |

| | | |
|-------|---|-----|
| 2.2.3 | Imaging Mode..... | 40 |
| 2.2.4 | Energy Dispersive X-Ray Spectroscopy (EDS) | 42 |
| 2.2.5 | Strain and Orientation Mapping in a TEM | 43 |
| 2.3 | In-situ TEM Tensile Testing | 43 |
| 2.4 | Digital Image Correlation..... | 48 |
| 2.5 | In-situ SEM Fatigue Testing | 49 |
| 2.6 | TEM Sample Preparation | 50 |
| 2.6.1 | Twin-Jet Electro-Polishing | 50 |
| 2.6.2 | Focused Ion Beam..... | 51 |
| 2.6.3 | In-situ TEM Heating Holder..... | 52 |
| 3 | Quantitative in-situ TEM nanotensile testing of a single crystal Ni sample with reduced FIB damages | 54 |
| 3.1 | Introduction | 55 |
| 3.2 | Materials and methods | 57 |
| 3.3 | Results and discussion..... | 59 |
| 3.4 | Conclusions | 67 |
| 4 | Nanomechanics of dislocations near surfaces in almost FIB damage-free single crystal Ni sample | 68 |
| 4.1 | Introduction | 69 |
| 4.2 | Materials and Methods | 71 |
| 4.3 | Results and discussion..... | 76 |
| 4.4 | Conclusions | 92 |
| 5 | Investigation of Dislocations –Twin Boundary Interactions by In-situ TEM Tensile Testing..... | 93 |
| 5.1 | Introduction | 94 |
| 5.2 | Experimental conditions..... | 97 |
| 5.3 | Result and discussion | 99 |
| 5.3.1 | Slip plane determination | 101 |

| | | |
|-------|---|-----|
| 5.3.2 | Dislocation characterization..... | 102 |
| 5.3.3 | Interaction of screw dislocations with the CTB..... | 103 |
| 5.3.4 | Interaction of a non-screw dislocation with the CTB | 114 |
| 5.3.5 | The fracture | 116 |
| 5.4 | Conclusion..... | 117 |
| 6 | Dislocation microstructure in cyclically deformed Ni micropillars | 119 |
| 6.1 | Introduction | 120 |
| 6.2 | Materials and methods | 122 |
| 6.3 | Results and discussion..... | 124 |
| 6.4 | Conclusions | 139 |
| 7 | Summary and perspectives | 141 |
| | References..... | 152 |
| | List of abbreviations | 165 |
| | Appendix..... | 167 |
| | List of scientific contributions | 170 |
| | Journal articles related to the PhD work | 170 |
| | Journal articles NOT related to the PhD work | 170 |
| | Conference contributions | 170 |
| | Acknowledgment | 172 |

Chapter 1:

Introduction

1 Introduction

Nanotechnology is playing a significant role in the advancement and the development of various industries. For instance, there is a great tendency in microelectronics to smaller components in order to integrate various functions in a small volume. Now micro- and nano-fabrication techniques allow fabricating complex devices by using small components and in some commercial devices such as cell phones and sensors, components of a few nanometres have already been used, e.g., central processing units (CPUs), micro- or nano-electro-mechanical systems (MEMS/NEMS), etc.

Nanotechnology has, furthermore, introduced a new class of materials, so-called nanomaterials [1] which are materials with structural features (e.g., grain sizes or dimensions) smaller than ~ 100 nm in at least one dimension, e.g., nanoparticles, nanowires, nanofilms, and nanostructured materials [2-4]. The low-dimensional structure of nanomaterials causes interesting and different physical, chemical, or mechanical properties compared to the corresponding bulk materials. For example, semiconductor nanomaterials have a unique quantum-mechanical effect (amplified spontaneous emission and stimulated emission) different from bulk materials [5]. Nanostructured materials have shown simultaneous better strength and toughness than their bulk counterparts [6-8]. The different characteristics of nanomaterials have already shown and still promise many novel applications, e.g., as nanosensors [9, 10], nanogenerators [11] and nanolasers [12]. Nanomaterials have become one of the most active research areas in materials science in the last decades.

However, one of the main important issues of using small-scale components and nanomaterials is their mechanical reliability during the production processes or in service. For example, cyclic loading due to external loads or temperature fluctuations, can cause plastic deformation or even fracture of the components which can either change the functional properties, such as electric properties, or lead to local malfunction of the components and consequently the whole device. Therefore, determining the mechanical properties of nanostructures and nanomaterials and understanding the governing mechanisms are crucial factors in designing predictable and durable devices containing nano-components.

At the macro scale, various mechanical testing methods have been designed and are used to measure various mechanical properties required in designing and prediction of the behaviour of particular components. For instance, tensile and fatigue tests are the most important ones

which are used to obtain the strength of materials under static loading and the durability of the samples (components) under cyclic loading. In a tensile test, the yield strength is an indicator of the maximum strength of a material before having a permanent deformation while in a fatigue test the endurance limit shows the maximum amount of stress amplitude below which the material will not fail for any number of cycles.

Similarly, in order to measure the mechanical properties of small-scale materials (or components), various types of micro- and nanomechanical testing methods have been developed in the last decades. In 2004, Uchic et al. introduced and used for the first time microcompression to study the mechanical properties of Ni and Ni₃(Al,Ta) [13]. Since then, a considerable amount of studies on the mechanical properties of various small-scale materials have been done by adopting various developed nanomechanical testing methods [14, 15].

Since the time of Galileo it was generally believed that material strength is a size-independent property [16]. However, nanomechanical testing showed different mechanical properties of small-scale samples compared to bulk (macro) samples [17]. “Smaller is Stronger” was the main observation in those studies; e.g., the thickness dependency of the yield strength of metallic thin films on substrates [18], the depth dependency of indentation [19], the volume-dependent fracture strength of brittle materials [20] or the thickness dependency of the strength of nanowires [6, 21-23]. Since then, dimensions began to be considered as a significant factor in the mechanical properties of materials, especially at the micron/submicron scales.

In spite of many investigations on mechanical properties and governing mechanisms of small-scale samples, there is a lack of quantitative in-situ TEM tensile testing in the literature, especially on FIB defect-free samples, mainly due to difficulties of the sample preparation and the performance of such experiments.

Nickel is one of the commonly used materials in small-scale technologies. Nickel provides a simple and cheap technology with superior material properties and device performances [24] and has already been widely used in different MEMS devices such as pressure sensors, thermal actuators, microcoils, micromotors, and so on. It can be deposited by electroplating, evaporation, and sputtering processes which are cheap and highly productive. Its good mechanical properties can be exploited in movable structures in MEMS devices and its magnetic properties have made it a proper candidate for magnetic MEMS devices [25].

Therefore, from designing and fabrication points of view, it is very critical to investigate the mechanical properties and the relevant governing mechanisms of small-scale Ni components.

In this thesis, the plasticity mechanisms of small-scale pure Ni samples have been investigated using quantitative in-situ TEM and SEM mechanical testing techniques. A novel sample preparation method has been introduced enabling preparing well-designed Ni samples with minimum FIB-induced damages proper for quantitative in-situ TEM tensile experiments. As examples, the plasticity mechanisms in a single crystal tensile sample and the interactions of dislocations with a coherent twin boundary in a bi-crystal tensile sample have been quantitatively investigated using such in-situ TEM experiments.

1.1 Fundamental Concepts

The mechanical properties of crystalline materials mainly depend on the nucleation and interaction of crystal defects such as dislocations and structural interfaces (including grain boundaries (GBs)). In the following, some basic concepts of such defects are briefly described.

1.1.1 Dislocations

From the start, establishing predictive physical models for the mechanical response of materials, such as plastic deformation and fatigue behaviour, has been one of the main objectives of materials research. However, in spite of decades of efforts and due to the high complexity of most bulk materials (i.e., the presence of many playing factors in the mechanical processes), there are still no comprehensive models to predict all material behaviour at once. However, in essentially all models, dislocations, which are at the foundation of understanding mechanical properties, play a crucial role.

Dislocations are crystallographic line defects which can be imagined as a group of atoms along a line located in irregular positions, and can be basically classified as edge, screw, and mixed types, Figure 1-1. They were discovered in 1934 by Taylor, Orowan and Polanyi independently [26]. Dislocations were directly observed for the first time in 1955 by a TEM and their motion was observed for the first time in 1956 in an aluminium foil in a TEM [27, 28]. Dislocations are the most important players in the mechanical properties and in the deformation of the crystalline materials. When a crystalline material is deformed, dislocations can move and the plastic deformation (plastic strain) in the crystal can be accommodated by their motion, Figure 1-2 [29].

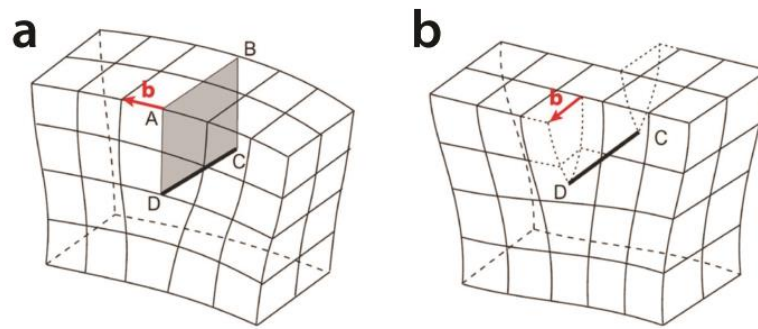


Figure 1-1, Model of (a) an edge dislocation (line DC) and (b) a screw dislocation (line DC) [30].

The standard definition of a dislocation is via its Burgers vector. The Burgers vector defines the local displacement of atoms in the vicinity of a dislocation. By knowing the angle between the line of a dislocation and the Burgers vector, the character of the dislocation can be identified; if the angle is 0° , the dislocation is a screw type, if it is 90° , it is an edge dislocation, and if the angle is between 0° and 90° , it is a mixed dislocation.

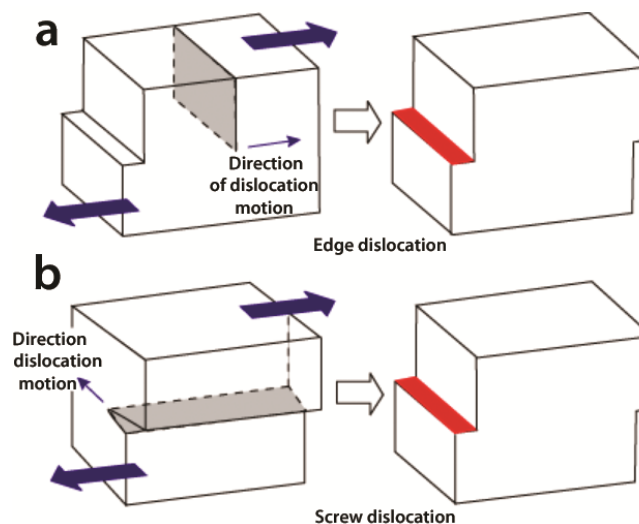


Figure 1-2, Schematics showing how motion of (a) an edge dislocation and (b) a screw dislocation can induce plastic deformation in a single crystal under shear loading [31].

The plane including the Burgers vector of a dislocation and the line of a dislocation is called the slip plane on which the dislocation is supposed to move. Obviously, defining a unique slip plane for a screw dislocation is not possible as the dislocation line and the Burgers vectors are parallel. When the slip plane and the Burgers vector are the closest packed ones in a crystal, they are called a slip system. For example, in face centre cubic (FCC) crystals, there are four close packed slip planes of $\{111\}$ and on each of them there are three $\langle 110 \rangle$ close packed slip directions, therefore, there are twelve slip systems in an FCC crystal.

When the Burgers vector of a dislocation is a translation vector of the crystal lattice, like $\frac{a}{2}\langle 110 \rangle$ dislocations in FCC crystals, the dislocation is called a perfect dislocation and glide of such dislocations leaves behind a perfect crystal. However, there are other types of dislocations, so-called partial dislocations, which, after gliding, leave behind faulted (imperfect) crystals. In an FCC crystal, dislocations with the Burgers vectors of $\frac{a}{6}\langle 112 \rangle$ are (Shockley) partial dislocations and their motion can locally change the stacking sequence of the atomic planes resulting in a planar defect, a so-called stacking fault (SF) [32].

Like all defects in a crystal, dislocations increase the internal energy of the crystal. In the case of a dislocation, this increase is proportional to the Burgers vector magnitude squared. Dislocations are able to interact with each other either to form new dislocations (combination), or to annihilate each other. In any reaction (either combination or annihilation), the vector sum of the Burgers vectors of the initial dislocations should be equal to the vector sum of the Burgers vectors of the newly produced dislocations (which should of course be zero in the case of annihilation). In addition, a reaction is only possible if it is energetically favourable which means the total energy of the newly formed dislocations should be less than the total energy of the initial ones. For example, in FCC crystals, the dissociation of a perfect dislocation into Shockley partial dislocations is an energetically favourable reaction. Interaction of dislocations can result in the formation of new dislocations which cannot glide easily. Such sessile dislocations generally act as a lock and make the glide of other dislocations difficult. For instance, in FCC crystals, the interaction of 2 Shockley partial dislocations lying on two different inclined slip planes may result in the formation of so-called Lomer-Cottrell locks, Figure 1-3.

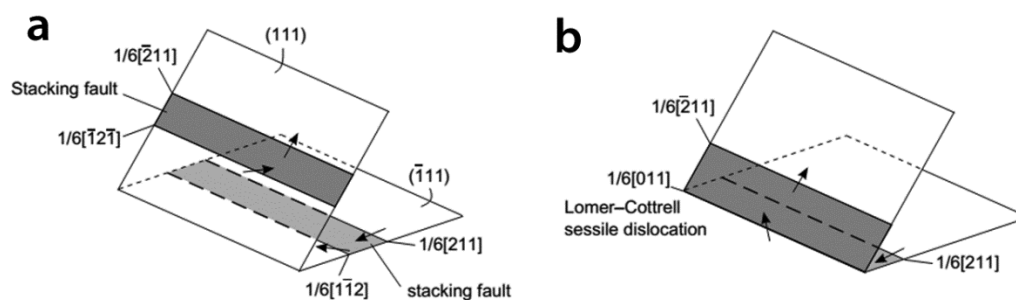


Figure 1-3, Formation of a Lomer-Cottrell sessile dislocation, (a) 2 pairs of dislocations glide on 2 different planes (b) interaction of 2 partial dislocations in the intersection of the planes [29].

Basically, dislocations are formed during crystal solidification and are always present in the microstructure of crystalline materials. It is known that the density of initial dislocations in

the structure is far too low to accommodate the plastic deformations during mechanical processes such as rolling or forging. Dislocations, thus, should multiply or be formed during deformation of a crystal. During deformation, the few present moving dislocations can intersect with each other and form steps on the dislocation line, which are called jogs. In some cases, the character of a jog on a dislocation is different from the character of the main dislocation. This means that the slip plane of the dislocation and that of the jog are different. This difference can locally hamper the motion of the dislocation so that the jogs act as pinning points for the dislocation. Furthermore, since screw dislocations do not have a unique slip plane, if they face some obstacles in their motion, they can change their slip plane locally and carry on gliding on a different slip plane which is called cross-slip, Figure 1-4. Again, in this condition, 2 segments of dislocations on both sides of the cross-slipped point would have different slip plane and behaviours. Cross-slipping therefore results in the formation of new pinning points for the dislocations. Interaction of segments of two dislocations to make a new dislocation can also result in the formation of new pinning points. Such pinning points have an important role in the multiplication of dislocations. A dislocation line segment confined between 2 pinning points can act as a dislocation source, which is called a Frank-Read source, and can act as a nucleation site for many dislocations into the structure. Figure 1-5 shows different steps of the operation of a Frank-Read source. Therefore, during plastic deformation, activation of dislocation sources causes a continuous increase of the density of dislocations. Consequently, the chance of dislocation intersections increases as well, which means a further increase of new dislocation sources in the structure.

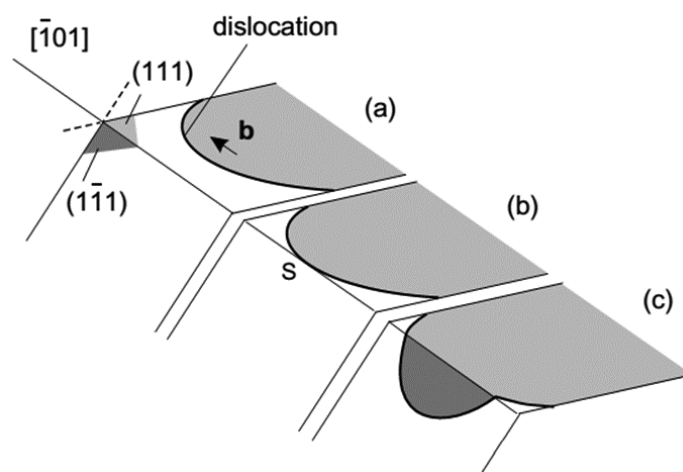


Figure 1-4, Sequence of events (a), (b) and (c) of cross-slip in an FCC crystal. The Burgers vector of the screw dislocation is parallel to the intersection of the planes, thus, it can cross-slip on different planes [29].

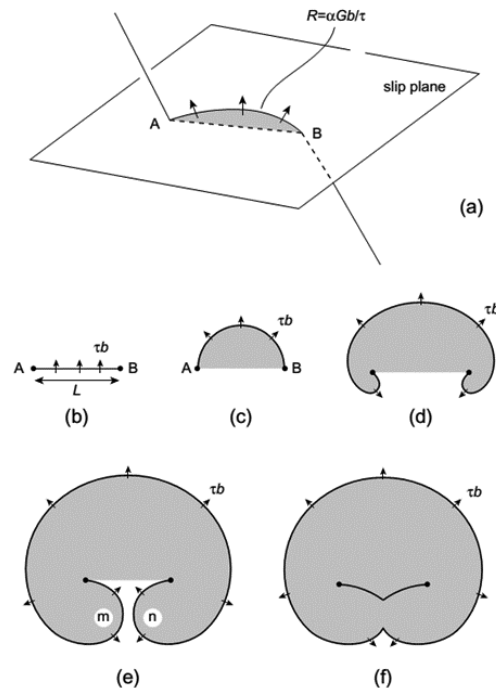


Figure 1-5, Schematic of the dislocation motion in a Frank-Read dislocation source [29].

Dislocations generated and stored in the microstructure of a deformed crystal can be classified in 2 categories: geometrically necessary dislocations (GNDs) and statistically stored dislocations (SSDs). GNDs are those dislocations (normally having the same sign) needed to accommodate the plastic strain gradient (like bending) in the material, while SSDs are random dislocations of which the total Burgers vector is 0 (statistically of equal positive and negative signs) and they do not induce any net strain gradient [33].

1.1.2 Interfaces

In addition to dislocations, various 2D interfaces can have a strong influence on the mechanical properties of polycrystalline materials, e.g., on the strengthening of metallic systems, crack initiation, fatigue crack initiation, stress corrosion cracking, irradiation embrittlement [34]. Polycrystalline materials generally contain grains (single crystals) with different crystallographic orientations which are separated by interfaces referred to as GBs. Changing and improving the mechanical properties of polycrystalline materials is possible by changing and controlling the type and the density of GBs in the microstructure of the polycrystalline material, which is often referred to as GB engineering. The geometry of a GB is macroscopically characterized by five degrees of freedom: three angles define the crystallographic orientation of the two crystals with respect to one another, while two parameters describe the inclination of the GB plane. Our knowledge about GBs and interfaces

is, although vast, still elementary and there are a lot of un-answered questions and answering these can help to design and develop new materials with better properties.

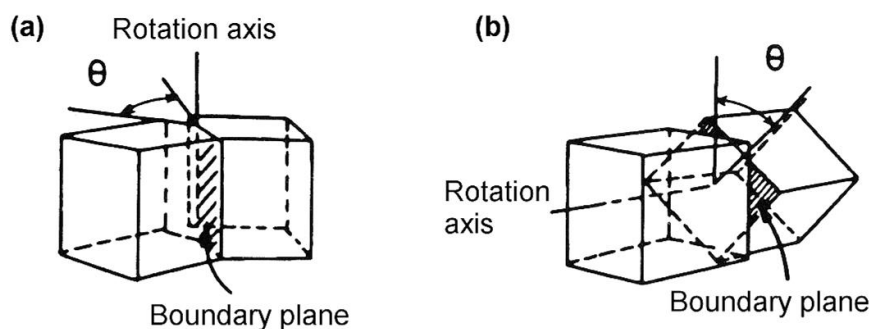


Figure 1-6, Schematic showing a tilt boundary, in which the rotation axis lies in the boundary plane and (b) twist boundary, in which the rotation axis is perpendicular to the boundary plane [35].

Depending on the misorientation, GBs are classified into 2 groups: the tilt type, when the rotation axis lies in the boundary plane, and the twist type, when the rotation axis is normal to the boundary plane (Figure 1-6). However, in reality a GB may have both tilt and twist components.

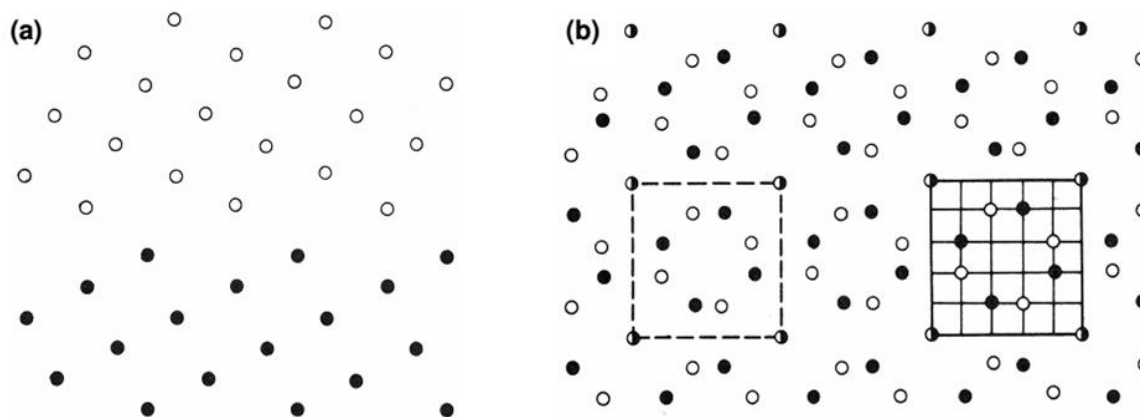


Figure 1-7, (a) Projection along the $\langle 001 \rangle$ axis of a $\Sigma 5$ boundary on a $\{013\}$ plane in FCC. (b) CSL made by overlapping both lattices. Half-filled circles are common lattice points. The dash square on the left represents the projection of the CSL unit cell; the DSC lattice is shown on the right by the solid lines (adapted from [29]).

GBs can be also classified according to the amount of misorientation between the two adjacent grains: (a) low-angle GBs with misorientation angles less than $10\text{-}15^\circ$ and in which the GB structure is well described by a periodic network of dislocations, and (b) high-angle

GBs with misorientation angles above $10\text{-}15^\circ$ for which description with dislocation networks is not possible.

For high-angle GBs the concept of the coincident site lattice (CSL) is used to describe the GB structure [36]. The lattices of two adjacent grains are hypothetically allowed to interpenetrate into each other. For certain misorientations, a proportion of the two sets of lattice points coincide; these lattice points yield the coincident site lattice. The CSL is defined by an odd integer Σ , where $1/\Sigma$ is the proportion of lattice sites that are common to both lattices. Figure 1-7 shows a schematic projection of a $\Sigma 5$ boundary in an FCC crystal and its corresponding CSL. For low-angle GBs such a CSL would become too large to be very useful.

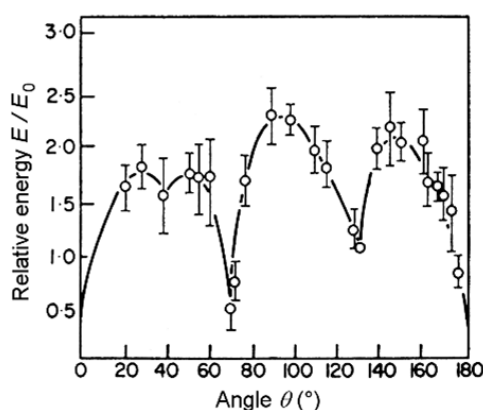


Figure 1-8, Measured relative energy of symmetric $\langle 110 \rangle$ tilt boundaries in aluminium as a function of misorientation angle. Three cusps can be distinguished at the angles corresponding to $\Sigma 9$, $\Sigma 3$ and $\Sigma 11$ boundaries, respectively [37].

Although the relationship between the Σ value and the GB energy is not fully understood, GBs of small Σ generally have a low energy, as shown by the cusps in the energy plot in Figure 1-8, such as the coherent twin boundaries ($\Sigma 3$) in FCC materials with misorientation of 70.53° having the lowest energies [38].

1.1.2.1 Image Force

The force acting on a dislocation near an interface or a free surface is called “image force”. The efficient distance for the image force to act is of the order of a few tens of nanometres. This force can be either attractive or repulsive depending on the stiffness of the environments on both sides of the interface. On the surface, since stiffness is 0 for air/vacuum, the image force is attractive [29]. In cubic materials, the image force from a GB is repulsive if the anisotropy factor, H in Equation 1-1, is positive and it is attractive if H is negative [36].

Equation 1-1

$$H = C_{44} - (C_{11} - C_{12})$$

where C_{44} , C_{11} and C_{12} are elastic constants of cubic materials.

1.1.2.2 Dislocations in Interfaces

GBs can be considered as (tiny) structures and dislocations can be defined within them. Such GB dislocations are linear defects like lattice dislocations but with different Burgers vectors that can only occur in GBs. When a GB dislocation moves inside its GB, the structure of the boundary (i.e., its CSL) before and after movement of the dislocation is the same and only the structure of the region around the dislocation is distorted.

Dislocations in a GB can be classified into 2 types: the primary intrinsic dislocations which are supposed to be perfect crystal dislocations, and the secondary dislocations which have a Burgers vectors smaller than perfect ones [36]. The set of all possible displacement vectors (the Burgers vector) which preserve the CSL defines a new kind of lattice which is the so-called Displacement Shift Complete (DSC)-lattice [39]. A DSC lattice of a $\Sigma 5$ boundary in an FCC crystal is shown in Figure 1-7 (b).

In special cases the possible dislocation Burgers vectors in a GB are very limited, e.g., in a coherent twin boundary (111) of an FCC crystal, the DSC Burgers vectors are $a/6 \langle 1 \ 1 \ \bar{2} \rangle$, $a/6 \langle \bar{2} \ 1 \ 1 \rangle$ and $a/3 \langle 1 \ 1 \ 1 \rangle$ of which the first 2 are glissile dislocations and the third one is a sessile dislocation.

Dislocations in a GB can be also classified in a different way: intrinsic or extrinsic [36]. The intrinsic dislocations are inherent dislocations which are needed in the GB and without them the GB cannot exist (also referred to as structural dislocations) [36] while extrinsic dislocations are those that moved into the GB from the grains during plastic deformation. Extrinsic dislocations normally produce long range elastic fields inside the GB [36]. An incorporated dislocation in a GB can either retain its lattice Burgers vector or dissociate into GB dislocations [34, 40, 41].

1.1.3 Interaction of Dislocations with Grain Boundaries

In polycrystalline materials there are numerous GBs which affect the glide of dislocations. To understand the plasticity and mechanical response of polycrystalline materials, understanding the influence of each type of GB on the glide of dislocations is crucial. Although the averaged effect of GBs on the mechanical properties can be predicted by some equations and

models have been proposed to explain them, the models are still a conjecture due to the lack of direct quantitative and dynamic evidences of the interaction between a dislocation and a GB [42, 43].

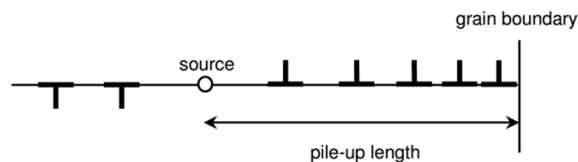


Figure 1-9, Dislocation pile-up [35].

In general, GBs are considered as effective obstacles to the motion of dislocations due to the lack of coherency between slip planes and slip directions inside the GB which makes further slip of dislocations in the adjacent grain difficult [42]. Therefore, dislocations pile-up occurs against GBs [44], Figure 1-9. Dislocation pile-up increases the local stress on the GB and when this local stress reaches a critical value, the elastic interaction of dislocations with a GB changes to a plastic interaction through different mechanisms. An overview of different plastic interaction mechanisms is shown in Figure 1-10. Similar to the interaction of the dislocations in a crystal, the mechanisms are possible if the sum of the Burgers vectors is conserved, Equation 1-2. If the total energy of all new dislocations sent into the sides of an interface and inside the interface is very high, then the interaction is unlikely and the interface acts as a barrier [42].

Equation 1-2

$$\sum_i \mathbf{b}_i^{(in)} = \sum_j \mathbf{b}_j^{(out)} + \sum_k \mathbf{b}_k^{GB}$$

On the other hand, if the slip planes on the both sides intersect along a line that lies in the GB plane, the geometrical conditions on both sides permit dislocations to transmit directly across the GB. This condition is satisfied in coherent twin boundaries. For example, if a pure screw dislocation interacts with a coherent twin boundary, it can be directly transmitted by cross-slip. The Burgers vector of the passing dislocation remains unchanged and no residual dislocation is left in the GB, Figure 1-10 (a). However, transmission of a pure edge dislocation requires leaving a residual GB dislocation, which is a DSC dislocation in the GB, Figure 1-10 (b).

Also, during the interaction of a dislocation with a GB, the dislocation can be totally absorbed by the GB without the emission of any dislocations in the adjacent grains,

Figure 1-10 (c). It can dissociate into DSC dislocations and according to their type, they can glide along the GB [34]. Successive absorption of dislocations may lead to the formation of a series of glissile DSC dislocations in the GB, which might form dislocation pile-ups at an obstacle inside the GB, such as a ledge. High local internal stresses due to the pile-up of GB dislocations inside the GB can cause either crack formation or dislocation nucleation from the GB into the adjacent grains, Figure 1-10 (d). The mechanisms by which dislocations are emitted in the adjacent grains (i.e., Figure 1-10 (a), Figure 1-10 (b), and Figure 1-10 (d)) are referred to as the slip transfer [36, 41].

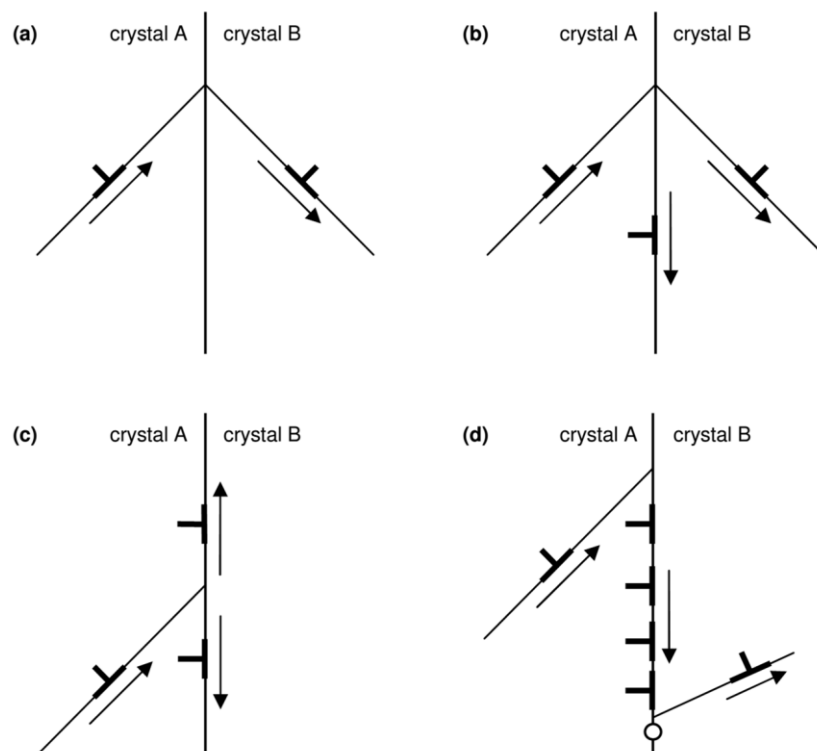


Figure 1-10, Dislocation-GB interaction mechanisms, (a) direct transmission by cross-slip of a screw dislocation, (b) direct transmission of a dislocation creating a residual GB dislocation, (c) absorption of a dislocation by dissociation into GB dislocations, and (d) absorption and re-emission following pile-up of GB dislocations at an obstacle in the boundary [35].

1.1.4 Size Effect

At micron and submicron scales, the mechanical properties of materials deviate from their bulk samples which this phenomenon is so-called size effect. There are 2 types of size effect, microstructural (intrinsic) size effects arising due to microstructural length scales, such as grain size and extrinsic size effects caused by dimensional constraints, such as sample size.

The dependency of strength of polycrystalline materials to the grain size is as an example of the microstructural (intrinsic) size effect. It has been observed that the strength of

polycrystalline materials can be enhanced by increasing the density of GBs, according to the Hall-Petch equation, Equation 1-3 [45, 46].

Equation 1-3

$$\sigma_i = \sigma_0 + \frac{k}{\sqrt{D}}$$

where σ_0 and k are constants and D is the grain size. This equation thus indicates that when reducing the grain size, i.e., increasing the density of grain boundaries, the strength of a material increases [42]. In the literature, three main models have been proposed to explain the Hall-Petch. (I) A first model is based on the concept of dislocation pile-up against a GB. In this model, the pile-up length is limited by the grain size and accordingly the stress on the dislocation on the head of the pile-up is limited. It is assumed that the macroscopic yielding occurs when dislocations are emitted into the adjacent grain which depends on the amount of stress exerted on the dislocation at the head of the pile-up. (II) A second model is based on the fact that GBs can act as dislocation sources at yielding. Therefore, the density of dislocations in the grains increase during the deformation and according to the Taylor law, the density of dislocations influences the strength of materials. Indeed, by increasing the density of GBs in the structure, the number of the GB dislocation sources increases and may result in a high rate of dislocation multiplication in the microstructure and consequently result in strengthening. (III) A third model is based on the fact that compatible deformation of grains in a polycrystalline material requires the introduction of geometrically necessary dislocations (GNDs) whose density is inversely proportional to the grain size. Therefore, due to the Taylor equation, the density of GNDs affects the strength. The detailed explanation of these models can be found in the 2016 review paper by Cordero et al. [43].

However, it has been observed that by decreasing the grain size below a critical value, materials may become softer and the Hall-Petch equation is not valid, as seen in Figure 1-11 by decreasing the grain size in Cu and Pd, the strength is decreasing, which is referred to as the so-called inverse Hall-Petch effect. A transition from intragranular to intergranular plasticity mechanisms has been observed in very fine-grained samples, i.e., dislocations cannot accumulate in nanocrystalline metals as they do in coarse-grained samples, dislocations emitted from GB junctions are often rapidly absorbed by other GBs after they traverse the grain interior, and intergranular deformation mechanisms such as GB sliding, GB migration, grain rotation start playing a dominant role in the plastic flow [43].

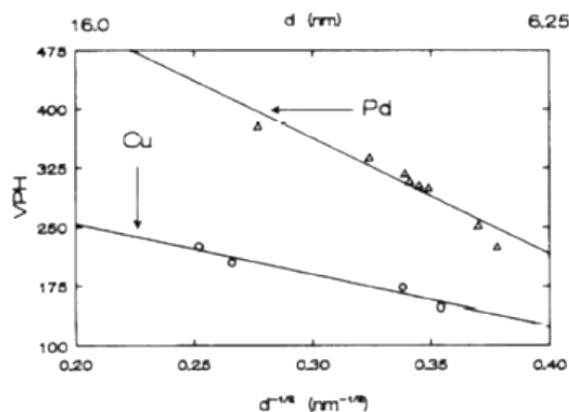


Figure 1-11, Inverse Hall-Petch trend for Cu and Pd [47].

The dependency of mechanical properties of small-scale samples to their external geometric sizes is an example of extrinsic size effect that has been observed in mechanical testing of small-scale materials [17]. “Smaller is Stronger” was the main observation in those studies and in general the strength inversely scales with the smallest dimension of the sample such as the thinfilm thickness, the nanopillar diameter or the size of nanoparticles [6, 18-23]. In addition, in such scales the plasticity can be totally different from bulk samples as in small-scale single crystal samples the plastic flow might be jerky and intermittent [48].

In general, the mechanical properties can be related in what extent dislocations can nucleate, propagate and interact. In small-scale samples, depending on the external sample size and the microstructure length scales, one or some of these processes might be affected and different mechanical properties might be obtained. For example, depending on the density of dislocations in a small-scale single crystal sample, the plastic flow can be intermittent or smooth- as in bulk materials- which is the influence of a microstructure length scale (intrinsic size effects). However, regardless of the density of dislocations, the size of the sample (extrinsic size effects) does limit the maximum length of the dislocation sources in the microstructure which affects the strength by influencing the nucleation process. Since in small-scale single crystal samples with low density of dislocations, the influence of extrinsic size effect is trivial and the extrinsic size effect is the main strengthening mechanism, the mechanical properties of such samples have been widely investigated and models have been observed and proposed to explain their behaviour [49-51]. For example, in single crystal FCC nanofibers or nanopillars, lack of dislocation sources, shutdown of present dislocation sources, or high rate of annihilation of dislocations on the surfaces might result a crystal without any dislocation source. Therefore, new dislocations have to be nucleated to

accommodate the plastic strain which it requires significant applied stresses [15, 52]. More information about the mechanisms involved in extrinsic size effect on single crystal samples is presented in Ch. 4.

1.2 Mechanical Testing,

Nowadays, standard mechanical testing methods are used to obtain mechanical properties of materials under various types of loading conditions (e.g., static and dynamic). These properties are used to guide the design of the maximum loading condition and the life expectancy of a component. For instance, tensile tests are used to obtain the strength of a material under a monotonic loading condition and the fatigue test is used to obtain the durability of a component under a cyclic loading condition.

1.2.1 Tensile Test

Many components experience a static loading condition during service and permanent plastic deformation or fracture are possible modes of failure in such components. Tensile testing is a standard mechanical testing method which is used to predict the failure. A typical engineering stress–strain curve obtained from a tensile test of a ductile metallic sample is shown in Figure 1-12 from which various mechanical properties can be obtained [53]. For example, Young’s modulus of the material is the slope of the first linear part of the curve, i.e. the part of the elastic behaviour, the yield point (σ_y) in the figure is the first point in the curve after the elastic part and where the stress and strain no longer show a linear behaviour and after which the macroscopic plastic deformation starts, the maximum stress of the engineering stress–strain curve, point M, is the ultimate tensile strength representing the maximum stress that a structure can sustain in tension. Beyond point M, the specimen starts necking and all deformation is confined to the necking part. As a result of necking, the stress decreases till the eventual fracture at point F. The fracture strength is the stress value at which fracture occurs [53].

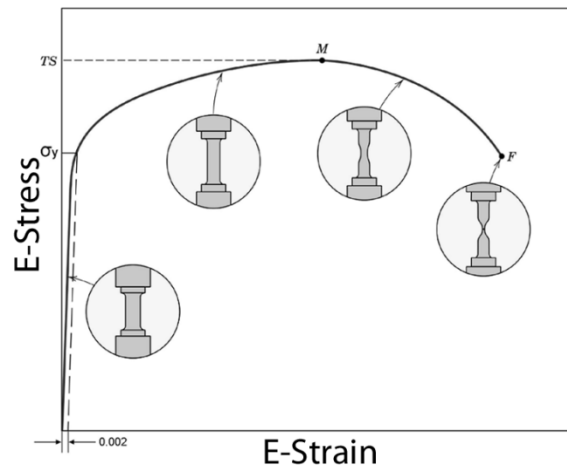


Figure 1-12, A typical engineering stress–strain curve for metals [53].

1.2.2 Compression Test

As an alternative mechanical testing, the compression test can be used to investigate the mechanical properties. In this case, cylindrical samples are often prepared and compressed by a flat punch. The results of a compression test are similar to those from tensile testing and most of the indicated properties can also be extracted from a compression test. However, ductility cannot be extracted and failure will occur in the shape of crushing or buckling.

1.2.3 Fatigue Test

Components can experience cyclic loading during service and failure can often happen at stresses below the yield point. The structural changes or damages during cyclic loading below the ultimate strength of a material are called Fatigue [54]. Fatigue has been a concern for industrial designs, as it is the main failure mode of components under cyclic (variable) loading and often occurs without any pre-macroscopic sign. Generally, fatigue behaviour of a component is presented by an S-N curve (load (as stress S) versus maximum number of cycles N before failure) which determines the fatigue limits. Figure 1-13 is an S-N diagram representing the fatigue limit of a component which is the initiation of the first crack at the microscopic scale. According to the load magnitude, the lifetime can change from infinite to few cycles and accordingly the S-N curve has been divided into 2 regimes:

- High-cycle fatigue regime (HCF)
- Low-cycle fatigue regime (LCF)

In general, in the HCF regime, no irreversible deformation is found at the macroscopic level while in the LCF regime a significant macroscopic irreversible deformation is detectable.

Within the HCF regime, at loads lower than a certain amount the lifetime seems to be infinite (e.g., more than 10^8 cycles) while at higher loads the lifetime is finite [55].

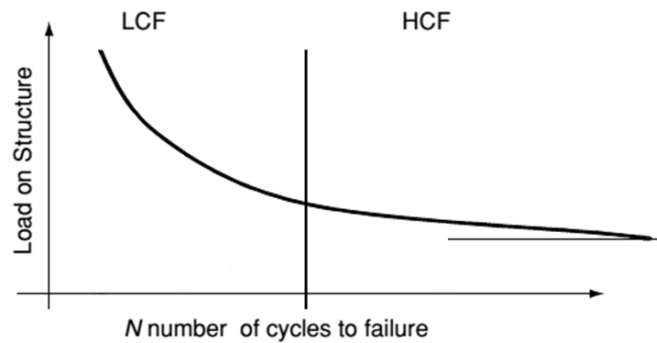


Figure 1-13, Schematic S-N curve marked by different fatigue domains [55].

1.2.4 Schmid's Law

To investigate the microstructural evolution of a crystal being subjected to mechanical testing, characterizing the local resolved shear stress τ , which acts on a specific slip plane along a specific slip direction, is important. Figure 1-14 schematically presents a diagram of a single crystal experiencing a monotonic tensile load, showing the orientations of the preferred slip plane and the slip direction. The slip plane normal (\mathbf{n}) and the slip direction (\mathbf{b}) are oriented at angles of φ and λ , respectively, with respect to the loading direction. The initial resolved shear stress τ on the slip plane should be expressed by Equation 1-4 in which the resolved shear force along \mathbf{b} , $F \cos \lambda$, is divided by the area of the slip plane, $A/\cos \varphi$:

Equation 1-4:

$$\tau = \frac{F}{A} \cos \varphi \cos \lambda = \sigma \cos \varphi \cos \lambda = \Omega \sigma$$

where σ is the stress and $\Omega = \cos \varphi \cos \lambda$ is the Schmid factor, which has a maximum value of 0.5. Therefore, in monotonic loading of single crystals, the resolved shear stresses applied on each slip system can be measured. In general, the slip systems with the highest resolved shear stress (the Schmid factor) are activated first. When a crystal loaded in a way that the 2 highest Schmid factor values are not close to each other, the deformation initiates by activation of just one slip system and this condition is generally called the single-slip condition. All other cases, i.e., where deformation is initiated by the activation of more than 1 slip system are referred to as the multi-slip condition.

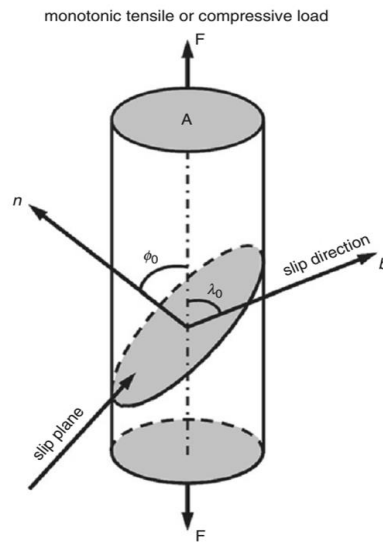


Figure 1-14, Slip elements of a single crystal in monotonic tensile or compressive load [56].

1.2.5 Microstructural Investigation

To understand the elementary governing mechanisms in monotonic deformation and fatigue, microstructural investigations are inevitable. Microstructures can be investigated from different aspects, such as dislocation behaviours, GB structure transformation and phase transformations. Microstructural investigation of dislocation behaviour in deformed polycrystalline materials is complicated since the grains are typically under complex, possibly unknown, 3-dimensional loading conditions and the interpretation of the origin and behaviour of dislocation structures becomes very difficult. Moreover, the observed macroscopic mechanical behaviour of polycrystalline materials is the average behaviour of all the grains, so correlating the dislocation structural changes in an individual grain to the observed macroscopic mechanical properties is not straightforward. Therefore, to decrease the complexities, single crystal samples have been used to investigate the dislocation behaviour during mechanical testing, e.g., tensile and fatigue tests.

A schematic stress-strain curve from a monotonic deformation test of a single FCC crystal is presented in Figure 1-15. For an FCC (such as Ni) single crystal oriented for single slip, the stress-strain curve can be divided into three stages. Stage I in Figure 1-15 commences after the initial elastic deformation (far left of the figure); this region is referred to as “easy glide” which is generally characterized by the slip of dislocations on the highest Schmid factor slip system, the primary slip. In the “easy glide” regime, dislocations move in the structure very easily and deformation progress does not need a significant load increase. In the transition from stage I to stage II in Figure 1-15, the loading condition (due to the crystal lattice

rotation) changes in such a way that dislocations on the other slip systems, so-called secondary dislocations, can also participate in the deformation. Activation of different slip systems increases the chance of the interactions and intersections of dislocations which means a dramatic increase of the density of dislocations and dislocation locks in the microstructure in stage II. The dislocation structure becomes like a complex tangled net of threads which is called “dislocation jungle” and which becomes denser by increasing plastic deformation. In this condition, dislocation motions and consequently plastic deformation become difficult. When the density of dislocation reaches to a certain amount, stage III in Figure 1-15, the “exhaustion hardening” region, starts where the mechanisms, as dislocation annihilation, play an effective role and counteract the further increase of the dislocation density. In this process, which is called “recovery”, the dislocation structure converts to areas almost dislocation-free surrounded by dense dislocation walls often referred to as a “cell structure”. Further plastic deformation of the crystal is accompanied by the shrinkage of the dislocation-free areas and the formation of the finer dislocation cell structure [57].

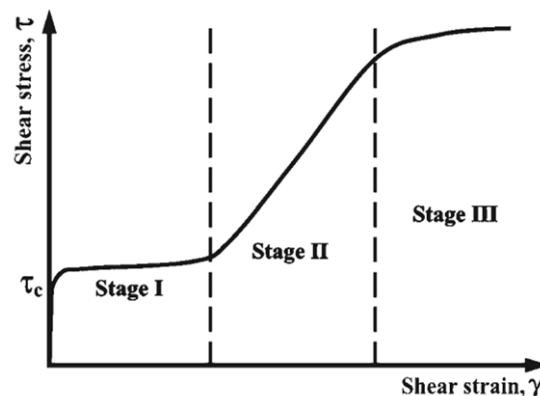


Figure 1-15, Schematic of the typical shear stress-shear strain curve of an FCC single crystal [56].

Microstructural investigations have also been carried out on fatigued single crystals. To investigate and to correlate the fatigue properties with dislocation structure evolutions in single crystals, cyclic stress-strain (CSS) curves were established. To draw a CSS curve, single crystal samples oriented for single slip were subjected to cyclic deformations with constant plastic strain amplitudes, γ_{pl} , under a fully reversed loading which means the sample experiences sequential tensile and compressive loading cycles with the same amount of force. It has been observed that generally a crystal under such experiment faces hardening and the peak stress increases slowly and approaches the saturation stress, τ_s , after N_s cycles, Figure 1-16 (a) [58]. A CSS curve is, then, obtained by drawing different τ_s obtained by

different γ_{pl} from different samples as shown in Figure 1-16 (b). Mughrabi [59] performed a microstructural investigation on single slip-oriented Cu single crystal samples from different regimes of the CSS curve, and observed the evolution of the dislocation microstructure in 3 regions marked by A, B, and C, Figure 1-16 (c). The fatigue properties of single crystals are controlled by the collective behaviour of dislocations. Depending upon the load magnitude, the dislocation configurations can be veins and channels, persistent slip bands (PSBs), labyrinth, or a cell structure as shown in Figure 1-16 (c).

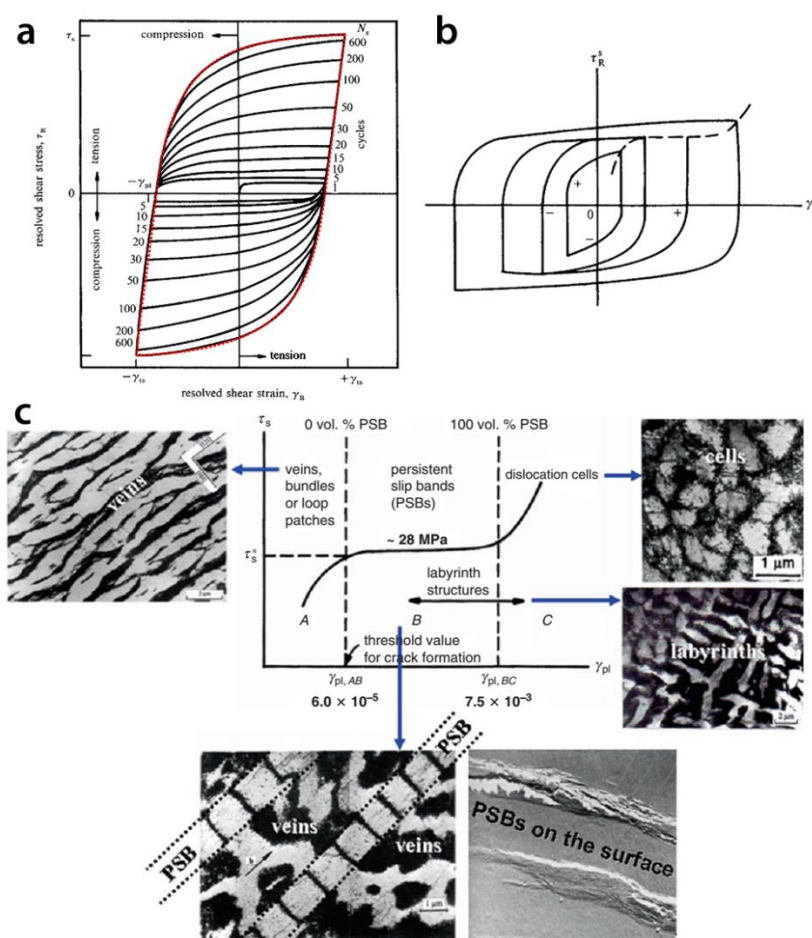


Figure 1-16, (a) Schematic of typical variation in resolved shear stress τ as a function of the resolved shear strain γ for a single slip oriented FCC single crystal, (b) and (c) schematics of the CSS curve of Cu single crystals oriented for single slip showing three distinct regions as well as the corresponding features of dislocation structures [56, 58].

At low values of plastic strain amplitude, region A, work hardening occurs during cyclic loading and the dislocation microstructure in this region consist of veins and channels with parallel dense patches of dislocations in between dislocation free areas. Region A is then followed by a strain independent region B, known as the plateau.

One of the visible features of cyclic saturation in the plateau regime is the formation of the localized persistent slip bands, PSBs, which often act as preferential sites for fatigue crack nucleation. Formation of the first PSBs starts at the lower end of the plateau region and the dislocation structure is 100% PSBs at the end of the plateau, Figure 1-16 (c) [60]. A further increase in plastic strain amplitude leads to an increase in the saturation stress, region C. The dislocation microstructure in this region is either a labyrinth or cell structure which indicates the large contribution of a secondary slip system, Figure 1-16 (c).

Basically, the materials with mentioned dislocation microstructures behave like composite materials; the regions with high density of dislocations act as reinforcement elements and the dislocation free areas act as soft matrix regions. The plastic deformation is thus mainly, accommodated by dislocation free areas.

The shape of CSS curves for double slip and multislip condition samples will be different and some of the mentioned dislocation structures cannot appear in the structure. Due to the fact that from the start at least 2 slip systems are activated simultaneously, the most common observed dislocation structures are either labyrinth or cell structures.

1.3 Overview on Micro- and Nanomechanical Testing

Since small-scale technologies have found so many applications in the last decades, studying the mechanical properties of small-scale materials has become one of the hot topics in mechanics of materials and various micro/nano mechanical testing methods have been developed. Mechanical testing of materials at small-scales started by indentations at the micron scales (referred to as nanoindentation) [61] and scanning probe microscopy (SPM) techniques [62].

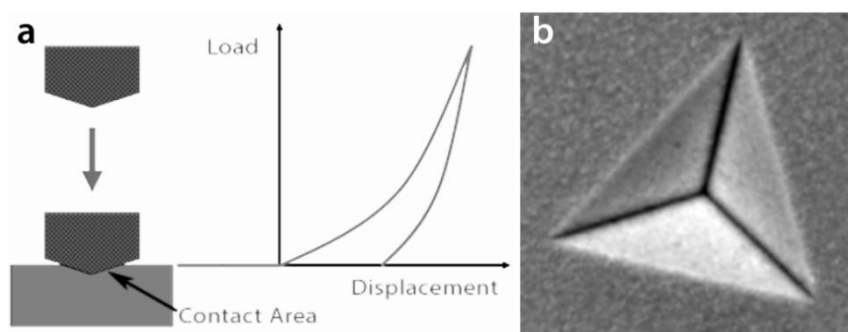


Figure 1-17, (a) Schematic of an indentation test and (b) nanoindentation in Ni [63].

Nanoindentation is very similar to hardness test experiments while the load applied to the surface by a Berkovich diamond indenter is very low (lower than few mN). During nanoindentation, the tip penetrates the surface of the sample, Figure 1-17 (a). The load and displacement data of the indentation allow for the determination of mechanical properties such as elastic modulus and hardness [63]. Nanoindentation is used at surfaces of bulk materials and coatings, Figure 1-17 (b) [64].

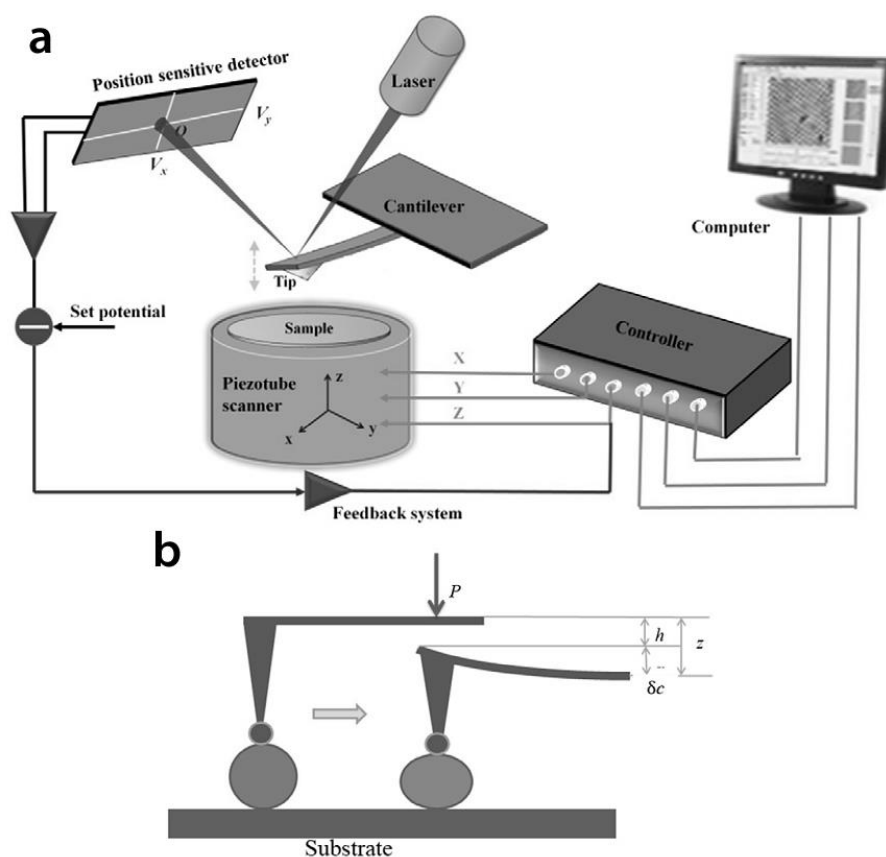


Figure 1-18, Schematic of (a) the basic principle of AFM, and (b) deformations of the particle by an AFM tip. Left: before deformation of the particle and right: during deformation [65].

SPM related techniques such as atomic force microscopy (AFM) started to be used in the field of mechanics of nanoscale materials [64]. The advantage of AFM compared to nanoindentation was that it allows observing the surface (particles) and selecting the proper location for indentation. Furthermore, since the size of the tip is finer than nanoindentation, it allows measuring the properties in smaller areas. Figure 1-18 (a) shows the image formation in an AFM. The sample surface is scanned by a tip connected to a cantilever and the deflection of the cantilever is quantified through a laser beam system which will be converted to the height and accordingly a 3d view from the surface can be obtained. Once the topographic image of the sample is obtained, the proper location or particle for indentation

can be selected and indentation can be done, Figure 1-18 (b). The valuable information of nanoparticles, such as hardness, elastic modulus and the adhesion between nanoparticle and substrate can be obtained. However, since determining the exact shape and dimensions of AFM tips is difficult and the cantilever has multiple degrees of freedom as it is approaching the surface, obtaining the reliable absolute measurements by AFM is challenging. At high forces, the cantilever can also be damaged. However, AFM is certainly only option to measure and compare the mechanical properties from very small areas (phases) or of very thin samples [66].

In 2004 for the first time, Uchic et al. introduced a micropillars fabrication technique by focused ion beam (FIB, see also chapter 2.6.2) and performed microcompression tests of those micropillars using the flat-punch tip of a nanoindenter, Figure 1-19 [13]. It was a revolution in mechanical testing of small-scale materials since the authors could resolve the main difficulties of such experiments, e.g., controlling the geometry (shape) and the orientation of the micropillar samples and proper aligning of the sample and the indenter to perform the experiment.

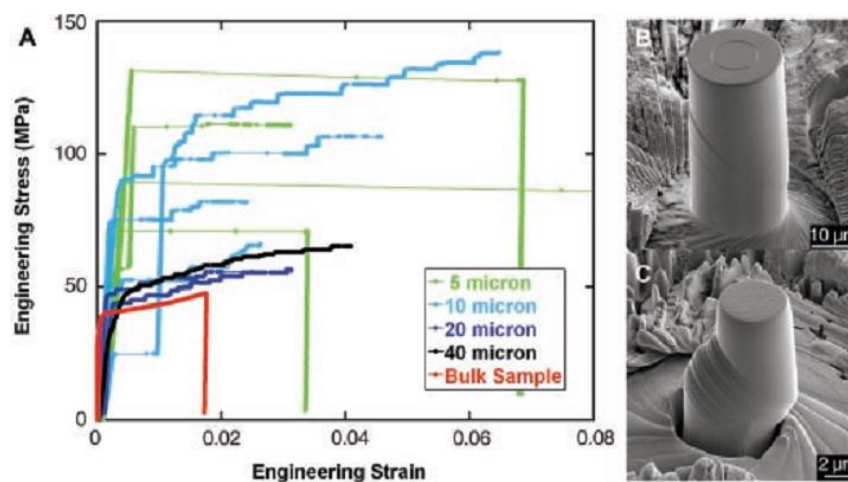


Figure 1-19, (A) Stress-strain curves for pure Ni microspheres ranging in size from 40 to 5 μm in diameter, as well as the stress-strain curve for a bulk single crystal. (B) A SEM image of a 20 μm diameter micropillar tested to 4% strain. (C) A SEM image of 5 μm diameter micropillar after testing, where the sample achieved 19% strain [13].

First, size-effect in small-scale single crystal plasticity started being investigated [67], and then evolved into studying the fundamental questions, such as the interplay between plastic deformation and microstructure components such as second phase inclusions [68, 69], GBs [70-74], and interfaces in multi phases materials [75, 76]. Also fracture of micropillars was investigated [77-79].

In the last decade, the development of the miniaturized mechanical testing methods went so fast that nearly all types of mechanical testing, e.g., compression, tensile, bending, fatigue and fracture tests, are at the moment possible at the micro/nanoscale. These tests can be performed in-situ in scanning electron microscopy (SEM), (scanning) transmission electron microscopy ((S)TEM) or X-ray diffraction techniques.

However, in spite of the technical improvement in instruments for micro/nanomechanical testing with improved resolution of the load and the displacement data acquisition, several challenges and pitfalls remain such as the sample preparation (e.g., imperfections in sample geometry and FIB induced damages) and the performance issues (e.g., uncontrolled friction between flat punch and compression sample, and lateral stiffness of the system) and need careful thoughts to prevent misinterpretation of the results.

1.3.1 Miniaturized Deformation Methods

Nowadays, two principal methods are used for micro- and nanomechanical testing:

- (i) Miniaturized test rigs which can exert small forces and fine displacements [80-83],
- (ii) MEMS-based designs [84-86] where the sample either is directly integrated into a mechanical chip or needs to be mounted on a chip. MEMS-based designs either are self-actuated or require external actuation; examples are the straining chip developed by Saif et al. [84] which are stretched by conventional biasing TEM holders or lab-on-chip test platforms in which thin films are stretched due to the internal stress stored in an actuator beam in the chip [87] or the push-to-pull chips [88], which is loaded by TEM nanoindenter holders.

1.3.1.1 The Modes of Deformation

In general, the current available instrumented machines (the rigs and nanoindenter) have following modes of deformation: (i) Load Control Machines and (ii) Displacement Control Machines.

Typically, load controlled indenters are actuated by either electrostatic or magnetic forces. The applied force scales with the applied signal (voltage or current). In this mode, during the experiment, the load on the sample is controlled and can be continuously increased. The systems operating in this mode have proven to work very well for a steady force increase and yielding can be detected by the first displacement burst. Piezo ceramic actuators having linear

expansion behaviour with an electric field allows for a displacement controlled mode of deformation. It is assumed that the bulk ceramic actuators have high stiffness whose contribution in the displacements is negligible [15].

1.3.2 Micro- and Nanomechanical Testing Methods

1.3.2.1 Micropillar Compression

Among the micro- and nanomechanical testing methods micropillar compression testing is the most preferred one owing to the simple and straightforward FIB sample preparation, and the highly available required instrumentation, the test rigs and SEMs. Furthermore, compared to some other techniques, such as bending test and nanoindentation, the interpretation of the mechanical data is considered to be less complicated.

However, there are some considerations about the interpretation of the results in this method. It has been proven that FIB milling can affect the material properties close to the surface. Since the ratio of the surface to the volume is very high, using FIB for milling the sample, as used for preparing micropillars, can alter chemically and structurally the surface characteristics. Consequently, the obtained mechanical properties cannot be generalized [89, 90]. Misalignment or a non-parallel arrangement of the flat punch surface with respect to the sample top surface obviously can lead to a non-uniaxial stress loading condition by which the sample deformation mode or even the failure mode can drastically change [91, 92]. The friction between the top surface and the flat punch indenter can also result in barrelling of the sample, which changes the designed uniaxial loading condition and makes quantitative analyses of hardening challenging. The other issue about the compression of the micropillars is the tapering which makes the shape of the pillars non-uniform resulting in a non-uniform deformation along the sample. Without considering the mentioned issues, misinterpretation of the mechanical results from the compression test is, therefore, very likely and plausible.

1.3.2.2 Tensile Test

Most disadvantages of the micropillar compression testing can be prevented by microtensile testing, as introduced by Kiener [50]. The tensile specimens are either clamped by a counter body with opposing shape (gripper) [50], Figure 1-20, or mounted on a Push-to-pull (PTP) MEMS device using a gas injection system in a FIB system [83, 93], Figure 1-21. Tensile testing is not prone to mechanical instabilities such as buckling [81, 94] and the straining can be considered uniaxial. Therefore, the obtained mechanical data is very reliable and interpretation of the results is more straightforward than other methods.

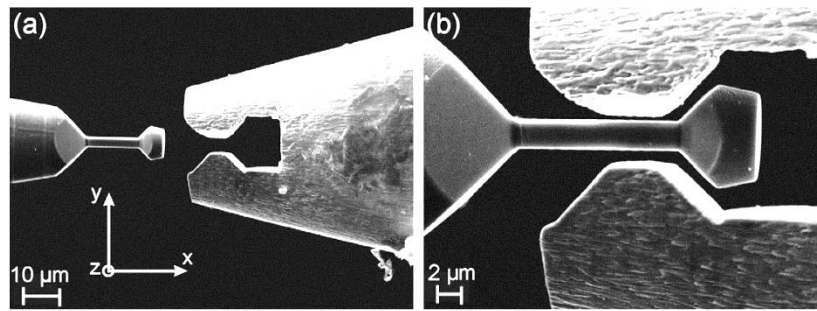


Figure 1-20, SEM image showing a single-crystal copper tension sample and the corresponding tungsten sample gripper (a) before the test and (b) prior to loading at a low magnification [50].

However, the tedious and time-consuming sample preparation by FIB and FIB induced-artefacts have made it a less common but interesting since it offers various alternative approaches.

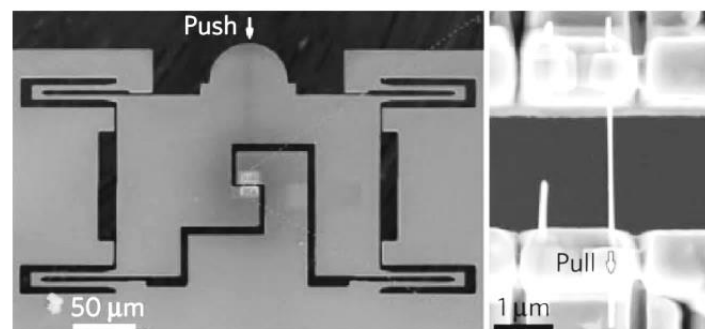


Figure 1-21, Push-to-Pull device with a mounted NW using FIB [93].

1.3.2.3 Bending

Although the homogenous uniaxial stress condition is the main advantage of the micro tension experiments, it is not well-suited to probe the influence of the strain gradient [95] on the material response which in some cases can be important [19]. The bending test has the advantages of the compression test; however, as mentioned before the interpretation of the mechanical results is difficult and simulation should be used. [96].

1.4 In-situ Approaches in Micro- and Nanomechanical Testing

Using special instruments to observe, to manipulate, to prepare the small objects and to perform the experiment is inevitable and this challenge of micro- and nanomechanical testing might be a benefit. Combination of the miniaturized testing systems with the characterization techniques present in different instruments, such as electron microscopes, permits to obtain valuable information before, during and after mechanical testing, such as the local strain and the orientation changes, defect characterization and defect behaviour.

Extremely powerful techniques for in-situ micro- and nanomechanical testing are SEMs and (S)TEMs. SEMs can provide high resolution images during deformation which reveal the changes of the morphology of a sample during the experiment. They can be equipped by an electron backscatter diffraction (EBSD) detector which allows accurate orientation mapping. Furthermore, using high resolution EBSD technique allows mapping the distribution of GNDs near the surface after deformation. Electron channelling contrast imaging (ECCI) technique can be used in SEMs which allows imaging the crystal extended defects near the surface (<100 nm) with the resolution of a few nanometer [97].

On the other hand, (S)TEMs can provide other valuable information about a sample. Due to the nature of the technique, (S)TEMs enable to observe real time dynamics of defects, like dislocations, in different stages of deformation. New advanced techniques like automated crystallographic orientation mapping (ACOM) [98] and strain mapping [99] also allow following the variation of the orientation and the strain gradient in a sample during in-situ experiments. Furthermore, the recent advent of fast direct electron detectors allows to record hundreds of images per second which can be used to resolve the dynamics of defects in such experiments [44, 99-101]. However, the main disadvantage of in-situ (S)TEM nanomechanical testing is that the sample should be electron transparent which limits the thickness of the sample to 300 nm.

X-ray diffraction by synchrotron radiation is the other available technique which can provide quantitative insights into the local orientation changes as well as the evolution of GNDs and SSDs in the microstructure [102-104]. Due to the high penetration of X-rays, using thicker samples is possible.

1.5 In-situ Testing in Transmission Electron Microscopes

1.5.1 Mechanical Straining Holders

Nowadays there are various approaches of mechanical testing inside a TEM. They span from simple mechanical actuation TEM holders (classical holders) to miniaturized MEMS (Micro Electro-Mechanical Systems)-based testing machines (nanoindentation TEM holders) [105].

1.5.1.1 Classical Holders

The very basic commercially available straining holders are the classical ones. The sample to be used in such holders is either the electron transparent sample glued to a grid or a dog-bone shape sample with a thinned region in the centre Figure 1-22 (a). Then the sample (the grid or

the dog-bone sample) is fixed on the holder as shown in Figure 1-22 (b) and (c). The holder stretches the sample by a gear box actuated by an electric motor located in the holder section outside of the TEM, Figure 1-22 (b) and (c).

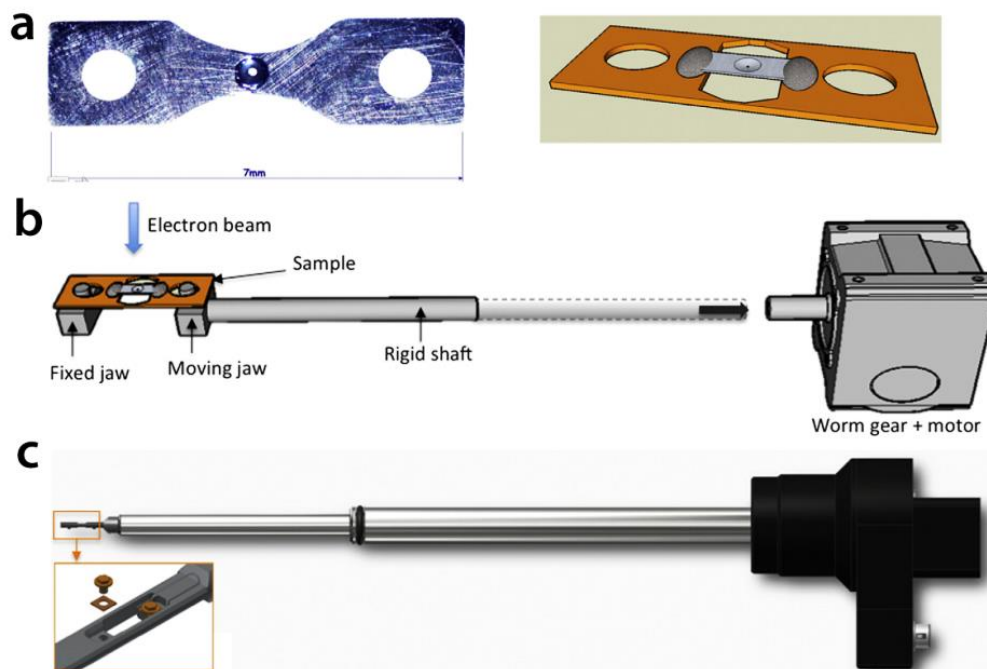


Figure 1-22, (a) Samples for in-situ TEM straining, the dog-bone shaped sample and the tensile sample glued on a copper grid, (b) Schematic showing the sample mounting on holder and the holder components and (c) a commercial holder for FEI microscopes made by Gatan Co, [105].

The classical holders have some advantages making them very widely used today. They are very versatile, any thin or thinned sample can be used, and they can include heating or cooling options. In general, for metals, electro-polishing is used for thinning which means the presence of a hole in the sample with electron transparent edges. The deformation occurs in a relatively wide area of the sample and therefore following the microstructural changes of the whole thin part of the sample is impossible. However, due to presence of the hole, early fracture of the sample is very likely [105].

1.5.1.2 Nanoindentation holders

Nanoindentation TEM holders are the other type of holders in which the advantages of the accurate positioning, controllability and measurability of the force and the displacement in nanoindentation instruments is used.

Nowadays, the commercial indentation holders are mainly from two companies: Bruker (Hysitron®) Pi 95 Picoindenter holder, Figure 1-23 (a), and Nanofactory Instruments AB®,

Figure 1-23 (b). At first, Bruker [106] holders used a loading mode based on the capacitance variation similar to the large scale nanoindenters [107, 108] and were only available for JEOL microscopes because of their larger holder space, while Nanofactory holders were based on MEMS technologies [109] and could fit to more models of TEM. The other difference of these 2 holders is that in Bruker holders, a hard tip is pressed against a fixed sample while in the Nanofactory holder, the tip is fixed on the top of the force sensor and a sample is pressed against the tip, Figure 1-23.

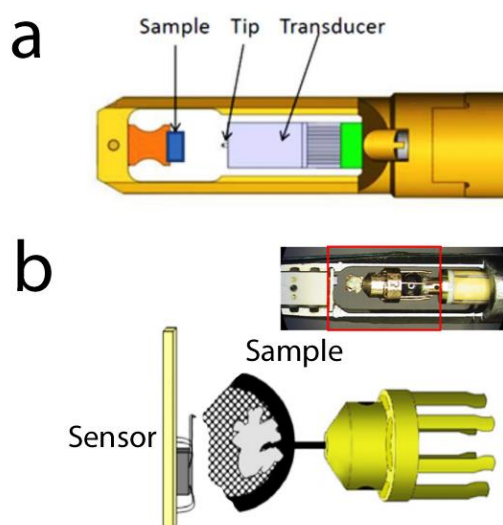


Figure 1-23, Schematics showing (a) Bruker PicoIndenter holder and (b) Nanofactory Instruments AB holder [110, 111].

Nanofactory stopped producing the holders on 2013 and so Bruker holders became the only available commercial holders. Later on, Bruker holders were, as well, equipped with MEMS-based indenters which allowed having the holders for various models of TEMs [105].

Figure 1-24 shows various types of available indenters on the market and the corresponding prepared shapes of the sample to perform indentation. In general, the main difficulty of using such holders is to set the tip and the sample at the same height during operation. The other intrinsic drawback of such mechanical tests is a complex mode of deformation of the samples which makes a proper and quantitative interpretation of the results without simulation impossible [105].

However, converting the diamond tip of an indenter into a gripper or using special MEMS devices, for instance PTP devices, enables one to perform tensile tests by such nanoindenter holders as mentioned before.

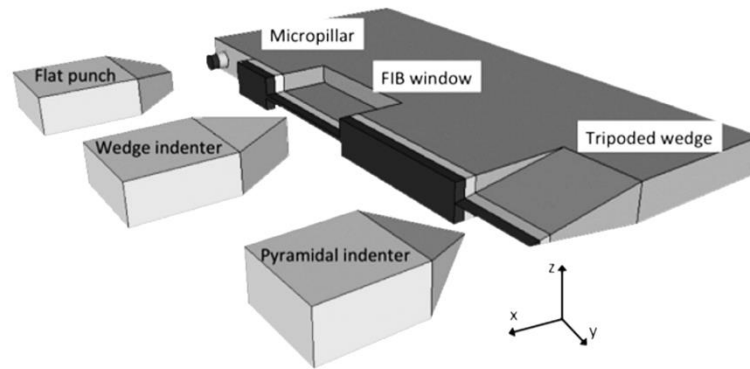


Figure 1-24, Different configurations of various indenters and different modes of the sample, the shape of the tip can be either pyramidal (sharp tip), wedge-shaped or flat punch-type. The sample can be also a FIB prepared micropillar, an H-bar window or a wedge [105].

1.5.2 Micro Electro-Mechanical Systems

Passive MEMS Push-to-Pull devices are among the simplest MEMS which can be processed in very few lithography steps on Si wafers. Due to their geometrical designs, Figure 1-25, a pushing force applied usually by a nanoindentation holder converts to a pulling force in the gap in the centre of the device where a tensile sample is mounted. The Gas Injection System (GIS) and corresponding metal deposition by FIB are used for mounting/attaching the sample onto the platforms on either side of the device gap. The applied compression force on the device and the geometry of the arms produce opposite movements of the platforms. In these set-ups, the resulting stress–strain curve has to be corrected by removing the stiffness of the empty PTP [112].

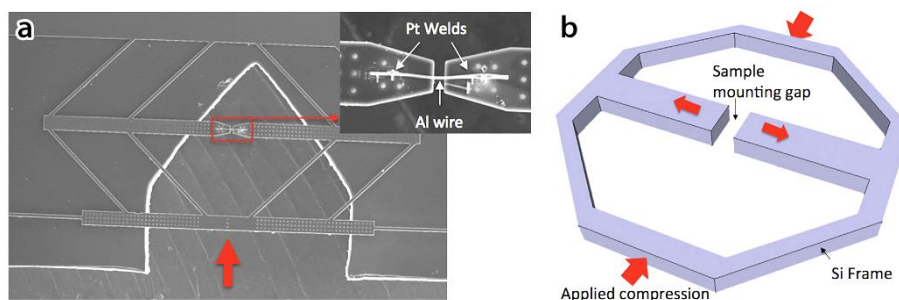


Figure 1-25, (a) Passive MEMS Push to Pull device fabricated through Si lithography, and (b) mechanical principle to convert a compression force into tension, [105].

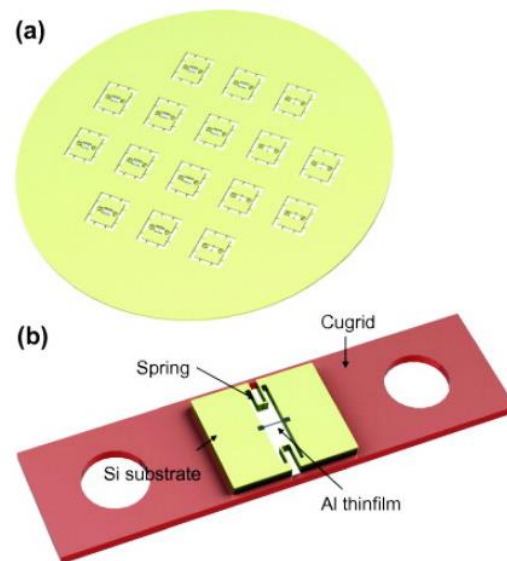


Figure 1-26, (a) An assembly of micro test MEMS devices containing Al thin films and (b) the final configuration of the test setup [113].

To avoid micromanipulation (harvesting, mounting) of samples (wires, fibers, films), the next step was the co-fabrication of the sample together with its testing frame. These tensile MEMS were inspired from complex passive structures designed by Saif and co-workers [84, 114]. In this case, the MEMS design facilitates the handling of the sample (the thin film) and fewer defects due to FIB milling will be introduced. Momprou et al. used a Si structured block supporting a nanocrystalline Al thin film prepared using vapour deposition and tested them successfully in a classical straining holder, Figure 1-26 [113]. The co-fabrication, however, has some drawbacks; the large scale FIB cutting increases the chance of contamination by Ga ions, the force measurements are either impossible or should be done by viewing a part of the device far from the sample and switching the viewing area is thus needed. Also, the stiffness of the machine/device is limited.

On the other hand, the lab-on-chip test platforms which are elementary test structures are designed to enable mechanical testing without using external actuators. In this technique, micro-fabrication methods including lithographical depositing, patterning and etching are used to produce long beams of actuator and the test specimens which are attached to the actuator on a chip [87, 115]. The actuator material is chosen and deposited in a way to have a controlled and designed amount of internal stress. The loading on the sample is initiated by removing a sacrificial layer separating both the sample and the actuator from the substrate by selective etching. This leads to the relaxation of the internal stress in the actuator and consequently uniaxial tensile loading of the sample. Figure 1-27 (a) shows schematically

different steps of the preparation. The behaviour of one specimen provides one point on the stress-strain curve. In order to extract a full stress-strain curve, the specimen/actuator length ratio is tuned. Recently, the lab-on-chip was extended to study creep/relaxation behaviour of thin films by producing tests structures adapted to 3 mm classical TEM holders, Figure 1-27 (a) [116].

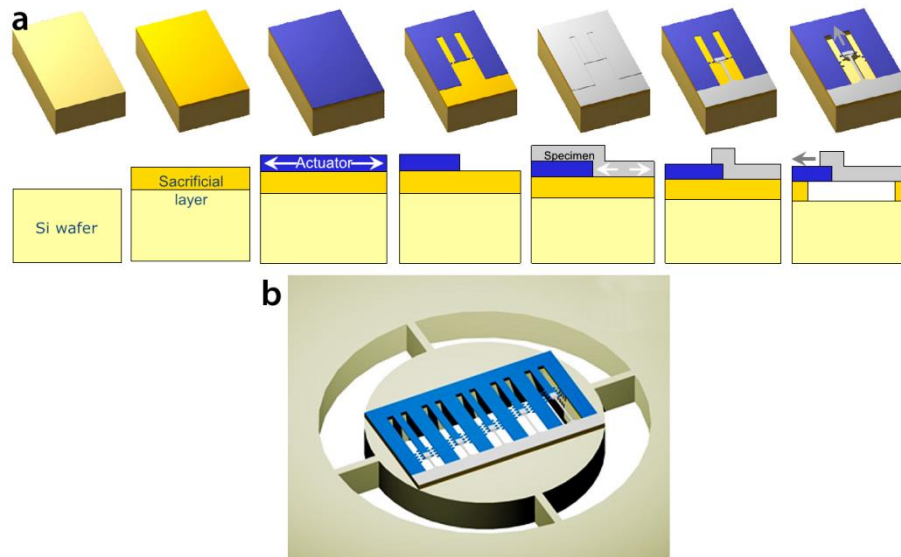


Figure 1-27, (a) The steps of preparing a lab-on-chip by lithographical processes and (b) the schematic in-situ TEM version of lab-on-chip [87].

Furthermore, some MEMS devices have been designed with built-in actuators and sensors, Figure 1-28. Espinosa et al. were among the first who developed such active MEMS devices [117]. Injected electrical power serves to apply a stress, and capacitance variations can be calibrated to directly obtain the displacement [118]. However, these techniques are very complex, time consuming and the available types of materials and their microstructures are very limited.

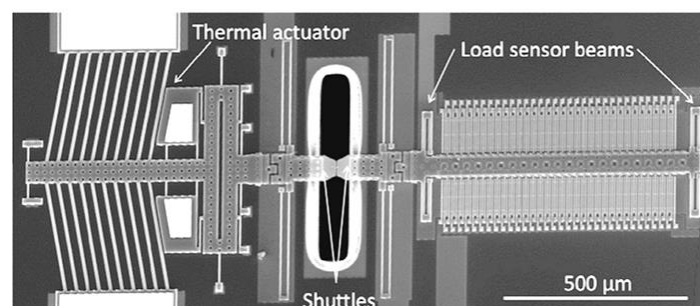


Figure 1-28, Active tensile test MEMS device with force-displacement measurement platform [105].

Chapter 2:

Materials and Methods

2 Materials and Methods

2.1 Materials

In this work high purity Ni (99.999%) (Goodfellow GmbH, Bad Nauheim, Germany) were used for in-situ TEM and in-situ SEM mechanical testing.

2.2 Transmission Electron Microscopy (TEM)

2.2.1 Introduction

Transmission Electron Microscopy (TEM), a very powerful and now common technique for the observation of the internal microstructure of materials and crystal defects such as dislocations, SFs, and GBs, was first developed by Ernst Ruska and Max Knoll in the 1930's. A transmission light microscope and a TEM operate on the same basic idea. Instead of the light in an optical microscope, an electron beam is used in TEM; therefore, in the structure of the microscope the electro-magnetic lenses are used instead of glass ones and the beam pathway has to be in vacuum.

A conventional TEM consists of an electron gun, the condenser lens system, the specimen stage and the imaging system, Figure 2-1. The electrons are generated by the electron gun with a specific range of energy (order of several hundred thousand V). The electron beam is, then, condensed by the condenser lens system to form a small spot on the sample. The electron beam interacts with and passes (at least in part) through the specimen. The imaging system enlarges the transmitted beam and yields a projected-like image of the materials internal structure on a fluorescent screen or a camera.

The resolution of a microscope is defined as the closest distance between two points in the sample which can be distinguished through the microscope. The theoretical resolution "r" (m) is proportional with the wavelength λ (nm) of the probe based on the Rayleigh criterion [119]:

Equation 2-1:

$$r = \frac{0.61\lambda}{\mu \sin\alpha}$$

where μ is the refractive index of the medium between the object and the objective lens and the semi-angle α is referred to the microscope apertures. It is clear that decreasing λ and/or increasing μ and/or α can improve the resolution. A high energy electron beam has a much

smaller wavelength than light (factor of many thousands) which yields a much better resolution for the TEM than for optical microscopes. By using the wavelength of an electron beam accelerated by 100 kV ($\lambda=0.0037$ nm), the refractive index of 1 for vacuum and $\alpha=0.02$ radians (around 5 degree), it is theoretically possible to have a resolution of 0.1 nm using TEM which is smaller than the typical distances between two adjacent atoms in a crystal [119]. Adding aberration correctors to the lens systems and a monochromator to the gun can even yield resolutions down to the pm range.

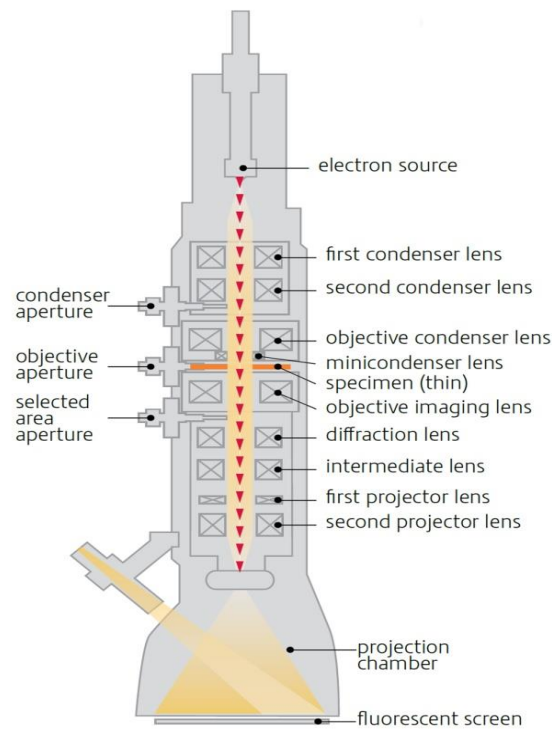


Figure 2-1, A cross-sectional view through a conventional transmission electron microscope [119].

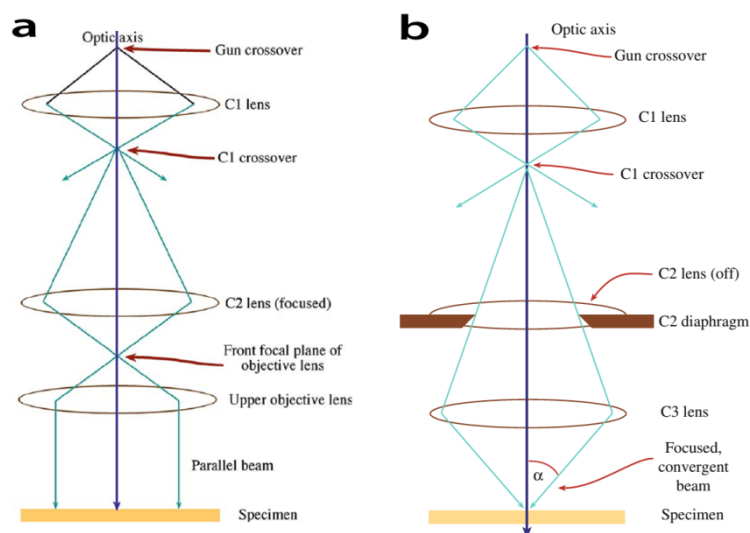


Figure 2-2, Schematic illustration of (a) a parallel beam in TEM mode and (b) a focused beam in STEM mode [119].

A specimen can be exposed by the electron beam in essentially 2 ways; a broad parallel beam or a focused beam. These beam conditions are obtained by settings in the condenser lens system (C1, C2, etc.). The parallel beam is used in TEM mode operation and the focused beam is used mainly in STEM mode. Schematics in Figure 2-2 (a) and Figure 2-2 (b) show the way an electron beam converts to a parallel and a focused beam respectively.

The first lens just underneath the specimen, the objective lens, collects the transmitted electrons and condenses the beam in the back focal plane where an image of the reciprocal space or diffraction pattern (DP) is formed. In the image plane of the objective lens, the first image of the specimen or real space is formed. In Figure 2-3, the back focal plane of the objective lens is the first place where the beam rays cross on another. In order to magnify and project the DP or the image on the fluorescence screen or the camera, the intermediate lens in the imaging system should be adjusted in a way that the object plane of the imaging system falls in either the back focal plane or the image plane of the objective lens respectively, Figure 2-3 (a) and (b) [119]. It should be noted that the imaging systems shown in Figure 2-3 are highly simplified. In most TEMs, many more projection lenses are used which give better flexibility and larger ranges for magnifying.

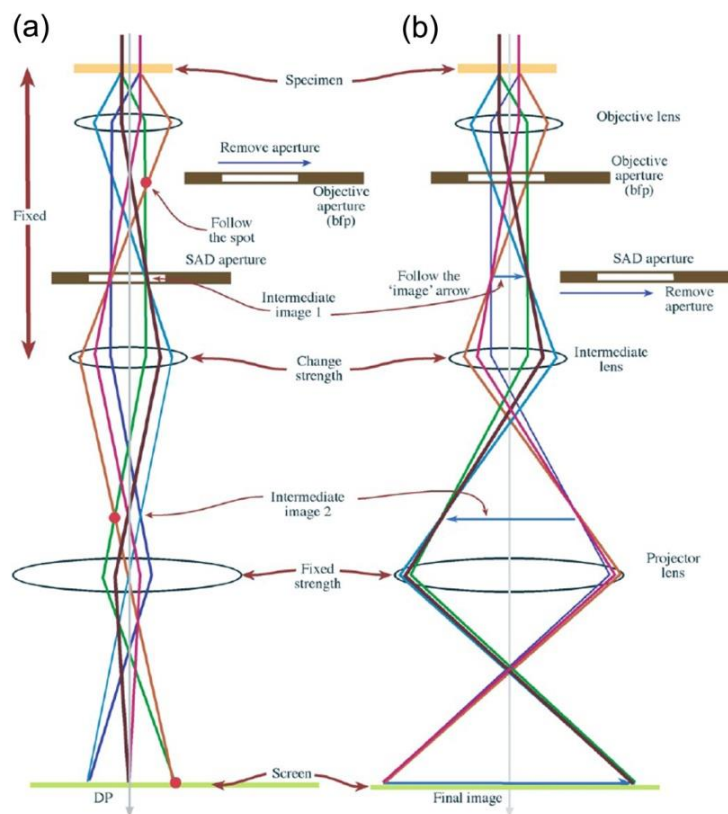


Figure 2-3, The two basic operation modes used in TEM for (a) projection of the diffraction pattern and (b) projection of the image onto the viewing screen [119].

2.2.2 Diffraction Mode

As mentioned before, in the back focal plane of the objective lens a diffraction pattern is formed. The same principle as for diffraction with other probes, i.e., the Bragg law, holds for electron diffraction (ED). Figure 2-4 shows atomic planes of a crystal with spacing of d . The incident electron plane wave with wavelength λ interacts with the atoms and reflects at an angle θ equal to the incoming angle. Since the scattering within the crystal lattice generates a phase difference, constructive interference and maximum intensity will occur when the difference in travel distance between reflections on two successive planes ($2d\sin\theta$) equals an entire number of wavelengths:

Equation 2-2

$$2d\sin\theta = n\lambda$$

The Equation 2-2 is referred to as Bragg's law and θ is known as the Bragg angle.

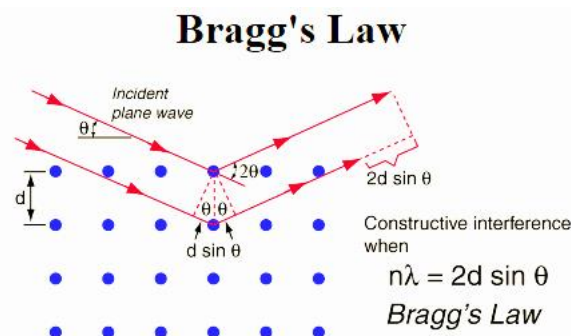


Figure 2-4, Schematic illustration of the reflection of an electron beam at an atomic plane based on Bragg's law.

The DP is a very common and useful tool to investigate different characteristics of the material such as its degree of crystallinity, its lattice parameters, its symmetry and the orientation of each grain and also phase recognition.

When the incident beam satisfies the Bragg law of a particular family of planes, the electron beam diffracts at the atomic plane and appears as a reflection in the DP (Figure 2-5). The distance between the central spot (the non-diffracted beam) and the diffracted spots can be used to find the planar distances in the crystal lattice. The distances of and the angles between the diffracted spots and central spot are indicators of the crystal orientation.

In order to limit the volume of the material from which the DP originates, a specific aperture (the selected-area aperture) can be used to limit the exposed area of the sample so that the DP originates from the selected area of the sample. This mode of operation is called selected-area diffraction (SAD) or selected-area electron diffraction (SAED) Figure 2-3 (a).

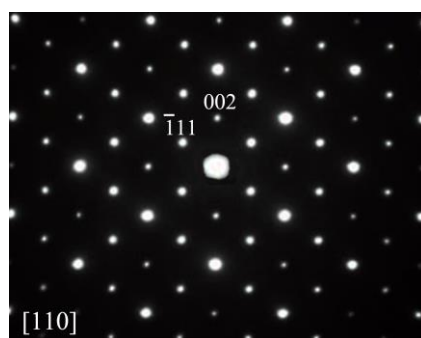


Figure 2-5, An example of a diffraction pattern (obtained from a Cu FCC crystal viewed along the [110] direction), showing the direct beam as central intense spot and many diffracted spots reflecting from different atomic planes, of which two are indexed.

2.2.3 Imaging Mode

The interaction of the electrons with the atoms of the sample can be either elastic or inelastic. If the deflection or scattering does not necessarily involve an energy transfer (no energy loss) then the interaction is elastic and if some energy is lost during scattering of the electron beam then the interaction (scattering) is called 'inelastic'.

The scattered electrons might be elastically or inelastically scattered again within the specimen. The probability of multiple scattering increases by the sample thickness. Elastic scattering at the electron cloud of the atoms in the sample is the main scattering mechanism used to produce electron diffraction patterns (DPs) and real space images, including high resolution (HR)TEM imaging.

Amplitude and phase of the electron wave can change during the transmission of the electron wave through the sample and this will contribute to the image contrast. In diffraction contrast, which is widely used for imaging of crystalline material (such as Ni investigated in this thesis), the amplitude changes induce the contrast, e.g. in bright and dark field modes. In mass-thickness which arises from incoherent elastic scattering of electrons both amplitude and phase changes are playing a role in the contrast. The mass-thickness contrast is mostly applied for imaging of non-crystalline materials such as polymers and biological materials

2.2.3.1 Diffraction contrast

Diffraction contrast is a special form of amplitude contrast. As it has been shown in Figure 2-6, the objective aperture in the back focal plane of the objective lens can allow the transmitted or one diffracted beam to pass and to participate in the image formation. If the objective aperture is used in the way that only the central transmitted electron beam in a DP is allowed to form the image, the imaging condition is called bright field (BF) imaging while if a diffracted beam in the DP is selected, the imaging condition is called dark field (DF) imaging.

In the BF imaging mode, Figure 2-6 (a), all the diffracted spots are blocked by the objective aperture. The image contains a bright background from the regions where the diffraction condition is not satisfied and dark areas from the regions where the diffraction condition is satisfied. If instead of the central beam, one of the diffracted spots is selected by the objective aperture, Figure 2-6 (b), the image is a DF image and contains a dark background with bright areas corresponding to the regions where the diffraction condition is satisfied.

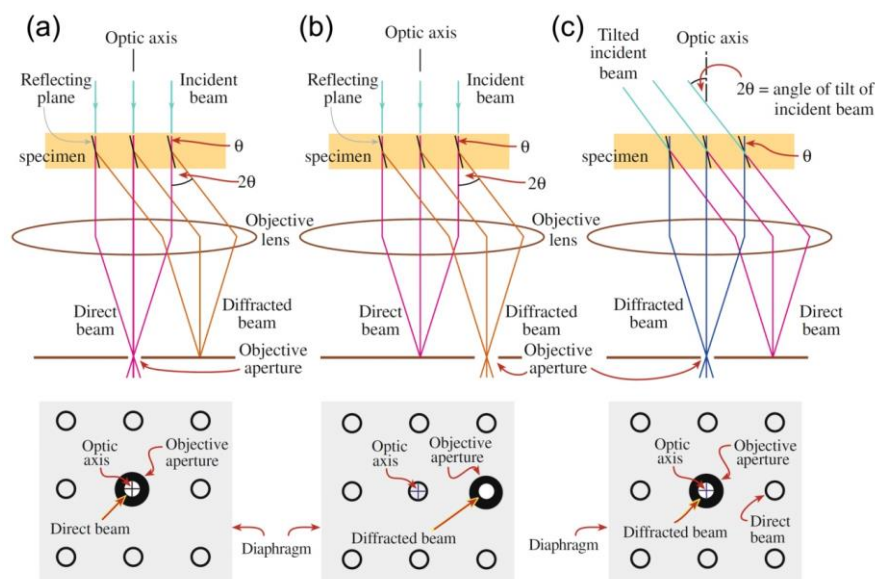


Figure 2-6, Schematic illustration showing the formation of (a) a BF image by selecting the central beam using an objective aperture (b) a DF image by moving the objective aperture to the diffracted spot to be selected and (c) a CDF image by tilting the electron beam in a way that the selected scattered beam remains on the optic axis [119].

In the case of DF imaging, either the aperture is displaced to select a diffracted spot, Figure 2-6 (b), or the entire DP can be displaced so that the diffracted spot falls in the centre of the objective aperture, Figure 2-6 (c). In comparison, in the first condition, off-axis electrons will cause high aberration and astigmatism and high-quality imaging is impossible. In the latter mode, the incoming beam tilt is adjusted by potentiometers above the objective lens in such a way that the incident beam hits the sample at an angle which results the diffracted electron beam to become parallel to the optical axis as shown in Figure 2-6 (c), improving the quality of the resulting image.

Interpretation of the (BF/DF) images depends on the DP of the sample. When the sample orientation is set in such a way that only one set of crystal planes satisfies the diffraction condition the DP typically contains 2 major spots, the central one and a diffracted one, then interpretation of the DF and BF images is easy and information can readily be obtained. This mode is referred to as two-beam imaging and it can be used to characterize the type of dislocations or other defects in the microstructure. E.g., dislocation types are in part recognized by their (in)visibility in different two-beam imaging conditions taken by different diffraction spots and this technique [119]. The contrast of a dislocation in a two-beam condition image correlates to the value of $\mathbf{g} \cdot \mathbf{b}$, where \mathbf{g} is the used reflection and \mathbf{b} is the dislocations Burgers vector. When $\mathbf{g} \cdot \mathbf{b}$ is equal to 0 for a particular dislocation, the latter

should be invisible (i.e., show no contrast) in the two-beam condition BF or DF image taken using g . Therefore, by taking different two-beam condition images for a given dislocation and finding the conditions when $g \cdot b = 0$, it is possible to determine the Burgers vector of the dislocation. When a DP contains more than 2 spots, interpretation of BF and DF images is more difficult.

2.2.3.2 Phase contrast

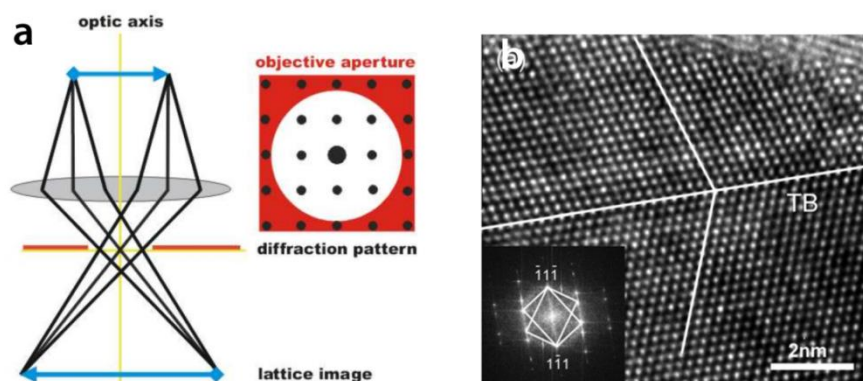


Figure 2-7, (a) Schematic illustration showing the formation of a HRTEM image by selecting the central beam and surrounding diffraction spots using an objective aperture and (b) HRTEM image of Pd showing one coherent twin boundary [115].

HRTEM is a powerful tool which allows direct imaging of the atomic structure of different materials. To obtain a HRTEM image, the sample should be aligned on a zone axis and then a collection of diffracted spots around the central beam in the DP should be selected by the objective aperture, as shown in Figure 2-7 (a), to participate in the image formation. A HRTEM image is formed by the interference of all selected diffracted spots in the DP. Since it relies on the difference between the phases of electrons leaving the sample, it yields a phase contrast image, Figure 2-7 (b) [119].

2.2.4 Energy Dispersive X-Ray Spectroscopy (EDS)

Inelastic interaction of an electron beam with a specimen generates X-rays. These signals can be used for chemical analysis of the specimen using energy dispersive X-ray spectroscopy (EDS or EDX).

Due to the inelastic scattering, removing an inner shell electron of an atom yields a vacancy in the respective shell. In order to return the atom to its low energy state, an electron from an outer shell moves into the inner shell to fill the vacancy. This results in the release of a specific amount of energy, usually in the form of X-rays which can be detected and measured by dedicated X-ray detectors inside a TEM.

Since each element has a set of specific energy levels, it is possible to determine the chemical composition of a material. The intensity of the X-ray spectrum of different elements is to some extent proportional to the concentration of the elements in a material. Therefore, a semi-quantitative analysis of the chemical concentration can also be done.

2.2.5 Strain and Orientation Mapping in a TEM

A recent evolution is to use diffraction patterns from very small electron probe for orientation and strain mapping in TEM. The automated crystallographic orientation mapping (ACOM)-TEM technique [98, 120] has a similar approach as the EBSD technique in SEM [121, 122]. In these techniques, the electron beam, Figure 2-8 (a), possibly including precession, is scanned over the sample, Figure 2-8 (b), and the DPs are collected from each point of the sample, Figure 2-8 (c). The obtained DPs are then compared with pre-calculated DP templates of different crystal orientations by using cross-correlation techniques and the best match is selected (e.g., by a commercial system as NanoMegas-ASTAR), Figure 2-8 (e). The collected DP can also be compared with DPs from a specific part of the sample which is considered as a reference point. This allows to measure the relative gradient of the internal strain due to the shift of the diffraction spots (e.g., by a commercial software as NanoMegas-TOPSPIN, Figure 2-8 (d) [99].

In these techniques, precession is used to minimize the diffraction dynamical effects so that simulated DPs can be calculated using kinematical approaches [123].

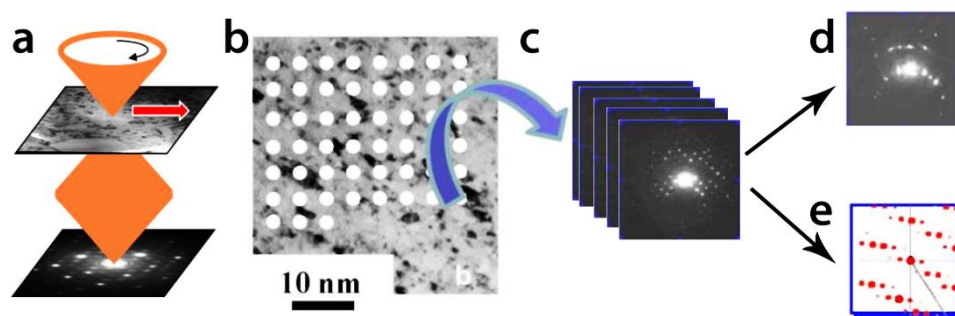


Figure 2-8, Schematic showing (a) the (precession) beam is scanning (b) over the interested area, (c) the collected diffraction patterns then compared to either (d) the selected diffraction pattern to obtain strain field maps or (e) simulated diffraction patterns to recognize phases and orientations [120].

2.3 In-situ TEM Tensile Testing

The PI 95 TEM PicoIndenter instrument [124], Bruker Co., is a single tilt TEM holder equipped with a quantitative indenter which allows a direct-observation of nanomechanical

testing inside a TEM. The most powerful function of this holder is that it provides precise force-time-displacement curves. In addition, the integrated video interface allows for synchronization between the load-time-displacement curves and the corresponding TEM video of the indentation.



Figure 2-9, PI 95 TEM PicoIndenter holder for usage in FEI TEM microscopes [124].

The basic hardware components of the PI 95 system include:

- PI 95 PicoIndenter transducer assembly (TEM holder),
- PI 95 PicoIndenter control unit, named the performech,
- Computer and data acquisition system.

Figure 2-9 shows this holder, and the enlarged schematic image of its front end. The PicoIndenter is used with a computer-driven control unit called the performech, a state-of-the-art electronic digital signal processor control unit. It provides users with exceptional control over nanomechanical testing. The PicoIndenter is connected to the control unit, which is connected to the data acquisition computer. All basic instrument operations, adjustment of parameters, data collection, and analysis are incorporated in a software, called TriboScan, in the data acquisition computer.

The PicoIndenter holder is suited for the investigation of nanoscale phenomena. It utilizes three levels of control for tip positioning and mechanical testing. In addition to a three-axis coarse positioner and a 3D piezoelectric actuator for fine positioning, the instrument is equipped with a transducer for electrostatic actuation and capacitive displacement sensing for acquiring quantitative nanoscale mechanical data. The holder has 2 modes of deformation, the displacement control and the load control. The maximum possible load and the maximum possible displacement are 1 mN and 2 μm with resolutions of <3 nN and $<0.02\text{nm}$, respectively [105].

The three-plate capacitive design provides high sensitivity, a large dynamic range, and a linear force or displacement. The transducer sensor consists of fixed outer electrodes (drive

plates), which are driven by AC signals 180 degrees out of phase with adjacent drive plates Figure 2-10. Since the signals applied to the drive plates are equal in magnitude but opposite in polarity at any instant, the electric field potential is maximised at 2 extremes and minimised (zero) at the site centred between the drive plates Figure 2-10. When a direct current bias is applied to the bottom plate of the capacitor, an attractive electrostatic force between the bottom plate and the centre plate pulls the centre plate downward. The magnitude of the force can be controlled by changing the applied voltage [124].

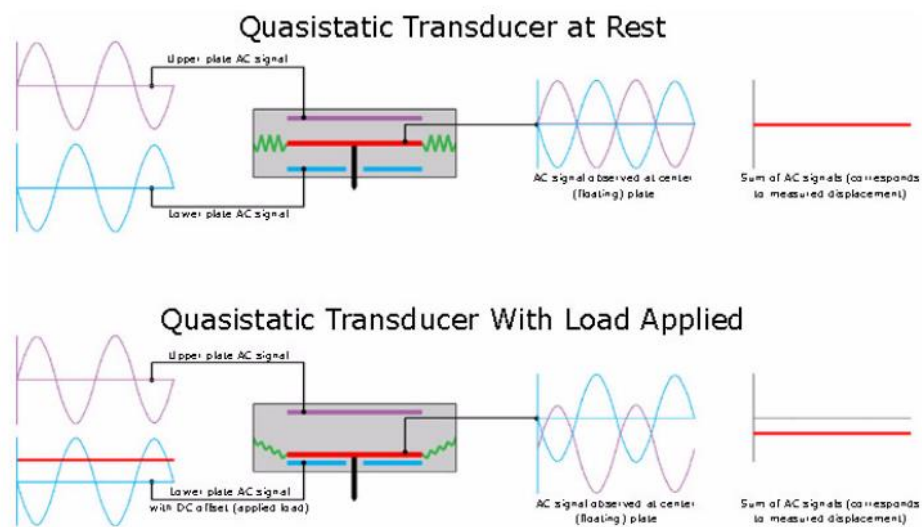


Figure 2-10, The transducer actuation diagram [124].

Using the Push-to-Pull MEMS device (designed by Bruker to work with the PI 95 PicoIndenter holder) allows performing quantitative in-situ TEM tensile tests with this holder, Figure 2-11. As mentioned before, the MEMS device converts the compressive force applied by the actuator into a tensile force in the centre of the PTP. The device has mobile and fixed parts which are connected by 4 identical springs. The compressive force applied on the outer half dome of the mobile part results in a relative movement of the mobile part toward the fixed part and a relative separation of the gap platforms in the middle of the device where the sample is mounted, Figure 2-11 (b) and (c). Currently consumable PTP devices with stiffness of 15, 150, and 450 N/m are available [125].

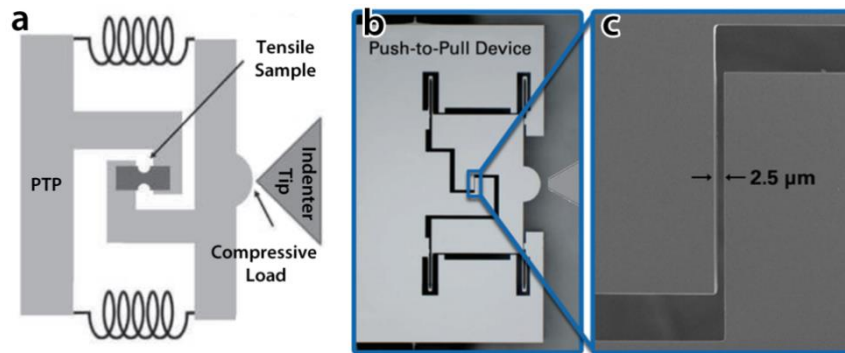


Figure 2-11, (a) Schematic presenting the basics of the PTP, (b) optical image of a PTP and (c) SEM image of the PTP device gap in higher magnification, [54, 106].

A FIB instrument should be used to mount the sample (nanotube, nano rod, or thin-film) on the PTP device. The sample sides can be attached on the PTP platforms by the GIS in a FIB.

Kang et al. showed that, in micro-nano tensile tests, the alignment of the sample axis compared to the loading direction is very important [126, 127]. They showed that sample misalignments may change the uniaxial uniform loading condition to a complex 3D non-uniform loading condition. The main two possible misalignments are a transverse misalignment and a rotational misalignment, see Figure 2-12 [126, 127], which might indeed be present in the tensile tests performed by PTP devices. Despite careful operation and handling, e.g., with an Omniprobe micromanipulator, when the sample is mounted on the top surface of the PTP device the sample central axis might not be perfectly in line with the central loading axis of the PTP which results in a transverse misalignment (Figure 2-12(b)). Moreover, the sample central axis might not be parallel to the loading direction or the sample FIB cut might not be perfectly parallel with the intended tensile direction, which in both cases results in a rotational misalignment (Figure 2-12(c)). In these conditions, slight bending could be induced in the sample which might affect the mechanisms and measured values. In the present work the loading condition was supposed to be ideal without any misalignment.

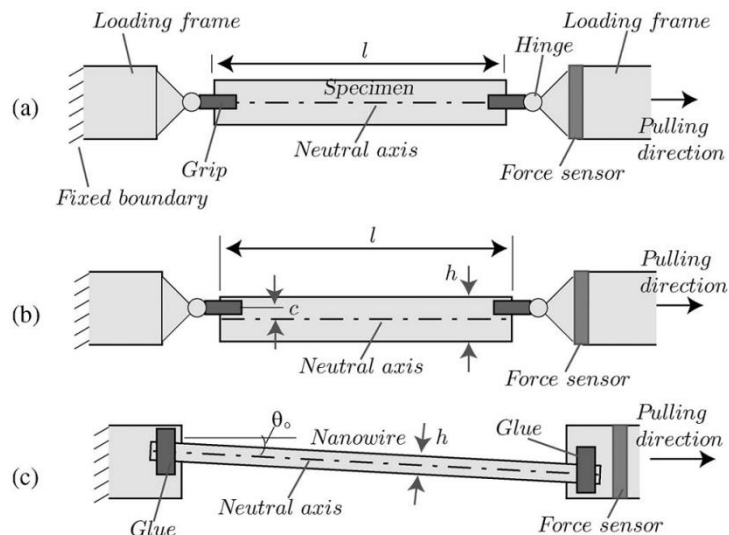


Figure 2-12, Tensile tests with (a) an ideal uniaxial loading condition, (b) a loading condition with a transverse misalignment and (c) a loading condition with a rotational misalignment [126, 127].

Once prepared, the device is transferred and mounted on the PicoIndenter holder. In this stage, performing quantitative tensile tests on the sample is possible. The data (load and displacement) obtained from the system is used to calculate the mechanical properties of the sample while the real time video of the microstructure evolution during the experiment can be used to reveal the governing nano- and microstructural mechanisms.

There are some points which should be considered in in-situ TEM nanotensile test experiments when using the Bruker PI95 PicoIndenter holder. As with most instrumentation, the longer the instrument is in continuous operation, the more stable it will be; therefore, it is very important to allow the instrument to stabilize for a few hours after switching on.

Due to the presence of a high (thermal) drift in the transducer, after locating the transducer close enough to the sample or PTP device (~ 2 micron), at least 30 min is required to stabilize the transducer. Meanwhile, the distance between the indenter and the sample (or the PTP device) should be checked. If this distance decreases to less than 1 micron in 30 min, the indenter location and the distance between the indenter and the sample (~ 2 micron) should be manually re-adjusted and another 30 min should be waited. In spite of these stabilizations, a remaining drift may still affect the displacement data from the instrument. Therefore, in order to obtain the real displacement data of the sample, an image cross-correlation of the deformation movies is needed which will be explained later.

Since the loading condition has been assumed to be ideal, the stress can be obtained by dividing the force applied on the sample by the sample cross-section area. To measure the area of the cross-section, a SEM image of the cross-section of the sample after fracture can be used. The cross-sectioning is done on a location away from the fracture site, however, due to the deformation, the measured area might be smaller than the initial one which can be a source of error. To measure the area of the cross-section, a MATLAB script was developed. In the SEM image, the cross-section area of the sample is manually painted to white and the rest of the picture is painted black. The script measures the cross-section area by counting the white pixels (indicating the cross-section area) in combination with the pixel size.

The uncertainty on the applied stress is mainly due to the precision of the measurement of the cross-sectional area (~ 3 nm) as well as that of the force applied on the sample (~ 0.2 μN). According to the standard errors on the measurements of the cross-sectional area with MATLAB (~ 500 nm²) and the maximum force (278 μN in one of the experiments), the error of the engineering stress is ~ 3 MPa at a stress level of 1170 MPa which is 0.2 % and at a low stress such as 213MPa, the error of the engineering stress increases to 0.45%. This percentage is used as a relative standard error of the stress measurements in all deformation cycles in this thesis.

2.4 Digital Image Correlation

A MATLAB code was developed to measure the displacement of the gage part of the tensile test samples from the deformation movies recorded during in-situ TEM tensile deformation (the script is given in the appendix). The code is able to correct the possible misalignment of the recorded movie, Figure 2-13 (a). To measure the displacement of the gage length, H in Figure 2-13 (b), the code initially calculates the pixel size in the movie. Then it changes the movie frames to black/white binary images as shown in Figure 2-13 (c). Then 2 areas, marked by red rectangles in Figure 2-13 (d), are defined. The code measures H by counting and averaging the number of the white pixels in each pixel column in the selected areas and converts this to the real length. According to the resolution of the recorded movies and the used magnifications in TEM imaging mode, the pixel size in the movies is in the range of 3 - 4 nm. In the case where 97 pixel columns are considered to measure the distances, the standard deviation becomes 1.0642 pixels and the standard error of the mean becomes 0.1081 pixels which corresponds with 0.4 nm.

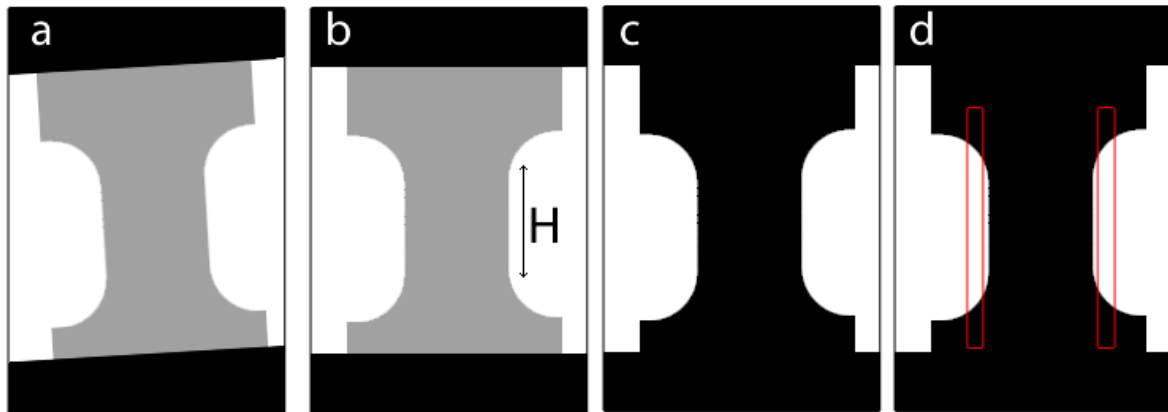


Figure 2-13, Schematics showing the steps of digital cross-correlation in the designed MATLAB code.

In order to see how drift affects the displacement data, the load-displacement curves of an experiment obtained from the instrumental data and the one after image cross-correlation are shown in Figure 2-14, showing a pronounced difference in the values and behaviour of the indicated displacement, confirming the need for the cross-correlation procedure.

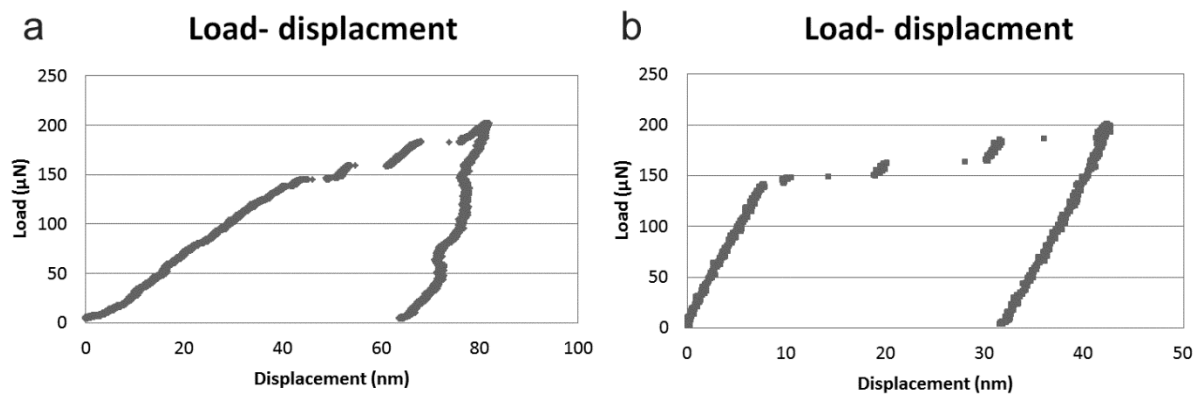


Figure 2-14, The load-displacement curves (a) obtained from the Picoindenter instrument displacement data and (b) corrected by the developed image cross-correlation procedure.

2.5 In-situ SEM Fatigue Testing

Cyclic compression tests on micropillars were performed by Jonas Groten and Ruth Schwaiger at the Karlsruhe Institute of Technology (KIT) using a Nanomechanics InSEM Nanoindenter equipped with a diamond flat punch of 5 μm diameter. More details on the actual experiments are given in chapter 6.

2.6 TEM Sample Preparation

The TEM samples prepared for all of the above experiments should be electron transparent which means a maximum thickness of 300 nm for metallic samples. Sample preparation is one of the most important steps for TEM related analyses since improper sample preparation can introduce artefacts, contamination, and defects in the sample which implies difficult interpretation of the TEM results in view of mechanical properties.

According to the type of the sample, different techniques can be used for TEM sample preparation. In this work, the samples for in-situ TEM nanotensile testing were prepared by using a combination of twin-jet electro-polishing, FIB, and in-situ TEM heating techniques. The details of the sample preparation will be explained in chapter 3 and 4. In the following the basics of each mentioned technique are briefly explained.

2.6.1 Twin-Jet Electro-Polishing

The most common technique to prepare metallic TEM samples is twin-jet electro-polishing. It can only be used for electrically conductive samples such as metals and alloys. The process starts by mechanically grinding the sample to an initial thickness of 100-150 μm , followed by cutting 3 mm disks punch cutting. The disks are then polished by fine (9-1 μm) diamond polishing particles and thinned (polished) further by a twin-jet electro-polishing system.

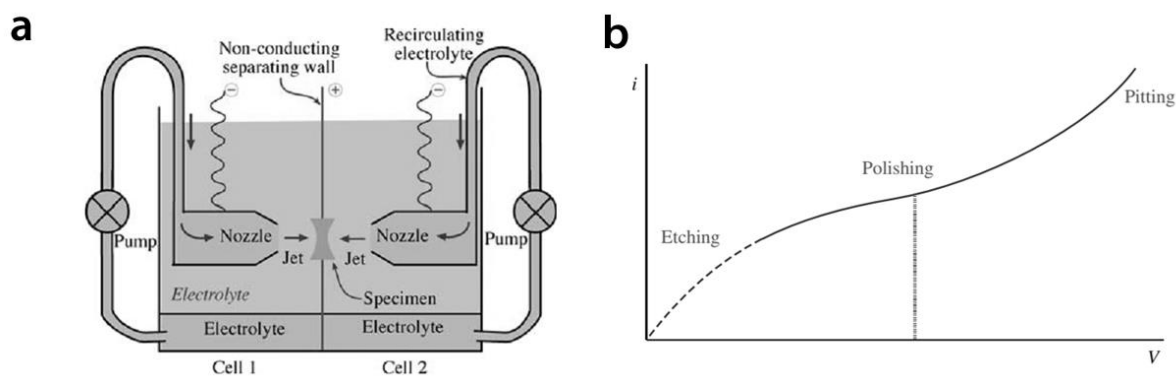


Figure 2-15, (a) Schematic of a twin-jet electro-polishing system, (b) Electro-polishing curve showing that in certain conditions (on the plateau) polishing occurs [119].

The basic principle of a twin-jet electro-polishing system is that the sample becomes the anode in an electro-chemical cell. Jets of the electrolyte of the cell are focused on both sides of the disk by the pump in the twin-jet apparatuses, as shown schematically in Figure 2-15 (a). When a voltage is applied to the sample, anodic dissolution of the specimen creates a polished surface. Figure 2-15 (b) shows that the ideal current/voltage combination should be located in a plateau regime of the V/A curve to avoid etching or pitting. A light beam with a

light sensor detects transparency of the sample at the end of the process and stops polishing when a hole appears. The disk must be rapidly extracted from the electrolyte and washed in water or solvent to remove any residual film of electrolyte which may further etch the surface. The thin area near the hole is the electron transparent area proper for TEM investigation.

For the present Ni material, a solution of Perchloric acid and Acetic acid, 1:4, has been used with the following conditions: 0°C, 18-19 V and 100 mA. The samples were immediately rinsed with Methanol and distilled water after the polishing.

2.6.2 Focused Ion Beam

As mentioned before, focused ion beam (FIB) is the most common technique to manipulate the micro/nano scale materials as well as one of the most powerful TEM sample preparation techniques. Most current FIB machines contain a FIB column and a SEM column which is then called a “dual-beam” FIB–SEM. These days, such instruments offer both high-resolution imaging and flexible micromachining in a single platform.

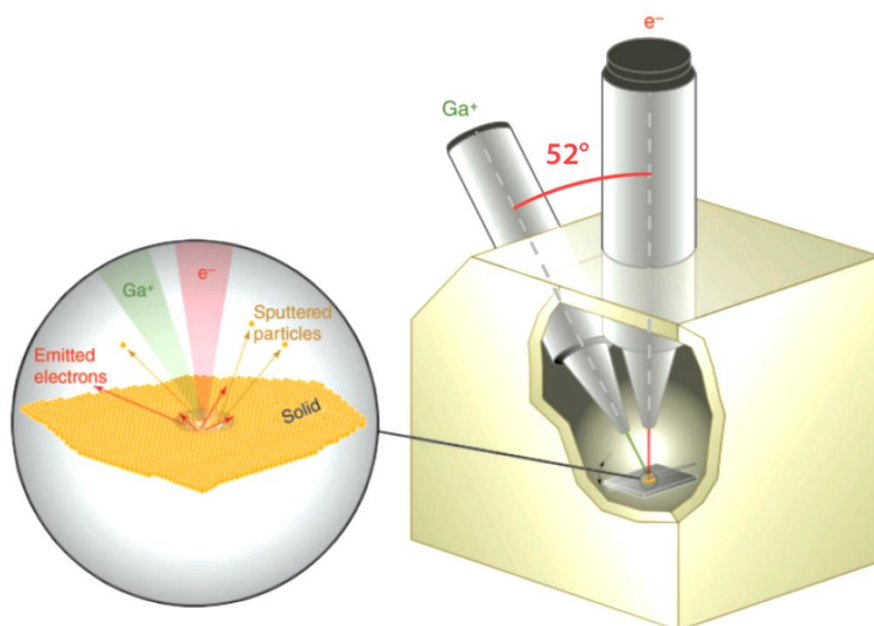


Figure 2-16, Schematic illustration of a dual-beam FIB–SEM instrument showing the interaction of the electron and ion beams with the surface of specimen [128].

The schematic illustration of a dual beam FIB-SEM system is shown in Figure 2-16. The ion beam and the electron beam are aligned in such a way that both are focused at the same point of the sample and with an angle of 52° between both beams. In the electron (SEM) mode, the focused electron beam is used to scan the sample. The digital image of the sample is formed

by collecting the secondary electrons (SE), resulting from the interaction of the electron beam and the sample surface, by a SE detector. The ion (FIB) mode consists of a finely focused ion beam which can be also used for imaging similar to the electron mode. Gallium (Ga) is commonly used in FIB due to its low melting temperature (30 °C) and low vapour pressure. A large negative potential of 500 V – 30 kV between the liquid metal ion source (Ga^+) and an extraction electrode accelerates the ions. The Ga^+ ions interact with the surface of the sample and SEs are emitted from the surface of the specimen, Figure 2-16. These signals are collected by the SE detector to generate a digital image in the ion mode [128].

The Ga^+ ions can also be used for sputtering the surface and thinning the specimen. In this condition, the ion energy is large enough to overcome the surface binding of the specimen atoms which will be removed from the surface. Therefore, small-scale milling by the ion beam is possible and can yields a TEM sample by the dimensions of $5 \times 10 \mu\text{m}^2$.

In addition, the used FIB-SEM machine in this thesis has been equipped by a gas-injection systems (GIS) and an Omniprobe micromanipulator. GIS enables depositing the element used in the GIS, often platinum (Pt), on the surface of the sample. One of the applications of Pt deposition, aside from sample surface protection from sprayed Ga^+ ions, is to attach the FIB prepared small sample to a TEM grid or any other device such as a PTP MEMS. GIS provides evaporated Pt gas in the FIB SEM chamber which can be deposited on the area exposed by the electron/ion beam. In Ion beam deposition mode, the energy of the beam should be selected in a way to avoid sputtering. The Omniprobe has a sharp tungsten needle which can be used to displace small-scale samples. Attaching the Omniprobe tip to a side of the sample by Pt deposition allows picking and moving the sample. To mount the sample on another device or location, the sample can be attached to a new location by Pt deposition and the Omniprobe should be detached from the sample by FIB cutting.

2.6.3 In-situ TEM Heating Holder

In-situ TEM holders are a class of holders allowing heating the TEM samples inside a TEM up to $\sim 800^\circ$, Figure 2-17. Like other in-situ TEM techniques, it allows real time observation and investigation of the microstructure of materials during heating. In the present work, the holder shown in Figure 2-17 was used to anneal out (most of) the FIB induced defects in FIB prepared samples.



Figure 2-17, Schematic and picture of the tip of a heating holder.

Chapter 3:

Quantitative In-situ TEM Nanotensile Testing of a Single Crystal Ni Sample with Reduced FIB Damages

In this chapter a new sample preparation method proper for in-situ TEM nanotensile testing is introduced and the quality of the prepared samples, the type of induced damages and the possible contribution of such damages in the deformation have been analysed and investigated.

3 Quantitative in-situ TEM nanotensile testing of a single crystal Ni sample with reduced FIB damages

3.1 Introduction

Recently, small-scale structures and materials are attracting a lot of attention from the materials science community due to high demands for smaller, more flexible and reliable microelectronics and micromechanical components, for example, in MEMS devices [129, 130]. Aside from the challenges of the preparation of such size-reduced materials, the investigation of their mechanical properties and deformation mechanisms raises several new challenges.

Recent advances in different electron microscopy techniques and of MEMS components now enable the simultaneous investigation of structural and mechanical properties using in-situ electron microscopy mechanical tests. Materials with reduced dimensions can be deformed using tensile deformation, compression, nanoindentation, and bending in either a SEM [13, 92, 131-133], or a TEM [44, 125, 134-141].

The small sample dimensions play an important role in the mechanical behaviour and active deformation mechanisms. Usually the attained material strength inversely scales with sample dimensions, i.e., thin film thickness or pillar and wire diameter [48, 142]. For example, the inverse scale-strength behaviour of small-sized single crystalline materials is mainly attributed to the lack of dislocation sources in the sample [143], dislocation source exhaustion due to the presence of truncated spiral dislocation sources [135] and enhanced dislocation starvation at the surface [138].

In the case of TEM research, most samples need to be trimmed and/or thinned in order to properly interpret the experimental data, artefacts induced by these thinning procedures need to be avoided or at least well documented. The sample preparation method used for most in-situ SEM and TEM mechanical tests is FIB thinning. Site selectivity, the range of materials for which FIB can be used, micro-level manipulation ability, machining flexibility as well as speed and reliability make FIB a very versatile technique for miniaturized sample preparation, in particular for TEM investigations [128, 144]. However, a thin amorphous layer at the surface [89, 145], implanted ions [89], induced vacancies, self-interstitial atoms, stacking faults or dislocation loops [146, 147], or even precipitations [148-150] as well as changes of the crystallographic orientation [144] are major artefacts introduced by FIB [151].

It has also been shown that such FIB damages can substantially affect the mechanical properties and the deformation mechanisms [1, 90, 138, 151-153] similar to other irradiation processes [154, 155]. For example, the amorphous layer can hinder the escape of dislocations to the surface [138], implanted Ga may cause solid-solution hardening [89], point defects and dislocation loops can pin glissile dislocations [146, 151] and facilitate nucleation of dislocations [1, 89, 145, 152]. Therefore, in most cases, the mechanical properties and the deformation mechanisms observed in conventional FIB-prepared samples in the micron and submicron range are not directly expandable to bulk materials.

In order to avoid FIB for in-situ SEM/TEM mechanical testing, other techniques based on electro-chemical processing have been used to produce small-sized metallic systems [49, 85, 114, 153, 156-158]. However, these techniques, which include selective etching and lithography, are not site selective and cannot be used to produce well-defined specimens with respect to orientation, defect content, etc. In the present work, a combination of twin-jet electro-polishing followed by FIB cutting has been used to minimize FIB damages on small-sized Ni specimens dedicated for in-situ TEM nanotensile testing experiments. Conventional twin-jet electro-polishing was used for thinning a Ni bulk sample, while FIB was only used for cutting and mounting the tensile sample on a PTP MEMS device, i.e., not for (further) thinning (see also next section). This combination was used before in order to perform in-situ TEM environmental investigations [159], in order to investigate the stress induced transformation in a shape memory alloy by a qualitative in-situ tensile test method [160] and in order to decrease the FIB milling time to prepare micropillars [161]. In the latter case, twin-jet electro-polishing was used to remove most of the material, and FIB was used for final micro-machining and shaping of the samples. Also in most cases, final thinning was performed with FIB, which is avoided in the present work. The aim of the present study is to perform a quantitative in-situ TEM nanotensile experiment on a Ni micron-sized sample produced with a central area (nearly) free of artefacts in which the pristine response to the applied stress can be investigated.

It is also worth noting that, because TEM thin foils prepared by twin-jet electro-polishing can be investigated prior to in-situ TEM straining, specimens with a pre-defined, selected crystallographic orientation and well-characterized initial microstructure can be selected. This facilitates, for example, studying specific grain boundaries or defined initial dislocation densities in high resolved shear stress situations and two-beam conditions for proper diffraction contrast imaging. In the literature, similar efforts have been made by combining

EBSD and FIB for the preparation of in-situ TEM samples with specific grain, twin or phase boundaries [136, 162]. However, other crucial information such as the initial dislocation density and structure, the local structure of the interfaces as well as the orientation of these interfaces below the surface, cannot be extracted from EBSD. Furthermore, as in these cases final FIB thinning cannot be avoided, the analyses of the genuine deformation mechanisms during in-situ TEM straining remain very difficult, if not impossible.

3.2 Materials and methods

To prepare the tensile sample, discs of 3 mm diameter and a thickness of $\sim 100\ \mu\text{m}$ were prepared from a high purity Ni foil (99.999%) (Goodfellow GmbH, Bad Nauheim, Germany). The discs were annealed for 1 hour at 400°C under high vacuum conditions in order to relax internal stresses in the structure. An average grain size of $18\ \mu\text{m}$ after the heat treatment was calculated from EBSD mapping. The discs were then twin-jet electro-polished and immediately rinsed with Methanol and distilled water.

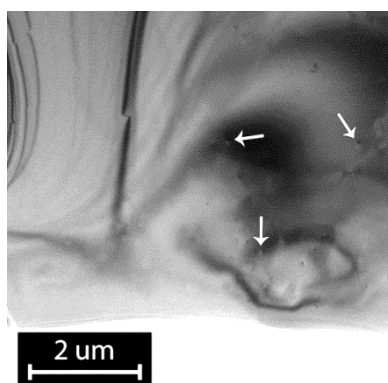


Figure 3-1, BF TEM image of the selected area, the white arrows mark the dislocation debris.

In order to select the appropriate position and crystallographic orientation for the tensile test samples, conventional TEM techniques including SAD and BF-TEM were used on the electro-polished samples. The sample location was selected from an electron transparent area in a dislocation-free grain near the electro-polished edge. Figure 3-1 shows the selected grain which is almost dislocation-free. The white arrows in Figure 3-1 indicate some dislocation debris in the structure remained from the heat treatment.

To cut, lift and mount the sample on a PTP device, a dual beam FIB/SEM was used. In order to obtain a uniform cross-section over the gage length of the sample, the length of the sample (i.e., tensile direction) was selected parallel to the edge of the hole made by the electro-polishing process, Figure 3-2 (a) and (b). This ensures a homogenous applied stress during

the in-situ tests. A sample of roughly 8 μm length and 2-3 μm width was cut from the electro-polished foil using an ion beam of 30kV / 80pA and transferred to the PTP device using Omniprobe micromanipulator, Figure 3-3 (a).

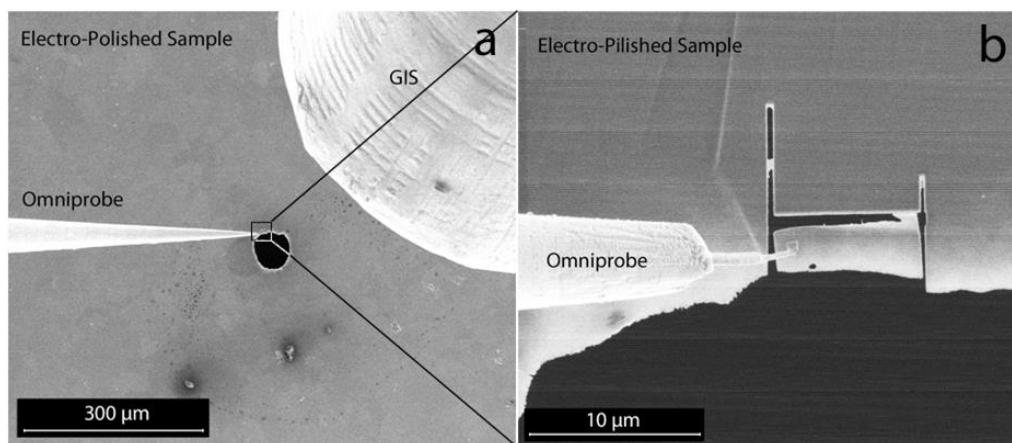


Figure 3-2, SEM images showing the sequence of FIB preparation steps, (a) a low magnification view of the electro-polished foil with the Omniprobe micromanipulator and GIS needle for Pt deposition, (b) FIB cut from the thin electro-polished edge of the hole.

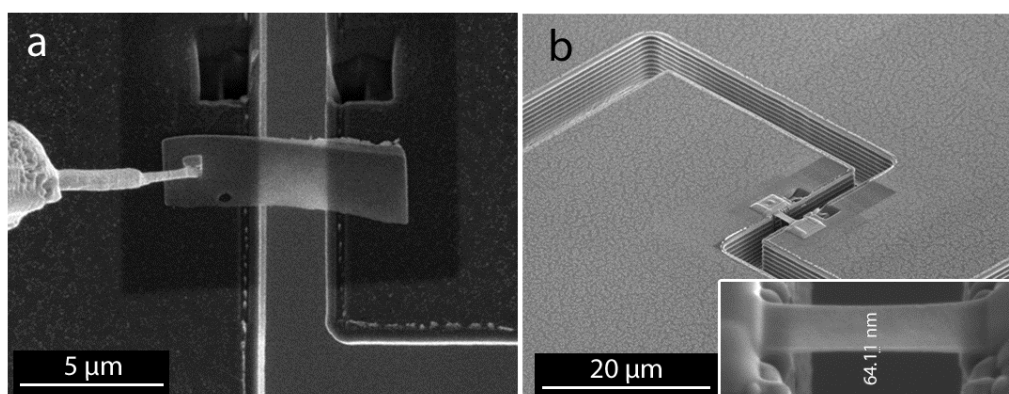


Figure 3-3, SEM images showing (a) the sample transferred to device before attaching, and (b) the final configuration of the tensile sample on the PTP device, the inset shows the sample in higher magnification.

The sample was then attached to the PTP device by electron beam assisted platinum deposition. In order to avoid Ga^+ ion beam damages to the gage section as much as possible during the transfer of the tensile sample to the PTP device, the tensile sample was only locally exposed to the ion beam, outside the gage section used for the tensile test. Then, the width of the tensile sample in the middle gap of the PTP was reduced to around 1 μm using an ion beam of 30kV/80pA Figure 3-3 (b). The inset in Figure 3-3 (b) shows that the thickness of the sample along the sample is indeed uniform. The main difference with other combined techniques is that in the present case the ion beam is used neither for further

thinning nor for imaging of the sample. In other words, the Ga^+ ion beam is oriented perpendicular to the surface and only touches the sample for cutting its edges.

Diffraction contrast imaging, HRTEM, and STEM together with EDX mapping have been used to characterize the microstructural and chemical changes induced by the FIB cuts at the edges of the tensile sample as well as the effects of the tensile deformation.

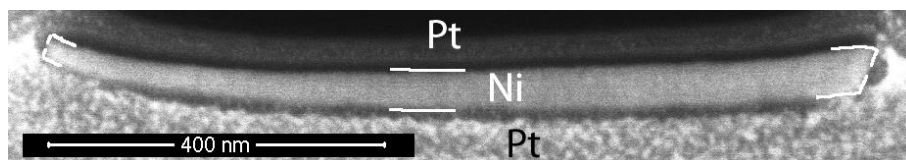


Figure 3-4, SEM image of the cross-section of the tensile test sample obtained from an area close to the mounted part on the PTP and away from the fracture site. The borders of the samples are marked with white lines. This area is expected to have been least affected by the deformation and thus the measured cross-section can be used to calculate the engineering stress. The difference in thickness yields a higher stress in the left thinner side from where most dislocations were seen to nucleate during deformation.

The in-situ nanotensile tests were performed by combining the PI 95 TEM PicoIndenter holder and PTP MEMS device (more information in chapter 2). In the present study, a PTP device with stiffness of 150 N/m was used and the experiment was performed in the displacement-control mode. The raw force data obtained from the indenter holder is a combination of the force applied on the tensile sample and that on the PTP device springs. The force on the Ni sample was extracted by subtracting the contribution of the PTP device from the raw force. The engineering stress was obtained by dividing the force on the sample by the cross-section area. It is measured on a SEM image after fracture of the sample from a location away from the fracture site, Figure 3-4. As seen from the figure the thickness in the sample cross-section is not uniform which results in the local stresses in the cross-section varying by a factor of 2. The engineering strain was calculated by dividing the raw displacement data by the initial gage length measured on the plan-view SEM images, Figure 3-2 (d). The raw displacement data was obtained by digital image cross-correlation.

3.3 Results and discussion

Figure 3-5(a) shows a BF-TEM image of the tensile sample mounted on the PTP device before deformation. The sample dimensions are $3074 \pm 7 \text{ nm} \times 990 \pm 7 \text{ nm} \times 54 \pm 3 \text{ nm}$ (dimensions obtained after sample preparation from SEM images at different magnification (see end of Ch. 2.3 for precision determination)). This sample was oriented for multiple slip condition with the tensile axis parallel to the $[\bar{1} 1 \bar{1}]$ direction, and the pole normal to the foil

surface was close to $[\bar{2} 1 3]$. In this case, a maximum Schmid factor (Ω) of 0.27 can be reached in the $(1 1 1)[\bar{1} 1 0]$, $(1 1 1)[0 \bar{1} 1]$, $(\bar{1} \bar{1} 1)[1 0 1]$, $(\bar{1} \bar{1} 1)[\bar{1} 1 0]$, $(1 \bar{1} \bar{1})[1 1 0]$ and $(1 \bar{1} \bar{1})[0 \bar{1} 1]$ slip systems, while Ω is equal to 0 for the other 6 systems.

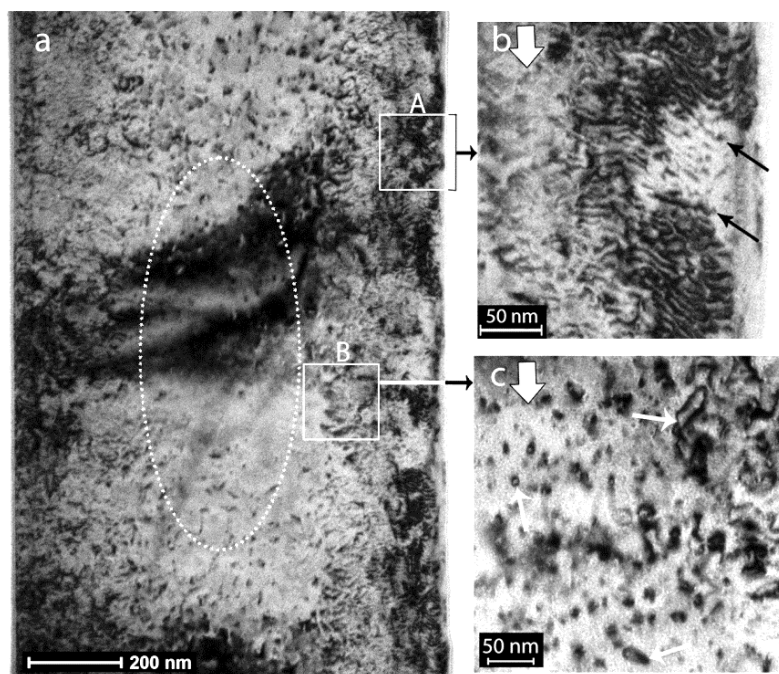


Figure 3-5, (a) BF micrograph of sample before deformation, with highlighted regions A and B near the edges. (b) and (c) BF micrographs taken in two-beam condition with $g = 1 1 \bar{1}$ (large white arrows) from area A containing tangled dislocation structure (black arrows) and area B containing different size dislocation loops (small white arrows), respectively.

As can be seen in Figure 3-5 (a) the reduction of the sample width by the FIB cut has severely affected the edges, while the centre of the sample, indicated with a dashed ellipse, is nearly damage-free; there are still a few discrete small FIB damage sites, seen as black dots in the centre, resulting from the fact that the ion beam used for cutting out the sample from the electro-polished foil and trimming the edges will always have a certain spread with some Ga ions straying further away from the edge towards the centre of the sample and creating some dislocation loops in the near damage-free area. Along the edges, two types of FIB induced defect areas (labelled A and B) can be observed. Area A, enlarged in Figure 3-5 (b), exhibits a ripple shaped contrast similar to that observed in FIB irradiated Cu and Fe-Cr alloy [89, 163] and is expected to be due to the strong diffraction contrast of the dislocation structure formed from the superposition and interaction of dislocation loops and the formation of long parallel tangled dislocation structures. From Figure 3-5 (c), the defects in area B can be identified as small dislocation loops with a diameter up to 50 nm, and it can be seen that the size of the loops increases towards the edge of the sample. However, smaller

loops remain the majority. Dislocation loops generated by the collapse of vacancies or interstitials are indeed frequently observed in irradiated materials [164].

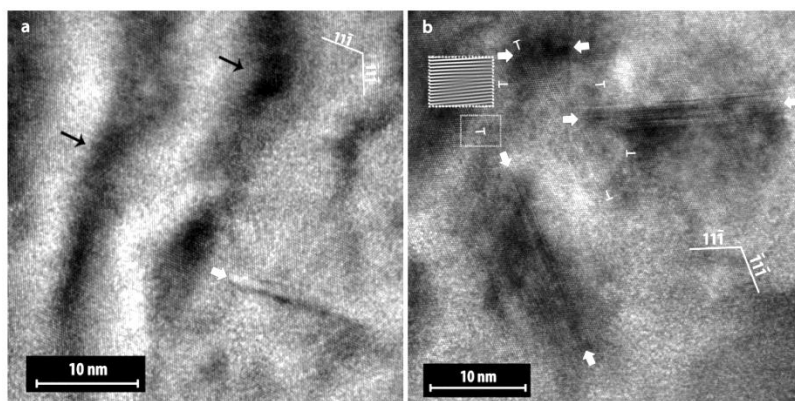


Figure 3-6, HRTEM micrographs showing (a) FIB induced parallel dislocations indicated by black arrows from area A, and (b) nanoscale planar defects (white arrows) and some edge dislocations (\perp mark) in area B.

The HRTEM image of Figure 3-6 (a) reveals details of the defects from area A in Figure 3-5 (a). In this figure, the strong strain field associated with long dislocations can still be observed. The HRTEM of Figure 3-6 (b) was obtained in area B of Figure 3-5 (a). It shows that the FIB-induced dislocation loops are planar defects lying in the $\{1\ 1\ 1\}$ planes. Such feature is typical of interstitial or vacancy type stacking faults delimited by Frank partial dislocations with Burgers vector of $\frac{a}{3}[1\ 1\ 1]$ [151]. In the present study, the small size of these defects (compared to the thickness of the tensile sample) as well as the strong strain field surrounding them makes their individual identification at the atomic scale extremely difficult and is beyond the scope of this work.

The chemical composition of areas near the edges of the tensile sample was investigated using STEM-EDX mapping. Figure 3-7 (a) shows a HAADF-STEM image, in which FIB damages at the edge are still visible due to the high strain field and moderate camera length. 10 ± 1 at. % Ga was measured in the area delimited by the white rectangle in Figure 3-7 (a). Figure 3-7 (b) shows a Ga rich strip of ~ 50 nm at the edge of the sample. In that region the Ga atoms are distributed in a uniform manner and neither precipitate nor segregate at the defects, Figure 3-8. Still, some weaker Ga traces are recognized further away from the edge, as seen in Figure 3-7 (d), which is due to a slight spreading of the Ga ion beam.

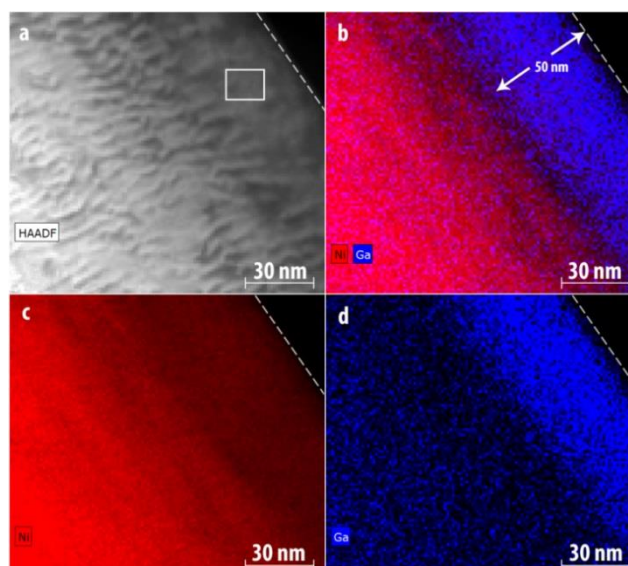


Figure 3-7, (a) HAADF-STEM image, the Ga amount in the selected white rectangle is 10 ± 1 at. % (using camera length of 330 nm still showing some dislocation contrast), (b) superposed HAADF-STEM image, Ni and Ga EDX chemical maps, (c) Ni EDX chemical map, and (d) Ga EDX chemical map, (displayed as signal counts).

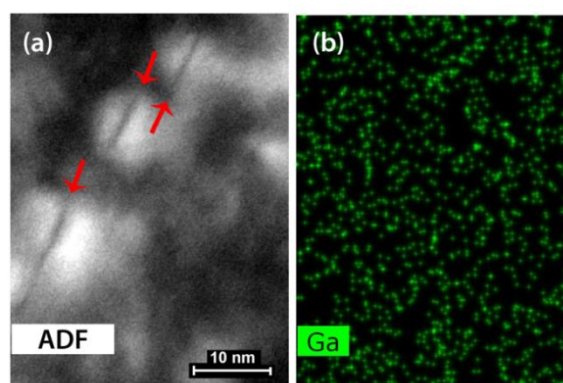


Figure 3-8, (a) Annular dark field (ADF) STEM image showing the planar defects near the edges and (b) the corresponding Ga EDX chemical map revealing no agglomeration, segregation or precipitation of the Ga, (displayed as signal counts).

These results indicate that by using this combined procedure of electro-polishing thinning and FIB cutting, genuine deformation defects and plasticity mechanisms can be investigated in the almost FIB damage-free area in the centre of the sample. For example, the intrinsic mobility of deformation dislocations can be measured in the absence of severe FIB damages, which could act as obstacles for moving dislocations. The characterization of the mechanisms controlling the interaction of deformation dislocations with pre-selected structural boundaries can be achieved in samples with interfaces located in the centre of the sample. Indeed, such interactions can be highly affected by the FIB-induced defects in the vicinity or inside the boundaries in cross-sectional samples prepared only by FIB. The method can also be used to

observe strengthening mechanisms in samples containing nano-precipitates or dispersed small particles. Indeed, the discrimination between these defects and the FIB-induced loops or precipitates can be expected to be extremely difficult (at least at the low magnification scale required to observe the interaction between the defects and moving dislocations during in-situ TEM straining). Moreover, as will be shown below, the remaining FIB-induced defects at the edges of the sample can be used to the advantage of the experiment.

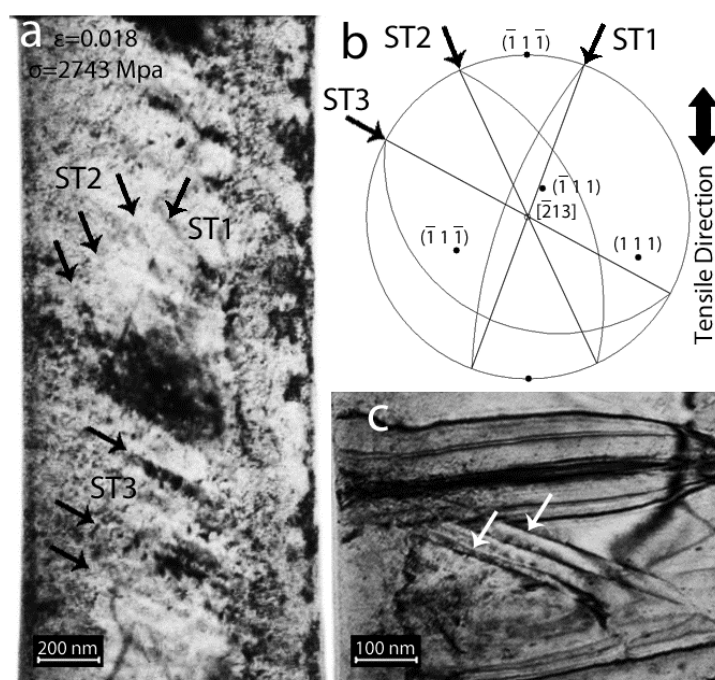


Figure 3-9, (a) A BF-TEM snapshot taken during deformation at $\epsilon = 0.018$ and $\sigma = 2743$ MPa. Three different slip traces (STs) can be observed, (b) the stereographic projection of the sample showing the intersections of $\{1\ 1\ 1\}$ planes with the surface plane $(\bar{2}\ 1\ 3)$, and (c) the BF image of some deformation dislocations originating from the left edge and being halted after unloading.

Figure 3-9(a) shows a BF-TEM snapshot obtained during the in-situ tensile deformation of the sample shown in Figure 3-3 at $\epsilon = 0.018$ and $\sigma = 2743 \pm 6$ MPa. The experiment was carried out at an initial strain rate of $3.3e^{-4}s^{-1}$. In this figure, three slip traces caused by the glide of dislocations in the $(\bar{1}\ 1\ 1)$, $(\bar{1}\ \bar{1}\ 1)$ and $(1\ 1\ 1)$ glide planes can be seen as in the $(\bar{2}\ 1\ 3)$ stereographic projection of Figure 3-9 (b). These dislocations nucleated from the edge of the sample damaged by the FIB cut. In Figure 3-9 (c), dislocations nucleated from the left edge in the $(\bar{1}\ 1\ 1)$ plane and stopping close to the right edge of the tensile sample can be observed after unloading. Note the ‘clean’ diffraction contrast of these dislocations due to the absence of severe FIB damage in the centre of the sample. Although the three observed slip planes exhibit identical Schmid factors (0.27), it can be concluded from Figure 3-9 (a) that

the slip traces ST3 and ST2 induced by the glide of dislocations in the $(\bar{1} 1 1)$ and $(\bar{1} \bar{1} 1)$ planes, respectively, are dominant. This can be attributed to the nature of the dislocation sources on the edge of the sample and induced by FIB and/or to inaccuracies in the mounting procedure of the sample on the PTP device which can induce small deviations between the gage length axis and the tensile axis leading to changes in the resolved shear stresses on dislocations. Still, as indicated above, these results confirm that the FIB damage induced at the edges can act as preferential sites for the nucleation of dislocations while the nearly damage-free centre of the sample is well-suited for the determination of the dislocations and their response to the in-situ deformation. Also, the participation of the FIB defects as dislocation sources prevents early fracture due to the lack of dislocation sources in such small samples [135, 165].

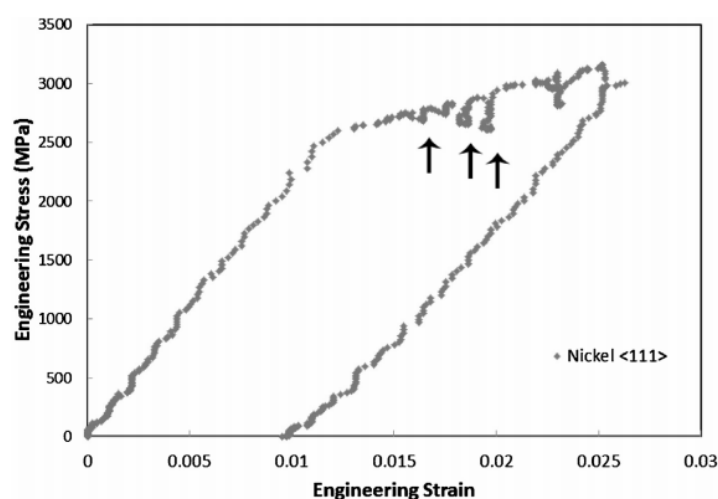


Figure 3-10, Engineering stress - engineering strain curve extracted from the in-situ TEM nanotensile testing, the black arrows show increasing load drops with increasing deformation.

Figure 3-10 shows the engineering stress - engineering strain curve extracted from the above in-situ TEM tensile test. Young's modulus extracted from the pure elastic loading part of Figure 3-10 equals 220 GPa, very close to Young's modulus of bulk polycrystalline pure Ni (207 GPa [166]). However, the calculated Young's modulus using the elastic constants for the $[1 1 1]$ orientation is 303 GPa [167], while the average modulus determined for micropillars of the same orientation was 308 GPa with a standard deviation of 79 GPa [168]. The smaller value observed in our case can be due to either a slight misalignment resulting in a lower modulus (since the modulus along the $[1 1 1]$ direction is the maximum one) or to a size effect related to the effect of the surface elastic modulus on thin samples [169].

Furthermore, a high yield stress of 2.5 GPa can be measured from the graph of Figure 3-10 in agreement with values of ~ 3 GPa reported in a single-crystalline Ni nanopillar with a

diameter of 165 nm [168]. The small difference in slope between the loading and unloading parts is expected to be due to the existence of the plastic regime and the bending of the nanoscale sample without breaking during unloading.

The plastic behaviour of such small-sized specimens is often controlled by the dislocation nucleation stage. For a dislocation source, such as a Frank-Read (F-R) source or a loop, a critical resolved shear stress is needed to expel a dislocation from the F-R source or to expand the loop. The critical resolved shear stress, τ , for a dislocation to form is controlled by the line tension and can be approximated by Equation 3-1[29]:

Equation 3-1

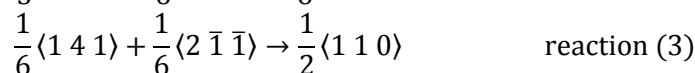
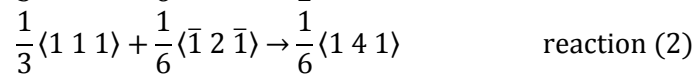
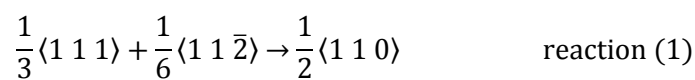
$$\tau = \frac{\mu b}{2r}$$

where μ is the shear modulus of the material (76 GPa for the bulk single crystal value) [152]), b is the magnitude of the Burgers vector of a perfect glissile dislocation of type $\frac{a}{2}$ [110] (0.24 nm), and r is the source radius. The 2.5 GPa engineering yield stress (σ) measured in the sample of Figure 3-10 corresponds to a critical resolved shear stress of 680 MPa taking into account the corresponding Schmid factor (Ω) of 0.27 via Schmid's law, Equation 3-2:

Equation 3-2

$$\tau = \sigma \cdot \Omega$$

This corresponds to the critical resolved shear stress of a dislocation source with a radius of ~ 15 nm which is consistent with the size of the FIB-induced loops observed at the edge of the sample (Figure 3-5). Furthermore, in such a thin sample the image forces are relatively large so they can accelerate the escape of the dislocations to the free surfaces. However, the critical stress for source opening might not be the only limiting factor. Indeed, because the FIB-induced loops are sessile Frank faulted loops [151], the critical stress for operating the source will also be controlled by the transformation of Frank faulted loops into perfect loops. Molecular dynamic simulations [170] have revealed that unfauling of Frank loops could occur under an external shear stress by the creation and the sweep across the loop of Shockley partial dislocations following the reactions



For a vacancy Frank loop, reaction (1), and for an interstitial Frank loop, reactions (2) and (3), are required. Because such reactions are energetically unfavorable, high stress levels (such as those attained in the present study) are required. Furthermore, on the basis of elasticity theory, the energy of the perfect loop becomes significantly smaller than that of the Frank faulted loop if the loop size exceeds some critical radius [171]. In FCC metals with high stacking fault energy, such as Ni and Al, this critical limit is very small (in Al, the perfect loop is energetically favourable for any size [29]). Therefore, large Frank loops can transform into unfaulted loops even without the presence of external stress.

To sum up this part, larger dislocation loops in the investigated Ni sample, regardless of their types, faulted or unfaulted, can open and participate in deformation at lower stress levels. Most of the large dislocation loops in the Ni sample, having high stacking fault energy, are likely unfaulted according to the small critical size for stability of faulted loops. Larger loops need lower shear stress for opening following Equation 3-1. For faulted dislocation loops, simulations have also proven that their unfaulting stress decreases as the size of the dislocation loop increases [170].

From Figure 3-10 a very high strain hardening rate of 43 GPa is measured in the macroscopic plastic regime. Similar behaviour has been reported for Ni single crystal nanopillars with a diameter of ~156 nm and compressed along the $\langle 111 \rangle$ direction [168]. Observed size effects on the strain hardening of micron and sub-micron samples are generally attributed to either the formation and development of dislocation structures [172] or to dislocation source exhaustion and dislocation starvation [138, 162]. However, in the present case, none of these cases was observed. The high strain hardening can, thus, be attributed to the nucleation of dislocations from the different sized dislocation loops. The plastic deformation starts when the stress level is high enough to activate large loops. To accommodate further plastic deformation, more dislocation loops that are smaller will be activated, which requires an increase of the applied stress leading to strain hardening.

From the deformation movie obtained from the PicoIndenter system, it can further be noticed that the load drops (indicated by the black arrows in Figure 3-10) were accompanied by simultaneous nucleation and glide of high numbers of dislocations from the defect areas at the edges of the specimen. Interestingly, the magnitude of the load drops increased with increasing strain indicating that the number of dislocations participating in the deformation

process increased with the plastic strain, which is in agreement with our observations of a greater number of small loops than large loops being present.

The present work provides a new approach to quantitative in-situ TEM tensile testing of micron-sized samples. The dedicated sample preparation method not only yields a nearly defect-free central area, in which pristine dislocation movement can be followed, but the FIB artefacts are even beneficial and can be used to the advantage of the experiment as they provide the dislocation sources needed to avoid premature fracture. The present approach can also be used for in-situ TEM tensile testing of samples containing a single defect, such as a grain or twin boundary in the centre of the sample, since such a defect can be identified and characterized by conventional TEM on the electro-polished sample before the final FIB cutting is performed.

3.4 Conclusions

In the present work, a combination of twin-jet electro-polishing for thinning to TEM transparency and FIB cutting for final shape selection has been used to prepare micron-sized Ni specimens with pre-selected orientation for in-situ TEM nanotensile experiments. The centre of the sample is nearly free of FIB induced artefacts, while a Ga-rich layer, long dislocations and dislocation loops have been induced at the edges of the sample due to the FIB cut. The latter artefacts at the sample edges were found to act as nucleation sites for deformation dislocations during the in-situ TEM straining, which prevents early fracture typically caused by the lack of sufficient dislocation sources in micron-sized samples. Strain hardening was observed and attributed to an increase of the stress level required for the opening of dislocation loops with different radius with increasing deformation. These results constitute the first step towards a better control of sample preparation techniques for quantitative in-situ TEM nanomechanical testing of materials.

Chapter 4:

Nanomechanics of Dislocations Near Surfaces in almost FIB Damage-free Single Crystal Ni Sample

Although the centre of the prepared tensile samples in chapter 3 shows less FIB-damaged than conventional FIB samples, the dominant participation in the deformation mechanism of FIB-induced defects present on the edges of the sample has made such samples less interesting for the investigation of plasticity mechanisms. In the present chapter it is explained how the previous sample preparation has been improved resulting in samples with minimum FIB-induced damages. In the following, the plasticity mechanisms in a small-scale single crystal Ni sample have been quantitatively investigated by using a single crystal tensile sample prepared by the new method.

4 Nanomechanics of dislocations near surfaces in almost FIB damage-free single crystal Ni sample

4.1 Introduction

As already pointed out before, the unique properties of small-scale materials, such as thin films, nanowires or nanoparticles are very promising [15, 52] and this motivated several research groups to start investigating the mechanical properties and elementary deformation/failure mechanisms in such systems [13, 173, 174].

So far three unexpected observations were made in most nanomechanical tests of single crystal metals: (i) a significant increase in yield strength at smaller length scales which is called “size effect”, (ii) a stochastic change of yield stress for the same size samples, and (iii) a jerky-flow, i.e., displacement jumps in load controlled experiments or load drops in displacement controlled tests [13, 48, 158]. All of these are generally attributed to the size and limited number of dislocation sources.

Depending on the ratio of an internal length scale (e.g., mean free path of dislocations) to the external length scale (sample size), three different scenarios can be distinguished in Figure 4-1:

- In the bulk-like regime, a high number of dislocations are present and their collective behaviour determines the material’s response. In this case, similar to bulk samples, during deformation new dislocation sources are progressively formed due to interaction of the dislocations which provides sufficient dislocations needed for deformation.
- On the other hand, in samples with very small dimensions there is a lack of dislocations in the structure which results in a strength as high as the theoretical limit.
- In the intermediate regime, the number and size of individual dislocations dominate the mechanical response of the samples and the material’s response is therefore stochastic. Larger samples with numerous initial dislocations tend to approach the bulk-like-regime with almost the same behaviour, while small samples can show a similar behaviour as small dislocation-free samples. [48, 175-177].

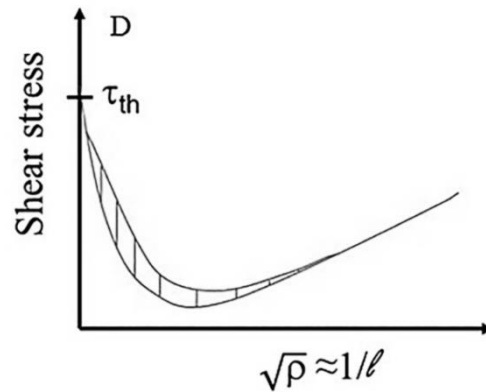


Figure 4-1, Schematic explaining the size effect: when the dislocation density ρ is close to zero the sample strength reaches theoretical values, while for high dislocation densities classical work hardening is observed. In the transition part a stochastic behaviour is observed [15].

Indeed, by decreasing the sample size, the size of available dislocation sources in the sample, mainly single arm sources [49-51], becomes smaller (source truncation mechanism) [162] and consequently their activation needs higher stress levels which means high yielding strength. During deformation, the high probability of interactions of dislocations with each other guarantees the sustainability of the dislocation structure; interaction of dislocations results in the formation of new dislocation sources (new pinning points) which participate in plastic deformation. Statistically, smaller samples have fewer dislocation sources in the microstructure (dislocation exhaustion) [168, 178]. Furthermore, a high surface-to-volume ratio and the image forces [138] dramatically increase the annihilation rate of dislocations in such samples (e.g., dislocation starvation mechanism) [51, 138]. In addition, the existing dislocation sources can shut down during deformation [51, 179]. Therefore, all these mechanisms cause a decrease the probability for dislocation interactions and the formation of new dislocation sources. Consequently, the microstructure is depleted of dislocations [174]. As a result, strength increases, plastic flow becomes stochastic, and eventually dislocations nucleate at or near surfaces, which requires higher stresses compared to pre-existing dislocation sources inside the sample [1] (nucleation-controlled plasticity). When the initial dislocation structure is sustainable, e.g., samples with high density of pre-existing dislocations [152] and samples bigger than a critical size [44, 138, 180], plasticity is multiplication-controlled [136], similar to bulk crystals, and dislocation pattern formation has been observed [103, 181-183].

Although “smaller is stronger” leads to beneficial performance of submicron single crystals, the intermittent and strongly heterogeneous plastic deformation of such samples can cause

problems in the fabrication and design and therefore, understanding the discrete properties of dislocations becomes of high importance.

In literature, it has been proposed that the main dislocation sources in small-scale materials are single arm sources (SAS) [50]. However, quantitative experimental characterization of the direct correlation between the discrete SAS mechanism and the submicron plastic behaviour is still very limited. Furthermore, a general understanding of the evolution of the flow stress after yielding is still missing. For example, several experimental studies reported contradictory data regarding the presence of strain hardening in submicron FCC single crystals under uniaxial compression [143, 168, 183-185]. Some researchers also highlighted the role of external conditions such as FIB-damage on the mechanical size effect.

In the previous chapter it has been shown that a combined twin-jet electro-polishing and FIB procedure could be designed in order to minimize the amount of FIB damages in Ni specimens dedicated for quantitative in-situ TEM tensile testing [186]. In spite of an overall decrease of FIB damages in the middle of the samples, the edges were still highly damaged by the FIB cut. A high density of FIB-induced dislocation loops with different sizes was observed to act as sources for the nucleation of mobile dislocations upon in-situ TEM straining. Although the latter implied a useful condition for the study of the mobility of dislocations in the damage-free central zone of the sample, the samples still contained too much FIB artefacts to relate the overall results to pristine nanomechanical objects.

The objective here is to contribute to a better understanding of the role of SASs in plasticity mechanisms by using Ni samples not affected by sample preparation induced extrinsic artefacts. Thus, we used the aforementioned preparation method and added an in-situ TEM annealing step prior to in-situ tensile testing to anneal out the remaining FIB induced defects. Comprehensive quantitative observation of the intrinsic discrete dislocation mechanisms under dedicated imaging conditions was performed to investigate the origin of the size dependent stochastic plasticity of small sized single crystals.

4.2 Materials and Methods

A high purity Ni foil (99.999%) was annealed for 1 hour at 400°C and then punched, ground and mechanically polished. After electro-polishing, the 3 mm discs were investigated by conventional TEM techniques in order to select proper regions in terms of thickness, electron transparency, crystallographic orientation, nature and density of defects, etc. A dual beam FIB/ SEM was then used to cut out the tensile samples By the Ga⁺ ion beam at the

appropriate locations. In order to minimize the FIB induced damages during the imaging by ion beam, the selected regions were as little as possible exposed to the FIB beam. Micron-sized dog-bone patterns were thus designed and milled by FIB. One end of the dog-bones was cut like a spring shape, red arrow in Figure 4-2 (a) in order to accommodate possible thermal expansion and prevent bending of the samples during heat treatment. To ensure that the thickness along the tensile sample is uniform, the tensile axis of the samples was selected parallel to the edge of the electro-polishing hole or from regions where no clear thickness contrasts were observed.

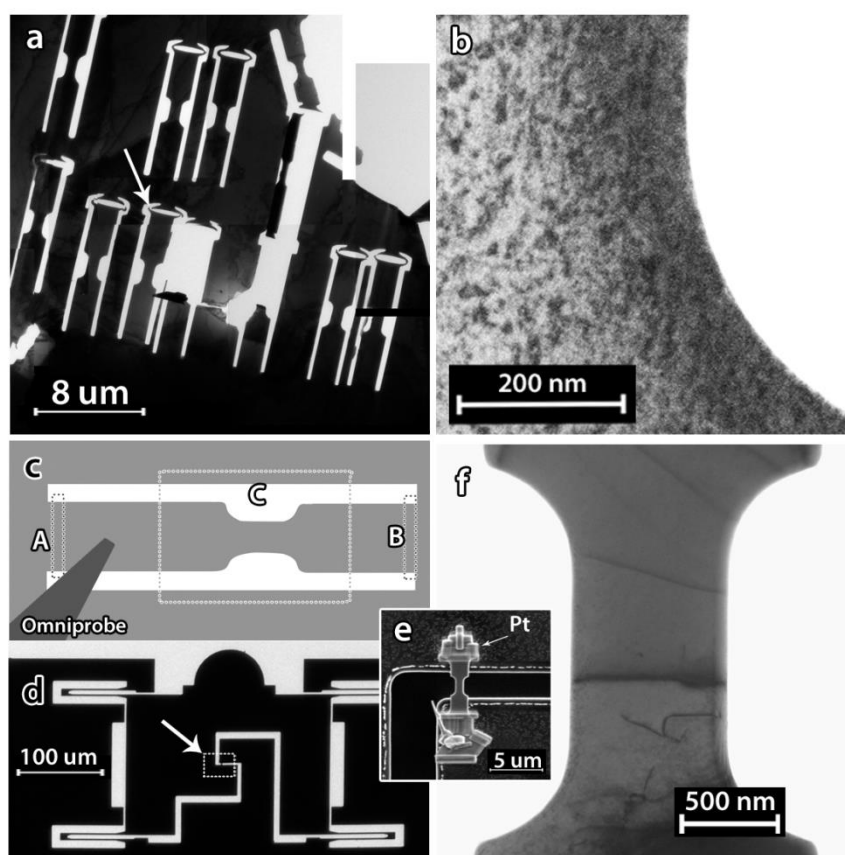


Figure 4-2, TEM BF images of (a) 3-mm electro-polished sample after FIB cutting, (b) the edge of a dog-bone showing FIB induced defects. (c) A schematic of a dog-bone sample showing the location where the Omniprobe attaches to the sample, the areas A and B which will be cut after the annealing and the area C which should be kept unexposed during mounting. (d) TEM image of a PTP device, (e) SEM image showing a final configuration of a dog-bone on a PTP device, (f) TEM-BF image showing a near dislocation-free sample after annealing and mounting on the PTP device.

In the previous chapter, it has been shown that FIB milling to cut the edges still induces damages in the microstructure of the sample. The amount of FIB damages and the span of these damages over the sample mainly depend on the FIB conditions, the required current/voltage and the cutting duration which varies also with the thickness of the electro-

polished foil and the type of material. In general, the thicker the sample, the wider the affected zone because of the longer duration of the FIB exposure. In Figure 4-2 (b), a TEM BF image of the dog-bone sample edge before heat treatment shows FIB induced defects.

After 30KV/80pA FIB cutting of the edges of the dog-bones using the designed pattern, the electro-polished sample was heat treated using a Gatan in-situ TEM heating holder for ~1 hour at 700°C in order to remove FIB-induced defects. The main advantages of using the heating holder are the high-quality vacuum in the microscope and simultaneous observation of defect evolution during treatment. Heat treatment was already used in the literature to remove FIB induced damages but just for micropillars and larger tensile samples for in-situ SEM deformation [141]. In this work, during the in-situ TEM heating, it was observed that the FIB induced dislocations were either annihilated at the surfaces or coagulated with each other to form long dislocations and junctions, some of which again were annihilated at the surface. TEM observation of the different samples with different thicknesses showed that the rate of annihilation of dislocations in thin parts of the sample is faster than in thicker parts, which can be attributed to the effect of the image force [29]. In general, the final density of dislocations highly depends on the time and temperature of the heat treatment. Increasing both factors up to the values mentioned above, leads to large dislocation-free areas in the present Ni samples. After heat treatment and depending on the original selected site, the sample can be totally dislocation free, Figure 4-3 (a), can have some remaining long dislocations Figure 4-3 (b), can have a selected grain boundaries, black arrow in Figure 4-3 (c) including coherent twin boundaries along the tensile direction, black arrow in Figure 4-3 (d).

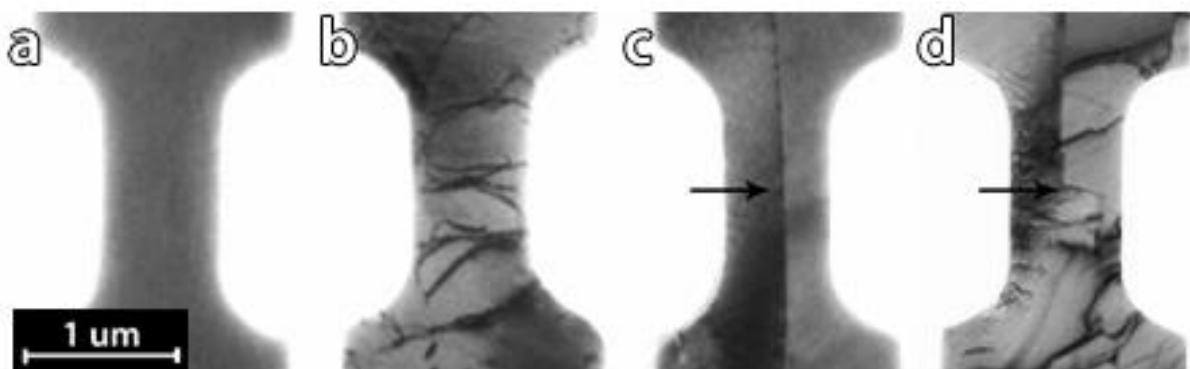


Figure 4-3, TEM-BF micrographs of samples with different initial microstructure. (a) defect-free single crystal; (b) sample with ‘high’ initial density of dislocations; (c) sample with grain boundary; (d) sample with $\Sigma 3$ 111 twin boundary exhibiting a step indicated by black arrow.

These samples experienced similar heat treatment procedure as the sample discussed in the paper.

To perform quantified in-situ TEM tensile testing, the PicoIndenter holder and PTP device were used, (cfr. chapter 2). Following the in-situ TEM heat treatment, the dog-bone samples were cut and mounted on PTP devices using the Omniprobe in the FIB instrument. Once the Omniprobe is attached by Pt deposition to one side of the dog-bone, as shown in Figure 4-2 (c), the remaining edges of the dog-bones were cut from the sides, point A and B in Figure 4-2 (c), by FIB. The samples were then mounted on PTP devices, Figure 4-2 (d), by Pt deposition on the sides, and then the Omniprobe was detached from the sample by FIB. Figure 4-2 (e) shows the final configuration of a mounted sample on a PTP device. The significance is in the whole process of mounting, so great care was taken to avoid any exposure of the gages, the area C in Figure 4-2 (c), by the ion beam. Conventional TEM revealed that FIB has not induced any extra defects during the mounting step of the samples, as seen in Figure 4-2 (f).

The chemical composition of one of the samples was checked by EDX - ADF-STEM in a FEI Osiris TEM operating at 200 kV. Figure 4-4 (a), (b), and (b) show the distribution of gallium and nickel (Ni) in the sample. Quantitative analysis on different areas showed that the gallium amount in the sample is negligible (less than 1% which is below the EDX precision) so any gallium present after the FIB cutting of the shape of the sample [186] has diffused during the annealing and formed a dilute solid solution. Ideally, the performed heat treatment to remove FIB induced defects should be performed of the entire setup after FIB mounting, but this is not possible due to a risk of diffusion of the platinum, used to clamp the sample onto the PTP device, into the MEMS device or into the sample at high temperatures.

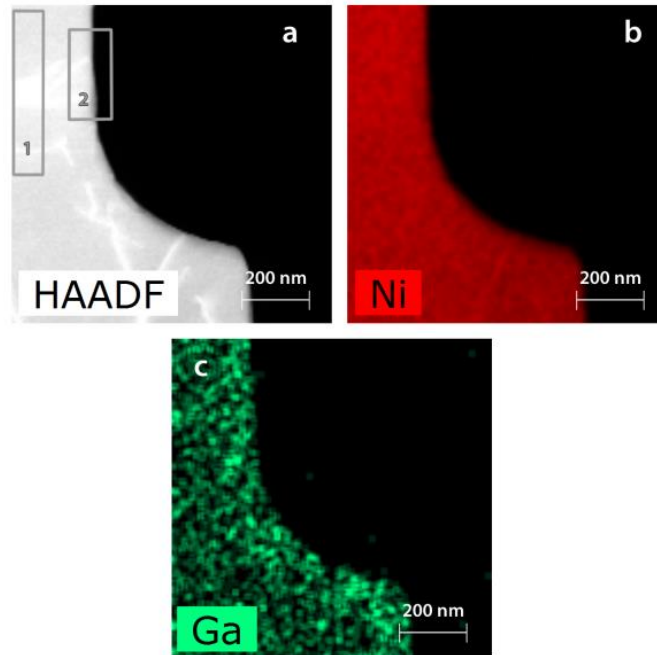


Figure 4-4, (a) ADF-STEM image), (b), and (c) EDX chemical maps of Ni, and Ga, respectively, displayed as counts.

The sample preparation procedure described here has attractive advantages. Indeed, TEM investigation of the electro-polished sample before FIB cutting offers the possibility of an accurate crystallographic characterization and defect analyses which allows some freedom for prescribing the tensile sample condition in terms of loading direction, imaging conditions and crystallographic defects. Figure 4-3 shows TEM-BF micrographs obtained on different samples including single crystal samples and bi-crystal samples with different interfaces. In addition, the obtained cleanliness of the samples allows improving the quality of the TEM observation of the intrinsic deformation/failure mechanisms as well as a quantitative correlation between these mechanisms and the load-displacement characteristics.

The in-situ TEM tensile experiments were carried out in load control mode with a loading rate of 2 nN/s (initial strain rate of $2 \times 10^{-4} \frac{1}{s}$) in a FEI Osiris TEM operating at 200 kV. The sample was mounted on a PTP device with a spring constant of 490 N/m which was measured by a loading cycle of the PTP device after the sample fracture. The thickness of the sample was around 300 nm and other dimensions were shown in Figure 4-5.

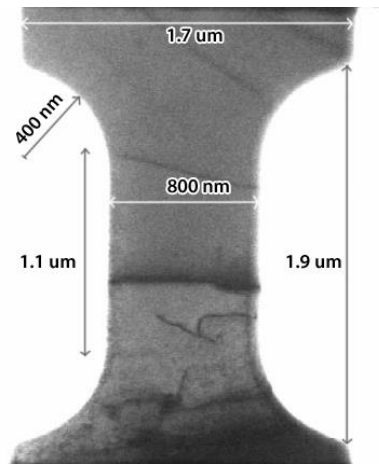


Figure 4-5, Dimensions of the sample, the thickness was measured as $300 \text{ nm} \pm 16 \text{ nm}$ by FIB cross-sectioning.

According to the spring constant and the displacement data obtained from digital image cross-correlation of the deformation movies, the actual applied load on the sample, which is the subtraction of the spring load from the applied load, was calculated. The engineering stress (E-stress) was extracted by measuring the initial cross-section area of the gage length of the sample by FIB cross-sectioning after fracture. The uncertainty on the applied stress is mainly due to the precision of the measurement of the cross-sectional area of the tensile samples in the SEM images ($\sim 3 \text{ nm}$) as well as that of the measurement of the force applied on the sample ($\sim 0.2 \text{ } \mu\text{N}$). According to the standard errors on the measurements of the cross-sectional area with MATLAB ($\sim 500 \text{ nm}^2$) and the maximum force, the maximum error of the engineering stress is $\sim 3 \text{ MPa}$. Image cross-correlation of the deformation movies provided the gage length displacement data, allowing the calculation of the engineering strain (E-strain).

4.3 Results and discussion

Figure 4-6(a) exhibits the stereographic projection of the Ni sample shown in Figure 4-2 (f). The tensile direction and the normal to the foil surface were close to $[\bar{5} \bar{4} \bar{1}]$ and $[2 \bar{1} \bar{5}]$, respectively. Schmid factors on the different slip systems are listed in Figure 4-6 (b). The sample was oriented close to multiple slip conditions (the ratio of the Schmid factor of the secondary to the primary slip systems $\frac{\tau_s}{\tau_p}$ is 0.83). The red (dashed) arrow in Figure 4-6 (a) shows the Burgers vector with the highest Schmid factor while the grey dashed line indicates the trace of the $(1 \bar{1} \bar{1})$ plane. In Figure 4-2 (f) it can be seen that the initial microstructure consists of few tangled dislocations that survived the heat treatment. In the literature, both experiments and simulations have shown that the final dislocation structure after thermal

relaxation of FIB defects is a 3D tangled network of dislocations containing mobile/immobile pinning points [141, 179, 187].

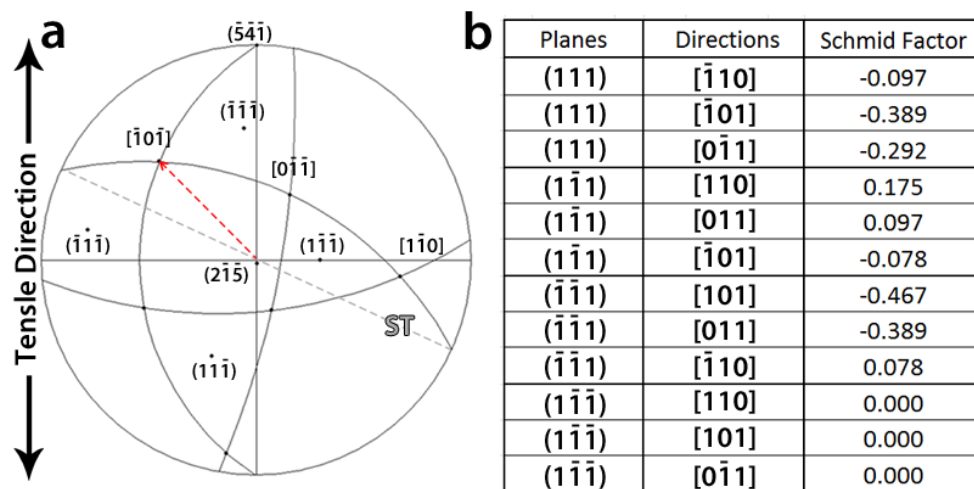


Figure 4-6, (a) Stereographic projection of the tensile sample and (b) Schmid factor values of slip systems in the sample.

The sample was subjected to 5 loading-unloading cycles with maximum stress equal to 420 MPa, 770 MPa, 800 MPa, and 1209 MPa with failure during the last cycle at 1200 MPa. Figure 4-7 shows the stress-strain curves of the sequential tensile experiments. Note that, after each cycle, the experiment was stopped in order to set the parameters of the following cycle. During cycle 1 (blue plot in Figure 4-7) the behaviour was elastic and relaxation of the initial dislocation structure was observed. Indeed, as depicted in Figure 4-8 (b), the blue dislocation was unlocked from the debris at point 5 and glided around the pinning point 2 as indicated by the dashed arrow in Figure 4-8 (b), before being pinned again at point 6 by another debris, black arrow in Figure 4-8 (b). The resulting configuration, including the left-over debris as a small black dot at point 5, can still be observed in Figure 4-8 (c) after unloading. These debris points are probably residual small sessile dislocation loops associated to point defect clusters generated by FIB [141, 151]. The slip trace (ST) left by the glide of the blue dislocation (marked by the red arrow in Figure 4-8 (b)) indicates that this dislocation slips along the $(1\bar{1}\bar{1})$ plane. During the setting of the parameters for cycle 2 (orange plot in Figure 4-7), the segment of the blue dislocation pinned between point 6 and the surface (labelled “s” in Figure 4-8) of the sample, was unlocked from the surface in order to shorten its length, Figure 4-8 (d).

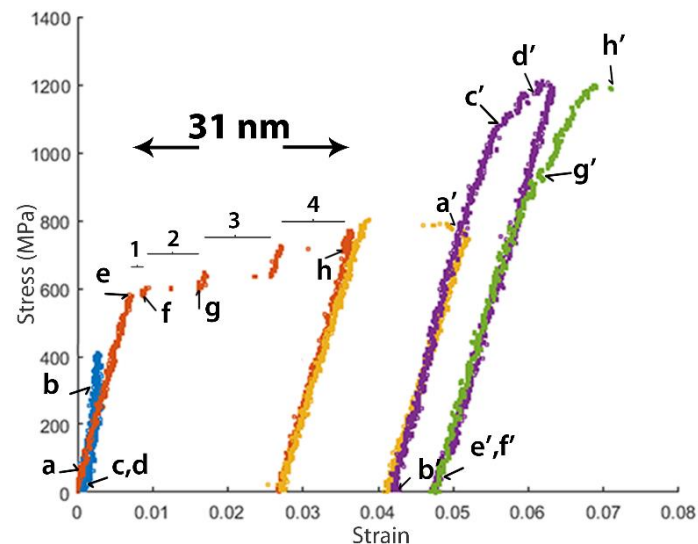


Figure 4-7, Engineering tensile stress-strain curves involving 5 loading cycles. Letters correspond to the snapshots shown in Figure 4-8 and Figure 4-16. The numbers and segments indicate the strain bursts in cycle 2.

In cycle 2, the sample yielded at 580 MPa which is one order of magnitude higher than the typical yield stress reported in macroscopic Ni single crystal (~ 50 MPa in [152]). The stress-strain curves in Figure 4-7 clearly exhibit discrete strain bursts separated by intervals of nearly elastic loading. The lack of points between the bursts is due to the sudden increase of displacement that cannot be captured in the movie used for accurately measuring the displacements. The loss of contact between the indenter and the PTP device can be excluded as responsible for such behaviour because no load drop is detected. In the following paragraphs, the origin and characteristics of the staircase behaviour in cycle 2 are discussed based on the TEM snapshots shown in Figure 4-8.

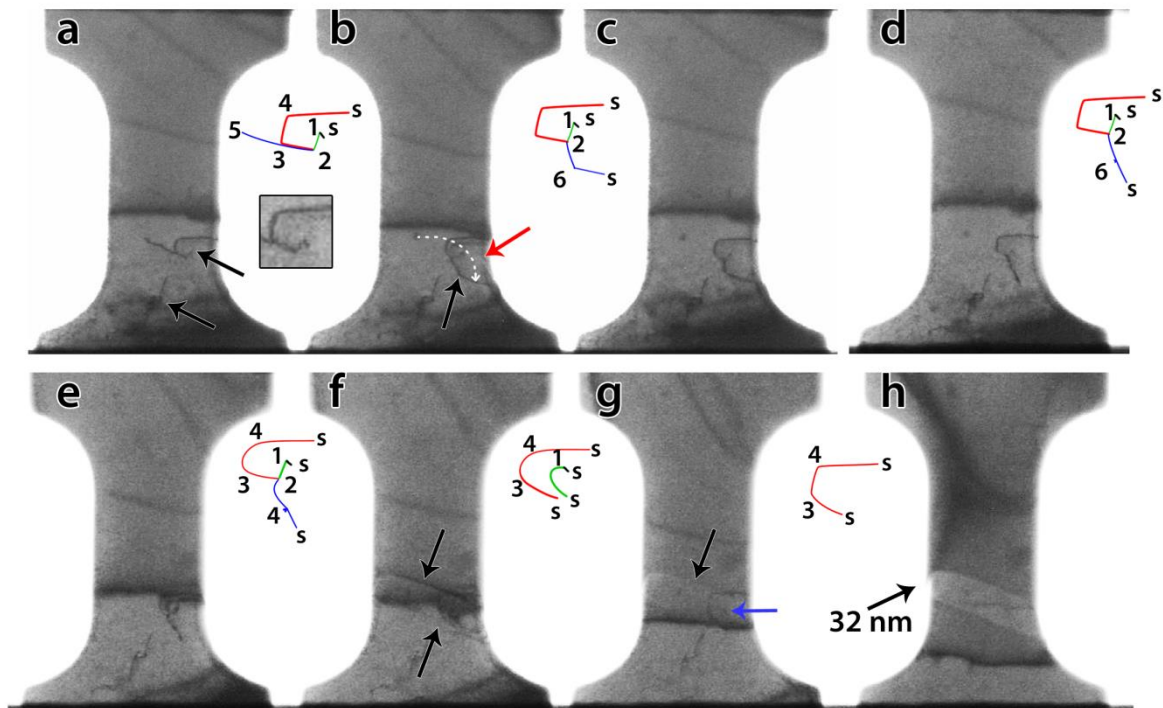


Figure 4-8, Snapshots from the in-situ TEM deformation movie during cycle 1 (a-c) and cycle 2 (d-h). Schematic configurations of dislocations were drawn to the right of some snapshots. The numbers indicate the position of pinning points due to debris or cross-slip of dislocations. The sites in which the dislocations emerge to the free surface are indicated by “s”. A magnified image of the initial dislocation configuration is shown in the right inset of (a).

In the BF image of Figure 4-8 (e) obtained just before yielding, bowing out of the dislocations between pinning points can be observed. After yielding, the first strain burst occurred which was accompanied by the destruction of the dislocation configuration shown in Figure 4-8 (e) and the formation of STs parallel to the $(1\ 1\ \bar{1})$ plane as indicated by black arrows in Figure 4-8 (f). The new dislocation configuration consists of the red, green and black dislocations shown in Figure 4-8 (f) while the blue dislocation has disappeared. It is worth noting that the ST induced by the glide of the blue dislocation in cycle 1 (red arrow in Figure 4-8 (b)) is different from the ST shown in Figure 4-8 (f) as shown in Figure 4-9.

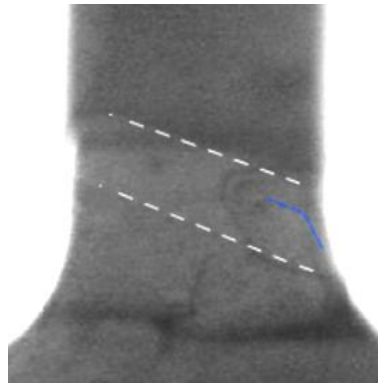


Figure 4-9, Overlapping of slip traces from the first (the blue marked slip trace) and the second cycle (the white dashed lines). Note that the blue dislocation has experienced cross-slip close to the surface.

Furthermore, Figure 4-8 (g) confirms that the red dislocation remains immobile in cycle 2. This is probably due to the complex structure of this dislocation composed of segments lying in different planes as evidenced by the sharp angles between these segments in Figure 4-8 (d). Thus, the most plausible scenario is that, after yielding, the pinning point 2 was destroyed by surface annihilation or unzipping [188], leading to the formation of a single arm source 1 (SAS1) at the pinning point 1 (the green dislocation in Figure 4-8 (f)). Avalanches of green dislocations nucleated from SAS1 to create the ST shown in Figure 4-8 (f) and the first strain burst in cycle 2. A magnified image of the SAS1 indicated by the blue arrow in Figure 4-8 (g) is shown in Figure 4-10.

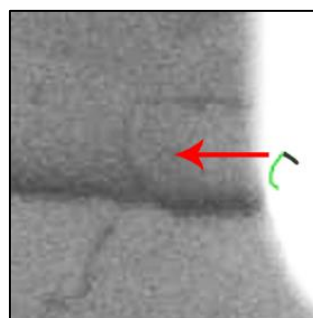


Figure 4-10, Snapshot at point g of Figure 4-7. The red arrow indicates the position of the active SAS1 in cycle 2.

In Figure 4-8 (g) and Figure 4-8 (h), the height of the ledge created by the glide of the green dislocations in the $(1\ 1\ \bar{1})$ plane has increased after the successive strain bursts. This, as well as the nearly identical amount of plastic deformation induced after the strain bursts between ‘f’ and ‘h’ in Figure 4-7 confirm that the bursts in cycle 2 were induced by the same SAS1. However, it should be noted that the first strain burst between points ‘e’ and ‘f’ in the same figure is smaller. This can be explained by the difficulty of the first dislocations to escape

from the sample due to the presence of a thin oxide layer at the surface. Indeed, the black diffraction contrast at the ST in Figure 4-8 (f) might indicate the presence of one or very few dislocations near the surface. The presence of dislocations pile-up at this position is unlikely since it cannot explain the occurrence of the first strain burst [189]. The black diffraction contrast at the ST in Figure 4-8 (f) cannot be observed in Figure 4-8 (g) and Figure 4-8 (h), indicating that, with increasing deformation, the oxide layer ceased acting as an obstacle retarding the escape of dislocations at the free surfaces, a mechanism that has been reported before in thin films with native oxide layers [190]. Hence, it can be concluded that the macroscopic yielding observed in cycle 2 of Fig. 3 is mainly controlled by the nature/length of the initial dislocations. The role of a thin oxide layer at the surface can be excluded as a dominant mechanism controlling the yield stress. This is also in agreement with the absence of the clear observation of an oxide layer at the surface using conventional high resolution TEM and EELS.

Based on the total plastic displacement (31 nm in Figure 4-7) and the height of the ledge (32 nm in Figure 4-8 (h)) induced by the SAS1 in cycle 2, it is possible to determine the active slip system and also to calculate the number of dislocations produced from activation of the source.

The direction of the parallel STs made in cycle 2, Figure 4-8 (h), shows that the dislocations have glided on the $(1\ 1\ \bar{1})$ plane. The corresponding Burgers vector can be determined based on the measurement of the height of the ledge and the total plastic displacement in cycle 2. The displacement induced by the activation of a specific slip system in a single crystal can be calculated using the following geometrical equation:

Equation 4-1

$$t = \alpha b \sin \lambda \cos \beta$$

where λ is the angle between the Burgers vector \mathbf{b} and the normal to the foil surface; β is the angle between the Burgers vector's projection on the foil surface plane and the unknown displacement vector t while α is the number of dislocations.

The measured displacement along the tensile direction, 31 nm, and the measured final height of the step on the edge of the sample (i.e., normal to the tensile direction), 32 nm, confirm that the value of β for both cases (parallel and normal to the tensile direction) should be close to 45° . Among the slip systems in the $(1\ 1\ \bar{1})$ plane Figure 4-6 (a), only the one with Burgers

vector of $\frac{a}{2}[\bar{1} 0 \bar{1}]$ yields such a value of β . Therefore, the active slip system is $\frac{a}{2}[\bar{1} 0 \bar{1}](1 1 \bar{1})$.

Accordingly, λ equals 64° and due to Equation 4-1, approximately 200 dislocations have been nucleated and reached the surface in cycle 2.

Therefore, the observed stair case flow in cycle 2 of Figure 4-7 is due to the intermittent operation of the SAS1 in the $\frac{a}{2}[\bar{1} 0 \bar{1}](1 1 \bar{1})$ slip system. In literature the stair case flow is often attributed to the sequential activation and deactivation of different SASs [135, 174, 179, 187, 191, 192]. This interpretation, which is understandable for samples with high dislocation density (including FIB induced dislocations), is not consistent with the present observations. Thus, the present result offers the unique possibility to directly investigate plastic flow for individual SASs in a quantitative manner.

Strain hardening due to source size reduction has been reported by Chisholm et al., [178]. However, details regarding the elementary mechanisms controlling the formation and the operation of the individual SASs as well as the relationship between these mechanisms and the plastic flow of the sources have not been investigated as yet. A deeper analysis of the TEM images in Figure 4-8 helps us to understand the origin of the strain hardening accompanying the operation of the SAS1 in cycle 2 of Figure 4-7. Indeed, it can be seen in this cycle that the stress increases elastically after each strain burst. Usually, in FIB-prepared samples, once dislocations emitted from the weakest SAS get blocked by the abundant FIB damages and then the source is shut down by the exerted back stress or changes of the local stress state. Therefore, a second weak source starts to operate at slightly higher stresses, leading to strain hardening and staircase behaviour [135, 136]. In cycle 2 of Figure 4-7, such scenario can be excluded as only one SAS is active. Furthermore, interactions of dislocations nucleated from SAS1 with other dislocations were not observed. In the following, the strain hardening observed in cycle 2 of Figure 4-7 is explained by the decrease of the SAS1 length (the green segment in Figure 4-8 (f)) due to the decrease of the mobile dislocation glide area. Such effect is schematically illustrated in Figure 4-12. Due to the activation of a SAS in a slip plain, the slip area progressively becomes smaller, Figure 4-12 (b). Considering that the pinning point of the green SAS in Figure 4-12 is fixed compared to the lower part of the crystal, due to shrinkage of the slip area, the length of the SAS has also become progressively shorter by activation of the SAS.

Figure 4-11(a) shows the stereographic projection of the sample with $[1\ 1\ \bar{1}]$ as zone axis. The direction of the $\frac{a}{2}[\bar{1}\ 0\ \bar{1}]$ Burgers vector as well as the $[2\bar{1}\bar{1}]$ direction which is parallel to the intersection of the slip plane $(1\ 1\ \bar{1})$ with the surface plane $(2\ \bar{1}\ \bar{5})$ is marked by 2 arrows. The intersection of the slip plane $(1\ 1\ \bar{1})$ with the surfaces of the sample delimits the slipped area. Let's consider the rectangle ABCD in Figure 4-11 (b) as the area swept by one dislocation with Burgers vector $\frac{a}{2}[\bar{1}\ 0\ \bar{1}]$. The edges AD and BC correspond to the intersection of the slip plane with the top surface plane $(2\ \bar{1}\ \bar{5})$ while the edges AB and CD define the intersection of the slip plane with the sample surface on the sides. Figure 4-11 (b) shows that, after the glide of the dislocation, the slipped area changes from ABCD to A'B'C'D. According to the slip geometry, the width of the slip area rectangle decreases by $0.5|b|$ while its length decreases by $0.86|b|$ ($|b| = 0.24\text{ nm}$). Therefore, the slip of around 200 dislocations at the end of the burst 4 of the cycle 2 would decrease the initial width ($AB = 356\text{ nm}$) and length ($BC = 875\text{ nm}$) of the rectangle by $\sim 24\text{ nm}$ ($135 \times 0.5|b|$) and $\sim 41\text{ nm}$ ($136 \times 0.86|b|$), respectively. This decreases the slip area by $\sim 12\%$ leading to an increase of the resolved shear stress acting on the source on the glide plane by $\sim 13\%$.

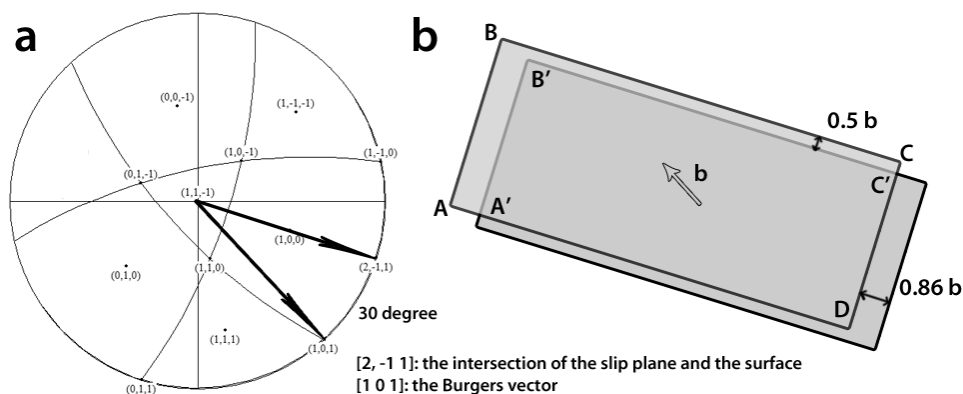


Figure 4-11, (a) Stereographic projection showing the direction of intersection of the slip plane $(1\ 1\ \bar{1})$ with the surface $(2\ \bar{1}\ \bar{5})$ and the Burgers vector, $\frac{a}{2}[\bar{1}\ 0\ \bar{1}]$, (b) schematic illustration showing the slipped area before (ABCD) and after the glide of one dislocation (A'B'C'D).

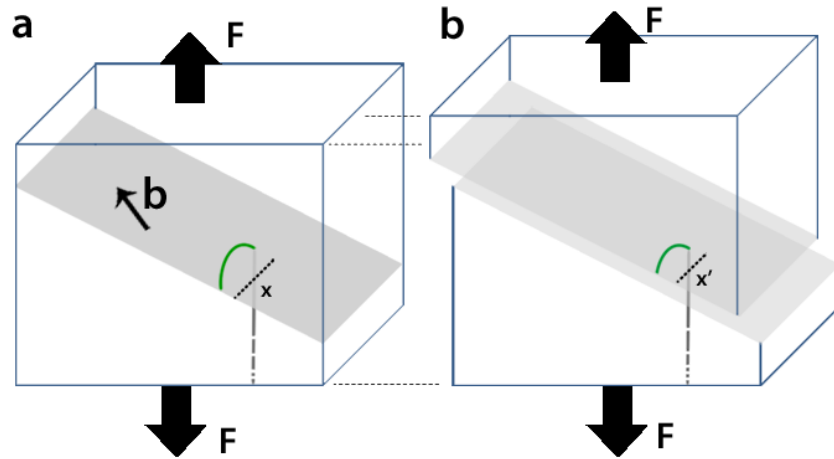


Figure 4-12, (a) and (b) Schematic illustrations showing the effect of the decrease of the slipped area on the length of the source after a strain burst ($x' < x$).

This way the decrease of the SAS1 length and its relationship with the intermittent plastic flow of this source can be explained.

Changes of the length of the SAS1 in cycle 2 can be extracted by analysing the evolution of the critical stress needed to activate the source with the accumulated plastic displacement. The critical resolved shear stress (CRSS) to activate a SAS can be predicted using Equation 4-2, modified from the known equation for a Frank-Read source by replacing the length l by $l/2$ [29, 50].

Equation 4-2

$$CRSS = \frac{\alpha G \mathbf{b}}{4\pi l} \left(\ln \left(\frac{2l}{b} \right) + 1 \right)$$

where α is a coefficient equal to 1 or $1/(1 - \nu)$ for edge or screw dislocations, respectively. G is the shear modulus (76 GPa), \mathbf{b} is the magnitude of the Burgers vector (0.249nm), Poisson coefficient $\nu = 0.31$ and l is the SAS length.

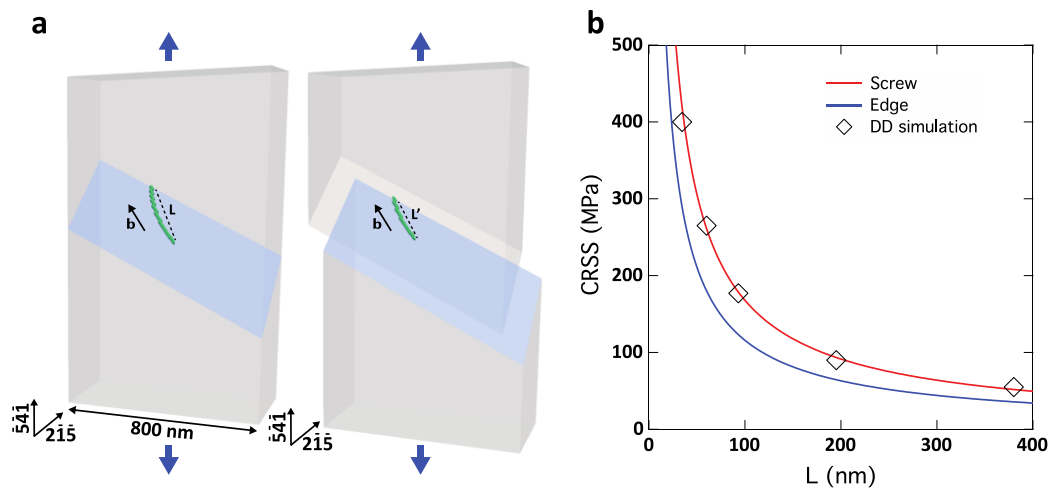


Figure 4-13, (a) Illustration from DD simulations showing the effect of the slipped area reduction on the SAS critical length after a strain burst. (b) CRSS vs. SAS length calculated with Equation 4-2 for screw or edge dislocation character compared with DD simulation results when using the exact crystal geometry.

To support the predictions of Equation 4-2, Dislocation Dynamics (DD) simulations [193] were performed by R. Gatti and B. Devincere (ONERA Châtillon, France) with the Discrete Continuous Model [194]. As illustrated in Figure 4-13 (a), DD simulations reproduced precisely the plastic deformation of the TEM sample. Different scenarios have been tested by changing the SAS1 location and length. Those computations established that the CRSS predicted with Equation 4-2 is in very good agreement with DD simulations accounting for dislocation-surface elastic interactions, Figure 4-13 (b). Furthermore, in agreement with elastic theory predictions we confirmed that the SAS1 critical configuration is close to the screw dislocation orientation (Figure 4-13(a)).

In Figure 4-14, Equation 4-2 was used to draw the evolution of the CRSS with the length of a SAS exhibiting pure screw and pure edge character. The horizontal thin grey lines in Figure 4-14 indicate the CRSSs obtained at the strain bursts 1 and 4 in cycle 2 in Figure 4-7 (270 and 358 MPa), based on the Schmid factor of the activated slip system. During this interval, the length of the source was reduced by ~ 16 nm (resp. ~ 11 nm) for pure screw (resp. pure edge) dislocations as can be seen in Figure 4-14.

On the other hand, it was shown that the glide of 200 dislocations in the slip system $a/2 [\bar{1} 0 \bar{1}](1 1 \bar{1})$ can reduce the slipped area by $\sim 12\%$ and the length of the source (distance X in Figure 4-12) by 24 nm (by assuming that the pinning point of the source is closer to the surfaces than edges which is in agreement with TEM observation). Taking into account the reduction of the slipped area at the end of the strain burst 4, the critical resolved shear stress

should increase by ~13% (~405 MPa, the red dash line in Figure 4-14). The corrected resolved shear stresses (RSSs) at the end of each strain burst are listed in Table 1.

Table 1, The corrected RSS at the end of the bursts.

| | E-Stress (MPa) | RSS (MPa) | The corrected RSS at the end of the bursts (MPa) |
|---------|-----------------------|------------------|---|
| Burst 1 | 580 | 270 | 272 |
| Burst 2 | 610 | 284 | 295 |
| Burst 3 | 671 | 313 | 339 |
| Burst 4 | 768 | 358 | 405 |

It can also be seen in Figure 4-14 that this correction changes the reduction of the source length to 22 nm and 14 nm for pure screw and pure edge dislocations, respectively. As the simulations showed that the dislocation character is close to the screw character, 22 nm is in a very good agreement with the decrease of the source length obtained from the reduction of the slip area (24 nm). Therefore the results show that the observed strain hardening is due to decrement of the length of SAS.

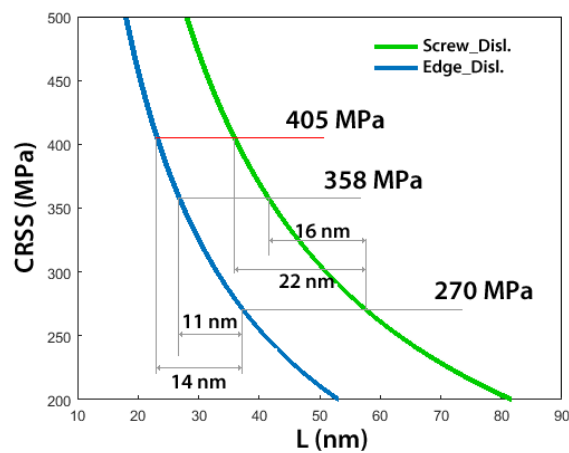


Figure 4-14, CRSS vs. length of SAS (L) curves drawn using Equation 4-2. The grey lines correspond to CRSS measured in burst 1 and 4 of cycle 2. The red line indicates the CRSS for burst 4 after correction by taking into account the reduction of the slipped area.

According to the data shown in the previous section, it can be assumed that the length of the source, l , changes by Equation 4-3:

Equation 4-3

$$l = R - n(0.5b) \quad \rightarrow \quad nb = 2(R - l)$$

where n is the number of the nucleated dislocations and R is the initial length of the SAS. On the other hand, the evolution of the shear stress due to the reduction of the slip area, τ_{area} , can be described using Equation 4-4:

$$A_{area} = (356 - 0.5 nb) \times (875 - 0.86nb)$$

$$A_0 = 356 \text{ (nm)} \times 875 \text{ (nm)}$$

$$\tau_{area} = \tau_0 \times \frac{A_0}{A_{area}}$$

Equation 4-4

$$\tau_{area} = \tau_0 \times \frac{356 \times 875}{(356 - 0.5 nb) \times (875 - 0.86nb)}$$

where τ_0 is initial resolved shear stress in the slip plane, A_0 is the initial area of the slip plane and A_{area} is the new area of slip area.

By combining Equation 4-3 and Equation 4-4, the Equation 4-5 that describes the evolution of the shear stress as function of the length of the source can be obtained:

Equation 4-5

$$\tau_{area} = \tau_0 \times \frac{356 \times 875}{(356 - 0.5 (2R - 2l)) \times (875 - 0.86(2R - 2l))}$$

Based on these results it seems that two main competing factors, being the reduction of the slipped area (i.e., softening due to the increase of the local applied stress τ_{area}) on the one hand and the decrease of the source length (i.e., strengthening due to the increase of the CRSS) on the other hand, are controlling the mechanical response of the SAS1 in cycle 2.

Figure 4-15 exhibits the evolution of the resolved shear stress in the SAS1 slip plane as a function of the source length during cycle 2. In this figure, the red curve is the Equation 4-2 prediction for a screw dislocation. Except for the arrow (e) at 270 MPa that indicates the onset of yielding in cycle 2, the other arrows report the resolved shear stress at the end of each burst by considering the slip area reduction effect at the end of the bursts, Table 1.

The scenario illustrated in Figure 4-15 can thus explain the origin of the intermittent plastic flow of this source, based on the assumption that an immobile SAS needs a stress overshoot to be activated. In this figure, the black dashed lines indicate the evolution of τ_{area} deduced

when considering the slip area reduction effect, Equation 4-5. At the beginning of each strain burst, $\tau_{area} > CRSS$ and the SAS activation is made possible. Progressively, the increment of τ_{area} ($\Delta\tau_{area}$) is not sufficient to allow further operation of the source and the SAS stops when $(\tau_{area} + \Delta\tau_{area}) < (CRSS + \Delta CRSS)$. Such competition between a softening and a strengthening mechanism explains the existence of intermittent flow. Here, one must notice that it is not possible to predict the amplitude of plastic bursts. Indeed, this calculation would require the measurement of the stress overshoot needed to re-activate the SAS. Such quantity is difficult to define since it is impacted by many features such as the loading control, pinning effects that might exist on immobile dislocations ending at a surface and internal stress sources neglected in our DD simulations.

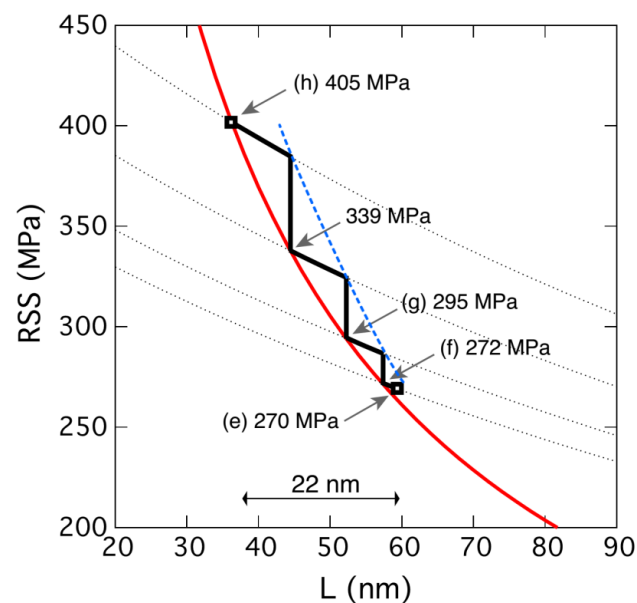


Figure 4-15, The red line presents Equation 4-2 (CRSS) for screw dislocations and the black dashed lines present Equation 4-5 (τ_{area}) for the conditions where they intersect the red lines in the corrected RSS at the end of the bursts. The full black line shows how the RSS changes by SAS size. The blue dashed line schematically shows the re-activation stress of a SAS.

In cycle 3, one strain burst occurred at 800 MPa and was accompanied by the formation of a new ST parallel to those formed by the operation of the SAS1 in cycle 2, black arrow Figure 4-16 (a'). This can be explained by the destruction of SAS1 upon unloading in cycle 2 and the activation of a new SAS2. Indeed, the imposed compressive force of the springs of the PTP on the sample and the slight buckling after full unloading could destabilize SAS1.

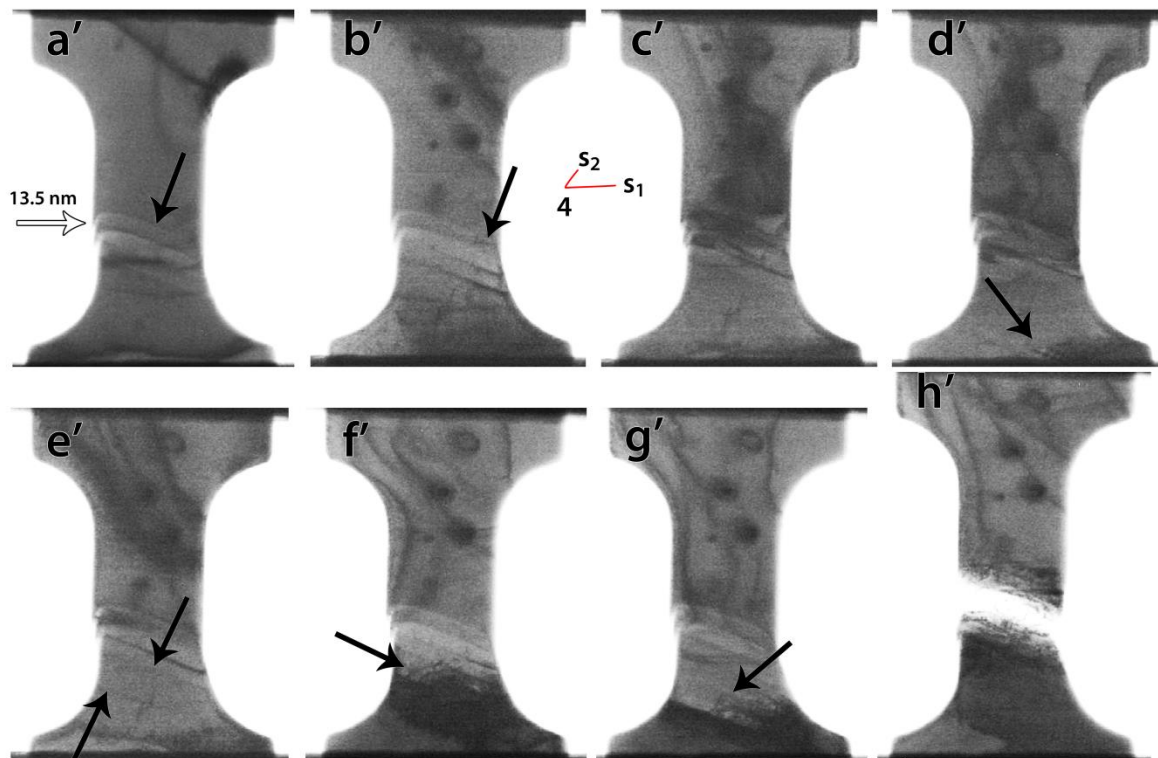


Figure 4-16, Snapshots from the deformation movie of the third cycle (a), of the fourth cycle (c-e) and of the fifth cycle (f-h) (prime notes (') are used to correlate with fig).

Figure 4-16 (b') shows that, after unloading in cycle 3, the configuration of the red dislocation has changed in comparison with Figure 4-8 (g). Indeed, only segment $4s_1$ connected to another segment $4s_2$ can be observed while segments $3s_1$ and $3s_2$ disappeared. Therefore, it can be anticipated that point 3 was annihilated at the surface, leading to the formation of SAS2 with a new segment $4s_2$ rotating around pinning point 4. Based on the measurements of the total plastic displacement (14 nm), the height of the ledge (13.5 nm) induced by the SAS2 in cycle 3 (white arrow in Figure 4-16 (a')) and Equation 4-1, it can be concluded that around 80 dislocations have been nucleated in the slip system $a/2 [\bar{1} 0 \bar{1}](1 1 \bar{1})$. However, in contrast to cycle 2, no clear strain hardening can be observed in cycle 3 because of the setting of the experiment. Indeed, the maximum load imposed in this cycle (800 MPa) was very close to the load required to activate the SAS2. Thus, extra information on the plastic flow of this source cannot be extracted from this cycle.

After the third cycle of deformation the ACOM-TEM technique [98, 123] was used in a Tecnai G2 TEM operating at 200 kV in order to generate orientation mapping. A $30 \mu\text{m}$ C2 aperture, precession angle of 0.5° , probe size of 3-4 nm and step size of 50 nm have been used. Figure 4-17 shows the relative misorientation along the tensile axis revealing the

misorientation by 1° - 2° at the position of the STs and which can be due to the deformation constraints imposed by the PTP mounting setup. Due to non-uniform deformation of the sample, the sample needs to have lateral relaxation, however due to the design of the PTP, a lateral movement (relaxation) of the sample is not possible. Any dispersion of the measurements is due to the fact that the measured misorientations fall within the angular resolution limits of the technique (around 1°). The effect of such behaviour on the Schmid factor in the active slip system is very small (from 0.4686 to 0.4633). It can thus be concluded that the strain hardening in cycle 2 is mainly due to the shortening of the length of the source induced by the reduction of the slipped area with the accumulative plastic displacement.

This is an important finding which provides a self-stabilization mechanism of SAS induced plasticity. Indeed, the absence of strain hardening is always leading to propensity for localization processes and earlier fracture.

It is also worth noting here that, because the theoretical calculations shown in Figure 4-15 are not including a contribution from frictional stress, the effect of Ga atoms (which might be present in the form of solid solution after annealing) on the plastic flow of the SAS cannot be considered as a dominant mechanism. However, the contribution of such feature in the high yield stress (compared to pure Ni) cannot be totally excluded since higher concentration of Ga atoms might be present in the form of a Cottrell atmosphere at the core of the initial dislocations.

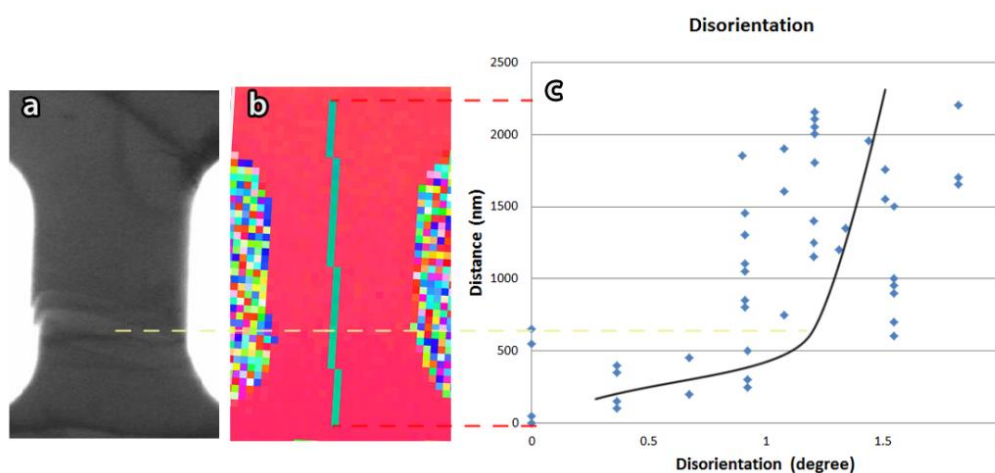


Figure 4-17, (a) BF micrograph after cycle 3, (b) Orientation map after cycle 3 obtained by ACOM-TEM. (c) Corresponding orientation changes along the green vertical line in (b). (it should be mentioned that the angular resolution of ACOM-TEM is ~ 1 degree).

In cycle 4 (purple plot in Figure 4-7), a clear transition in the mechanical response occurred as evidenced by the drastic increase of the yield strength in this cycle (1030 MPa) compared to cycles 2 and 3. Furthermore, a more homogenous plastic flow and higher strain hardening capacity can be observed in cycle 4. In Figure 4-16 (d'), dislocation pile-up gliding in the $(1\ 1\ \bar{1})$ plane towards the bottom grip of the sample can be observed. (The black spots in Figure 4-16 are contamination on the surface formed during ACOM-TEM alignment and measurements).

New STs and other pile-ups of dislocations can also be seen after unloading, Figure 4-16 (e') and at the beginning of cycle 5 Figure 4-16 (f'). This confirms the shutdown of SAS2 in cycle 4 which can be explained by the cross-slip of the mobile segment $4s_2$ out of the $(1\ 1\ \bar{1})$ plane during unloading in cycle 3.

The dislocation pile-ups shown in Figure 4-16 (d') and Figure 4-16 (f') could have been nucleated from the surface or from the dislocations left after annealing at the bottom grip of the sample (which has a bigger cross-section), indicated by the lower black arrow in Figure 4-8 (a). This can be attributed to the absence of active dislocation sources within the gage, leading to a significant increase of the yield stress after cycle 3. Surface nucleation might require higher stresses than observed in the present work [195], however, it's contribution cannot be totally excluded.

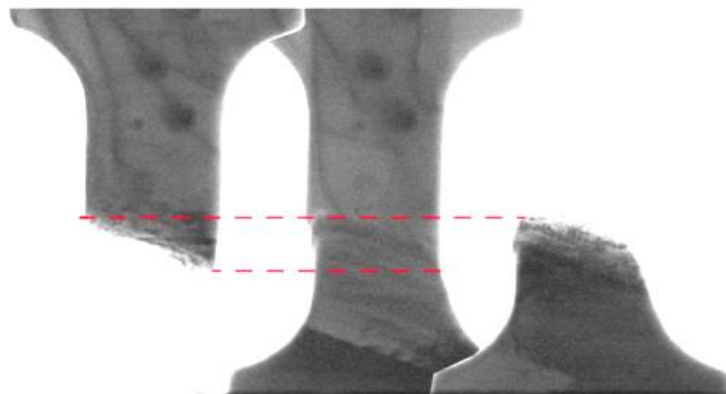


Figure 4-18, Snapshots before and after the fracture of the sample showing that the fracture occurred along the slip plane from the upper step made by the SAS2, as indicated by the red dashed lines.

The strain hardening observed in cycle 4 can be attributed to the deformation on constrained $(1\ 1\ \bar{1})$ slip planes at the bottom grip of the sample with the formation of dislocation pile-ups and the resulting back stress (i.e., kinematical hardening). Kiener et al. inferred the presence

of dislocation pile-ups near the gauge section-grip interface in Cu samples after unloading by measuring the local crystal misorientations via electron backscatter diffraction (EBSD) [50]. In cycle 5 (green plot in Figure 4-7), a decrease of the yield strength compared to cycle 4 was observed due to the lower stress needed to re-activate the glide of the pre-existing dislocations within the pile-ups as can be seen in Figure 4-16 (f') and Figure 4-16 (g'). Finally, the sample failed parallel to the $(1\ 1\ \bar{1})$ slip plane, Figure 4-16 (h') at 1200 MPa. The fracture occurred at the ledge induced by the operation of the SAS2 in cycle 3 according to Figure 4-18.

4.4 Conclusions

In the present work, a new dedicated sample preparation method has been successfully used in pure Ni samples to re-visit the nanomechanics of single arm sources in small-scale single crystals. Nearly defect-free samples allow observing the elementary discrete mechanisms controlling the nucleation and glide of dislocations near the free surface in a quantitative manner without the artefacts of typical FIB prepared specimens. Furthermore, because dislocations induced by FIB could affect the strength and the plastic flow by acting as sources and obstacles for mobile dislocations, the present work brings new experimental evidences on the so-called staircase hardening behaviour of single crystals. The results reveal that, in the absence of FIB damages, the initial relaxation of the few dislocations left after annealing leads to the formation of stable SASs. The lifetime of these sources was also increased allowing detailed investigation of their intrinsic properties. Indeed, an original strain hardening behaviour resulting from the operation of one SAS was observed. It was mainly attributed to the shortening of the length of the source with the accumulative plastic displacement due to the reduction of the slipped area. Thus, a scenario involving a possible effect of the surface on the strength of the SAS was proposed to explain the origin of the staircase behaviour of SASs in the load control mode.

Chapter 5:

Investigation of Dislocations –Twin Boundary Interactions by In-situ TEM Tensile Testing

In chapter 3 and 4, a novel method was introduced to prepare “clean” in-situ TEM tensile test samples. In the present chapter, the interactions of dislocations with a coherent twin boundary are quantitatively investigated using a bi-crystal Ni tensile sample containing a coherent twin boundary which was prepared by the sample preparation method explained in the previous chapter.

5 Investigation of Dislocations –Twin Boundary Interactions by In-situ TEM Tensile Testing

5.1 Introduction

As the Hall–Petch equation, Equation 1-3, illustrates, the mechanical properties of bulk polycrystalline materials are determined by the density of GBs [45]. Recently it has been shown that the dominant type of GBs in the microstructure is also significant. For instance, nanostructured materials with high density of CTBs have revealed excellent mechanical properties combining high strength and toughness [42, 196-200] or small-scale bi-crystal samples with various types of GBs manifested different mechanical properties compared to single crystals [70-72, 201, 202].

Plasticity and mechanical properties of ductile single crystalline materials are controlled by glide of dislocations. In polycrystalline materials, the glide of dislocations is influenced by the presence of GBs. An incoming dislocation interacts with a GB either in an elastic way or in a plastic way, which means that in the former case the interaction is reversible while in the latter case permanent structural changes occur. At low temperatures, the interaction is basically elastic and the GB act as a barrier against the gliding dislocations [41, 42]. At high applied stresses and/or high temperatures, interactions between dislocations and GBs can be plastic, i.e., absorption, desorption and transmission of dislocations occur [35].

Understanding the dislocation-GB interaction mechanisms is an increasingly important area in GB engineering [203]. It helps to design new polycrystalline materials at different scales, i.e., micro and macro-scales, with new advanced mechanical properties. Recently several studies have been reviewed by Kacher et al. [34]. The type of GB, the type of dislocation, the local stress condition in the impingement site, the RSS on the dislocation, the residual GB dislocations, the relative location of slip systems on the sides of the GB, etc. are all important influential factors of the dislocation-GB interaction [34, 41, 204].

TBs are the most studied type of GBs in FCC metals. Excellent mechanical properties were manifested in metals with a high density of coherent twin boundaries (CTBs); e.g., unusual concurrent high strength-ductility and a high work hardening rate have been observed in nanotwinned metals or in metals with pre-existing TBs containing high density of CTBs [196-200]. It was also observed that CTBs are the preferential sites for nucleation and initiation of cracks during cyclic and monotonic deformation [205, 206]. However, although

improved mechanical properties were observed in FCC polycrystalline materials with high density of TBs, hardly any improvement of strength and hardening has been seen in bi-crystal micropillars containing a discrete CTB compared to corresponding single-crystal micropillars [70, 74, 207].

The well-defined stable structure of CTBs has enhanced the investigation of dislocations-CTB interactions. Experimental studies as well as simulations respectively revealed and proposed a variety of interactions mechanisms for different conditions and in different materials [34, 39, 208-223]. In FCC metals, the CTB has an image force which causes an elastic interaction between an approaching dislocation and the CTB at large distances [224]. When the dislocation is very close to the CTB (the cores of defects are very close to each other), the elastic interaction can be either repulsive (in nickel) [224] or attractive (in aluminium) depending on the type of material and their elastic properties [225].

Concerning the plastic interactions of dislocations with CTBs (interaction of the cores of the defects), an incoming perfect dislocation may be either absorbed in a CTB or transmit through it. The absorbed dislocation may dissociate into partial dislocations in the CTB and the transmitted one may glide in the adjacent grain causing permanent change in the structure. Depending on the gliding direction of the partial dislocations in the CTB (if glissile), CTB migration or CTB sliding might occur [226]. Partial dislocation pile-ups against a TB ledge in a CTB might also cause a high local internal stress and, consequently, the nucleation of dislocations or cracks from the ledge [34].

Regarding the interaction of screw dislocations (with the Burgers vector parallel to the CTB) and a CTB, the incoming screw dislocations might form pile-ups against the CTB due to the image force [210]. By increasing the applied stress, a screw dislocation might cross slip either into the TB plane (absorption) [209] or into a plane very close and parallel to the TB plane [210]. The dislocation might also transmit through the CTB (slip transmission) [41, 209, 222, 223, 227].

However, the interactions are not as simple as mentioned above. It has been shown that in FCC materials perfect dislocations always tend to dissociate into two partial dislocations located on the sides of a stacking fault (SF) whose width depends on the stacking fault energy (SFE) of the material. Therefore, instead of a perfect dislocation, a pair of dissociated dislocations (a leading and a trailing partial dislocation) interacts with a CTB. Atomic

simulations have shown that the partial dislocations dissociated from a screw dislocation interact with a CTB by two mechanisms:

(1) The Friedel–Escaig (FE) mechanism; the high stress on the partial dislocations allows the leading and trailing partials to form a perfect dislocation by constriction. Then, it might re-dissociate in the CTB or transmit and re-dissociates in the adjacent grain [220, 228, 229]. The character of leading and trailing partial dislocations in the adjacent grain is reversed compared to the initial partial dislocations before interaction.

(2) The Fleischer (FL) mechanism; the leading partial dislocation penetrates into and interacts with the CTB while the trailing partial dislocation remains in the matrix. This process temporarily forms a sessile stair-rod dislocation on the CTB. This only disappears when the trailing partial dislocation catches up with the leading partial dislocation [228].

In high SFE metals, the FE mechanism requires less activation energy and is more likely. Simulations have also highlighted that the length of the dislocation line, its curvature as well as the local stress can change the governing mechanisms in the interaction of a screw dislocation with the CTB. For example, depending on the stress magnitude, two partial dislocations in the CTB might glide in opposite directions, in the same direction, or desorb as a new dislocation into the adjacent grain [229].

In spite of numerous studies [34, 39, 208-223], the debates continue concerning the mechanisms involving the role of the CTBs on mechanical properties; the dislocations-TBs interactions and the underlying mechanisms are still not well understood and cannot be used to explain the observed mechanical properties. In most experimental studies, the local stress conditions (RSS on different slip planes) are unknown and the results were qualitative. Those qualitative results arise from the un-designability of the earlier in-situ TEM mechanical testing methods which has, e.g., impeded the validation of the observed mechanisms in simulations.

In-situ TEM mechanical testing is a unique experimental method to investigate such interactions. In chapter 2, various types of TEM nanomechanical holders were reviewed. So far the mainly used holders for the phenomenological studies on dislocation-interface interactions were the classical in-situ TEM straining holders [39, 41, 204, 230]. As mentioned in chapter 2, the disadvantages of using such holders are the lack of quantitative data, unknown local loading conditions on the sample and early fracture of the sample. Because of

these shortcomings, most studies have been dedicated to qualitatively understanding the early stages of deformation as initial interaction of dislocations with GBs [34]; henceforth, the studies in high strain levels and fracture remained limited. Interestingly, newly developed MEMS-based holders now allow performing accurate quantitative mechanical testing experiments on well-designed samples. For instance, Kondo et al. [42] directly observed the interaction of dislocations with GBs in SrTiO₃ via in-situ TEM nanoindentation experiments. However, in experiments such as nanoindentation, there is little control over the local stress condition. As was pointed out in chapter 2, among the in-situ TEM nanomechanical testing methods, the loading condition in tensile test is less complex which makes it ideal for the investigation of dislocation-GB interactions [15].

FIB is the most commonly used technique to prepare the nanomechanical testing samples. In chapters 3 and 4 it was discussed that in spite of its high reliability, speed, and accuracy [140, 144], FIB can induce damages on the surface of metallic samples which not only change the mechanical properties [90, 144, 146, 231] but also block the insight to on-going interactions and mechanisms during in-situ TEM testing [186]. In chapter 4, a new sample preparation method for in-situ TEM nanotensile testing was introduced allowing preparing FIB defect-free metallic samples. The method allows designing the sample in terms of crystallographic orientations and type of included defects, such as a TB, in the crystal.

The objective of the present part is to contribute to a better understanding of the interaction of dislocations with CTBs by using a bi-crystal Ni sample not affected by the sample preparation. Thus, we used the aforementioned preparation method to prepare a bi-crystal sample containing a CTB parallel to the loading direction and a comprehensive quantitative observation of the interactions under dedicated imaging conditions was performed. In addition, this experiment is to investigate the probable size effect on mechanical properties of small-scale bi-crystal materials.

5.2 Experimental conditions

The sample preparation method based on electro-polishing, FIB and in-situ TEM heating was explained in chapter 4. It was used to prepare a bi-crystal nickel tensile sample containing a CTB parallel to the tensile direction suitable for the quantitative in-situ TEM tensile experiment. The CTB was selected parallel to the loading direction to avoid probable early fracture of the sample from the CTB. This configuration leads to zero resolved shear stress on the CTB plane which makes the system less complex.

After electro-polishing, the 3 mm discs were investigated by conventional TEM techniques in order to select the proper regions in terms of thickness, electron transparency, crystallographic orientation and type of the GB. The milling of dog-bone shape samples was designed on the location of annealing CTBs in order to have a bi-crystalline dog bone tensile sample with a CTB parallel to the tensile direction, Figure 5-1 (a). After in-situ TEM heating for ~1 hour at 700°C to remove most FIB damages, a bi-crystal dog-bone sample was then mounted on a PTP device by using a dual beam FIB/SEM workstation equipped with an Omniprobe and a GIS. Figure 5-1 (b) shows the final configuration of the sample on the PTP device after mounting. As emphasized in chapter 4, a great consideration has been paid to not expose the gage part of the dog-bone sample to the FIB beam during the mounting step.

In this work a PTP MEMS device with the stiffness of 150 N/m was used in the PI 95 PicoIndenter holder and the quantitative in-situ TEM nanotensile experiment was performed with the load control mode in a FEI Osiris Tecnai TEM. The sample was subjected to 5 loading-unloading cycles with maximum engineering stresses equal to $550 \pm 2 \text{ MPa}$, $693 \pm 3 \text{ MPa}$, $703 \pm 3 \text{ MPa}$, $793 \pm 4 \text{ MPa}$ and $1084 \pm 5 \text{ MPa}$ while the failure occurred in the last cycle. In each cycle, the sample was kept under the maximum load for 1 minute (load plateau). Figure 5-2 shows the schematically a loading cycle on the sample. In the second cycle, due to a technical problem the sample was unloaded after reaching to its maximum stress without any plateau.

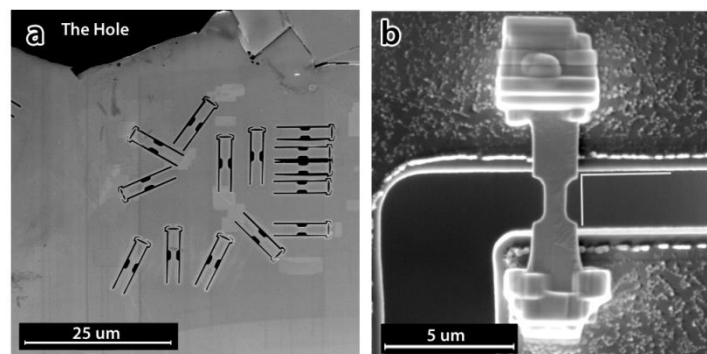


Figure 5-1, SEM images showing (a) the configuration of the dog bone samples on an electro-polished TEM foil after the heat treatment and (b) the final configuration of the tensile sample on a PTP device after the mounting step (it shows a slight rotational misalignment)

The TEM DF mode was used in most deformation cycles. Due to the low contrast in such images, digital image cross-correlation of the DF movies was inaccurate. Therefore, engineering stress-strain curves were not provided. The engineering stresses in different

locations were nevertheless calculated using the cross-section area of the sample. By knowing the angle of slip planes with the sample surfaces, the alpha rotation of the holder and compensating the projection nature of the TEM images, the cross-section area was estimated from the slip traces appearing during the deformation.

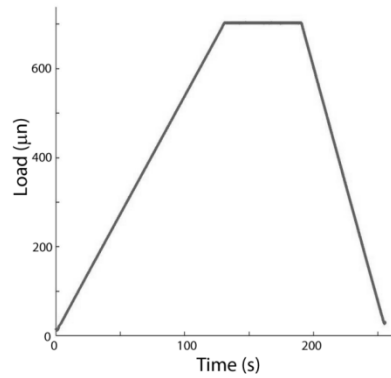


Figure 5-2, Schematics showing a loading cycle of the sample with the load plateau.

5.3 Result and discussion

With respect to the quality of the sample after mounting, Figure 5-3 shows that the sample does not have typical FIB defects features (shown in chapter 4). Figure 5-3 (a) also shows that the CTB is parallel to the tensile direction and that there are a few ledges in the structure of the CTB, highlighted by blue arrows in the figure. Furthermore, Figure 5-3 shows the dislocation remnants in both grains (white arrows). Some of them have been formed by coagulation of FIB induced defects during the in-situ TEM heat treatment as discussed in chapter 4 [141]. Their presence might be desirable as they might act as dislocation sources during deformation and provide the dislocations required to investigate dislocation-CTB interactions. White arrows in Figure 5-3 (b) also remark the dislocations within the CTB.

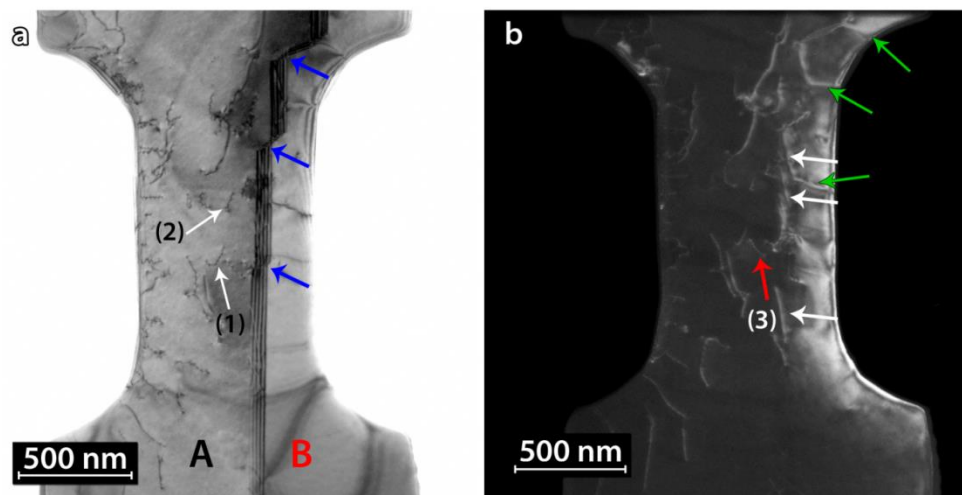


Figure 5-3, (a) TEM BF image of the sample showing the dislocation structure in grain A and CTB, blue arrows show the CTB ledges, (b) TEM DF image of the sample taken by diffraction spots of (420) and $(420)T$ of grain A and B respectively. The dislocations marked in these 2 images participate in the deformation and will be explained in the text. The green arrows in (b) indicating the present dislocations.

In terms of the crystallographic orientation of the sample, the stereographic projection of the sample grains when the sample is at 0° alpha tilt is shown in Figure 5-4 (a). Since the tensile axis is (almost) parallel to the CTB plane (dashed blue line in Figure 5-4 (a)), the tensile direction in both grains is close to the $\langle 5\bar{4}1 \rangle$ direction and the loading conditions of both grains is symmetrical. The Schmid factors of the slip systems in grain A are tabulated in Figure 5-4 (b). The 2 highest Schmid factor systems are on the $(1\bar{1}\bar{1})$ and $(1\bar{1}1)$ planes whose slip would make close to horizontal STs in grain A and diagonal STs in grain B according to Figure 5-4 (a).

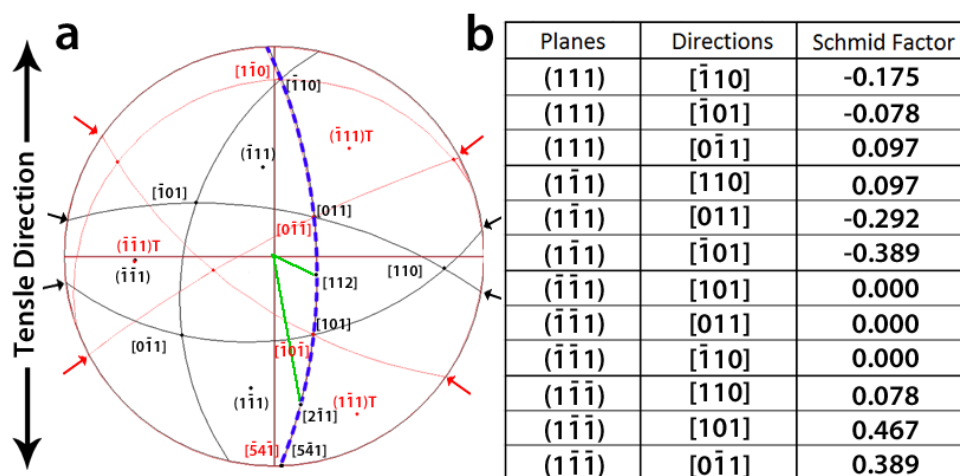


Figure 5-4, (a) Stereographic projections of grain A and B (black and red, respectively), and (b) Schmid factor values of slip systems in grain A.

5.3.1 Slip plane determination

In such a thin sample, gliding dislocations on a slip plane induce a pair of parallel STs on the top and bottom surfaces of the sample. They define the intersection of the slip plane and the surface. On the question of the characterization of the slip systems, the orientation of a pair of STs and the distance between the two STs in TEM images can be used to determine the corresponding active slip plane. The slip planes can be determined by comparing the STs orientation in the TEM images and the orientation of the slip planes in the stereographic projection. For instance, in grain B, the direction of STs of slip planes $(1\bar{1}\bar{1})$ and $(1\bar{1}1)$ are distinguishable (the red arrows in Figure 5-4 (a)). In the case when the directions of STs of two slip planes are rather identical, the distance between STs can be used instead. The distance between the STs in TEM images depends on the angle between the slip plane and the sample surface, i.e., when the angle is high (close to 90), the distance between 2 STs is short and when the angle is low, the distance is long. For example, the STs of planes $(\bar{1}11)$ and $(1\bar{1}1)$ in grain A are rather horizontal (Figure 5-4 (a)). However, since the distance between the STs of plane $(\bar{1}11)$ is longer than the ones of plane $(1\bar{1}1)$ (Figure 5-4 (a)), the slip planes are recognizable. Figure 5-5 shows the examples of the STs of $(\bar{1}11)$ and $(1\bar{1}1)$ planes in grain A. The shorter distance between the STs in Figure 5-5 (a) and (b) than ones in Figure 5-5 (c) shows that the slip plane in Figure 5-5 (a) and (b) is $(1\bar{1}1)$ and the slip plane in Figure 5-5 (c) is $(\bar{1}11)$. This method was used to recognize the active slip planes in the following sections of the chapter.

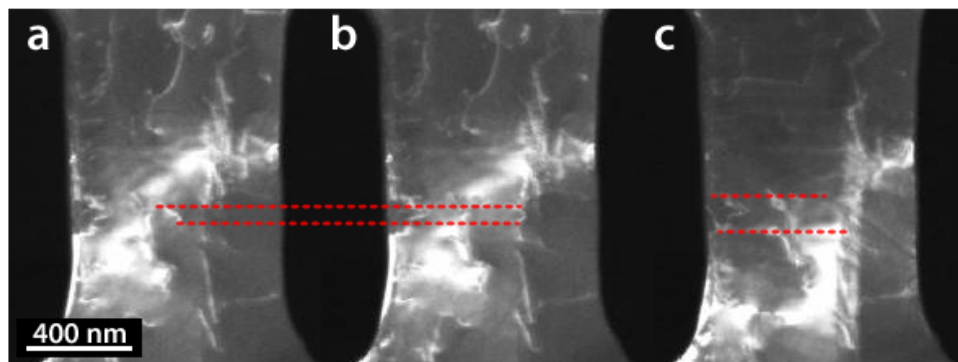


Figure 5-5, In DF snapshots of the movie of cycle 3 (a and b), the ends of the gliding dislocation on a $(1\bar{1}1)$ plane was used to find the STs which is marked by dashed lines, and in DF snapshot of the movie of cycle 4, (c), the STs due to the glide of a dislocation on a $(\bar{1}11)$ plane were visible and marked by dashed lines.

5.3.2 Dislocation characterization

Although the single tilt nature of the holder impedes comprehensive application of the systematic contrast analysis technique to characterize the type of dislocations, this technique can be used to find the probable nature of the dislocations. Figure 5-6 shows the two-beam condition BF micrographs taken by [220] and [200] in grain A which will be used to determine the type of dislocations studied in this work. Furthermore, due to the orientation of the ledge planes in Figure 5-6 (an edge-on condition), the plane of the ledge may be very close to the $(\bar{1}1\bar{1})$ plane in grain B and close to the $(\bar{1}0\ 2\ \bar{1})$ plane in grain A.

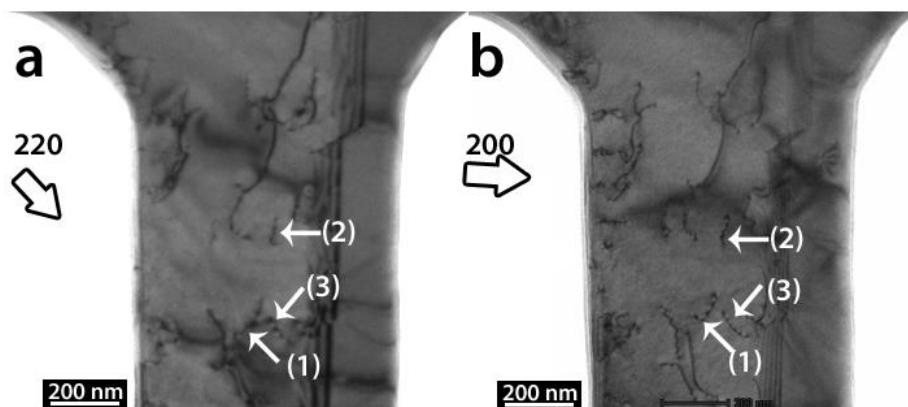


Figure 5-6, Two-beam condition TEM BF images taken by (a) 220 diffraction spot and (b) 200 diffraction spot (The marked dislocations participate in deformation and are further explained in the text.)

As shown in chapter 4, the activation of a SAS can be predicted by considering a half Frank-Read (FR) source. As activation of few SASs was observed during the experiment, the model can be used to validate the observation; the size of SASs obtained from the experiments can be compared to one obtained from the model. The CRSS to activate a SAS can be calculated using Equation 5-1 (modified from the known equation for a Frank-Read source by replacing the length L by $L/2$) [50, 232].

Equation 5-1

$$CRSS = \frac{\alpha G b}{4\pi l} \left(\ln \left(\frac{2l}{b} \right) + 1 \right)$$

where α is a coefficient equal to 1 or $1/(1 - \nu)$ for edge or screw dislocations, respectively, G is the shear modulus (76 GPa), b is the magnitude of the Burgers vector (0.249nm), Poisson's ratio ν is equal to 0.31 and L is the SAS length. Equation 5-1 is used to draw

CRSS-SAS length of a pure screw and a pure edge SAS as shown in Figure 5-7 which will be used in the following discussion.

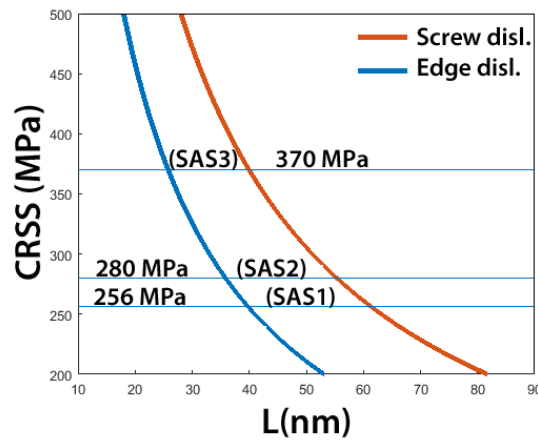


Figure 5-7, CRSS vs. SAS length calculated using Equation 5-1 for screw and edge character (Marked stresses are due to the activation SASs during deformation, which will be explained later).

In chapter 4 it was observed that the dislocation sources operate just for one cycle and in the next cycles no activation could be detectable. This was attributed to the probable effect of slight compression/bending of the sample during unloading causing shut down of the sources. In this experiment, the same behaviour was observed as the sources were active just in one cycle.

5.3.3 Interaction of screw dislocations with the CTB

5.3.3.1 Absorption

In the following, the observed plastic interaction of dislocations with the CTB will be shown and discussed. In cycle 1, during the loading in elastic regime only few dislocations glided and annihilated on the surfaces. In the corresponding plateau at 550 MPa, SAS1 (marked by (1) in Figure 5-3 (a)) started operating. After a very short time (e.g., after creating a few dislocations), it stopped operating before the end of the plateau. Figure 5-8 shows the configuration of the source before and after the activation of SAS1. The distance between the STs in Figure 5-8 (b), indicated by white arrows, shows that the slip plane is $(\bar{1} 1 1)$.

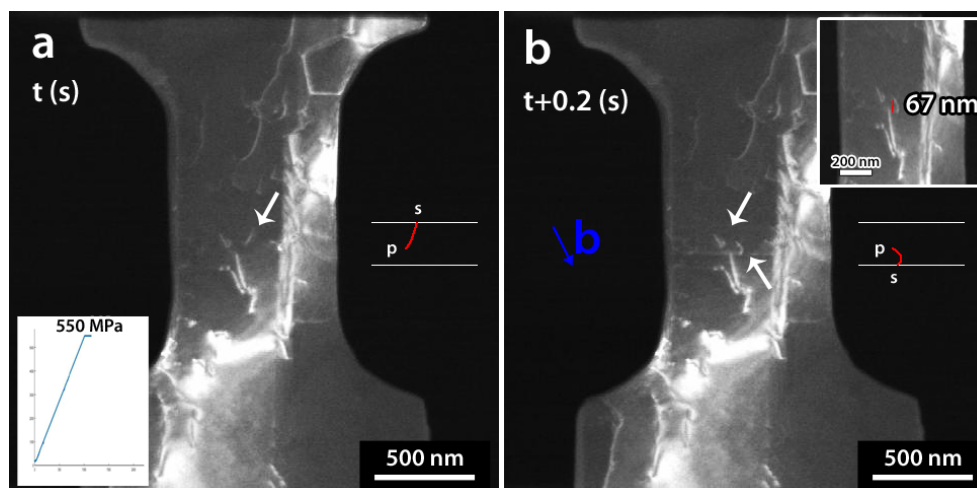


Figure 5-8, Snapshots from the deformation movie of cycle 1, (a) showing SAS1 configuration, marked with white arrow, just before activation, and (b) showing SAS1 configuration just after activation and white arrows mark the STs made by the operation of the source.

The visibility of SAS1 in Figure 5-6 indicates that among the dislocations in the $(\bar{1}11)$ plane ($a/2[110]$, $a/2[101]$ and $a/2[0\bar{1}1]$), SAS1 is either $a/2[110]$ or $a/2[101]$. Since the Schmid factor of $(\bar{1}11)[101]$ (0.467) is higher than that of $(\bar{1}11)[110]$ (0.078), the Burgers vector of SAS1 is probably $a/2[101]$.

Regarding the operation of the SAS1, the shutdown of SAS1 in the plateau might be due to either decrease of the length of SAS1 by the shrinkage of the slip plane (as observed in chapter 4 in single crystal) or to possible changes of the stress state on the sample due to local bending of the sample as a result of dislocations glide. To re-activate an immobile SAS, the RSS should increase to a specific amount (the overshoot stress) which cannot occur in the plateau.

By correcting the projection nature of the TEM images, the length of SAS1 is measured ~ 67 nm in Figure 5-8 (b). Due to Figure 5-7 and RSS on SAS1 ($256 \text{ MPa} = 0.467 \times 550 \text{ MPa}$), the corresponding lengths of a pure screw SAS and a pure edge SAS are 61.5 nm and 40 nm, respectively. A good agreement between measurement and calculation shows that the stress values are trustful. Since no dislocation pile-up against the TB was observed during and after the source operation, the nucleated dislocations might have interacted with the TB. The role of a dislocation pile-up in the shutdown of the source can thus be excluded also. The Burgers vector of the nucleated dislocations is parallel to the TB plane in agreement with calculations. Following the conclusion of earlier simulation results [220], transmission or absorption of

screw dislocations can thus be expected. However, since no dislocation STs were observed in grain B, the dislocations are apparently absorbed within the CTB.

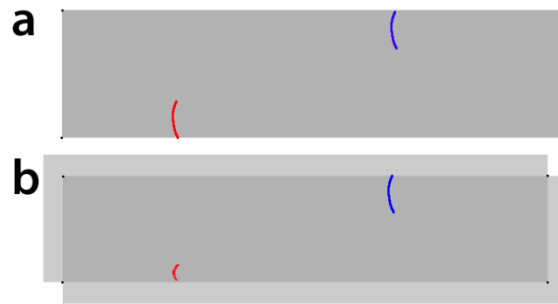


Figure 5-9, Schematics showing SASs configuration (a) before and (b) after the glide of dislocations on a slip plane. The length of the blue SAS is fixed, while the length of the red SAS decreases due to the glide in the slip plane (Light grey areas in (b) are newly formed free surfaces).

5.3.3.2 Transition of transmission process to absorption

In cycle 2, the sample was loaded up to the maximum stress of 693 MPa and unloaded without a plateau (due to a technical problem). During the loading, SAS2 (marked as (2) in Figure 5-3 (a)) started operating at a stress level of 600 MPa and continued operating until the end of the cycle loading part (693 MPa).

A question which might arise is why SAS2 did not show the intermittent behaviour observed in chapter 4. Indeed, continuous operation rather than successive shutdown and activation of this source was observed in the TEM movie. For a SAS, the term of ‘critical length’ can be defined by the shortest length of the source when the source sweeps the slip area once. In other words, the critical length is normally the shortest distance between the pinning point and the edges of the slip plane. Since it defines the CRSS required to activate the SAS, the length is very important. Figure 5-9 shows that depending on the location of the pinning point, the critical length of a SAS can decrease (red source) or can be fixed (blue source) during the reduction of the slip area. The former is the case where intermittent behaviour is observed (chapter 4). In the latter case, since the CRSS is constant and RSS is increasing progressively, the SAS can operate for an infinite time and intermittent plastic flow is not expected. Thus, continuous operation of SAS2 in cycle 2 implies that the latter case happened. This observation also shows that possible local changes of the stress state due to the local bending of the sample cannot shutdown an active source and therefore this cannot be considered as an influential reason for SAS1 shutdown.

Figure 5-10 shows the snapshots of the SAS2 operation movie (the source is highlighted by white lines). Just after SAS2 activation, a pair of STs appeared in grain B, as shown by white arrows in Figure 5-10 (b). Since the STs in both grains intersect with each other on the CTB (shown in Figure 5-10 (b) and illustrated schematically) transmission of the dislocations through the CTB can be inferred. The continuation of the SAS2 operation was accompanied by a gradual increase of STs contrasts in grain A (yellow arrows in Figure 5-10); however, no further changes of the STs contrast could be detectable in grain B. Instead, the formation and condensation of fringe-like contrasts along the CTB (red arrows in Figure 5-10 (c) and (d)) were observed. Expansion of the fringes contrast till the ledge in the CTB (white dot in Figure 5-10) implies that nucleated dislocations might be either absorbed within the CTB [204] or cross-slipped in a slip plane parallel to the CTB plane [210].

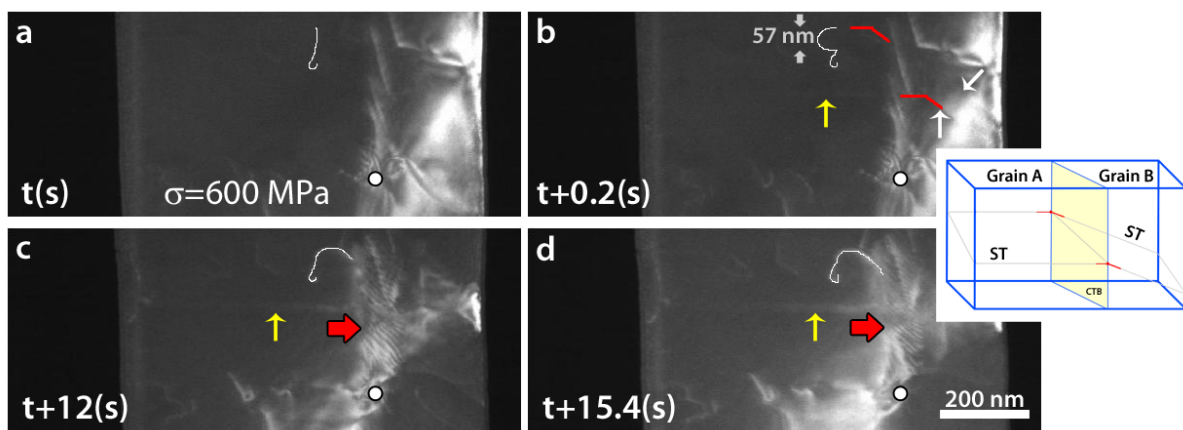


Figure 5-10, Snapshots from the deformation movie of cycle 2, showing the configuration of SAS2 (a) just before activation, and (b), (c) and (d) at different times during deformation. Yellow arrows indicate the newly produced STs in grain A and so do white arrows in grain B. Red lines in (b) show that STs intersect with each other on the TB, as also shown in the schematic of the inset. Red arrows show the formation of the fringe-like contrasts in CTB (The white dot shows the location of the TB ledge).

Since in cycle 4 the similar interactions in cycle 2 observed, in the following this cycle will be explained. In cycle 4, an interaction similar to one in cycle 2 was observed. A SAS (SAS4) starts operating at a stress level of 793 MPa in the plateau region. Appearance of new STs in grain B (blue arrow in Figure 5-11 (b)) just after the source activation showed transmission of the nucleated dislocations through the CTB [41].

After a very fast interaction (too fast to be captured), no further operation of SAS4 was observed in the plateau. The shutdown of SAS4 in the plateau might be due to decrease of the length of SAS4 by the shrinkage of the slip plane. After interaction, some dislocations gliding downward in or parallel to the CTB plane were appeared (white arrows and the inset in

Figure 5-11 (c) and (d)). The intensified contrast of STs in grain A (red arrow in Figure 5-11 (b)) indicates the further operation of SAS4 in the interaction. Again, no changes of STs contrast in grain B could be recognized. The above observations in cycle 2 and 4 indicate that the first dislocations transmitted through the CTB and the next dislocations cross slipped in or parallel to the CTB.

In cycles 2 and 4, dislocation pile-up against the CTB was not observed. This might be due to the fact that the RSSs to activate the dislocation sources were higher than the critical RSS required activating dislocation transmission/absorption at the CTB.

Due to the width of STs formed in cycles 2 and 4, the slip planes were $(\bar{1}11)$ and according to contrast analysis (Figure 5-6) the Burgers vector of SAS2 was likely $a/2 [101]$. The direct recognition of SAS4 in cycle 4 was not possible due to the imaging condition and the fast interaction. However, later it will be shown that SAS4 has the same Burgers vector as SAS2.

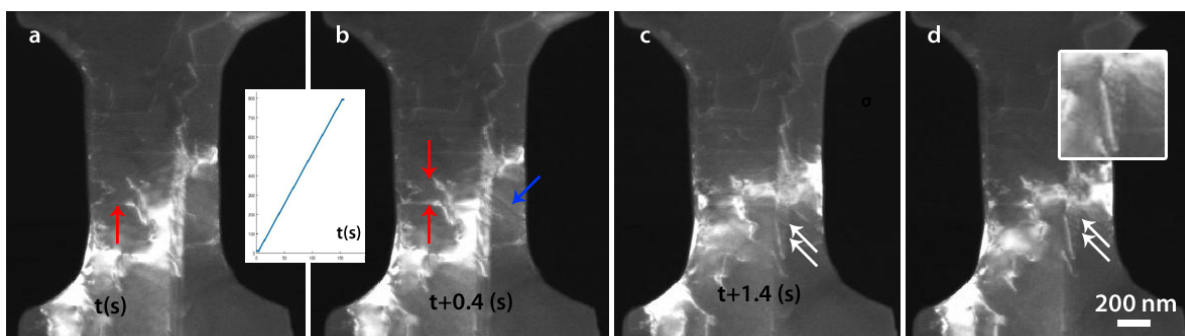


Figure 5-11, Snapshots from the deformation movie of cycle 4 showing the microstructure (a), (b), (c) during operation of SAS4 on different times, and (d) after shutdown. The inset between (a) and (b) shows the stress vs. time curve for the initiation of the dislocation/TB interaction. Red and blue arrows show the newly produced STs in grain A and grain B, respectively. White arrows mark the dislocations in or parallel to the CTB. The inset in (d) shows the downward glide of dislocations.

Again, a good agreement between measured and calculated length of SAS2 using Equation 5-1 was observed; the length of SAS2 was measured 57 nm from the deformation movie (Figure 5-10 (b)) and it was modelled 55.3 nm and 35.9 nm for a pure screw and a pure edge SAS, respectively, at the stress of 600 MPa (Figure 5-7).

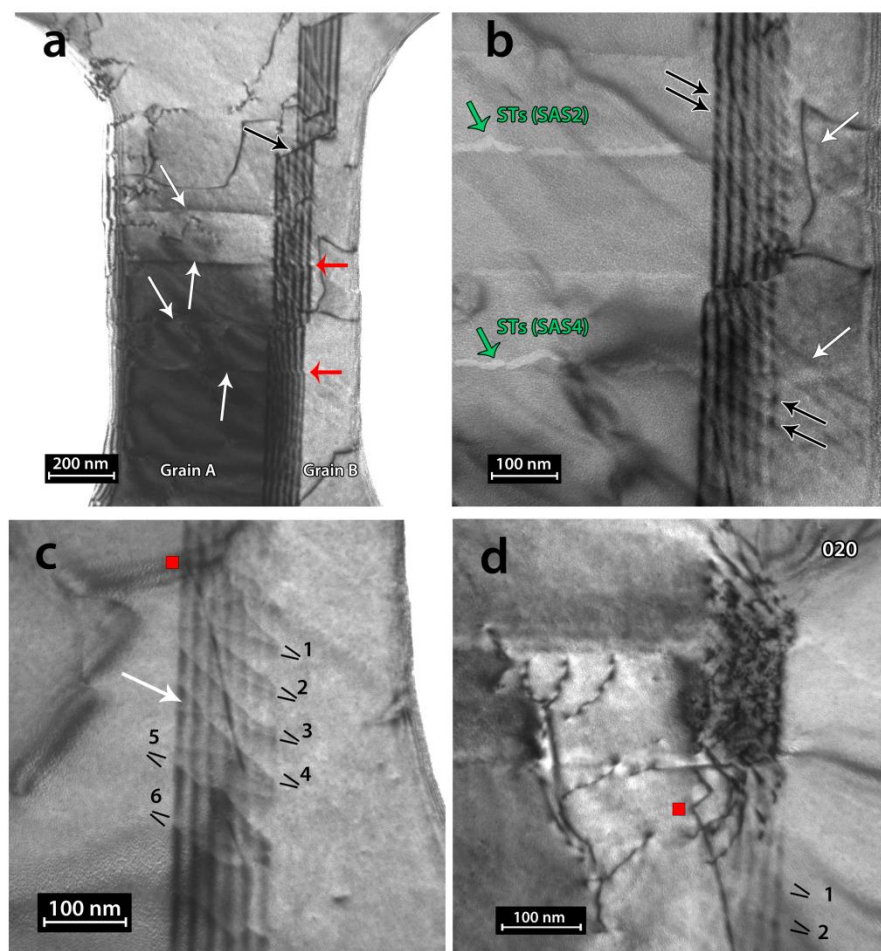


Figure 5-12, (a) and (b) TEM BF images of the sample after cycle 4 showing the sample dislocation structure, white arrows marking STs produced by the operation of SAS2 and SAS4. (c) and (d) TEM BF images of the sample after cycle 5 (fracture), showing the dislocation structure in the TB. (d) is a two-beam condition image with $g = 020$ excited. The red dot in (c) and (d) indicate the reference point.

Figure 5-12 (a) and (b) show the dislocation structure in the CTB after cycle 4. The shift of the CTB fringes in both locations of dislocation-CTB interactions sites (red arrows in Figure 5-12 (a)) as well as the confinement of the dislocations by a CTB ledge (black arrow in Figure 5-12 (a)) imply that incoming dislocations of SAS2 and SAS4 have interacted with and cross-slipped in the CTB. This is contrary to what Chassagne et al. [210] reported about cross slipping of screw dislocation in a slip plane parallel to the CTB in copper. Green arrows in Figure 5-12 (b) show the STs contrast in grain A made by breaking of the oxide and/or the contamination layer on the surface. The STs in this figure can thus be used to determine the Burgers vector of the active slip systems. The identical displacement vectors of STs of either case, green arrows in Figure 5-12 (b), show that the Burgers vectors of the sources are the same, i.e., $a/2 [1 0 1]$. The STs of in both grains in Figure 5-12 (b) also clearly shows the

direct transmission of dislocations. An interesting feature in Figure 5-12 (b) is that the dislocations in the CTB have a paired configuration (black arrows) very similar to dissociated dislocations in the CTB. After fracture, it was observed that the dislocation pairs have a V-shaped configuration, as seen in Figure 5-12 (c). Again, this points towards an interaction mechanism involving the cross-slip and dissociation of screw dislocation in the CTB.

Regarding to the type of V-shaped dislocations in the CTB, the two-beam condition BF TEM image taken after fracture (Figure 5-12 (d)) revealed that the dislocations are $\frac{a}{6}\langle 2\ 1\ 1\rangle$. The invisibility of dislocations in the CTB in Figure 5-12 (d) means that the dot product of the dislocation's Burgers vector and the used two-beam condition spot $[020]$ is ~ 0 . (as a rule of thumb, in FCC metals the dislocations whose dot product is less than $\frac{1}{3}$ are invisible in TEM images [119]) According to Table 2, it is possible to assume that the dislocations are $\frac{a}{2}[101]$. However, accordingly explaining the V shape configuration of dislocations is difficult. Therefore, the dislocations might be $\frac{a}{6}[112]$ and $\frac{a}{6}[2\bar{1}1]$ which were observed to have such a configuration [233].

Table 2, Dot products of the Burgers vectors of all possible dislocations in the TB and the used diffraction spot in Figure 5-12 (b) (020) showing the visibility or invisibility of dislocations in the TB (As a rule of thumb, in FCC crystals, dislocations become invisible when $|\mathbf{g} \cdot \mathbf{b}| \leq \frac{1}{3}$, [119]).

| Type of dislocations → | $\frac{a}{2}[101]$ | $\frac{a}{2}[011]$ | $\frac{a}{2}[1\bar{1}0]$ | $\frac{a}{3}[\bar{1}\bar{1}1]$ | $\frac{a}{6}[112]$ | $\frac{a}{6}[2\bar{1}1]$ | $\frac{a}{6}[12\bar{1}]$ |
|------------------------|--------------------|--------------------|--------------------------|--------------------------------|----------------------|--------------------------|--------------------------|
| Used diff. spot ↓ | | | | | | | |
| 020 | 0 | 1 | -1 | $-\frac{2}{3}$ | $\frac{2}{6} \sim 0$ | $-\frac{2}{6} \sim 0$ | $\frac{4}{6}$ |

Two sets of parallel dislocations in Figure 5-12 (c) suggest a dissociation process. After cross slipping, a perfect dislocation dissociates into two partial dislocations in a CTB which is energetically favourable due to Equation 5-2 and shown in Figure 5-13.

Equation 5-2

$$\frac{a}{2}[101] = \frac{a}{6}[112] + \frac{a}{6}[2\bar{1}1]$$

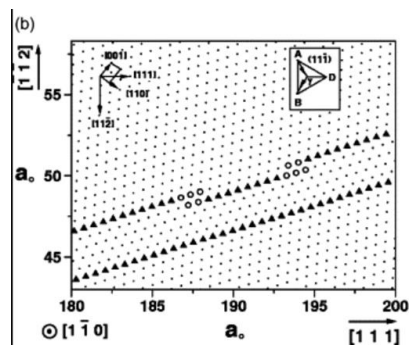


Figure 5-13, MD simulation showing two partial dislocations in a CTB of Al dissociated from a perfect dislocation [234].

Observation of the V-shape configuration of partial dislocation pairs in the TBs of the pristine pure nickel sample (see Figure 5-14), a Ni-Al alloy [235], and in an austenitic stainless steel [233] is another evidence of the presence of the same dislocations in the CTB.

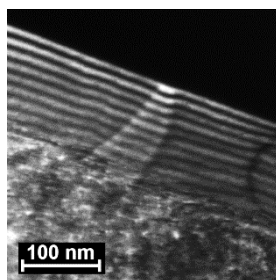


Figure 5-14, V configuration of Shockley partial dislocations in a CTB of undeformed Ni sample.

The comparison between the dislocation line orientations in Figure 5-12 (c) and the Burgers vectors of the partial dislocations ($a/6 [11\bar{2}]$ and $a/6 [2\bar{1}1]$) in the stereographic projection (green arrows in Figure 5-4 (a)), implies that dislocations have aligned themselves along their Burgers vectors to minimize the line tension. The image force has also been mentioned as a reason for the V configuration of dislocations [233].

So far, we showed that some dislocations have cross slipped in the CTB. However, Pumphrey [233] showed that cross-slipping and dissociation of a perfect screw dislocation into a plane parallel and close enough to the CTB plane might locally affect the structure and the location of the CTB.

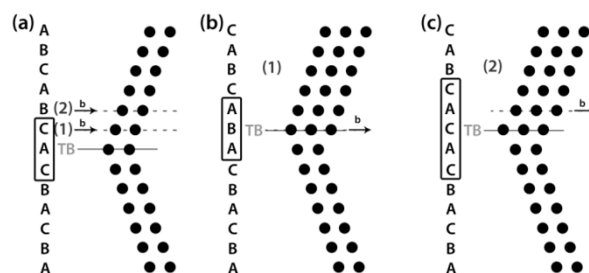


Figure 5-15, Schematics showing the atomic structure in the vicinity of a CTB, (a) before slip of the partial dislocations, (b) after gliding of a leading partial dislocation on plane (1) and (c) after gliding of a leading partial dislocation on plane (2).

Figure 5-15 (a) shows schematically the atomic structure of an FCC crystal in the vicinity of a CTB. An incoming dislocation can cross slip to the first plane (marked by (1)), the second plane (marked by (2)) or even farther planes close to the CTBs. Figure 5-15 (b) and (c) show how the gliding of a leading partial dislocation on the first or second slip plane parallel to the CTB plane can locally move the TB location by one atomic plane. In the former case (Figure 5-15 (b)), the structure of the CTB does not change and therefore such a reaction is energetically favourable due to the absence of a SF. However, in the latter case (Figure 5-15 (c)), the structure of the CTB locally changes to a hexagonal closed pack structure with higher energy which is less favourable. Cross-slipping and dissociation of a dislocation on the planes farther from the CTB plane can also occur but is energetically less favourable. In these conditions, the energy of the system gets close to the infinitely apart defects, i.e., a perfect dislocation (or dissociated dislocation with SF in between) and a CTB [233]. It is worth mentioning that the unfavourable cases might still happen under a high applied stress. The sign of an incoming dislocation and accordingly the type of the leading dislocation do not change these results.

In addition, a dislocation might glide in the CTB plane. Figure 5-16 (a) again shows schematically the atomic structure in the vicinity of a CTB. Depending on the sign of the incoming dislocation and accordingly the type of the leading partial dislocation, two cases might happen; (1) Glide of the leading partial dislocation \mathbf{b} in the CTB plane which locates the same type of planes on top of each other, (Figure 5-16 (b)), and (2) glide of the leading partial dislocation \mathbf{b}' in the CTB plane which changes the location of the CTB by one atomic plane (Figure 5-16 (c)). The former condition needs substantial energy and its occurrence is unlikely while the latter is energetically favourable. As Figure 5-15 and Figure 5-16 show, a SF cannot be defined between dissociated dislocations in the CTB. Therefore, it can be

expected that the partial dislocations in a CTB are arranged to form an equilibrium configuration due to a balance of the repulsive forces applied on each other.

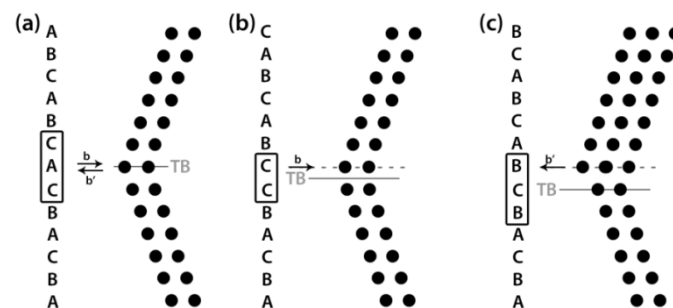


Figure 5-16, Schematics showing the atomic structure in the vicinity of a CTB, (a) before slip of the partial dislocations in the CTB, (b) after gliding of the leading partial dislocation b in TB, and (c) after gliding of the leading partial dislocation b' in TB.

Furthermore, the crossed configuration of a leading partial dislocation and a trailing partial dislocation (white arrow in Figure 5-12 (c)) can be evidence that the dislocations cross slipped and dissociated on various slip planes parallel to the CTB.

Concerning the mechanisms controlling the interaction of screw dislocations with the CTB, direct transmission of a screw dislocation can properly be explained by the FE mechanism. In the FL mechanism, the re-combination process of the leading and partial dislocations in the CTB which is required to emit a new perfect dislocation to the adjacent grain (by transmission) is very difficult [220, 236]. In addition, the SFE in nickel is high and the applied stress can easily combine the dissociate dislocations to form a perfect dislocation. Therefore, the FE mechanism is the probable mechanism in nickel as it was regularly observed in the simulation studies [210, 220, 229].

As far as transmission or absorption processes are concerned, Jin et al. [220] tried to predict the on-going processes in a screw dislocation-CTB interaction based on the estimated “resistance parameter”. However, Chassangne et al. [210] showed that the resistance parameter is only valid to predict the spontaneous combination process in aluminium, and not to predict the active mechanisms in materials such as nickel. They also highlighted the importance of the stress in the interactions and proposed that at RSSs less than 400 MPa absorption is preferred over transmission [210]. However, in this work, transmission followed by absorption was observed at RSSs less than 400 MPa (280 MPa and 370 MPa). Jin et al. [220] found a threshold RSS of 300-380 MPa for the transmission of screw dislocations through the CTB in nickel by MD simulation which is in a good agreement with the RSS

obtained in this work. To the best of author's knowledge, this is for the first time that the RSS of a dislocation-TB interaction is measured.

In spite of MD simulation results showing that depending on the type of FCC materials, the screw dislocations might either transmit (in nickel) or absorb in the CTB (in aluminium) [220, 229], both processes (transmission and absorption) were observed in cycles 2 and 4. However, it should be mentioned that the loading conditions used in these simulations are different from those used in this work.

The transition of the transmission process to the absorption process in these cycles indicates that there are other determining factor(s) apart from the stress levels. Indeed, slip transmission of dislocations can progressively decrease the slip area and consequently increase the local RSS on dislocations as shown in Figure 5-17 (a). Figure 5-17 (a) also shows that the slip transmission might induce a slight local bending in the sample due to the PTP mounting setup which can contribute to the transition from transmission to absorption.

In terms of absorption of screw dislocations in a CTB, simulations have mainly shown that dissociated partial dislocations in the CTB glide in the opposite directions thereby causing CTB migration [229]. However, Xu et al. [229] observed in simulation that in aluminium the partial dislocations glide in the opposite directions only at low RSSs (<200 MPa) and at higher RSSs (in the range of 200-1200 MPa) they glide in the same direction [229]. In this work, in agreement with Xu's observations, the glide of the dissociated dislocations in the CTB in the same direction was observed which induces TB sliding (Figure 5-17 (b)) although the loading conditions are not the same. Figure 5-17 (b) shows that dislocation absorption in the CTB can progressively increase the local RSS on the slip plane and the local bending in the sample by decreasing the slip area. Figure 5-17 (c) shows how gliding of a trailing dislocation locally eliminates the TB migration caused by the glide of a leading partial dislocation.

To understand the involved mechanisms and to find out the other contributing factors in this work, simulations with similar geometrical and loading condition on the nickel sample are needed. However, according to the observations, it is expected that the stress state in the slip planes and the CTB, the changes in the geometry of the slip plane and the CTB and also a slight local bending might play a role.

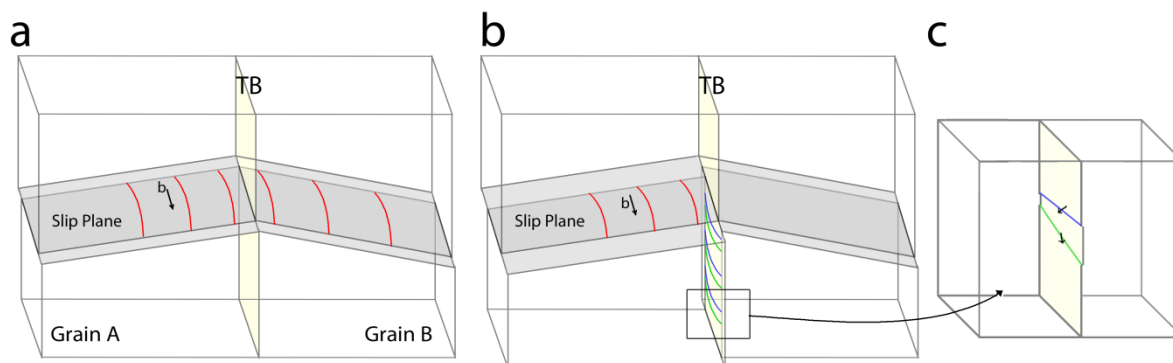


Figure 5-17, Schematics showing (a) transmission of dislocations, (b) following cross slipping of next dislocations in the TB and (c) the dissociation of the dislocations in the TB.

5.3.4 Interaction of a non-screw dislocation with the CTB

After having shown the observed plastic interactions, in the following the observed elastic interaction of a non-screw dislocation with the CTB will be explained and discussed. In the loading part of cycles 3 and 4, a dislocation dent from SAS3 (red arrow in Figure 5-3 (b)) towards the CTB, Figure 5-18 (a) and (b). A comparison between the length of SAS3 before and after sending the dislocation, Figure 5-18 (a) and (b), respectively, shows that the length of SAS3 becomes shorter and as it needs a higher CRSS it cannot operate further.

Due to the width of the pair of STs, the slip plane was determined as $(1\bar{1}1)$ and the Burgers vector of the dislocation was either $a/2[\bar{1}01]$ or $a/2[110]$, following from systematic contrast analyses, neither of which is parallel to the CTB plane.

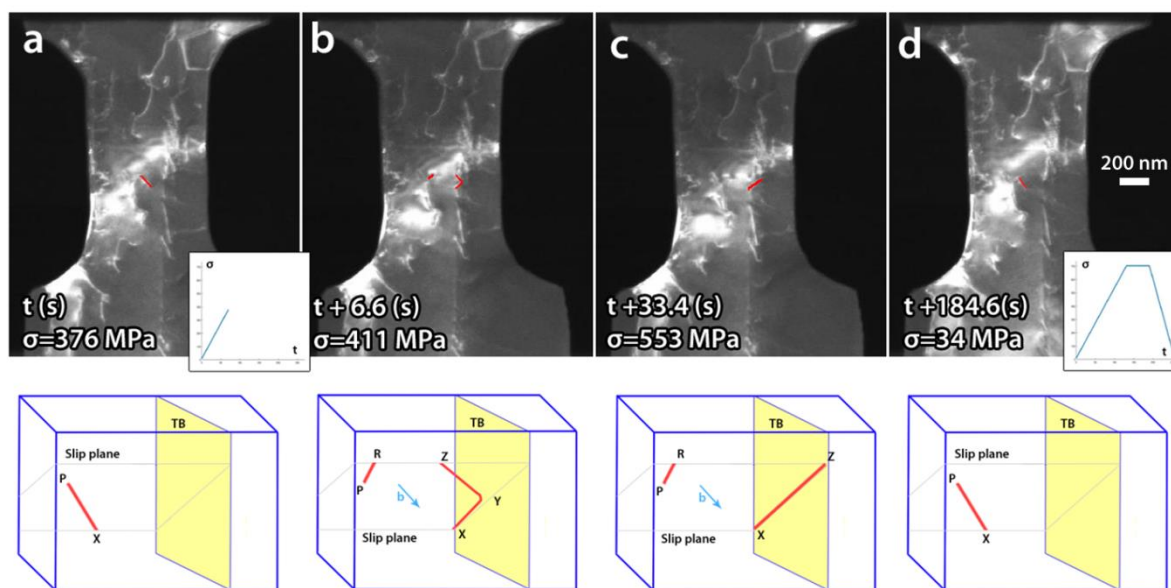


Figure 5-18, (a-c) Snapshots from the deformation movie of cycle 3 showing the microstructure and the corresponding schematics showing SAS3 configurations at different times.

Concerning the configuration of the incoming dislocation in Figure 5-18 (b), the dislocation segment XY is blocked at the TB plane (no cross-slip) while the dislocation segment ZY is free to keep its preferred configuration. Due to the difference in the mobility of screw and non-screw dislocations (the non-screw parts are much faster than the screw parts), free-ends moving dislocations are always close to the screw character. Furthermore, the dislocations prefer to be as close as possible to the screw character to minimize the total line tension energy. Therefore, the dislocation part ZY is close to the screw character. Comparing its direction with the Burgers vectors $a/2 [\bar{1} 0 1]$ and $a/2 [1 1 0]$ in the stereographic projection of grain A (Figure 5-4 (a)) implies that SAS3 might be $a/2 [\bar{1} 0 1]$, which has the highest Schmid factor.

As mentioned in the introduction, the image force due to the CTB in nickel is repulsive. Therefore, an external force is needed to move the dislocations toward the TB. Figure 5-18 (c) and (d) show that by increasing the applied stress, the dislocation line totally overlapped with the TB plane and during unloading glides back to its initial configuration without interaction with the CTB. This observation shows that the RSS of 308 MPa ($793 \text{ MPa} \times 0.389$) on the non-screw dislocation was not enough to initiate a plastic interaction with the CTB. The observation also reveals the presence of the repulsive image force of the CTB which can be predicted by the anisotropy factor, H , by Equation 1-1 [36];

Equation 5-3

$$H = C_{44} - (C_{11} - C_{12})$$

where C_{44} , C_{11} and C_{12} are elastic constants of cubic materials. The image force of a GB can be repulsive or attractive when H is positive or negative, respectively. In nickel, the three coefficients are $C_{11}=247\text{GPa}$, $C_{44}=125\text{GPa}$ and $C_{12}=147\text{GPa}$ and the H value is positive which implies that the image force is repulsive [36].

The stress at which the dislocation glides back due to the repulsive force applied by the CTB can be considered as the image-force stress due to the CTB (Figure 5-18 (d)). At the averaged distance of 130 nm from the TB plane, the dislocation was experiencing a RSS of $\sim 13 \text{ MPa}$ (regarding to the Schmid factor of $(1 \bar{1} 1)[\bar{1} 0 1]$ slip system, 0.389). This can be compared to the theoretical estimation where the stress field (τ_{img}) due to the CTB image force on an edge dislocation can be obtained by the following equation; [29, 224, 237]

Equation 5-4

$$\tau_{img} \cong \frac{\mu b}{2\pi} \cdot \frac{1}{2x} \cdot \frac{1}{(1-\nu)}$$

where μ is shear modulus (72 GPa), ν is Poisson's ratio (0.31) [238], b is the magnitude of the Burgers vector (0.24 nm), and x is the distance between the dislocation and the CTB. By using the measured distance between the dislocation and the CTB (130 nm) in Equation 5-4, the image force stress is ~14.5 MPa which is in a good agreement with the experimental result, 13 MPa. Since the source is very small in Figure 5-18 (b), its attractive back stress on the dislocation should be trivial.

5.3.5 The fracture

In cycle 5, a fast interaction accompanied by the appearance of several STs in both grains (black arrows in Figure 5-19 (b)) was observed at the stress level of ~ 830 MPa. This can be correlated with a very sharp strain burst in the corresponding strain–stress curve (the inset in Figure 5-19 (a)). The inset in Figure 5-19 (b) shows that the structure of the CTB has changed so that the thickness contrast of the TB is ruined. This can be due the fact that many dislocations have been introduced in the TB structure as seen in Figure 5-12 (b).

The sample eventually fractured at an engineering stress of 940 MPa. Comparing the sample before and after fracture (Figure 5-19 (c)) reveals that fracture passed through the CTB ledge (black arrow in Figure 5-12 (a)) confirming the suggestion that the ledges on GBs can act as crack nucleation sites [41]. The stress concentration of dislocation pile-ups within the CTB on the ledges, might initiate the nucleation of dislocations and the nucleation of a crack. Figure 5-19 (c) also shows that the fracture surfaces are parallel to the $(\bar{1} 1 1)_T$ and $(\bar{1} 1 1)$ planes which have the highest Schmid factor in both grains and the deformation movie showed high activation of dislocation in grain A in $(\bar{1} 1 1)$ planes just before fracture (less than one second). After fracture, new STs in grain B along $(\bar{1} 1 1)_T$ planes were observed as well (arrows in Figure 5-19 (c)). High activation of dislocations just before confirms that the fracture in such small-sized nickel sample is controlled by dislocations.

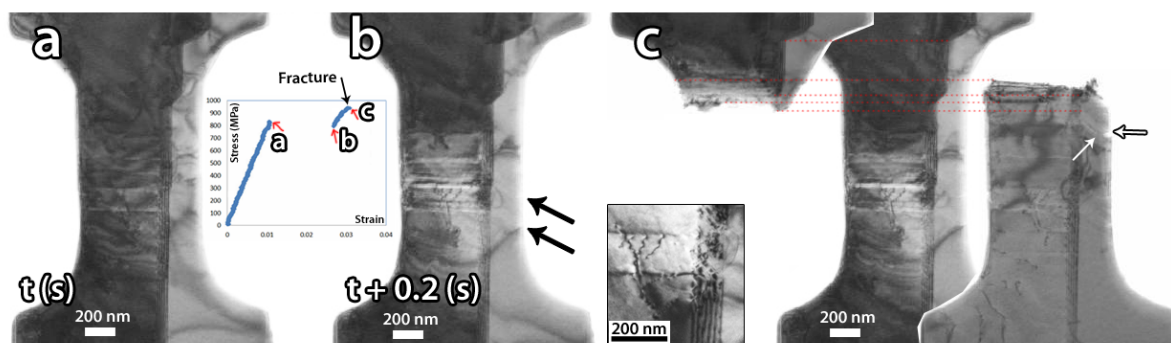


Figure 5-19, Snapshots from the deformation movie of cycle 5 showing the microstructure (a) before and (b) after the strain burst in the engineering stress-strain curve. The inset shows the dislocation structure of the CTB after the plastic interaction. (c) The comparison of snapshots before and after fracture, red dashed lines, shows the fracture passed across the ledge.

5.4 Conclusion

A bi-crystal nickel sample containing a CTB was prepared by a new sample preparation method combining twin-jet electro-polishing, FIB and in-situ TEM heating. This allowed investigating the interaction of dislocations with CTB in quantitative manner using in-situ TEM nanotensile testing. The results can be summarized as follows:

- A transition from slip transmission to dislocation absorption was observed during the interaction of screw dislocations with the CTB. The fact that the transmission is observed first can be attributed to the high stress required to activate the small SASs as well as the null (or very low) RSS in the TB plane compared to higher RSSs in both sides on the CTB. However, the transition can be explained by geometrical changes with increasing deformation. For example, decreasing the slip areas as well as geometrical constraints imposed by the PTP mounting setup could induce bending that might change the RSS in the CTB plane.
- Incoming screw dislocations cross-slip and dissociate at the CTB into paired 30° partial dislocations which glide in the same direction leading to CTB sliding rather than CTB migration. To the best of our knowledge, this is the first time that experimental evidences of such dislocations are provided. The paired configuration is probably due to the dominant screw character that can increase the attractive interactions between the partials. The presence of a planar defect (i.e. SF) between each couple of partials which can apply attractive forces on the partials is not expected in a CTB.
- For the first time, the image-force stress of a CTB acting on a non-screw dislocation was extracted in experiment. The extracted value needs to be validated by numerical simulations

as will be shown in chapter 6 for random GBs. This is a very important finding as significantly increase of the elastic limit and yield stress have been observed in nanotwinned small-scale FCC metals [224].

- The fracture of the bi-crystal occurred at a pre-existing ledge on the CTB, which highlights the importance of these defects in the failure of the twinned materials. The accumulation of moving dissociated dislocations at the ledge could induce significant stress concentrations in the ledge. In order to reveal the accurate governing factors and mechanisms, simulation of a sample with exact loading condition and dimensions is needed.

Chapter 6:

Dislocation microstructure in cyclically deformed Ni micropillars

In this chapter, the evolution of dislocation structures in small-scale Ni samples during cyclic deformation has been investigated by different ex-situ TEM techniques.

6 Dislocation microstructure in cyclically deformed Ni micropillars

6.1 Introduction

Fatigue failure is one of the main failure modes of materials. It defines the durability and life time of materials under cyclic loading conditions. For instance, temperature fluctuations in microsystems and components can induce cyclic loading conditions with the formation of dislocation structures and micro-cracks. This can change the electrical and mechanical properties of the components and, in the worst case, lead to failure of the device [239]. Therefore, investigating the fundamental fatigue mechanisms in small-scale materials is needed not only to design reliable small components but also to better understand these mechanisms near free surfaces in bulk materials.

The fatigue response of single crystals is often determined by the collective behaviour of individual dislocations and of the resulting dislocation patterns [240, 241]. For decades, intensive efforts have been made to investigate the relationship between the fatigue properties in bulk materials and the evolution of the dislocation microstructures [57, 58, 242]. The applied loading conditions, the crystal orientation as well as the initial microstructure are the determining factors for the type of dislocation patterns developing during fatigue [243]. Different types of dislocation patterns have been observed in fatigue microstructures of bulk single-crystal FCC metals, e.g., vein-channel, persistent slip bands (PSBs), labyrinth and cell structures [59]. However, complete understanding of the fundamental dislocation mechanisms controlling the transition from a homogenous to a heterogeneous microstructure and the resulting patterns is still missing [244]. Several questions also remain regarding the origin of local changes of internal stress and lattice rotation accompanying the formation of the dislocation patterns [243, 245-247].

Monotonic deformation of small-scale single crystals has been widely investigated in recent years. The general conclusion of most experiments was the inverse size-dependency of the strength of materials. However, experimental investigations of the mechanisms controlling cyclic deformation in such small-scale samples remain very limited. For instance, the improved fatigue properties of small-scale single crystals compared to bulk samples have been reported in copper micropillars [181] and magnesium alloy micro cantilevers [248]. However, microstructural characterizations of the governing mechanisms remain rare and

contradictory. For example, Schamel et al. [181] reported the formation of a non-uniform dislocation microstructure in single-crystal copper micropillars during cyclic deformation, while mechanical annealing of dislocations was observed in sub-micron single-crystal aluminium pillars during cyclic deformation [138, 249, 250].

In polycrystalline materials, GBs play an important role in strengthening and fatigue crack initiation [34, 251]. Indeed, the incompatibility of slip systems on both sides of a GB can hinder the slip of dislocations while the interaction of slip bands with GBs during fatigue might generate local stress concentration and initiation of a crack in the vicinity of the boundaries. Recent advances in micro/nanomechanical testing allow investigating the mechanical response of bi-crystal small-scale samples with single GBs.

However, several questions remain regarding the nature of the elementary mechanisms such as the dislocation/GB interaction mechanisms. Smaller strain bursts, higher strength and higher strain hardening capacity (compared to corresponding single crystal micropillars) have been reported in aluminium and copper bi-crystal micropillars with high angle GBs [70, 72] which was attributed to dislocation storage in the crystal or source truncation hardening in the individual grains. Other studies on similar systems did not reveal significant differences between single-crystal and bi-crystals [73, 201]. Such behaviour was attributed to the transmission/absorption of dislocations through/in GBs and the absence of dislocation pile-ups. When investigating the size effect on the slip transfer in nickel bi-crystal micropillars, Kheradmand et al. observed that dislocation transmission through a GB can be decreased by reducing the size of the micropillars down to 1 micron which was attributed to the increase of the transmission stress in small samples [71, 202]. On the other hand, experimental investigations of bi-crystal micropillars with CTBs did not reveal changes in strength and hardening compared to corresponding single-crystal micropillars due to easy transmission of dislocations through the twin boundary without significant dislocation storage in the structure [70, 74, 207].

It is generally argued in the literature that the mechanical response of bi-crystals strongly depends on the type of GB and the nature of the dislocation/GB interactions. When interfaces act as obstacles, increase in strength and hardening can be obtained while significant changes are not expected when the interface acts as a sink or is transparent to dislocations. However, so far, experimental or simulation investigations of the fundamental fatigue mechanisms at GBs have not received enough attention. Therefore, the main objective of this chapter is to

investigate the effect of cyclic loading on the evolution of the dislocation structures in single and bi-crystal nickel micropillars using in-situ SEM compression tests as well as ex-situ conventional and advanced TEM methods. The results provide valuable information for quantitative understanding of the possible size effect of cyclic deformation near a free surface and an interface or confined boundary.

6.2 Materials and methods

In this work, the SEM sample preparations and the in-situ SEM mechanical testing were carried out by Jonas Groten and Ruth Schwaiger at the Karlsruhe Institute of Technology (KIT), the simulation was done by Stefan Sandfeld at TU Bergakademie Freiberg and the TEM sample preparation and TEM investigations were carried out at EMAT.

A high purity Ni foil (99.999%) was prepared by mechanical polishing using different diamond suspensions down to 1 μm grain size followed by vibratory polishing with alumina for 3 h (Buehler Vibromet 2). The foil was then annealed at 800°C in high vacuum for 4 h to obtain grains in the 100 micrometer range and a homogeneous crystallographic orientation over the grain areas. EBSD maps were obtained with a Bruker eFlash EBSD detector. Micropillars were fabricated in selected grains and at a GB in-between. The micropillars were fabricated by FIB milling using an FEI Scios DualBeam microscope operated at 30 kV acceleration voltage. The pillars had a square cross-section with nominal side lengths of 2 μm , an aspect ratio of approximately 3:1 and almost perpendicular side walls. They were cut from the top with over-tilting the sample to compensate for the widening of the beam when penetrating deeper into the sample. The final milling was conducted by single-pass patterning at a beam current of 100 pA. For this study, single-crystal pillars with $[\bar{6} 1 10]$ and $[\bar{6} 1 16]$ normal orientations, referred to as G5 and G6 in the following, and a bi-crystal micropillar, i.e., G56, at the GB in-between, respectively, were prepared. The EBSD map of the local grain structure together with the single and bi-crystal micropillars are shown in Figure 6-1. Pillars G5 and G6 were both oriented in a multi-slip orientation, while the G56 GB misorientation was $\sim 20^\circ$.

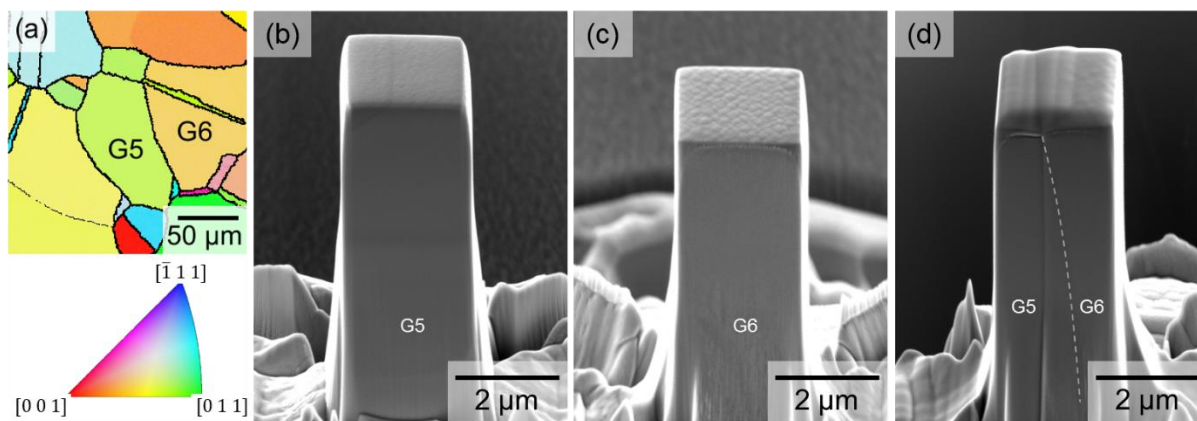


Figure 6-1, (a) EBSD map of the high-purity Ni foil after annealing, (b), (c) SEM micrographs (taken at a tilt angle of 52°) of single-crystal micropillars, which were FIB-milled from inside selected grains G5 and G6, and (d) a bi-crystal pillar G56 at the grain boundary in-between.

Table 6-1 lists the Euler angles and compression directions parallel to the micropillar vertical axis, and the two slip systems exhibiting the highest resolved shear stresses (RSS). The ratios of RSS of the secondary to the primary slip systems, $\frac{\tau_s}{\tau_p}$, show that the deformation conditions are close to multi-slip in both grains.

Table 6-1, Crystallographic orientations of the pillars and the slip systems with the highest Schmid factors. The ratios of the resolved shear stresses of the respective slip systems indicate multi-slip conditions.

| Pillar | Euler angles $\varphi_1, \phi, \varphi_2$ | Compression direction | Primary slip system | Schmid Factor | Secondary slip system | Schmid factor | $\frac{\tau_{secondary}}{\tau_{primary}}$ |
|--------|--|--------------------------|------------------------|------------------|------------------------------------|------------------|---|
| G5 | $261^\circ, 33^\circ, 83^\circ$ | $[\bar{6} 1 \bar{1}0]$ | $(1 1 1)[0 1 \bar{1}]$ | 0.492 | $(\bar{1} 1 \bar{1})[0 1 \bar{1}]$ | 0.456 | 0.93 |
| G6 | $261^\circ, 22^\circ, 101^\circ$ | $[\bar{6} 1 \bar{1}6]$ | $(1 1 1)[0 1 \bar{1}]$ | 0.497 | $(\bar{1} 1 \bar{1})[0 1 \bar{1}]$ | 0.481 | 0.97 |

In order to investigate the effect of a GB on the formation of dislocation microstructures during cyclic loading, compression-fatigue cycles of micropillars were performed. The pillars were deformed at a loading rate of $150 \mu\text{N/s}$ to a nominal displacement of 200 nm using a Nanomechanics InSEM 1 nanoindenter equipped with a diamond flat punch of $5 \mu\text{m}$ diameter. Then, the pillars were unloaded to 15 % of the maximum load and reloaded to the same maximum load. After 100 loading cycles the pillars were unloaded completely. The displacement of the indenter tip was determined from the images recorded during the in-situ experiments to account for uncertainties in the tip displacement measurement of the nanoindenter due to thermal drift.

A FIB-SEM dual beam FEI Helios NanoLab 650 instrument was then used for TEM sample preparation. The micropillars were embedded in an ion beam-assisted (30 kV) platinum protective layer, lifted out, mounted on TEM grids, and milled by a Ga⁺ ion beam of 30 kV/0.79 nA till 2 kV/39 pA to reach a thickness of 200-300 nm (see Figure 6-2). In order to investigate the microstructure of the deformed micropillars, two-beam BF-TEM imaging, ACOM-TEM and nanostrain mapping in TEM were used in an FEI Tecnai G2 microscope. PED was used to minimize dynamical effects and to facilitate the automated indexing of the diffraction patterns. Furthermore, to further analyse the experimental observations, the influence of GB image forces on internal stresses was investigated with a finite element based discrete dislocation simulation framework, where dislocations are represented through their eigenstrains, see [252, 253].

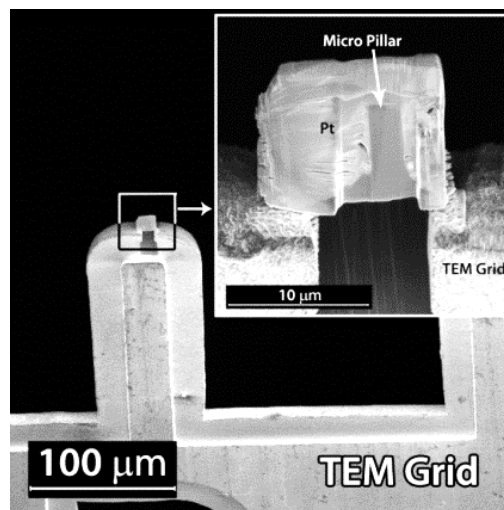


Figure 6-2, SEM images of micropillar G56 on a TEM grid after lifting out and thinning by FIB.

6.3 Results and discussion

In Figure 6-3, the deformed pillars after 100 loading cycles are shown together with the identified slip systems. In all micropillars, slip steps or traces on the surfaces indicate the activation of at least two different slip systems in agreement with the multi-slip condition. The single-crystal pillar G5 exhibits large slip steps (Figure 6-3 (a)), while the pillar G6 exhibits much smaller ones (Figure 6-3 (b)). As evidenced by the pronounced slip steps, pillar G5 accumulated higher plastic strains along the loading direction compared to pillars G6 and G56, i.e. ~15% compared to ~5% and ~7%, respectively, based on the height of the deformed micropillars. Due to the pronounced slip in G5 during the first loading cycle (Figure 6-4 (a)), the initial nominal displacement of 200 nm was exceeded significantly resulting in a much

higher accumulated strain. The large strain bursts are indicators of a low density of dislocations in the microstructure [243]. The single-crystal pillar G6 showed smaller strain bursts than G5, while plastic deformation was initiated at a lower stress. While the loading curve of pillar G56 exhibits steps in the first cycle (Figure 6-4 (a)), overall the deformation can be regarded as continuous. The different slopes of the loading curves of G5 and G6 can be rationalized by the difference in Young's modulus, i.e., 204 GPa and 168 GPa for G5 and G6, respectively, differences resulting from the single crystal nature and the difference in crystallographic orientation of the pillars. The reduced slope of the G56 pillar is caused by the rather thick Pt layer deposited on the pillar top (Figure 6-1 (d)) to account for height differences of the two different grains.

The strain increases with increasing number of cycles (Figure 6-4 (b)), which is expected for compression-compression cycles and possibly enhanced by cyclic creep effects [58, 254]. The strain increases at a somewhat higher rate in the case of G5, which is likely related to the higher stress amplitude and mean stress of 160 MPa and 190 MPa, respectively, when compared to G6 and G56, which were deformed at similar stress amplitudes and mean stresses, i.e., 125 MPa and 140 MPa in the case of G6, and 125 MPa and 150 MPa for G56.

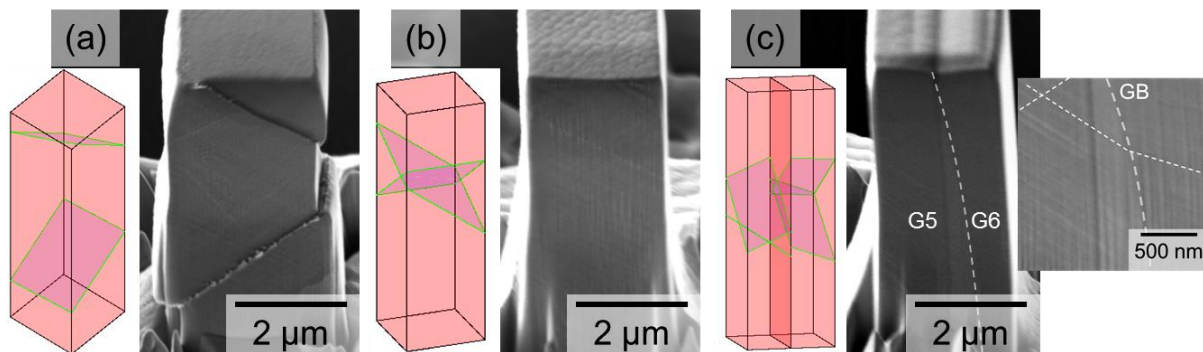


Figure 6-3, SEM micrographs (taken at a tilt angle of 45°) of deformed micropillars (a) G5, (b) G6, and (c) G56 after 100 loading cycles. The corresponding sketches show the activated slip planes. The outset of (c) shows the slip lines on the pillar face of the two crystal orientations in G56 at higher magnification.

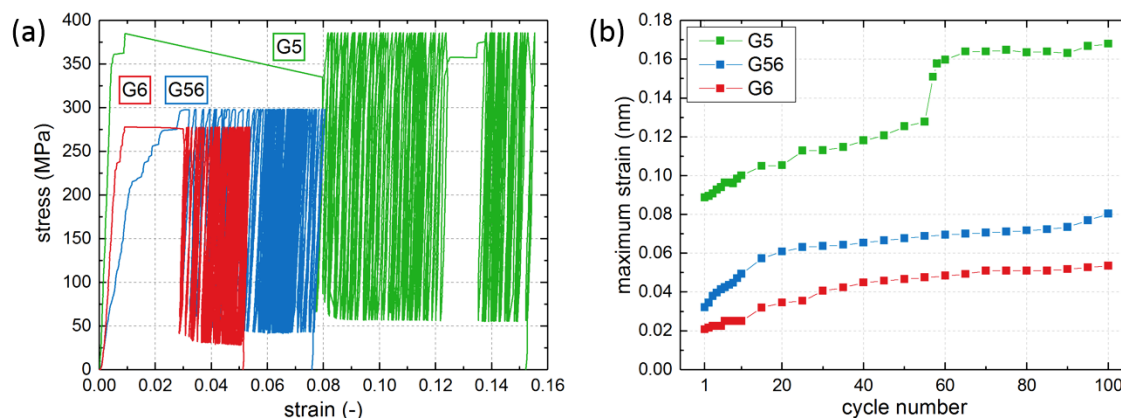


Figure 6-4, (a) Stress-strain curves of the three tested pillars G5, G6, and G56. The strain was quantified based on the analysis of the micrographs recorded during the experiments. The accumulated plastic strain of pillar G5 was ~15% compared to ~5% and 7% for pillars G6 and G56, respectively. (b) The strain at the maximum load per loading cycle increased with increasing cycle number and this somewhat more pronounced for G5 compared to G6 and G56.

TEM investigation of the pristine Ni bulk sample revealed a very low density of dislocations within the grains and near GBs (see Figure 6-6). Figure 6-7 (a) and Figure 6-7 (b) show the presence of a parallel dislocation vein-channel like structure in both single crystal micropillars after deformation (white arrows in both figures). In fatigued microstructures of single crystals, different dislocation patterns are observed: vein-channel and PSB structures consisting of dislocation dipoles are formed in single slip while the labyrinth and cell structures are composed of a network of tangled dislocations involving dislocation locks and junctions that can be formed in single or multi-slip conditions [58]. In Figure 6-7 (c) and Figure 6-7 (d) it can be seen that the dislocation patterns are composed of randomly oriented dislocations involving a high density of junctions. Therefore, while the dislocation patterns are not fully developed yet, it is reasonable to expect them to be the early stages of either labyrinth or cell structures rather than vein-channels or PSBs. This is also in agreement with the presence of cell walls in DD fatigue simulated microstructure of multi-slip oriented Ni single-crystal micropillars [243]. Furthermore, the fact that the slip systems with the highest Schmid factor (see Table 6-1) are not coplanar increases the probability for short-range dislocation interactions, required for the formation of cell structures.

It is also worth mentioning that the uniformly distributed black dots observed in all the BF-TEM images are FIB induced defects while the faint parallel horizontal lines visible on the top part of Figure 6-7 (b) are attributed to a curtaining effect resulting from FIB milling.

Systematic contrast analysis on some dislocations confined between the dislocation walls in Figure 6-7 (c) and Figure 6-7 (d) showed that most of these dislocations have been activated in slip systems with high RSSs (Figure 6-5). These dislocations also exhibit a dominant screw component in both grains (Figure 6-5), similar to dislocations observed after fatigue in bulk samples [255].

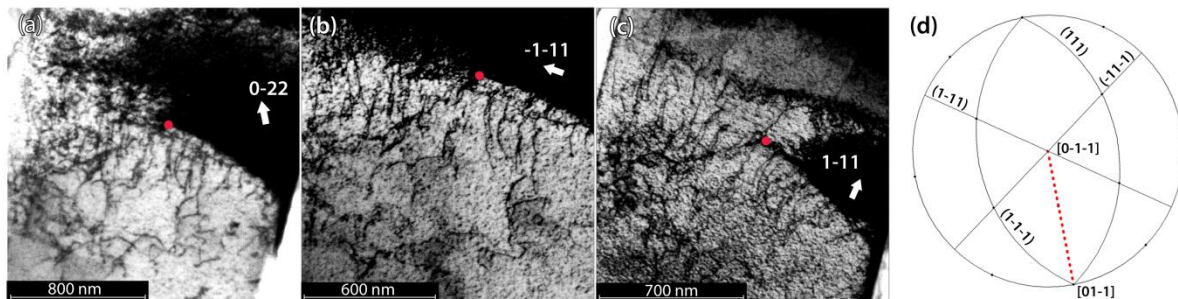


Figure 6-5, (a), (b), and (c) Two-beam condition images of micropillar G5 with $g = \bar{1}\bar{1}1$, $g = 0\bar{2}2$ and $g = 1\bar{1}1$ excited, respectively. The red dot is the reference point. Due to systematic contrast analysis, the dislocations visible in all images are $\frac{a}{2} [01\bar{1}]$. (d) Stereographic projection of G5 in which $\frac{a}{2} [01\bar{1}]$ is shown by the red dashed line. Comparing dislocation lines and the Burgers vector shows that the dislocations have dominant screw components.

In both single-crystal micropillars in Figure 6-7 the wall-like structures were mainly found halfway the height of the pillars. Very few such features were observed in regions close to the base and the top of the micropillars. Close to the top of the micropillars, the microstructure is dominated by an almost homogeneously distributed tangled dislocation structure. In monotonic deformation of micropillars, accumulation of dislocations has been observed to initiate from the areas close to the top and to the base of the micropillar, where the mechanical constraint is significant. This arises from the friction stress between the flat punch indenter and the contact surface of the pillar as well as from the low stress at the flat base part of the sample [256, 257]. The indenter surface can prevent the annihilation of dislocations on the top surface, and similarly, the lower stress level in the underlying material prevents further glide of dislocations out of the pillar base [257]. This leads to the formation of dislocation pile-ups in these regions and the shutdown of the sources.

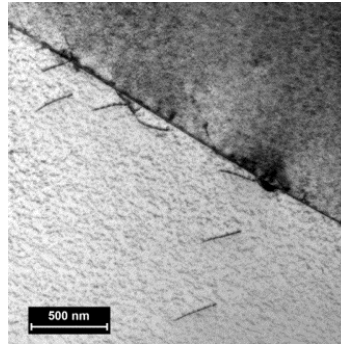


Figure 6-6, BF-TEM micrograph of the Ni material before deformation, the black small dot like contrasts in the matrix are FIB induced defects.

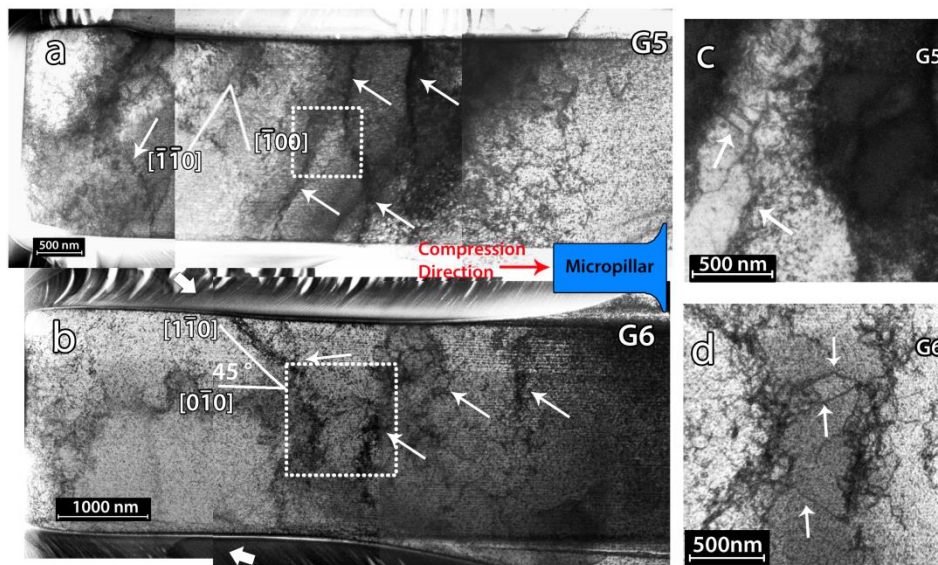


Figure 6-7, (a, b) BF-TEM micrographs of micropillars G5 and G6, respectively. The zone axis in both samples is close to $[001]$. White arrows show the dislocation cell walls in the structure. Schematic illustration of the pillars and the compression directions are shown in the lower right inset of (a). (c, d) BF micrographs of the selected regions in (a) and (b) showing screw dislocations confined between the channels and indicated by white arrows.

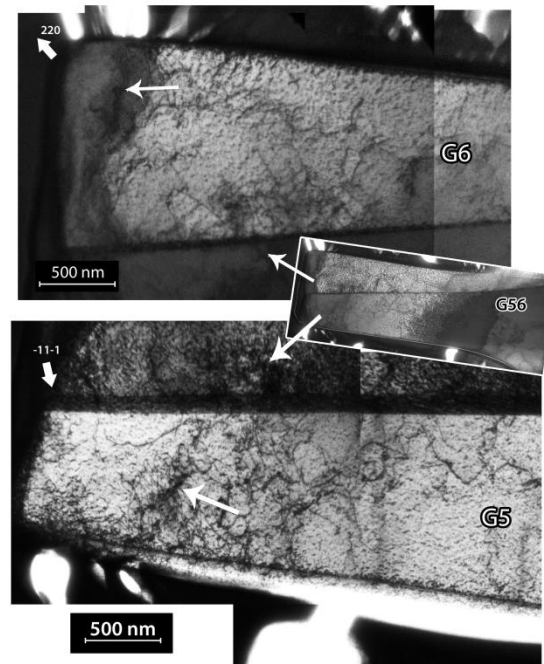


Figure 6-8, BF micrographs of micropillar G56 showing the dislocation structures in grains G6 and G5. The white arrows show the position of a ‘non-mature’ dislocation wall in both grains.

Figure 6-8 confirms the absence of ‘mature’ cell walls in the bi-crystal micropillar G56. Indeed, only some nuclei of dislocation walls as well as few dislocations can be observed in this micropillar, which might be related to the lower accumulated plastic strain. On the other hand, the dense character of the cell walls in G5 compared to sample G6 in Figure 6-7 can be attributed to the larger accumulated plastic strain in sample G5 as shown in Figure 6-4. The absence of cell walls in G56 implies that the GB has hampered the formation of the walls. Such behaviour is in agreement with the observation of a critical size of dislocation cells in previous experimental and simulation works found in the literature. For example, it has been observed that the minimum length scale required for dislocation patterns to be able to develop is around $1\ \mu\text{m}$ in Cu [239]. In Cu films with a thickness below $1\ \mu\text{m}$, no cell structures or long-range dislocation structures but rather individual dislocations were observed after cyclic deformation [258, 259]. Also, fatigue DD simulations in single-crystal Ni micropillars oriented in multi-slip have shown that, with similar initial density of dislocations, cell structure formation occurs in micropillars larger than $2\ \mu\text{m}$ [243]. Therefore, the absence of dislocation walls in the bi-crystal G56 sample (Figure 6-8) can be attributed to a shorter mean free path of dislocations on both sides of the GB. Such a behaviour is also in agreement with the observation of a ‘non-mature’ cell wall close to the top of the micropillar G56 in the widest part of grain G6 (white arrow in Figure 6-7 (c)). The presence of the GB can also

decrease the rate of the multiplication of dislocations while enhancing the rate of dislocation annihilation at the GB and the free surface (i.e., dislocation starvation). Indeed, image forces - with an effective depth of tens of nanometers from free surfaces and GBs - can accelerate the escape/absorption of dislocations [260]. In most cubic metals, image forces arising from free surfaces and at GBs have been reported to be attractive and repulsive, respectively [36]. It should also be mentioned that most of the cell walls observed in Figure 6-7 are almost perpendicular to the compression axis. In sample G6, a dislocation wall oriented at 45° can be observed (Figure 6-7 (b)). Figure 6-7 also shows that the crystallographic orientation of the walls is in agreement with previous studies in the literature. Indeed, formation of walls along $\langle 001 \rangle$ and $\langle 101 \rangle$ directions was reported in fatigued bulk Ni single crystals oriented along $\langle 001 \rangle$ [261]. The average distances between the walls in the present work (~ 630 nm and ~ 730 nm for samples G5 and G6, respectively) are in line with the dislocation cell sizes observed in DD simulations ($0.6 \mu\text{m}$) in multi-slip oriented $2 \mu\text{m}$ Ni micropillars [243].

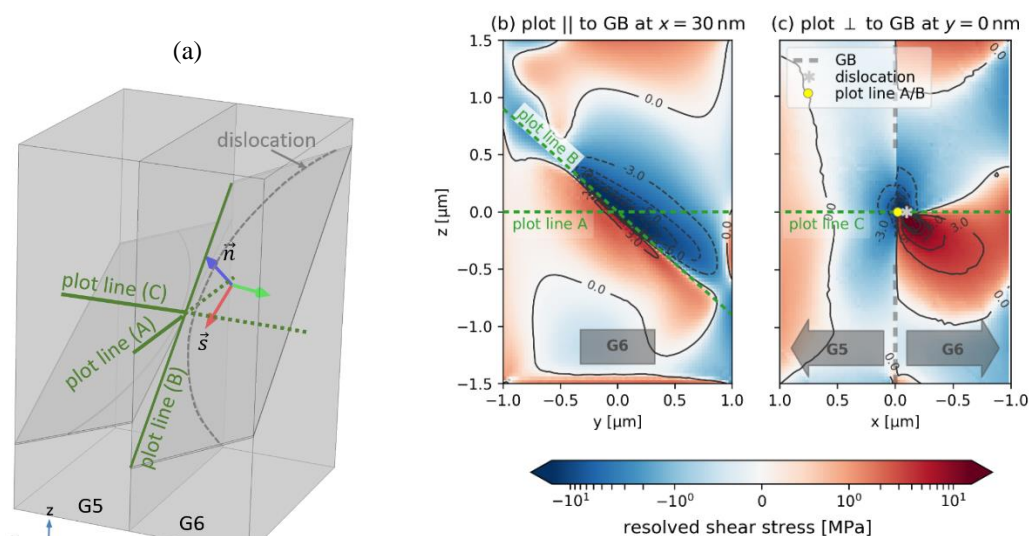


Figure 6-9, (a) Geometry of the bi-crystal used for the discrete dislocation simulation. The origin of the x-y-z coordinate system is in the centre of the pillar, \vec{n} is the slip plane normal and \vec{s} the slip direction parallel to the Burgers vector \vec{b} . (b) shows the RSS for the $(111)[011]$ G6 system near the GB-plane (left plot) and in a plane cutting perpendicularly through the GB (right plot).

To investigate the influence of the GB on the strain field in the presence of dislocations, an idealized bi-crystal containing a dislocation near a GB as depicted in Figure 6-9 (a) was simulated. For the grains G5 and G6 the anisotropic elastic response is given by the three elastic coefficients of cubic Ni, i.e., $C_{11}=247$ GPa, $C_{44}=125$ GPa, and $C_{12}=147$ GPa. The crystal orientations for G5 and G6 were considered according to the Euler angles given in

Table 6-1. The pillar has a square cross-section of $4 \mu\text{m}^2$, and the grain boundary is a perfect plane dividing the pillar into two grains of equal dimensions that are assumed to be welded together perfectly. The numerical simulation is based on a high resolution finite element approach. A dislocation line is the termination of a plastically swept area, where the surfaces below and above this area are displaced by the length of the Burgers vector $|\vec{b}|$. In the numerical simulation the area is approximated by a very thin layer of height $\Delta h \approx 6|\vec{b}|$ within which a constant shear eigenstrain distribution $\varepsilon^0 = |\vec{b}|/\Delta h$ is prescribed (cf. the coordinate system in Figure 6-9 (a)). Outside this region the eigenstrain is zero. The spatial discretization, i.e., the size of the finite elements, is adaptively chosen such that the stress field of a single dislocation can be recovered at all points that are located outside the dislocation core. For further details of this approach see [252, 253]. Since the experiments showed that plastic deformation is initiated in G6 rather than in G5 (Figure 6-4 (a)), the G6 slip-plane $(111)[01\bar{1}]$ was chosen, which has the highest Schmid factor. The curved dislocation on this plane (shown as the dashed grey line in the right half of the pillar in Figure 6-9 (a)) has an approximate screw orientation at the position closest to the GB. The distance to the GB is $\approx 90 \text{ nm}$ at this position. Assuming linear elasticity – no dislocation core effects or atomic details of the GB are considered – the stresses resulting from multiple dislocations can be additively superimposed and, thus, for simplicity, only a single dislocation is considered in this study. The pillar is fixed on the bottom, no external tractions or displacements are prescribed.

The resulting RSSs for the bi-crystal are shown in Figure 6-9 (b) and Figure 6-9 (c). The narrow red area at the bottom of the left plot (corresponding to the centre of the plot in Figure 6-9 (c)) results from the elastic anisotropy and the fact that the bottom of the pillar is fixed. The larger red area at the top of the pillar is caused by the interaction of the dislocation with the free surfaces, which results in rather high stress values comparable to the stresses much closer to the dislocation. Stresses above and below the slip plane exhibit a sign change, which is due to the shear stress field of the screw dislocation. Its characteristic shape (the horizontal “8”) can partially be seen in Figure 6-9 (c). RSSs in the left half of this plot are shown with respect to the slip system of G5. The different crystallographic orientations of G5 vs. G6 are the reason for the abrupt change of the stresses across the GB and the strong reduction in the G5 half of the pillar. Note that the different crystallographic orientation has an influence on both the elastic properties as well as on the orientation of the G5 slip system

(again $(111)[01\bar{1}]$ planes). These two effects together explain why in the experiment G5 exhibits a retarded dislocation activity.

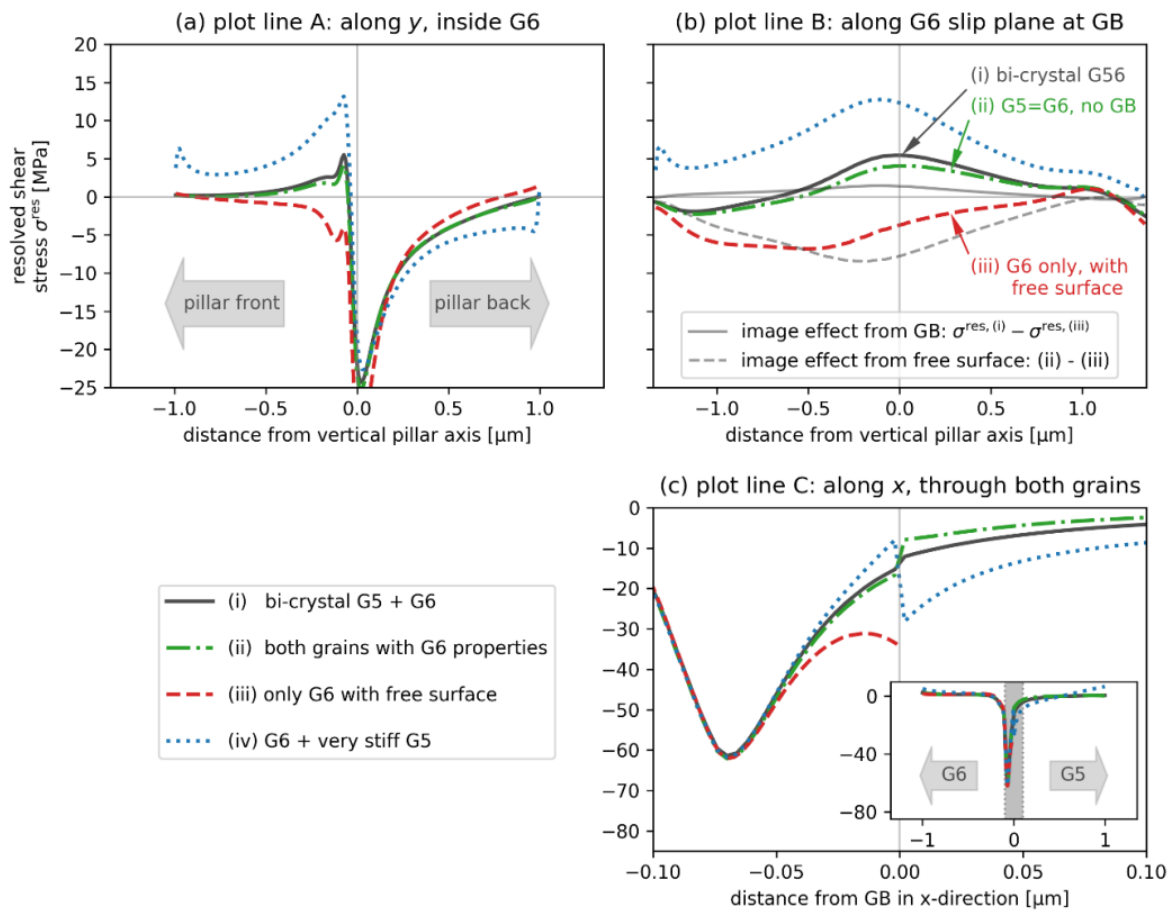


Figure 6-10, Resolved shear stress along three different lines (cf. plot lines in Fig. 6): (a) along a horizontal line parallel to the GB, (b) at a distance of 50 nm of the intersecting line of the G6 slip plane and the GB, and (c) through G5 and G6. The grey box in the inset shows the location of the magnified region around the GB in (c).

To further analyse the interaction between dislocations and the GB altogether four simulations of four different grain configurations were performed. In all cases, the dislocation remains fixed at its initial position and only the stresses resulting from this stationary situation are computed and analysed. The four grain configurations are:

- i. as before, true crystallographic orientations corresponding to the experimental data were used for G5 and G6, effectively representing a G56 bi-crystal (Figure 6-9 (b)) and the solid black lines in Figure 6-10 show the corresponding stresses);
- ii. the G6 crystal orientation was also used for the G5 part, effectively yielding a larger G6 single crystal without GB (dash-dotted green line in Figure 6-10);

- iii. the G5 half of the pillar was removed yielding the G6 orientation only, while instead of the GB there is now a free surface (dashed red line in Figure 6-10);
- iv. for G5 a very stiff material is assumed (Young's modulus $E_{G5} \approx 100E_{G6}$) resulting in a perfectly blocking, very stiff GB (dotted blue line in Figure 6-10)).

Comparing the resolved stress inside G6 for (i) and (ii) in the vicinity of the GB (Figure 6-10 (a) and Figure 6-10 (b)), it can be seen that the presence of the G5 crystal slightly reduces the local resolved stress. This difference is due to dislocation image forces resulting from the different elastically anisotropic properties of G5 and G6. An estimate for the upper limit of this influence is obtained by simulation setup (iv) with G5 implemented as extremely stiff thereby creating a perfectly blocking interface. Dislocation stresses are significantly amplified by a factor of ~ 2.5 as compared to the bi-crystal. Apart from that, the fundamental characteristics of the stresses inside G6 remain unaffected.

To investigate the influence of image forces in more detail, the grain G5 was completely removed such that the GB is now a free surface (lines labelled (iii) in Figure 6-10). Compared to (i), the stresses are strongly reduced (cf. the red line in Figure 6-10 (b)). The difference between the G5 “bulk” simulation (ii) and the “free surface” simulation (iii) (Figure 6-10 (b), grey solid line) is a measure for the strength and direction of the image forces. The fact that the stress level is negative implies that for the considered $(111)[01\bar{1}]$ system a screw dislocation with line orientation ξ opposite to the Burgers vector direction \vec{b}/b would experience a Peach-Köhler force pointing into a negative Burgers vector direction (cf. local coordinate system in Figure 6-9). Therefore, the dislocation would experience an attractive force towards the free surface. The GB, however, has the opposite effect of the free surface: Again using the “bulk” system (ii) as reference, it is found that the GB exerts a slightly positive stress and, thus, would repel a dislocation (Figure 6-10 (b), grey solid line). This is in agreement with calculations presented in [36]. While the calculations in [36] though were conducted for a perfect dislocation and GBs with three specific misorientation angles only, the computational approach presented in this work is valid for very general GBs and dislocation configurations.

Besides the image force effects due to the different elastic properties of G6 and G5, there are also effects that are related to the different crystallographic orientations of the G5 and G6 slip systems. This can be seen in Figure 6-10 (c) showing the RSS along a horizontal line cutting through both grains. The influence of the change of slip plane orientation across the GB results in a jump in the stresses, which is less pronounced for the G56 bi-crystal than for the

“bulk” crystal from simulation (ii) (note that for (ii) only the elastic properties were varied, while keeping the G5 slip system geometry). The reduction of the jump height is again the result of the image forces. Moving the dislocation closer to the GB does not change this behaviour significantly; only a small shift of the curve (iv) towards the interior of G6 is observed.

These findings and details relate to the microscopy data in different ways and explain some of the features that have been observed:

- The dislocation structure of G6 in Figure 6-8 does not seem to be strongly attracted or repelled by the GB, which is in agreement with the findings from the simulation. However, the effect of image forces will become more pronounced when the difference in elastic properties between two grains is larger.
- Stresses from dislocation pile-ups in G6 at the GB create only mild stress concentrations on the G5 side of the GB (Figure 6-9 (c)). This suggests that nucleation events in G5 due to pile-up stress concentrations are relatively unlikely, which is confirmed by the present experimental observations.
- Dislocation structures in G5 seem to accumulate towards the centre region of G5 (i.e. forming rather horizontal structures in Figure 6-8). This behaviour might be explained by the stress field shown in Figure 6 (c): initially, dislocations are nucleated in G6, and the resulting stress field is a superposition of their individual fields. Since the exact dislocation position in G6 plays a minor role for the stresses in G5, the resulting stress field will look qualitatively similar to that in Figure 6 (c). The G5 grain exhibits vertical bands of positive (left = close to the free surface), zero (centre of G5), and negative stresses (close to the GB), such that in G5 a newly nucleated dislocation would always move to the centre where the stress is zero.

In summary, it is found that in this specific bi-crystal configuration image forces of the GB have only a minor influence on internal stresses in the GB region. The bi-crystal behaves— from the point of view of image forces— almost identical to a bulk system. Thus, GB image forces can be excluded as a reason for the reduced occurrence of “mature” cell walls in the bi-crystal. At the same time, this suggests that the reason is indeed the insufficiently available volume, which may be simply too small to accommodate cell structures that would form under the given conditions of stress and dislocation density [262].

As a next step, in order to better understand the cell structure formation mechanisms, detailed TEM characterization of the gradients of orientation and internal stress associated to the dislocations confined within the walls has been performed. Indeed, the dislocation walls observed in Figure 6-7 did not vanish using all possible two-beam conditions, indicating that different types of dislocations are confined within these walls. However, the dense character of the walls and the presence of FIB defects made the characterization of the dislocations confined in the walls using diffraction contrast impossible. Local changes of diffraction contrast at the dislocation walls shown in Figure 6-7 (c) and Figure 6-7 (d) can be explained by local changes of the crystallographic orientation. In order to quantify these lattice misorientations, PED [123] and ACOM-TEM [120, 263] were used to generate orientation maps for the G5 and G56 samples. These maps were obtained using an electron probe of ~4 nm diameter, a step size of 40 nm and a precession angle of 0.5° while the sample was aligned along the [100] zone axis. In Figure 6-11 local changes of orientation can be seen close to the top of the G5 micropillar where some uniformly distributed tangled dislocations were observed. This can be explained by lateral friction and possible slight misalignment between the pillar top surface and the flat punch indenter [256, 257]. Figure 6-11 also shows clear sharp local lattice rotations at the position of the dislocation walls indicating that the walls contain stored GNDs. Indeed, contrary to SSDs, GNDs give rise to deformation-induced local misorientations and long-range internal stresses [264]. Veins and in particular PSBs that are formed by dislocation dipoles with almost zero net Burgers vector cannot induce misorientations or long-range strain fields. Again, this result confirms that the dislocation patterns observed in the present work are dislocation cell walls. This is an important finding which provides (to the best of our knowledge) a first experimental evidence on the correlation between the storage of GNDs in the walls and the resulting crystal lattice rotation. DD simulations have shown that the induced misorientation could increase the probability of simultaneous activation and short-range interaction of non-coplanar slip systems facilitating the formation of cell structures [265, 266]. The orientation map of the bi-crystal micropillar did not show any misorientation except in the region close to the tip where a ‘non-mature’ dislocation wall has been observed, Figure 6-12.

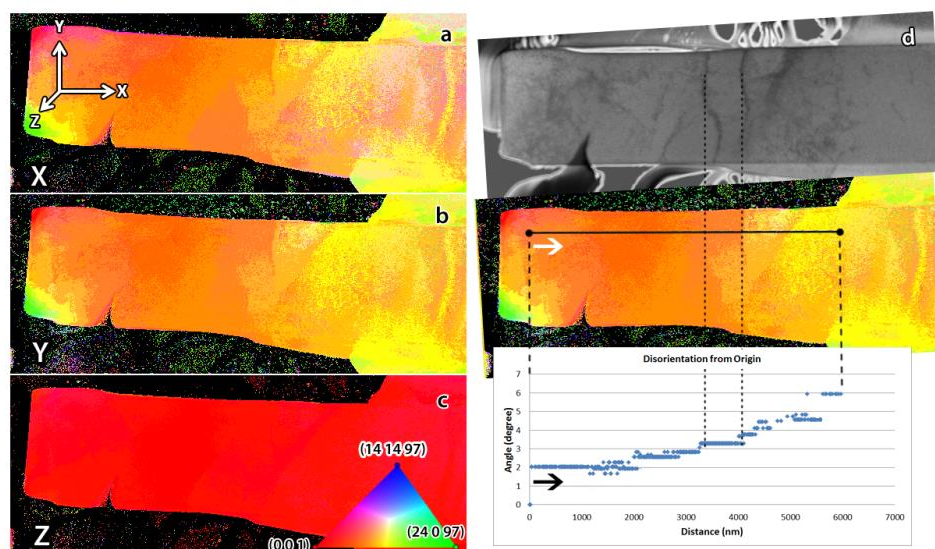


Figure 6-11, (a-c) The orientation maps of micropillar G5 along X, Y, and Z directions, respectively, taken by ACOM-TEM (an inverse pole figure was drawn for a small region of orientation to facilitate displaying misorientation). (d) From top to down: the virtual BF image; the relevant orientation map along Y; the misorientation profile obtained along the line shown in the orientation map. The latter shows sharp misorientations at the position of the dislocation walls.

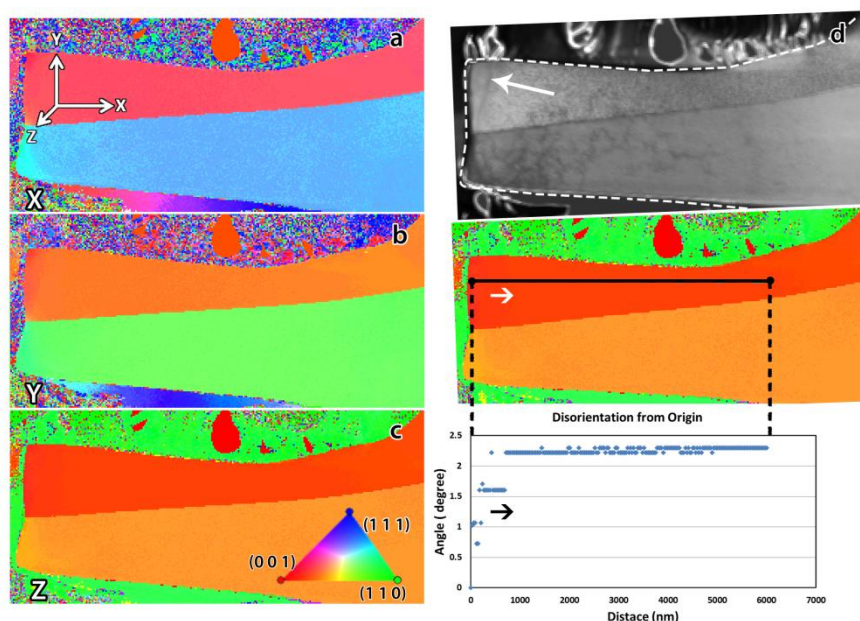


Figure 6-12, (a-c) the orientation maps of micropillar G56 along X, Y, and Z directions, respectively, taken by ACOM-TEM. (d) From top to down: the virtual BF image; the relevant orientation map along Y; the misorientation profile obtained along the line shown in the orientation map. Misorientations were not detected except at the tip of the sample where a dislocation wall is present.

Figure 6-13 exhibits PED strain maps obtained in the micropillar G5. The acquisition conditions were similar to those used to generate the orientation maps of Figure 6-12. The main advantage of strain mapping with PED is its capacity to generate large strain maps (up

to $\sim 8 \times 8 \mu\text{m}^2$) with high strain sensitivity and spatial resolution. However, this technique was so far mainly used in single crystal semi-conductors and very few polycrystalline metals in the literature [267-270] while dislocation patterns generated by cyclic deformation did not yet benefit from these recent advances. In Figure 6-13 long-range strain fields associated to the walls can be clearly observed confirming the presence of GNDs at the walls in agreement with local changes of orientations shown in Figure 6-12. Such a feature can be attributed to the locks, the junctions and perfect $\frac{a}{2} \langle 110 \rangle$ glissile dislocations accumulated in the walls as observed in DD simulations [243, 271, 272]. The origin of these dislocations is attributed to the enhancement of cross slip due to the presence of internal stress fields. The cell wall embryos initially contain immobile locks and junctions which act as obstacle for mobile dislocations. The internal stress field generated by the embryos facilitates the cross-slip and the storage of new incoming dislocations, leading to further increase of the long-range internal stresses surrounding the walls [243]. The results shown in Figure 6-13 thus provide first-of-kind experimental evidence for the presence of this internal stress field using automated nanostrain mapping in TEM. In the absence of the external applied stress, the elastic strain mapping of grain G6 and G5 in sample G56 (Figure 6-14 and Figure 6-15) shows a uniform distribution of internal stress in the main body of micropillar in both grains in all directions which is in agreement with the absence of ‘mature’ walls in Figure 6-8. The observed strain gradient close to the tip can be due to the presence of dislocation structure patterns in the structure.

It should be mentioned here that these maps reveal the strain gradient in a single grain and the values are not absolute. Therefore, by changing the location of the reference point, the sign and amount of strain would change and comparison of the maps of 2 different grains is not possible. Using Topspin to study deformed materials has not been used widely in the literature and further understanding and interpretation of the results needs further investigations.

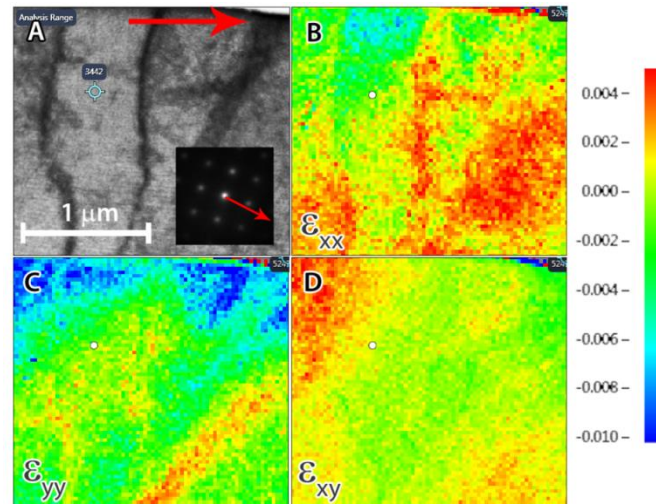


Figure 6-13, (a) Virtual BF image of micropillar G5. The corresponding experimental diffraction pattern is shown in the inset. The red arrows indicate ϵ_{xx} in both spaces (the teeth shape feature marked by a white arrow is a platinum piece detached from the side of the micropillar and bent over it). (b), (c) and (d) are elastic strain fields of ϵ_{xx} , ϵ_{yy} , and ϵ_{xy} , respectively. The white spot in the basis of all maps indicates the position from which the reference diffraction pattern was acquired.

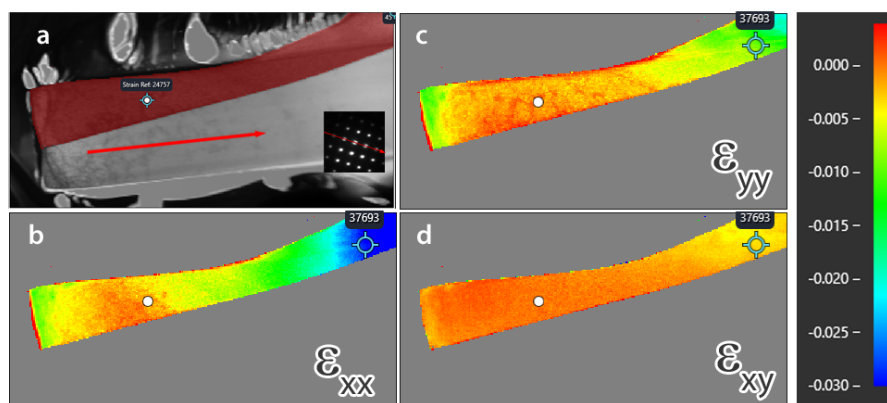


Figure 6-14, (a) The virtual BF image of grain G6 of micropillar G56 and the corresponding diffraction pattern inset, the red arrows indicate ϵ_{xx} in both spaces. (b), (c) and (d) are the elastic strain fields of ϵ_{xx} , ϵ_{yy} , and ϵ_{xy} , respectively; the reference point is indicated by the white spot on the maps in the base of the micropillar.

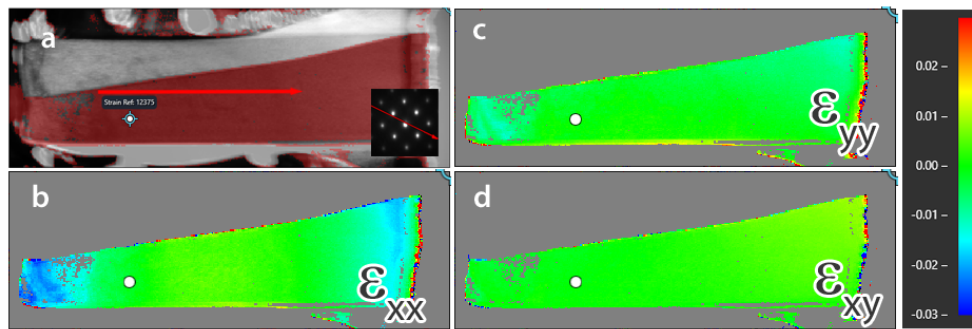


Figure 6-15, (a) The virtual BF image of grain G5 of micropillar G56 and the corresponding diffraction pattern inset, the red arrows indicate ϵ_{xx} in both spaces. (b), (c) and (d) are the elastic strain fields of ϵ_{xx} , ϵ_{yy} , and ϵ_{xy} , respectively; the reference point is indicated by the white spot on the maps in the base of the micropillar.

6.4 Conclusions

In the present chapter, single crystal and bi-crystal Ni micropillars have been subjected to cyclic loading in SEM. Advanced quantitative TEM was then used to better understand the elementary defect mechanisms controlling the formation of the dislocation structures and the associated heterogeneities. The results can be summarized as follows:

- Cyclic deformation in SEM revealed significantly higher accumulated plastic strain in the single crystal micropillar G5 compared to the bi-crystal. This is in agreement with TEM observations of ‘mature’ cell walls in the single crystal samples. In the bi-crystal sample, only a few ‘non-mature’ cell walls have been observed. These results confirm the role of the dislocation mean free path in the size dependency for the formation of dislocation patterns in cyclically deformed Ni micropillars. Although such behaviour has been previously reported in DD simulations, experimental validation was still missing in the literature.
- The computational analysis showed that, for the crystallographic configuration used in the present work, the image forces resulting from the GB do not change the internal stress landscape appreciably. Therefore, we exclude image forces as a reason for the reduced occurrence of “mature” cell walls in the bi-crystal.
- In the single crystal micropillars, TEM characterization of individual dislocations confirmed the activation of slip systems with the highest Schmid factors. Furthermore, it was observed that the cell walls in the single-crystal micropillar with higher accumulated plastic strain exhibit a denser and compact character due to a high density of dislocations confined within the walls. Tangled dislocations resulting from dislocation/dislocation interactions have been frequently observed in the single crystal micropillars indicating that the cell walls are initially formed by the accumulation of locks and junctions.

- Sharp local lattice rotations on the position of the dislocation walls were observed using ACOM-TEM. Also, nanostrain mapping in the single crystal micropillars revealed local strain fields associated to the dislocation walls. Direct correlation between the cell walls and local lattice rotations and strain fields in the unconstrained part of the micropillars indicates the presence of GNDs at the walls. The existence of GNDs and the associated heterogeneities including long range internal stresses are expected to play an important role in the activation of cross-slip and further storage of dislocations at the walls. These results also underline the role of the GB to impede crystal rotation accompanying the formation of dislocation patterns in the bi-crystal micropillars, which can be attributed to the different anisotropic elastic/plastic properties of the crystals on both sides of the boundary.

Chapter 7:

Summary and perspectives

Summary and perspectives

Interesting properties and promising applications of small-scale devices and materials, i.e., micro and nano-electronic devices, MEMS devices and nanomaterials, have made them increasingly important for science and technology. One of the important considerations about such scale materials and devices is mechanical reliability which has received considerable attention in recent years. After the advent of various nanomechanical testing techniques, many investigations have been performed to understand the mechanical response of such small-scale materials and devices.

Most of nanomechanical testing techniques should be performed in a microscope according to the small size of the samples. Fortunately, this allows studying different aspects of the response of the materials during the experiments. For instance, the morphological changes, the crystallographic orientation changes and the chemical composition on the sample surfaces can be studied by SEM during nanomechanical testing. In TEM, in addition to chemical and crystallographic orientation analyses, the direct observation of dynamics of defects inside the sample during the nanomechanical testing is possible.

Among the combination of microscopy techniques (SEM, (S)TEM and X-Ray microscopes), and nanomechanical testing methods (micropillar compression, bending, and tension tests) the in-situ SEM micropillar compression test is the most common one due to the availability of instruments, the ease of the experiment and the ease of the sample preparation. However, in this technique, direct observation of the mechanisms is not possible while the interpretation of the mechanical results remains a complex matter.

In terms of studying the mechanisms and also the complexity of interpreting the mechanical results, in-situ TEM nanotensile test is an interesting alternative. On the one hand, TEM allows the direct and in-situ investigation of mechanisms. On the other hand, uniaxial loading conditions of tensile tests facilitate the interpretation of the tensile test results when compared to the other nanomechanical testing techniques. However, the technical difficulties of sample preparation and of the experiments as such have made in-situ TEM nanotensile testing less common.

In this thesis, this testing method has been used to investigate the mechanical properties and also to study the plasticity mechanisms in small-scale pure nickel samples. Nickel has been chosen since it has been widely used in small-scale technologies, for example in MEMS

devices or in antireflection stamps, and its properties, such as cheap and easy fabrication methods and physical and mechanical properties, made it a certain candidate for further applications in small-scale technologies.

FIB is the most common technique used for sample preparation for TEM nanomechanical testing. In spite of FIB's unique capabilities such as site-specificity and design-ability, it has been shown that FIB might induce defects on the sample surfaces which may influence the mechanical response of the samples as well as the deformation mechanisms. Furthermore, FIB-induced defects can block the view on the ongoing mechanisms in the samples during in-situ TEM experiments. In the literature, few other sample preparation methods (mainly chemical-based processes) allowing preparing in-situ TEM tensile samples without FIB damages have been used; however, these methods are very dedicated (specific types of samples and for specific types of materials) and do not have the site-specificity and design-ability of FIB and can thus not be used widely. Therefore, the first step for performing quantitative in-situ TEM nanotensile testing was to develop a novel sample preparation method which retains the design-ability of FIB and at the same time enables to produce tensile samples with a minimum amount of FIB-induced defects near the surface.

In chapter 3, a combination of twin-jet electro-polishing and FIB was used to prepare in-situ TEM nanotensile test samples. The former was used to thin the samples to electron transparency while the latter FIB step was mainly used to cut the edges. This combination allows designing and preparing tensile samples with preselected crystallographic orientation and defects, e.g., dislocation density, pre-defined grain boundaries. Although the centre of the tensile sample was nearly free of FIB induced artefacts, a Ga-rich layer, long dislocations and dislocation loops have been induced at the edges of the sample due to the FIB cut. The prepared sample containing FIB-induced defects at the edges was then used for quantitative in-situ TEM tensile testing to study the role of such defects in the plasticity. The test revealed that, in the lack of genuine dislocation sources, FIB-induced dislocations loops controlled the plastic deformation. High yield stress and high strain hardening capacity were observed and attributed to opening of the dislocation loops with different sizes (i.e., the smaller loops need higher stress to open than larger ones).

In chapter 4, the mentioned sample preparation method was improved by an in-situ TEM heating step to anneal out the remaining FIB-induced defects generated at the edges of the sample. The results showed that during heat treatment, the FIB induced dislocations tend to

form new long perfect dislocations before annihilating at the free surface. Depending on the heating temperature and time, it is possible to obtain samples with different well-controlled densities of dislocations. In contrast with samples that did not undergo a heat treatment, homogenous low-concentration of Ga atoms was detected all over the sample due to the high diffusion of Ga atoms at high temperatures. Therefore, the new sample preparation method offers the site-specificity and design-ability of FIB and the cleanliness of other techniques.

Smaller is stronger is the general conclusion of many studies which have been done by nanomechanical testing techniques on metallic single crystal samples. Moreover, it has been shown that the values for the strength of samples of a given size are stochastically distributed and the plastic flow is jerky. In general, the reasons for such behaviour are not yet totally understood because of the lack of quantitative in-situ TEM nanomechanical testing on clean single crystal samples. Therefore, in order to investigate the intrinsic elementary mechanisms controlling the plasticity and the failure in single crystal samples, a clean tensile sample with very few dislocations was prepared and deformed inside a TEM. The results interestingly showed strain hardening during the operation of an individual SAS. It was shown that operation of the SAS shrinkages the slip plane area, which decreases the length of the active SAS. Therefore, strain hardening was attributed to the shortening of the length of the SAS while operating. In addition, a scenario accounting for the sample geometry evolution associated to SAS dynamics was proposed to explain the origin of the staircase behaviour observed in the tensile test under load control mode. The scenario involves the contribution of a stress overshoot for the activation of the SAS. This discovery highlights the key importance, beyond standard crystal orientation and boundary definitions, of accurate 3D measures of the sample geometry evolution during micro-mechanical tests when applied to small samples.

The role of GBs in strengthening of polycrystalline materials is very well-known and well-proved and for decades, mainly in-situ TEM deformation experiments have been used to unravel the governing mechanisms for this phenomenon. Though many mechanisms and interactions (interaction of dislocations with interfaces) have been observed and qualitatively investigated, because of technological barriers and sample preparation problems, these mechanisms have not been yet quantitatively investigated by TEM. Our new sample preparation method allows investigating this important issue by yielding a clean bi-crystal tensile sample with a desired type of GB. This type of samples can also be used to investigate the role of individual GBs on the mechanical response of small-scale materials.

CTBs are a common type of GB in FCC metals and it has been observed that metals with a high density of such boundaries manifest the concurrent improved strength and ductility but the reasons for such behaviour are not yet totally understood. In chapter 5, in order to investigate the interaction of dislocations with a CTB, a bi-crystal tensile sample containing a CTB parallel to the tensile direction was prepared by the new sample preparation. Quantitative in-situ TEM nanotensile testing showed a transition from slip transmission to dislocation absorption during the interaction of screw dislocations with the CTB. The origin of such behaviour was attributed to local geometrical changes that might occur during the transmission process which can change the resolved shear stress in the CTB plane and/or of the local stress state in the dislocation/CTB intersection point. It was also observed that the absorbed dislocations in the CTB dissociate into paired glissile twinning dislocations that glide in the same direction leading to TB sliding rather than TB migration. Furthermore, the elastic repulsive interaction of a non-screw dislocation with the CTB was observed and the image force stress of the CTB on the dislocation was extracted. Finally, the fracture of the bi-crystal from a pre-existing ledge highlights the significance of these defects in the failure of the twinned materials.

Small-scale devices might experience internal or external cyclic loading conditions during service and it is very important to understand the response of small-scale materials under such loading conditions. In spite of many investigations on the behaviour of small-scale materials under monotonic loading condition, few studies have been done on the behaviour of such scale materials under cyclic loading condition. Therefore, in chapter 6 attempts have been made to investigate the evolution of dislocation structures in cyclically deformed small-scale Ni samples using both conventional and advanced TEM techniques. Single crystal and bi-crystal Ni micropillars were cyclically deformed in a SEM and were investigated by TEM. The observed 'mature' dislocation cell walls in the single crystal samples and their absence in the bi-crystal sample were in agreement with higher accumulated plastic strain in the single crystal micropillars compared to the bi-crystal. This also confirms the role of the dislocation mean free path in the size dependency for the formation of dislocation patterns in cyclically deformed micropillars. Such behaviour has been previously reported in DD simulations for which our results provide new experimental evidences. The computational analysis also showed that, for the specific experimental conditions used in this work, the role of the image forces is negligible in the formation (or not) of dislocation structures in the bi-crystal sample. Sharp local lattice rotations and local strain fields associated at the position of the dislocation

walls revealed the presence of GNDs which are expected to play an important role in the activation of cross-slip and further storage of dislocations at the walls. The quantitative character of the observations opens windows for direct comparison with DD simulations, not addressed before in the literature.

Based on the above results, different interesting perspectives can be suggested. The new novel sample preparation offers new opportunities to investigate quantitatively the micro-nanoscale plasticity mechanisms without the omnipresent FIB damages. Several possibilities can be envisaged:

1- Investigating materials with controlled amount of Ga in order to improve our understanding of solid solution strengthening in small-sized systems. The effect of Ga on the stacking fault energy could also be analysed.

2- Investigating materials with pre-selected microstructure (i.e., crystallographic orientation and imaging conditions, dislocations and precipitate density, single or multiple interfaces including grain and phase boundaries, etc.)

3- Combining the method with different loading modes, e.g., (cyclic) tensile test, shear test, and bending test.

Although this work showed the powerful capability of in-situ TEM nanotensile testing to investigate and to study the governing mechanisms in small-scale samples, it should be considered that this technique can only be used for electron transparent samples (samples with a maximum thickness of ~300 nm). Furthermore, according to the different steps used in the sample preparation, the new sample preparation is applicable only on conductive materials which are required for twin-jet electro-polishing. Furthermore, due to the heat treatment step, the microstructure of the sample should not experience any permanent changes, such as phase transformations or precipitation during the heat treatment. Therefore, pure metals and thermodynamically stable solid solution alloys are preferred.

Although in terms of FIB induced damages the quality of the samples has been improved, there are still some other problems which should be considered and improved. The mounting step (installing a sample on a PTP device by a micromanipulator) is very prone to (rotational) misalignment. Furthermore, since the sample is mounted on the top surface of the PTP, out of the plane of PTP springs, (transverse) misalignment is very likely on the sample. All in all, these types of misalignment can cause considerable changes of the loading condition (mixture

of bending and tension) in the sample and should be taken into account when these results are compared with simulations.

It is also worth noting that complete characterization of the nature of the defects and their 3D arrangement near the free surface before and during in-situ TEM deformation would open windows for more accurate comparison with DD and MD simulations. In this context, recent advances of tilt-less 3D electron imaging and reconstruction of dislocations can be very promising. Such experiments could reveal new information about the defects' behaviour and their interaction mechanisms during deformation. Furthermore, the size, the well-defined shape and the well-designed loading condition of the samples enable a full size numerical simulation of such experiments which helps to discover more details of the actual mechanisms occurring during the experiment.

Samenvatting en perspectieven

Dit proefschrift richt zich op kwantitatieve nanomechanische TEM experimenten. Een eerste stap van het onderzoeksproces was het ontwikkelen van een nieuwe specimenbereidingsmethode om kleinschalige defectvrije FIB stalen te maken, specifiek voor kwantitatieve in-situ TEM nanomechanische treksterkte testen. De methode werd toegepast op pure nikkel monokristal- en bikristal treksterkte stalen om de intrinsieke elementaire mechanismen te onderzoeken die de plasticiteit en het falen van deze systemen bepalen. Bij het monokristallijne specimen concentreerden wij ons op het verband tussen de activering en werking van individuele enkele arm bronnen en de stapsgewijze plastische vloeijing. Wat betreft het bikristallijne specimen zijn inspanningen geleverd om de mechanismen, die de interacties tussen dislocaties en coherente tweelinggrenzen bepalen, op een kwantitatieve manier te ontrafelen. Tot slot werden de mechanismen onderzocht die betrokken zijn bij de vorming van dislocatiepatronen in cyclisch vervormde monokristallijne en bikristallijne nikkel micropilaren via het gebruik van zowel conventionele als geavanceerde TEM-technieken.

Eerst werd een combinatie van tweelingjet elektro-polijsten en FIB gebruikt om in situ TEM nanomechanische treksterkte proeven voor te bereiden. De eerstgenoemde methode werd gebruikt om de samples te verdunnen tot elektron transparantie terwijl de laatstgenoemde hoofdzakelijk werd gebruikt om de randen te snijden. Deze combinatie staat het vormgeven en voorbereiden toe van treksterkte stalen met vooraf geselecteerde kristallografische oriëntatie en defecten, zoals bijvoorbeeld dislocatiedichtheid of vooraf bepaalde korrelgrenzen. Hoewel het centrum van het treksterkte staal nagenoeg vrij was van FIB veroorzaakte artifacten, bevatten de randen van het specimen nog lange dislocaties, dislocatiekringen en een Ga-rijke laag, geïnduceerd door het FIB snijwerk. De in-situ TEM treksterkte testen van deze stalen toonden aan dat de geïnduceerde dislocatiekringen deelnemen in de vervorming, bij gebrek aan intrinsieke dislocatiebronnen. Voorts werd versteviging waargenomen en toegeschreven aan het verschil in afmetingen tussen de kringen (de kleinere kringen vergen namelijk een hogere stress om te groeien dan de grotere kringen).

Daarna werd de bovengenoemde bereidingsmethode verbeterd door een in-situ TEM-opwarmingsstap toe te voegen. Deze nieuwe stap werd geïntroduceerd om de FIB-gerelateerde defecten tijdens het snijden aan de randen te verwijderen. De resultaten toonden aan dat de door FIB veroorzaakte dislocaties ernaar neigen nieuwe lange perfecte dislocaties

te vormen tijdens deze thermische behandeling voor ze aan het vrije oppervlak verdwijnen. Afhankelijk van de verhitings temperatuur en -tijd is het zo mogelijk om specimens met verschillende dislocatiedichtheden te verkrijgen. In tegenstelling tot stalen die geen thermische behandeling ondergingen, werd een homogene lage concentratie van Ga-atomen gevonden in het volledige specimen, die toe te schrijven is aan de sterke diffusie van Ga-atomen bij hoge temperaturen. Vervolgens werd een monokristallijn staal met zeer weinig dislocaties vervormd m.b.v. in-situ TEM. De resultaten hiervan tonen versteviging aan. Dit is een gevolg van het krimpen van het slip vlak, hetgeen is toe te schrijven aan de activering van één enkele arm bron (SAS). Om de oorsprong van het trapsgewijs-gedrag te verklaren die in de treksterkte test werd waargenomen in de gecontroleerde belastingsmode, werd een scenario voorgesteld voor de evolutie van de staalgeometrie gekoppeld aan de SAS dynamica. Dit scenario impliceert de bijdrage van een te hoge stress voor de activering van de SAS. Deze ontdekking benadrukt, afgezien van standaard kristallografische oriëntatie en grensdefinities, het grote belang van nauwkeurige 3D-metingen tijdens de geometrische evolutie van het sample bij micro-mechanische tests op kleine samples.

Om de interactie van dislocaties met een coherente tweelinggrens (CTG) te onderzoeken, werd een bikristallijn treksterkte staal voorbereid met een CTG parallel aan de trekrichting. De kwantitatieve in-situ TEM nanomechanische treksterkte tests toonden een overgang van slip transmissie naar dislocatieabsorptie tijdens de interactie van schroefdislocaties met de CTG. De oorsprong van dergelijk gedrag werd toegeschreven aan lokale geometrische veranderingen die kunnen voorkomen tijdens het transmissieproces. Er werd opgemerkt dat de geabsorbeerde dislocaties in het CTG dissociëren in gepaarde Shockley partiële dislocaties. Zij bewegen in dezelfde zin en resulteren zo in het glijden eerder dan in de migratie van de tweelinggrens. Voorts werd de elastische interactie van een niet-schroefdislocatie met de CTG waargenomen en de beeldkracht stress van de CTG op de dislocatie werd gemeten. Tot slot benadrukt de breuk van het bikristallijn staal aan een vooraf bestaande richel het belang dat deze defecten kunnen hebben in het falen van materialen met een tweelinggrens.

In-situ SEM cyclisch vervormde mono- en bikristallijne Ni micropilaren werden gebruikt om de kenmerken van dislocatiestructuren te onderzoeken. De waargenomen “volwassen” dislocatiecelwanden in de monokristallijne stalen en hun afwezigheid in de bikristallijn specimen waren in overeenstemming met de relatief hogere geaccumuleerde plastische spanning in de monokristallijne micropilaren ten opzichte van het bikristal. Dit bevestigt ook

de rol van de gemiddelde vrije weglengte van de dislocaties in de afhankelijkheid van de afmetingen van het staal voor de vorming van dislocatiepatronen in cyclisch vervormde micropilaren. Dergelijk gedrag is al eerder gemeld in DD simulaties waarvoor onze resultaten nieuwe experimentele bewijzen leveren. De computationele analyse toonde ook aan dat, voor de specifieke experimentele voorwaarden die in dit werk worden gehanteerd, de rol van de beeldkrachten te verwaarlozen is in de al dan niet vorming van dislocatiestructuren in het bikristallijn staal. De scherpe lokale roosterrotaties en lokale spanningsvelden op de positie van de dislocatiemuren toonden de aanwezigheid van GNDs. Deze worden verondersteld een belangrijke rol te spelen in de activering van kruiselingse slip en verdere opslag van dislocaties ter hoogte van de muren. Het kwantitatieve karakter van de observaties opent mogelijkheden voor directe vergelijking met DD simulaties, wat nog niet eerder in de literatuur is aangetoond.

Gebaseerd op de bovengenoemde resultaten kunnen verschillende interessante perspectieven worden voorgesteld. De vernieuwende specimenbereiding biedt nieuwe kansen om de micro-nanoschaal plasticiteitsmechanismen kwantitatief te onderzoeken zonder alomtegenwoordige FIB-schade. Verscheidene mogelijkheden kunnen worden overwogen:

- Het onderzoeken van materialen met een gecontroleerde hoeveelheid Ga om ons begrip van de versterking van solide oplossingen in kleine systemen te verbeteren. Het effect van Ga op de stapelfoutenergie zou ook kunnen worden geanalyseerd.
- Het onderzoeken van materialen met een vooraf geselecteerde microstructuur (zoals kristallografische oriëntatie, dislocaties en precipitatendichtheid, enkele of meervoudige grensvlakken zoals korrel- en fasegrenzen, enz.) en beeldvormingsvoorwaarden
- Het combineren van de nieuwe bereidingsmethode met verschillende belastingsmodes, zoals (cyclische) treksterkte, schuifspanning en buigingstest.

Het is ook vermeldenswaardig dat een volledige karakterisering van de aard van de defecten en hun 3D arrangement dichtbij de vrije oppervlakte vóór en tijdens in-situ TEM-vervorming mogelijkheden zou openen voor nauwkeurigere vergelijkingen met DD en MD simulaties. In deze context kan de recente vooruitgang veelbelovend zijn voor niet-roterende 3D elektronenbeeldvorming en de reconstructie van dislocaties. Dergelijke experimenten zouden nieuwe informatie kunnen geven over het gedrag van de defecten en hun onderlinge interactiemechanismen tijdens de vervorming. Voorts maken de grootte, de duidelijk

omlijnde vorm en de in detail bepaalde belastingsconditie van de stalen een volledige numerieke simulatie mogelijk van dergelijke experimenten. Dit helpt om meer details te ontdekken van de mechanismen die voorkomen tijdens het experiment.

References

- [1] S.W. Lee, The Plasticity of Metals at The Sub-Micronmeter Scale and Dislocation Dynamics in A Thin Film Materials Science and Engineering, Stanford University, 2011, p. 162.
- [2] C.M. Lieber, Nanoscale Science and Technology: Building a Big Future from Small Things, MRS Bulletin 28(7) (2011) 486-491.
- [3] P. Yang, The Chemistry and Physics of Semiconductor Nanowires, MRS Bulletin 30(2) (2011) 85-91.
- [4] H. Guo, K. Chen, Y. Oh, K. Wang, C. Dejoie, S.A. Syed Asif, O.L. Warren, Z.W. Shan, J. Wu, A.M. Minor, Mechanics and Dynamics of the Strain-Induced M1–M2 Structural Phase Transition in Individual VO₂ Nanowires, Nano Letters 11(8) (2011) 3207-3213.
- [5] E. Kapon, D.M. Hwang, R. Bhat, Stimulated emission in semiconductor quantum wire heterostructures, Physical Review Letters 63(4) (1989) 430-433.
- [6] Y.B. Wang, L.F. Wang, H.J. Joyce, Q. Gao, X.Z. Liao, Y.W. Mai, H.H. Tan, J. Zou, S.P. Ringer, H.J. Gao, C. Jagadish, Super Deformability and Young's Modulus of GaAs Nanowires, Advanced Materials 23(11) (2011) 1356-1360.
- [7] L. Wang, P. Liu, P. Guan, M. Yang, J. Sun, Y. Cheng, A. Hirata, Z. Zhang, E. Ma, M. Chen, X. Han, In situ atomic-scale observation of continuous and reversible lattice deformation beyond the elastic limit, Nat Commun 4 (2013).
- [8] P. Bao, Y. Wang, X. Cui, Q. Gao, H.-W. Yen, H. Liu, W.K. Yeoh, X. Liao, S. Du, H.H. Tan, C. Jagadish, J. Zou, S.P. Ringer, R. Zheng, Atomic-scale observation of parallel development of super elasticity and reversible plasticity in GaAs nanowires, Applied Physics Letters 104(2) (2014) 021904.
- [9] Y. Cui, Q. Wei, H. Park, C.M. Lieber, Nanowire Nanosensors for Highly Sensitive and Selective Detection of Biological and Chemical Species, Science 293(5533) (2001) 1289-1292.
- [10] J. Hahm, C.M. Lieber, Direct Ultrasensitive Electrical Detection of DNA and DNA Sequence Variations Using Nanowire Nanosensors, Nano Letters 4(1) (2004) 51-54.
- [11] X. Wang, J. Song, J. Liu, Z.L. Wang, Direct-Current Nanogenerator Driven by Ultrasonic Waves, Science 316(5821) (2007) 102-105.
- [12] M.H. Huang, S. Mao, H. Feick, H. Yan, Y. Wu, H. Kind, E. Weber, R. Russo, P. Yang, Room-Temperature Ultraviolet Nanowire Nanolasers, Science 292(5523) (2001) 1897-1899.
- [13] M.D. Uchic, D.M. Dimiduk, J.N. Florando, W.D. Nix, Sample Dimensions Influence Strength and Crystal Plasticity, Science 305(5686) (2004) 986-989.
- [14] M. Uchic, P. Shade, D. Dimiduk, Micro-compression testing of fcc metals: A selected overview of experiments and simulations, JOM 61(3) (2009) 36-41.
- [15] G. Dehm, B.N. Jaya, R. Raghavan, C. Kirchlechner, Overview on micro- and nanomechanical testing: New insights in interface plasticity and fracture at small length scales, Acta Materialia 142(Supplement C) (2018) 248-282.
- [16] G. Galilei, Dialogues Concerning Two New Sciences. <http://oll.libertyfund.org/titles/galilei-dialogues-concerning-two-new-sciences>, 1952).
- [17] E. Arzt, Size effects in materials due to microstructural and dimensional constraints: a comparative review, Acta Materialia 46(16) (1998) 5611-5626.
- [18] Y. Xiang, J.J. Vlassak, Bauschinger and size effects in thin-film plasticity, Acta Materialia 54(20) (2006) 5449-5460.
- [19] W.D. Nix, H. Gao, Indentation size effects in crystalline materials: A law for strain gradient plasticity, J. Mech. Phys. Solids 46(3) (1998) 411-425.
- [20] W.W. Gerberich, J. Michler, W.M. Mook, R. Ghisleni, F. Östlund, D.D. Stauffer, R. Ballarini, Scale effects for strength, ductility, and toughness in "brittle" materials, Journal of Materials Research 24(3) (2011) 898-906.

- [21] Y. Chen, Q. Gao, Y. Wang, X. An, X. Liao, Y.-W. Mai, H.H. Tan, J. Zou, S.P. Ringer, C. Jagadish, Determination of Young's Modulus of Ultrathin Nanomaterials, *Nano Letters* 15(8) (2015) 5279-5283.
- [22] D.-M. Tang, C.-L. Ren, M.-S. Wang, X. Wei, N. Kawamoto, C. Liu, Y. Bando, M. Mitome, N. Fukata, D. Golberg, Mechanical Properties of Si Nanowires as Revealed by in Situ Transmission Electron Microscopy and Molecular Dynamics Simulations, *Nano Letters* 12(4) (2012) 1898-1904.
- [23] F. Xu, Q. Qin, A. Mishra, Y. Gu, Y. Zhu, Mechanical properties of ZnO nanowires under different loading modes, *Nano Research* 3(4) (2010) 271-280.
- [24] J.K. Luo, A.J. Flewitt, S.M. Spearing, N.A. Fleck, W.I. Milne, Young's modulus of electroplated Ni thin film for MEMS applications, *Materials Letters* 58(17) (2004) 2306-2309.
- [25] T. Du, A. Vijayakumar, K.B. Sundaram, V. Desai, Chemical mechanical polishing of nickel for applications in MEMS devices, *Microelectronic Engineering* 75(2) (2004) 234-241.
- [26] H. Foll, Defects in Crystals. http://www.tf.uni-kiel.de/matwis/amat/def_en/overview_main.html, 2018).
- [27] Laureate, 50 Years of Transmission Electron Microscopy of Dislocations: Past, Present, and Future, *Herald of the Russian Academy of Sciences* 76(5) (2006) 7.
- [28] P.B. Hirsch, Direct Observations of moving dislocations: Reflections on the thirtieth anniversary of the first recorded observations of moving dislocations by transmission electron microscopy, *Materials Science and Engineering* 84(0) (1986) 1-10.
- [29] D. Hull, D.J. Bacon, *Introduction to Dislocations*, Fifth ed., Butterworth-Heinemann, Oxford, 2011.
- [30] G.M. Morais Gaspar, A. Autruffe, J. Mário Pó, Silicon Growth Technologies for PV Applications, in: V.I. Talanin (Ed.), *New Research on Silicon*, IntechOpen2017.
- [31] linear_defects. https://www.nde-ed.org/EducationResources/CommunityCollege/Materials/Structure/linear_defects.htm, 2018).
- [32] M.S. Duesbery, Dislocation motion, constriction and cross slip in fcc metals, *Modelling and Simulation in Materials Science and Engineering* 6 (1998) 35-49.
- [33] Geometrically necessary dislocations. (https://en.wikipedia.org/wiki/Geometrically_necessary_dislocations), 2018).
- [34] J. Kacher, B.P. Eftink, B. Cui, I.M. Robertson, Dislocation interactions with grain boundaries, *Current Opinion in Solid State and Materials Science* 18(4) (2014) 227-243.
- [35] W.A. Soer, *Interactions between Dislocations and Grain Boundaries*, 2006, p. 35.
- [36] L. Priester, *Grain Boundaries From Theory to Engineering*, springer2013.
- [37] G.C. Hasson, C. Goux, Interfacial energies of tilt boundaries in aluminium. Experimental and theoretical determination, *Scripta Metallurgica* 5(10) (1971) 889-894.
- [38] D.L. Medlin, C.B. Carter, J.E. Angelo, M.J. Mills, Climb and glide of $a/3$ $\langle 111 \rangle$ dislocations in an aluminium $\Sigma = 3$ boundary, *Philosophical Magazine A* 75(3) (1997) 733-747.
- [39] J.W. Christian, S. Mahajan, Deformation twinning, *Progress in Materials Science* 39(1) (1995) 1-157.
- [40] Y.B. Wang, M.L. Sui, Atomic-scale in situ observation of lattice dislocations passing through twin boundaries, *Applied Physics Letters* 94(021909) (2009) 3.
- [41] T.C. Lee, I.M. Robertson, H.K. Birnbaum, TEM in situ deformation study of the interaction of lattice dislocations with grain boundaries in metals, *Philosophical Magazine A* 62(1) (1990) 131-153.
- [42] S. Kondo, T. Mitsuma, N. Shibata, Y. Ikuhara, Direct observation of individual dislocation interaction processes with grain boundaries, *Science Advances* 2(11) (2016).
- [43] Z.C. Cordero, B.E. Knight, C.A. Schuh, Six decades of the Hall–Petch effect – a survey of grain-size strengthening studies on pure metals, *International Materials Reviews* 61(8) (2016) 495-512.
- [44] P.J. Imrich, C. Kirchlechner, D. Kiener, G. Dehm, Internal and external stresses: In situ TEM compression of Cu bicrystals containing a twin boundary, *Scripta Materialia* 100(0) (2015) 94-97.
- [45] E.O. Hall, The Deformation and Ageing of Mild Steel: III Discussion of Results, *Proceedings of the Physical Society. Section B* 64(9) (1951) 747.

- [46] N.J. Petch, The Cleavage Strength of Polycrystals, *Journal of the Iron and Steel Institute* 174 (1953) 25-28.
- [47] M.A. Meyers, A. Mishra, D.J. Benson, Mechanical properties of nanocrystalline materials, *Progress in Materials Science* 51(4) (2006) 427-556.
- [48] J.R. Greer, J.T.M. De Hosson, Plasticity in small-sized metallic systems: Intrinsic versus extrinsic size effect, *Progress in Materials Science* 56(6) (2011) 654-724.
- [49] F. Moppiou, M. Legros, A. Sedlmayr, D.S. Gianola, D. Caillard, O. Kraft, Source-based strengthening of sub-micrometer Al fibers, *Acta Materialia* 60(3) (2012) 977-983.
- [50] D. Kiener, W. Grosinger, G. Dehm, R. Pippan, A further step towards an understanding of size-dependent crystal plasticity: In situ tension experiments of miniaturized single-crystal copper samples, *Acta Materialia* 56(3) (2008) 580-592.
- [51] S.-W. Lee, W.D. Nix, Geometrical analysis of 3D dislocation dynamics simulations of FCC micropillar plasticity, *Materials Science and Engineering: A* 527(7-8) (2010) 1903-1910.
- [52] L.C. Montemayor, L.R. Meza, J.R. Greer, Design and Fabrication of Hollow Rigid Nanolattices via Two-Photon Lithography, *Advanced Engineering Materials* 16(2) (2014) 184-189.
- [53] W.D. Callister Jr., D.G. Rethwisch, *Materials Science and Engineering: An Introduction*, 9th Edition, 9 ed., Wiley 2013.
- [54] M. Funk, *Microstructural stability of nanostructured FCC metals during cyclic deformation and fatigue*, KIT scientific publishing 2012.
- [55] A. Constantinescu, K. Dang Van, M.H. Maitournam, A unified approach for high and low cycle fatigue based on shakedown concepts, *fatigue fract engng mater structur* 26 (2003) 8.
- [56] X.-W. Li, Monotonic and cyclic deformation in single crystals, in: Q.J. Wang, Y.-W. Chung (Eds.), *Encyclopedia of Tribology*, SPRINGER 2013.
- [57] M. Sauzay, L.P. Kubin, Scaling laws for dislocation microstructures in monotonic and cyclic deformation of fcc metals, *Progress in Materials Science* 56 (2011) 725-784.
- [58] S. Suresh, *Fatigue of Materials*, Cambridge University Press 2004.
- [59] H. Mughrabi, The cyclic hardening and saturation behaviour of copper single crystals, *Materials Science and Engineering* 33(2) (1978) 207-223.
- [60] H. Mughrabi, F. Ackermann, K. Herz, Persistent slip bands in fatigued face-centered and body-centered cubic metals, *Fatigue Mechanisms*. 675 (1979).
- [61] F. Fröhlich, P. Grau, W. Grellmann, Performance and analysis of recording microhardness tests, *physica status solidi (a)* 42(1) (1977) 79-89.
- [62] G. Binnig, H. Rohrer, C. Gerber, E. Weibel, *Surface Studies by Scanning Tunneling Microscopy*, *Physical Review Letters* 49(1) (1982) 57-61.
- [63] 2018, How a Nanoindenter Works. <https://www.nanoscience.com/technology/mechanical-testing-technology/how-nanoindenter-works/>.
- [64] B. Bhushan, *Springer Handbook of Nanotechnology*, SPRINGER 2017.
- [65] G. Dan, X. Guoxin, L. Jianbin, Mechanical properties of nanoparticles: basics and applications, *Journal of Physics D: Applied Physics* 47(1) (2014) 013001.
- [66] M. Griepentrog, G. Krämer, B. Cappella, Comparison of nanoindentation and AFM methods for the determination of mechanical properties of polymers, *Polymer Testing* 32(3) (2013) 455-460.
- [67] R. Maaß, P.M. Derlet, Micro-plasticity and recent insights from intermittent and small-scale plasticity, *Acta Materialia* 143 (2018) 338-363.
- [68] B. Almangour, J.-M. Yang, Understanding the deformation behavior of 17-4 precipitate hardenable stainless steel produced by direct metal laser sintering using micropillar compression and TEM, *The International Journal of Advanced Manufacturing Technology* 90(1) (2017) 119-126.
- [69] W. Chen, J. Zhang, S. Cao, Y. Pan, M. Huang, Q. Hu, Q. Sun, L. Xiao, J. Sun, Strong deformation anisotropies of ω -precipitates and strengthening mechanisms in Ti-10V-2Fe-3Al alloy micropillars: Precipitates shearing vs precipitates disordering, *Acta Materialia* 117 (2016) 68-80.

- [70] P.J. Imrich, C. Kirchlechner, C. Motz, G. Dehm, Differences in deformation behavior of bicrystalline Cu micropillars containing a twin boundary or a large-angle grain boundary, *Acta Materialia* 73(0) (2014) 240-250.
- [71] N. Kheradmand, H. Vehoff, Orientation Gradients at Boundaries in Micron-Sized Bicrystals, *Advanced Engineering Materials* 14(3) (2012) 153-161.
- [72] K.S. Ng, A.H.W. Ngan, Deformation of micron-sized aluminium bi-crystal pillars, *Philosophical Magazine* 89(33) (2009) 3013-3026.
- [73] A. Kunz, S. Pathak, J.R. Greer, Size effects in Al nanopillars: Single crystalline vs. bicrystalline, *Acta Materialia* 59(11) (2011) 4416-4424.
- [74] N.V. Malyar, J.S. Micha, G. Dehm, C. Kirchlechner, Dislocation-twin boundary interaction in small scale Cu bi-crystals loaded in different crystallographic directions, *Acta Materialia* 129(Supplement C) (2017) 91-97.
- [75] R. Raghavan, J.M. Wheeler, D. Esqué-de los Ojos, K. Thomas, E. Almandoz, G.G. Fuentes, J. Michler, Mechanical behavior of Cu/TiN multilayers at ambient and elevated temperatures: Stress-assisted diffusion of Cu, *Materials Science and Engineering: A* 620 (2015) 375-382.
- [76] J.M. Wheeler, R. Raghavan, V. Chawla, J. Zechner, I. Utke, J. Michler, Failure mechanisms in metal-metal nanolaminates at elevated temperatures: Microcompression of Cu-W multilayers, *Scripta Materialia* 98 (2015) 28-31.
- [77] B.N. Jaya, C. Kirchlechner, G. Dehm, Can microscale fracture tests provide reliable fracture toughness values? A case study in silicon, *Journal of Materials Research* 30(5) (2015) 686-698.
- [78] F. Iqbal, J. Ast, M. Göken, K. Durst, In situ micro-cantilever tests to study fracture properties of NiAl single crystals, *Acta Materialia* 60(3) (2012) 1193-1200.
- [79] Z.-P. Luo, G.-P. Zhang, R. Schwaiger, Microstructural vortex formation during cyclic sliding of Cu/Au multilayers, *Scripta Materialia* 107 (2015) 67-70.
- [80] K.A. Rzepiejewska-Malyska, W.M. Mook, M. Parlinska-Wojtan, J. Hejduk, J. Michler, In situ scanning electron microscopy indentation studies on multilayer nitride films: Methodology and deformation mechanisms, *Journal of Materials Research* 24(3) (2011) 1208-1221.
- [81] B. Yang, C. Motz, W. Grosinger, W. Kamrath, G. Dehm, Tensile behaviour of micro-sized copper wires studied using a novel fibre tensile module, *International Journal of Materials Research* 99(7) (2008) 716-724.
- [82] C. Motz, T. Schöberl, R. Pippan, Mechanical properties of micro-sized copper bending beams machined by the focused ion beam technique, *Acta Materialia* 53(15) (2005) 4269-4279.
- [83] D.S. Gianola, A. Sedlmayr, R. Mönig, C.A. Volkert, R.C. Major, E. Cyranowski, S.A.S. Asif, O.L. Warren, O. Kraft, In situ nanomechanical testing in focused ion beam and scanning electron microscopes, *Review of Scientific Instruments* 82(6) (2011) 063901.
- [84] M.A. Haque, M.T.A. Saif, A review of MEMS-based microscale and nanoscale tensile and bending testing, *Experimental Mechanics* 43(3) (2003) 248-255.
- [85] S. Gupta, O.N. Pierron, MEMS based nanomechanical testing method with independent electronic sensing of stress and strain, *Extreme Mechanics Letters* 8 (2016) 167-176.
- [86] M.-T. Lin, C.-J. Tong, K.-S. Shiu, Novel Microtensile Method for Monotonic and Cyclic Testing of Freestanding Copper Thin Films, *Experimental Mechanics* 50(1) (2010) 55-64.
- [87] T. Pardoën, M.-S. Colla, H. Idrissi, B. Amin-Ahmadi, B. Wang, D. Schryvers, U.K. Bhaskar, J.-P. Raskin, A versatile lab-on-chip test platform to characterize elementary deformation mechanisms and electromechanical couplings in nanoscopic objects, *Comptes Rendus Physique* 17(3) (2016) 485-495.
- [88] Y. Oh, E. Cyranowski, Z. Shan, S.A.S. Asif, Micro/nano-mechanical test system employing tensile test holder with push-to-pull transformer Hysitron Incorporated, USA, 2013.
- [89] D. Kiener, C. Motz, M. Rester, M. Jenko, G. Dehm, FIB damage of Cu and possible consequences for miniaturized mechanical tests, *Materials Science and Engineering: A* 459(1-2) (2007) 262-272.

- [90] S. Shim, H. Bei, M.K. Miller, G.M. Pharr, E.P. George, Effects of focused ion beam milling on the compressive behavior of directionally solidified micropillars and the nanoindentation response of an electropolished surface, *Acta Materialia* 57(2) (2009) 503-510.
- [91] H. Zhang, B.E. Schuster, Q. Wei, K.T. Ramesh, The design of accurate micro-compression experiments, *Scripta Materialia* 54(2) (2006) 181-186.
- [92] R. Schwaiger, M. Weber, B. Moser, P. Gumbsch, O. Kraft, Mechanical assessment of ultrafine-grained nickel by microcompression experiment and finite element simulation, *Journal of Materials Research* 27(1) (2012) 266-277.
- [93] L.Y. Chen, M.-r. He, J. Shin, G. Richter, D.S. Gianola, Measuring surface dislocation nucleation in defect-scarce nanostructures, *Nat Mater* 14(7) (2015) 707-713.
- [94] Y. Chen, O. Kraft, M. Walter, Size effects in thin coarse-grained gold microwires under tensile and torsional loading, *Acta Materialia* 87 (2015) 78-85.
- [95] N.A. Fleck, G.M. Muller, M.F. Ashby, J.W. Hutchinson, Strain gradient plasticity: Theory and experiment, *Acta Metallurgica et Materialia* 42(2) (1994) 475-487.
- [96] D. Kiener, C. Motz, W. Grosinger, D. Weygand, R. Pippan, Cyclic response of copper single crystal micro-beams, *Scripta Materialia* 63(5) (2010) 500-503.
- [97] S. Zaeferrer, N.-N. Elhami, Theory and application of electron channelling contrast imaging under controlled diffraction conditions, *Acta Materialia* 75 (2014) 20-50.
- [98] D. Viladot, M. VÉRon, M. Gemmi, F. PeirÓ, J. Portillo, S. EstradÉ, J. Mendoza, N. Llorca-Isern, S. Nicolopoulos, Orientation and phase mapping in the transmission electron microscope using precession-assisted diffraction spot recognition: state-of-the-art results, *Journal of Microscopy* 252(1) (2013) 23-34.
- [99] C. Gammer, J. Kacher, C. Czarnik, O.L. Warren, J. Ciston, A.M. Minor, Local and transient nanoscale strain mapping during in situ deformation, *Applied Physics Letters* 109(8) (2016) 081906.
- [100] V.B. Ozdol, C. Gammer, X.G. Jin, P. Ercius, C. Ophus, J. Ciston, A.M. Minor, Strain mapping at nanometer resolution using advanced nano-beam electron diffraction, *Applied Physics Letters* 106(25) (2015) 253107.
- [101] P.J. Phillips, M.C. Brandes, M.J. Mills, M. De Graef, Diffraction contrast STEM of dislocations: Imaging and simulations, *Ultramicroscopy* 111(9) (2011) 1483-1487.
- [102] J. Miao, T. Ishikawa, B. Johnson, E.H. Anderson, B. Lai, K.O. Hodgson, High Resolution 3D X-Ray Diffraction Microscopy, *Physical Review Letters* 89(8) (2002) 088303.
- [103] R. Maaß, S. Van Petegem, C.N. Borca, H. Van Swygenhoven, In situ Laue diffraction of metallic micropillars, *Materials Science and Engineering: A* 524(1) (2009) 40-45.
- [104] A. Irastorza Lana In-situ Laue diffraction to follow dislocation patterning during fatigue, *ÉCOLE POLYTECHNIQUE FÉDÉRALE DE LAUSANNE*, 2016, p. 169.
- [105] M. Legros, in situ mechanical TEM: seeing and measuring under stress with electrons,, *Comptes Rendus Physique* 15 (2014) 224-240.
- [106] Hysitron. www.hysitron.com, 2018).
- [107] O.L. Warren, Z. Shan, S.A.S. Asif, E.A. Stach, J.W. Morris Jr, A.M. Minor, In situ nanoindentation in the TEM, *Materials Today* 10(4) (2007) 59-60.
- [108] A.M. Minor, S.A. Syed Asif, Z. Shan, E.A. Stach, E. Cyrankowski, T.J. Wyrobek, O.L. Warren, A new view of the onset of plasticity during the nanoindentation of aluminium, *Nat Mater* 5(9) (2006) 697-702.
- [109] A. Nafari, A. Danilov, H. Rödjegård, P. Enoksson, H. Olin, A micromachined nanoindentation force sensor, *Sensors and Actuators A: Physical* 123-124 (2005) 44-49.
- [110] J. Carpena-Núñez, D. Yang, J.-W. Kim, C. Park, L. F. Fonseca, Mechanical characterization of pristine and hydrogen-exposed palladium nanowires by in situ TEM, *Nanotechnology* 24(3) (2013) 035701.
- [111] Z. Liao, M. Gall, K.B. Yeap, C. Sander, A. Clausner, U. Muhle, J. Gluch, Y. Standke, O. Aubel, A. Beyer, M. Hauschildt, E. Zschech, In Situ Time-dependent Dielectric Breakdown in the Transmission

- Electron Microscope: A Possibility to Understand the Failure Mechanism in Microelectronic Devices, *Journal of visualized experiments : JoVE* (100) (2015) e52447.
- [112] Y. Lu, Y. Ganesan, J. Lou, A Multi-step Method for In Situ Mechanical Characterization of 1-D Nanostructures Using a Novel Micromechanical Device, *Experimental Mechanics* 50(1) (2010) 47-54.
- [113] F. Mompou, M. Legros, A. Boé, M. Coulombier, J.P. Raskin, T. Pardoën, Inter- and intragranular plasticity mechanisms in ultrafine-grained Al thin films: An in situ TEM study, *Acta Materialia* 61(1) (2013) 205-216.
- [114] M.A. Haque, M.T.A. Saif, In situ Tensile Testing of Nanoscale Freestanding Thin Films Inside a Transmission Electron Microscope, *Journal of Materials Research* 20(7) (2005) 1769-1777.
- [115] B. Wang, H. Idrissi, M. Galceran, M.S. Colla, S. Turner, S. Hui, J.P. Raskin, T. Pardoën, S. Godet, D. Schryvers, Advanced TEM investigation of the plasticity mechanisms in nanocrystalline freestanding palladium films with nanoscale twins, *International Journal of Plasticity* 37 (2012) 140-156.
- [116] M.S. Colla, B. Amin-Ahmadi, H. Idrissi, L. Malet, S. Godet, J.P. Raskin, D. Schryvers, T. Pardoën, Dislocation-mediated relaxation in nanograined columnar palladium films revealed by on-chip time-resolved HRTEM testing, *Nature Communications* 6 (2015) 5922.
- [117] Y. Zhu, H.D. Espinosa, An electromechanical material testing system for in situ electron microscopy and applications, *Proceedings of the National Academy of Sciences of the United States of America* 102(41) (2005) 14503-14508.
- [118] H.D. Espinosa, R.A. Bernal, T. Filleter, In Situ TEM Electromechanical Testing of Nanowires and Nanotubes, *Small* 8(21) (2012) 3233-3252.
- [119] C.B.C. David B. Williams Transmission Electron Microscopy.
- [120] s. Nicolopoulos, E.F. Rauch, M. Veron, B. Beausir, Novel EBSD-TEM like technique: texture analysis, orientation and phase maps on nanostructured materials.
- [121] F.J. Humphreys, Characterisation of fine-scale microstructures by electron backscatter diffraction (EBSD), *Scripta Materialia* 51(8) (2004) 771-776.
- [122] S. Zaefferer, On the formation mechanisms, spatial resolution and intensity of backscatter Kikuchi patterns, *Ultramicroscopy* 107(2) (2007) 254-266.
- [123] M.P. Vigouroux, V. Delaye, N. Bernier, R. Cipro, D. Lafond, G. Audoit, T. Baron, J.L. Rouvière, M. Martin, B. Chenevier, F. Bertin, Strain mapping at the nanoscale using precession electron diffraction in transmission electron microscope with off axis camera, *Applied Physics Letters* 105(19) (2014) 191906.
- [124] PI 95 TEM Picoindenter User Manual, in: H. incorporated (Ed.) 2011.
- [125] H. Idrissi, C. Bollinger, F. Boioli, D. Schryvers, P. Cordier, Low-temperature plasticity of olivine revisited with in situ TEM nanomechanical testing, *Science Advances* 2(3) (2016).
- [126] W. Kang, J.H. Han, M.T.A. Saif, A Novel Method for In Situ Uniaxial Tests at the Micro/Nanoscale—Part II: Experiment, *Journal of Microelectromechanical Systems* 19(6) (2010) 1322-1330.
- [127] W. Kang, M.T.A. Saif, A Novel Method for In Situ Uniaxial Tests at the Micro/Nano Scale—Part I: Theory, *Journal of Microelectromechanical Systems* 19(6) (2010) 1309-1321.
- [128] C.A. Volkert, A.M. Minor, Focused Ion Beam Microscopy and Micromachining, *MRS BULLETIN* 32 389-399.
- [129] S. Gravier, M. Coulombier, A. Safi, N. Andre, A. Boe, J.P. Raskin, T. Pardoën, New On-Chip Nanomechanical Testing Laboratory - Applications to Aluminum and Polysilicon Thin Films, *Journal of Microelectromechanical Systems* 18(3) (2009) 555-569.
- [130] S.M. Spearing, Materials issues in microelectromechanical systems (MEMS), *Acta Materialia* 48(1) (2000) 179-196.
- [131] B. Moser, J. Kuebler, H. Meinhard, W. Muster, J. Michler, Observation of Instabilities during Plastic Deformation by in-situ SEM Indentation Experiments, *Advanced Engineering Materials* 7(5) (2005) 388-392.

- [132] D. Kiener, C. Motz, G. Dehm, R. Pippan, Overview on established and novel FIB based miniaturized mechanical testing using in-situ SEM, *International Journal of Materials Research* 100(8) (2009) 1074-1087.
- [133] D. Kiener, C. Motz, T. Schöberl, M. Jenko, G. Dehm, Determination of Mechanical Properties of Copper at the Micron Scale, *Advanced Engineering Materials* 8(11) (2006) 1119-1125.
- [134] A.M. Minor, J.W. Morris, E.A. Stach, Quantitative in situ nanoindentation in an electron microscope, *Applied Physics Letters* 79(11) (2001) 1625-1627.
- [135] D. Kiener, P. Kaufmann, A.M. Minor, Strength, Hardening, and Failure Observed by In Situ TEM Tensile Testing, *Advanced Engineering Materials* 14(11) (2012) 960-967.
- [136] D. Kiener, A.M. Minor, Source Truncation and Exhaustion: Insights from Quantitative in situ TEM Tensile Testing, *Nano Letters* 11(9) (2011) 3816-3820.
- [137] S. Ho Oh, M. Legros, D. Kiener, G. Dehm, In situ observation of dislocation nucleation and escape in a submicrometre aluminium single crystal, *Nature Materials* 8 (2009) 95-100.
- [138] Z.W. Shan, R.K. Mishra, S.A. Syed Asif, O.L. Warren, A.M. Minor, Mechanical annealing and source-limited deformation in submicrometre-diameter Ni crystals, *Nat Mater* 7(2) (2008) 115-119.
- [139] F. Louchet, H. Saka, Comments on the paper: observation of dislocation dynamics in the electron microscope, by B.W. Lagow et al, *Materials Science and Engineering: A* 352(1-2) (2003) 71-75.
- [140] L. De Knoop, M. Legros, Absorption of crystal/amorphous interfacial dislocations during in situ TEM nanoindentation of an Al thin film on Si, *Scripta Materialia* 74(0) (2014) 44-47.
- [141] D. Kiener, Z. Zhang, S. Šturm, S. Cazottes, P.J. Imrich, C. Kirchlechner, G. Dehm, Advanced nanomechanics in the TEM: effects of thermal annealing on FIB prepared Cu samples, *Philosophical Magazine* 92(25-27) (2012) 3269-3289.
- [142] T.T. Zhu, A.J. Bushby, D.J. Dunstan, Materials mechanical size effects: a review, *Materials Technology* 23(4) (2008) 193-209.
- [143] S.-W. Lee, S.M. Han, W.D. Nix, Uniaxial compression of fcc Au nanopillars on an MgO substrate: The effects of prestraining and annealing, *Acta Materialia* 57(15) (2009) 4404-4415.
- [144] J. Mayer, L.A. Giannuzzi, T. Kamino, J. Michael, TEM Sample Preparation and FIB-Induced Damage, *MRS BULLETIN* 32 (2007) 400-407.
- [145] J. Marien, J.M. Plitzko, R. Spolenak, R.-M. Keller, J. Mayer, Quantitative electron spectroscopic imaging studies of microelectronic metallization layers, *Journal of Microscopy* 194(1) (1999) 71-78.
- [146] M.L. Jenkins, M.A. Kirk, Characterization of Radiation Damage by Transmission Electron Microscopy, IOP Publishing Ltd 2001.
- [147] R.M. Langford, M. Rogers, In situ lift-out: Steps to improve yield and a comparison with other FIB TEM sample preparation techniques, *Micron* 39(8) (2008) 1325-1330.
- [148] M. Kiritani, Y. Fukuta, T. Mima, E. Iiyoshi, Y. Kizuka, S. Kojima, N. Matsunami, Formation of vacancy clustered defects from cascade collisions during heavy-ion irradiation and their annihilation by freely-migrating interstitial atoms, *Journal of Nuclear Materials* 212-215, Part 1(0) (1994) 192-197.
- [149] N.M. Ghoniem, B.N. Singh, L.Z. Sun, T. Díaz de la Rubia, Interaction and accumulation of glissile defect clusters near dislocations, *Journal of Nuclear Materials* 276(1-3) (2000) 166-177.
- [150] M. Victoria, N. Baluc, C. Bailat, Y. Dai, M.I. Luppó, R. Schäublin, B.N. Singh, The microstructure and associated tensile properties of irradiated fcc and bcc metals, *Journal of Nuclear Materials* 276(1-3) (2000) 114-122.
- [151] H. Idrissi, S. Turner, M. Mitsuhashi, B. Wang, S. Hata, M. Coulombier, J.-P. Raskin, T. Pardoën, G.V. Tendeloo, D. Schryvers, Point Defect Clusters and Dislocations in FIB Irradiated Nanocrystalline Aluminum Films: An Electron Tomography and Aberration-Corrected High-Resolution ADF-STEM Study, *Microscopy and Microanalysis* 17 (2011) 983-990.
- [152] A.S. Schneider, D. Kiener, C.M. Yakacki, H.J. Maier, P.A. Gruber, N. Tamura, M. Kunz, A.M. Minor, C.P. Frick, Influence of bulk pre-straining on the size effect in nickel compression pillars, *Materials Science and Engineering: A* 559(0) (2013) 147-158.

- [153] H. Bei, S. Shim, E.P. George, M.K. Miller, E.G. Herbert, G.M. Pharr, Compressive strengths of molybdenum alloy micro-pillars prepared using a new technique, *Scripta Materialia* 57(5) (2007) 397-400.
- [154] P. Hosemann, J.G. Swadener, D. Kiener, G.S. Was, S.A. Maloy, N. Li, An exploratory study to determine applicability of nano-hardness and micro-compression measurements for yield stress estimation, *Journal of Nuclear Materials* 375(1) (2008) 135-143.
- [155] R. Raghavan, K. Boopathy, R. Ghisleni, M.A. Pouchon, U. Ramamurty, J. Michler, Ion irradiation enhances the mechanical performance of metallic glasses, *Scripta Materialia* 62(7) (2010) 462-465.
- [156] D. Zhang, J.M. Breguet, R. Clavel, L. Phillippe, I. Utke, J. Michler, In situ tensile testing of individual Co nanowires inside a scanning electron microscope, *Nanotechnology* 20(36) (2009) 365706.
- [157] S. Lee, J. Im, Y. Yoo, E. Bitzek, D. Kiener, G. Richter, B. Kim, S.H. Oh, Reversible cyclic deformation mechanism of gold nanowires by twinning-detwinning transition evidenced from in situ TEM, *Nat Commun* 5 (2014) 3033.
- [158] J.R. Greer, W.C. Oliver, W.D. Nix, Size dependence of mechanical properties of gold at the micron scale in the absence of strain gradients, *Acta Materialia* 53(6) (2005) 1821-1830.
- [159] X.L. Zhong, S. Schilling, N.J. Zaluzec, M.G. Burke, *Sample Preparation Methodologies for In Situ Liquid and Gaseous Cell Analytical Transmission Electron Microscopy of Electropolished Specimens, Microscopy and Microanalysis* (2016) 1-10.
- [160] S.C. Mao, H.X. Li, Y. Liu, Q.S. Deng, L.H. Wang, Y.F. Zhang, Z. Zhang, X.D. Han, Stress-induced martensitic transformation in nanometric NiTi shape memory alloy strips: An in situ TEM study of the thickness/size effect, *Journal of Alloys and Compounds* 579 (2013) 100-111.
- [161] G. Moser, H. Felber, B. Rashkova, P.J. Imrich, C. Krichlechner, W. Grosinger, C. Motz, G. Dehm, D. Kiener, *Sample Preparation by Metallography and Focused Ion Beam for Nanomechanical Testing Practical Metallography* 49 (2012) 343-355.
- [162] D. Kiener, A.M. Minor, Source-controlled yield and hardening of Cu(1;0;0) studied by in situ transmission electron microscopy, *Acta Materialia* 59(4) (2011) 1328-1337.
- [163] H.-H. Jin, C. Shin, J. Kwon, Fabrication of a TEM sample of ion-irradiated material using focused ion beam microprocessing and low-energy Ar ion milling *Journal of Electron Microscopy* 59(6) (2010) 463-468.
- [164] Z. Yao, M. Hernández-Mayoral, M.L. Jenkins, M.A. Kirk, Heavy-ion irradiations of Fe and Fe-Cr model alloys Part 1: Damage evolution in thin-foils at lower doses, *Philosophical Magazine* 88(21) (2008) 2851-2880.
- [165] Y. Lu, C. Peng, Y. Ganesan, J. Yu Huang, Quantitative in situ TEM tensile testing of an individual nickel nanowire, *Nanotechnology* 22(355702) (2011) 1-6.
- [166] J.R. Davis, *ASM Specialty Handbook: Nickel, Cobalt, and Their Alloys*, ASM International, The United States of America, 2000.
- [167] H.M. Ledbetter, R.P. Reed, Elastic Properties of Metals and Alloys, I. Iron, Nickel, and Iron-Nickel Alloys, *Journal of Physical and Chemical Reference Data* 2(3) (1973) 531-618.
- [168] C.P. Frick, B.G. Clark, S. Orso, A.S. Schneider, E. Arzt, Size effect on strength and strain hardening of small-scale [1 1 1] nickel compression pillars, *Materials Science and Engineering: A* 489(1-2) (2008) 319-329.
- [169] E.M. Ronald, B.S. Vijay, Size-dependent elastic properties of nanosized structural elements, *Nanotechnology* 11(3) (2000) 139.
- [170] T. Kadoyoshi, H. Kaburaki, F. Shimizu, H. Kimizuka, S. Jitsukawa, J. Li, Molecular dynamics study on the formation of stacking fault tetrahedra and unfauling of Frank loops in fcc metals, *Acta Materialia* 55(9) (2007) 3073-3080.
- [171] F. Kroupa, Dislocation Dipoles and Dislocation Loops, *Journal de Physique Colloques* 27 (C3) (1966) 154-167.

- [172] D. Kiener, P.J. Guruprasad, S.M. Keralavarma, G. Dehm, A.A. Benzerga, Work hardening in micropillar compression: In situ experiments and modeling, *Acta Materialia* 59(10) (2011) 3825-3840.
- [173] H.D. Espinosa, B.C. Prorok, B. Peng, Plasticity size effects in free-standing submicron polycrystalline FCC films subjected to pure tension, *J. Mech. Phys. Solids* 52(3) (2004) 667-689.
- [174] J.R. Greer, W. Nix, Nanoscale gold pillars strengthened through dislocation starvation, *PHYSICAL REVIEW* b73(245410) (2006) 6.
- [175] G. Dehm, Miniaturized single-crystalline fcc metals deformed in tension: New insights in size-dependent plasticity, *Progress in Materials Science* 54(6) (2009) 664-688.
- [176] L.M. Brown, Dislocation plasticity in persistent slip bands, *Materials Science and Engineering: A* 285(1-2) (2000) 35-42.
- [177] M.D. Uchic, P.A. Shade, D.M. Dimiduk, Plasticity of Micrometer-Scale Single Crystals in Compression, *Annual Review of Materials Research* 39(1) (2009) 361-386.
- [178] C. Chisholm, H. Bei, M.B. Lowry, J. Oh, S.A. Syed Asif, O.L. Warren, Z.W. Shan, E.P. George, A.M. Minor, Dislocation starvation and exhaustion hardening in Mo alloy nanofibers, *Acta Materialia* 60(5) (2012) 2258-2264.
- [179] C. Motz, D. Weygand, J. Senger, P. Gumbsch, Initial dislocation structures in 3-D discrete dislocation dynamics and their influence on microscale plasticity, *Acta Materialia* 57(6) (2009) 1744-1754.
- [180] T.A. Parthasarathy, S.I. Rao, D.M. Dimiduk, M.D. Uchic, D.R. Trinkle, Contribution to size effect of yield strength from the stochastics of dislocation source lengths in finite samples, *Scripta Materialia* 56(4) (2007) 313-316.
- [181] M. Schamel, J.M. Wheeler, C. Niederberger, J. Michler, A. Sologubenko, R. Spolenak, Cyclic loading for the characterisation of strain hardening during in situ microcompression experiments, *Philosophical Magazine* 96(32-34) (2016) 3479-3501.
- [182] C. Kirchlechner, J. Keckes, J.-S. Micha, G. Dehm, In Situ μ Laue: Instrumental Setup for the Deformation of Micron Sized Samples, *Advanced Engineering Materials* 13(8) (2011) 837-844.
- [183] D.M. Norfleet, D.M. Dimiduk, S.J. Polasik, M.D. Uchic, M.J. Mills, Dislocation structures and their relationship to strength in deformed nickel microcrystals, *Acta Materialia* 56(13) (2008) 2988-3001.
- [184] J.R. Greer, Bridging the Gap between Computational and Experimental Length Scales: a Review on Nano-Scale Plasticity. *Reviews on Advanced Materials Science, Rev. Adv. Mater. Sci.* 1(13) (2006) 59-70.
- [185] C.A. Volkert, E.T. Lilleodden, Size effects in the deformation of sub-micron Au columns, *Philosophical Magazine* 86(33-35) (2006) 5567-5579.
- [186] V. Samaeeaghmiyoni, H. Idrissi, J. Groten, R. Schwaiger, D. Schryvers, Quantitative in-situ TEM nanotensile testing of single crystal Ni facilitated by a new sample preparation approach, *Micron* 94 (2017) 66-73.
- [187] H. Tang, K.W. Schwarz, H.D. Espinosa, Dislocation-Source Shutdown and the Plastic Behavior of Single-Crystal Micropillars, *Physical Review Letters* 100(18) (2008) 185503.
- [188] L. Seok-Woo, A. Sylvie, D.N. William, C. Wei, Dislocation junctions and jogs in a free-standing FCC thin film, *Modelling and Simulation in Materials Science and Engineering* 19(2) (2011) 025002.
- [189] C. Zhou, S. Biner, R. LeSar, Simulations of the effect of surface coatings on plasticity at small scales, *Scripta Materialia* 63(11) (2010) 1096-1099.
- [190] H. Idrissi, A. Kobler, B. Amin-Ahmadi, M. Coulombier, M. Galceran, J.-P. Raskin, S. Godet, C. Kübel, T. Pardoën, D. Schryvers, Plasticity mechanisms in ultrafine grained freestanding aluminum thin films revealed by in-situ transmission electron microscopy nanomechanical testing, *Applied Physics Letters* 104(10) (2014) 101903.
- [191] D.M. Dimiduk, M.D. Uchic, T.A. Parthasarathy, Size-affected single-slip behavior of pure nickel microcrystals, *Acta Materialia* 53(15) (2005) 4065-4077.

- [192] Y.N. Cui, P. Lin, Z.L. Liu, Z. Zhuang, Theoretical and numerical investigations of single arm dislocation source controlled plastic flow in FCC micropillars, *International Journal of Plasticity* 55 (2014) 279-292.
- [193] B. Devincere, R. Madec, G. Monnet, S. Queyreau, R. Gatti, L. Kubin, Modelling crystal plasticity with dislocation dynamics simulations: The micromegas code, *Mechanics of Nano-Objects*, PRESSES DE L'ECOLE DES MINES, Paris, 2011, pp. 81-100.
- [194] O. Jamond, R. Gatti, A. Roos, B. Devincere, Consistent formulation for the Discrete-Continuous Model: Improving complex dislocation dynamics simulations, *International Journal of Plasticity* 80 (2016) 19-37.
- [195] M.B. Lowry, D. Kiener, M.M. LeBlanc, C. Chisholm, J.N. Florando, J.W. Morris Jr, A.M. Minor, Achieving the ideal strength in annealed molybdenum nanopillars, *Acta Materialia* 58(15) (2010) 5160-5167.
- [196] X. Li, Y. Wei, L. Lu, K. Lu, H. Gao, Dislocation nucleation governed softening and maximum strength in nano-twinned metals, *Nature* 464 (2010) 877.
- [197] L. Lu, Y. Shen, X. Chen, L. Qian, K. Lu, Ultrahigh Strength and High Electrical Conductivity in Copper, *Science* 304(5669) (2004) 422-426.
- [198] Y.F. Shen, L. Lu, Q.H. Lu, Z.H. Jin, K. Lu, Tensile properties of copper with nano-scale twins, *Scripta Materialia* 52(10) (2005) 989-994.
- [199] X. Zhang, H. Wang, X.H. Chen, L. Lu, K. Lu, R.G. Hoagland, A. Misra, High-strength sputter-deposited Cu foils with preferred orientation of nanoscale growth twins, *Applied Physics Letters* 88(17) (2006) 173116.
- [200] Q. Yu, Z.-W. Shan, J. Li, X. Huang, L. Xiao, J. Sun, E. Ma, Strong crystal size effect on deformation twinning, *Nature* 463 (2010) 335.
- [201] N.V. Malyar, J.S. Micha, G. Dehm, C. Kirchlechner, Size effect in bi-crystalline micropillars with a penetrable high angle grain boundary, *Acta Materialia* 129 (2017) 312-320.
- [202] N. Kheradmand, H. Vehoff, A. Barnoush, An insight into the role of the grain boundary in plastic deformation by means of a bicrystalline pillar compression test and atomistic simulation, *Acta Materialia* 61(19) (2013) 7454-7465.
- [203] T. Watanabe, Grain boundary engineering: historical perspective and future prospects, *J Mater Sci* 46(12) (2011) 4095-4115.
- [204] Z. Shen, R.H. Wagoner, W.A.T. Clark, Dislocation and grain boundary interactions in metals, *Acta Metallurgica* 36(12) (1988) 3231-3242.
- [205] A. Pineau, Crossing grain boundaries in metals by slip bands, cleavage and fatigue cracks, *Philosophical Transactions of the Royal Society A: Mathematical, Physical and Engineering Sciences* 373(2038) (2015).
- [206] P. Müllner, C. Solenthaler, P.J. Uggowitzer, M.O. Speidel, Brittle fracture in austenitic steel, *Acta Metallurgica et Materialia* 42(7) (1994) 2211-2217.
- [207] L.L. Li, X.H. An, P.J. Imrich, P. Zhang, Z.J. Zhang, G. Dehm, Z.F. Zhang, Microcompression and cyclic deformation behaviors of coaxial copper bicrystals with a single twin boundary, *Scripta Materialia* 69(2) (2013) 199-202.
- [208] Z. Shen, R.H. Wagoner, W.A.T. Clark, Dislocation pile-up and grain boundary interactions in 304 stainless steel, *Scripta Metallurgica* 20(6) (1986) 921-926.
- [209] J. Kacher, I.M. Robertson, Quasi-four-dimensional analysis of dislocation interactions with grain boundaries in 304 stainless steel, *Acta Materialia* 60(19) (2012) 6657-6672.
- [210] M. Chassagne, M. Legros, D. Rodney, Atomic-scale simulation of screw dislocation/coherent twin boundary interaction in Al, Au, Cu and Ni, *Acta Materialia* 59(4) (2011) 1456-1463.
- [211] L. Rémy, The interaction between slip and twinning systems and the influence of twinning on the mechanical behavior of fcc metals and alloys, *MTA* 12(3) (1981) 387-408.
- [212] F. Momprou, D. Caillard, M. Legros, H. Mughrabi, In situ TEM observations of reverse dislocation motion upon unloading in tensile-deformed UFG aluminium, *Acta Materialia* 60(8) (2012) 3402-3414.

- [213] J.P. Hirth, The influence of grain boundaries on mechanical properties, *Metallurgical Transactions* 3(12) (1972) 3047-3067.
- [214] R.W. Armstrong, 60 Years of Hall-Petch: Past to Present Nano-Scale Connections, *MATERIALS TRANSACTIONS* 55(1) (2014) 2-12.
- [215] Y. Zhu, X. Wu, X. Liao, J. Narayan, L. Kecskes, S. Mathaudhu, Dislocation–twin interactions in nanocrystalline fcc metals, 2011.
- [216] M. Sangid, T. Ezaz, H. Sehitoglu, I. Robertson, Energy of slip transmission and nucleation at grain boundaries, 2010.
- [217] W.Z. Abuzaid, M.D. Sangid, J.D. Carroll, H. Sehitoglu, J. Lambros, Slip transfer and plastic strain accumulation across grain boundaries in Hastelloy X, *J. Mech. Phys. Solids* 60(6) (2012) 1201-1220.
- [218] B.J. Pestman, J.T.M. De Hosson, V. Vitek, F.W. Schapink, Interaction between lattice dislocations and grain boundaries in f.c.c. and ordered compounds: A computer simulation, *Philosophical Magazine A* 64(4) (1991) 951-969.
- [219] Z.H. Jin, P. Gumbsch, K. Albe, E. Ma, K. Lu, H. Gleiter, H. Hahn, Interactions between non-screw lattice dislocations and coherent twin boundaries in face-centered cubic metals, *Acta Materialia* 56(5) (2008) 1126-1135.
- [220] Z.H. Jin, P. Gumbsch, E. Ma, K. Albe, K. Lu, H. Hahn, H. Gleiter, The interaction mechanism of screw dislocations with coherent twin boundaries in different face-centred cubic metals, *Scripta Materialia* 54(6) (2006) 1163-1168.
- [221] J. Zhang, H. Zhang, H. Ye, Y. Zheng, Twin Boundaries merely as Intrinsically Kinematic Barriers for Screw Dislocation Motion in FCC Metals, *Scientific Reports* 6 (2016) 22893.
- [222] N. Li, J. Wang, A. Misra, X. Zhang, J.Y. Huang, J.P. Hirth, Twinning dislocation multiplication at a coherent twin boundary, *Acta Materialia* 59(15) (2011) 5989-5996.
- [223] N. Li, J. Wang, X. Zhang, A. Misra, In-situ TEM study of dislocation-twin boundaries interaction in nanotwinned Cu films, *JOM* 63(9) (2011) 62.
- [224] C. Deng, F. Sansoz, Repulsive force of twin boundary on curved dislocations and its role on the yielding of twinned nanowires, *Scripta Materialia* 63(1) (2010) 50-53.
- [225] M.P. Dewald, W.A. Curtin, Multiscale modelling of dislocation/grain boundary interactions. II. Screw dislocations impinging on tilt boundaries in Al, *Philosophical Magazine* 87(30) (2007) 4615-4641.
- [226] Z.-J. Wang, Q.-J. Li, Y. Li, L.-C. Huang, L. Lu, M. Dao, J. Li, E. Ma, S. Suresh, Z.-W. Shan, Sliding of coherent twin boundaries, *Nature Communications* 8(1) (2017) 1108.
- [227] L.C. Lim, R. Raj, Slip-twin interactions in bicrystals of nickel at 573K at large strains, *Scripta Metallurgica* 20(4) (1986) 539-544.
- [228] T. Zhu, J. Li, A. Samanta, H.G. Kim, S. Suresh, Interfacial plasticity governs strain rate sensitivity and ductility in nanostructured metals, *Proceedings of the National Academy of Sciences* 104(9) (2007) 3031-3036.
- [229] S. Xu, L. Xiong, Y. Chen, D.L. McDowell, Sequential slip transfer of mixed-character dislocations across $\Sigma 3$ coherent twin boundary in FCC metals: a concurrent atomistic-continuum study, *Npj Computational Materials* 2 (2016) 15016.
- [230] J. Kacher, I.M. Robertson, In situ and tomographic analysis of dislocation/grain boundary interactions in α -titanium, *Philosophical Magazine* 94(8) (2014) 814-829.
- [231] C.R. Hutchinson, R.E. Hackenberg, G.J. Shiflet, A comparison of EDS microanalysis in FIB-prepared and electropolished TEM thin foils, *Ultramicroscopy* 94(1) (2003) 37-48.
- [232] A.J.E. Foreman, The bowing of a dislocation segment, *The Philosophical Magazine: A Journal of Theoretical Experimental and Applied Physics* 15(137) (1967) 1011-1021.
- [233] P.H. Pumphrey, K.M. Bowkett, Observation of partial dislocations on a coherent twin boundary, *The Philosophical Magazine: A Journal of Theoretical Experimental and Applied Physics* 24(188) (1971) 225-230.

- [234] V. Yamakov, D. Wolf, S.R. Phillpot, H. Gleiter, Dislocation–dislocation and dislocation–twin reactions in nanocrystalline Al by molecular dynamics simulation, *Acta Materialia* 51(14) (2003) 4135-4147.
- [235] H. Gleiter, The formation of annealing twins, *Acta Metallurgica* 17(12) (1969) 1421-1428.
- [236] J.P. Couzinié, B. Décamps, L. Priester, Interaction of dissociated lattice dislocations with a $\Sigma=3$ grain boundary in copper, *International Journal of Plasticity* 21(4) (2005) 759-775.
- [237] Z. Chen, Z. Jin, H. Gao, Repulsive force between screw dislocation and coherent twin boundary in aluminum and copper, *Physical Review B* 75(21) (2007) 212104.
- [238] S.I. Rao, D.M. Dimiduk, M. Tang, M.D. Uchic, T.A. Parthasarathy, C. Woodward, Estimating the strength of single-ended dislocation sources in micron-sized single crystals, *Philosophical Magazine* 87(30) (2007) 4777-4794.
- [239] G.C. Sih, *Multiscale Fatigue Crack Initiation and Propagation of Engineering Materials: Structural Integrity and Microstructural Worthiness, Fatigue Crack Growth Behaviour of Small and Large Bodies*, Springer, 2008, p. 386.
- [240] A.S. Argon, *Strengthening Mechanisms in Crystal Plasticity*, Oxford University Press 2008.
- [241] L.P. Kubin, C. Fressengeas, G. Ananthakrishna, Chapter 57 Collective behaviour of dislocations in plasticity, in: F.R.N. Nabarro, M.S. Duesbery (Eds.), *Dislocations in Solids*, Elsevier 2002, pp. 101-192.
- [242] H. Mughrabi, Fatigue, an everlasting materials problem - still en vogue, *Procedia Engineering* 2(1) (2010) 3-26.
- [243] A.M. Hussein, J.A. El-Awady, Quantifying dislocation microstructure evolution and cyclic hardening in fatigued face-centered cubic single crystals, *J. Mech. Phys. Solids* 91 (2016) 126-144.
- [244] R. LeSar, Simulations of Dislocation Structure and Response, *Annual Review of Condensed Matter Physics* 5(1) (2014) 375-407.
- [245] K. Shimizu, T. Torii, Y. Fujino, Evaluation of the Crystal Rotation Behavior at the Fatigue Crack Tip in Pure Titanium Films, *Journal of Solid Mechanics and Materials Engineering* 2(12) (2008) 1539-1546.
- [246] K. Shimizu, T. Torii, T. Mori, Crystal Rotation with Fatigue Crack Propagation in Copper Films, *Journal of the Society of Materials Science, Japan* 54(9) (2005) 903-908.
- [247] B. Perreault, J. Viñals, J.M. Rickman, Impact of lattice rotation on dislocation motion, *Physical Review B* 93(1) (2016) 014107.
- [248] T. Kakiuchi, Y. Uematsu, S. Tamano, S. Mizuno, Effect of Grain Orientation on Fatigue Behavior in Micro Cantilever of Magnesium Alloy AZ31, *Procedia Materials Science* 3 (2014) 967-972.
- [249] Y.-n. Cui, Z.-l. Liu, Z.-j. Wang, Z. Zhuang, Mechanical annealing under low-amplitude cyclic loading in micropillars, *J. Mech. Phys. Solids* 89 (2016) 1-15.
- [250] Z.-J. Wang, Q.-J. Li, Y.-N. Cui, Z.-L. Liu, E. Ma, J. Li, J. Sun, Z. Zhuang, M. Dao, Z.-W. Shan, S. Suresh, Cyclic deformation leads to defect healing and strengthening of small-volume metal crystals, *Proceedings of the National Academy of Sciences of the United States of America* 112(44) (2015) 13502-13507.
- [251] M.D. Sangid, H.J. Maier, H. Sehitoglu, The role of grain boundaries on fatigue crack initiation – An energy approach, *International Journal of Plasticity* 27(5) (2011) 801-821.
- [252] S. Stefan, M. Mehran, Z. Michael, From systems of discrete dislocations to a continuous field description: stresses and averaging aspects, *Modelling and Simulation in Materials Science and Engineering* 21(8) (2013) 085006.
- [253] O. Jamond, R. Gatti, A. Roos, B. Devincere, Consistent formulation for the Discrete-Continuous Model: Improving complex dislocation dynamics simulations, *International Journal of Plasticity* 80(Supplement C) (2016) 19-37.
- [254] B. Merle, H.W. Höppel, Microscale High-Cycle Fatigue Testing by Dynamic Micropillar Compression Using Continuous Stiffness Measurement, *Experimental Mechanics* 58(3) (2018) 465-474.

- [255] H. Mughrabi, The long-range internal stress field in the dislocation wall structure of persistent slip bands, *physica status solidi (a)* 104(1) (1987) 107-120.
- [256] C. Kirchlechner, J. Keckes, C. Motz, W. Grosinger, M.W. Kapp, J.S. Micha, O. Ulrich, G. Dehm, Impact of instrumental constraints and imperfections on the dislocation structure in micron-sized Cu compression pillars, *Acta Materialia* 59(14) (2011) 5618-5626.
- [257] D. Kiener, C. Motz, G. Dehm, Dislocation-induced crystal rotations in micro-compressed single crystal copper columns, *J Mater Sci* 43(7) (2008) 2503-2506.
- [258] R. Schwaiger, G. Dehm, O. Kraft, Cyclic deformation of polycrystalline Cu films, *Philosophical Magazine* 83(6) (2003) 693-710.
- [259] G.P. Zhang, R. Schwaiger, C.A. Volkert, O. Kraft, Effect of film thickness and grain size on fatigue-induced dislocation structures in Cu thin films, *Philosophical Magazine Letters* 83(8) (2003) 477-483.
- [260] Q. Yu, R.K. Mishra, J.W. Morris, A.M. Minor, The effect of size on dislocation cell formation and strain hardening in aluminium, *Philosophical Magazine* 94(18) (2014) 2062-2071.
- [261] K. Mecke, C. Blochwitz, Saturation Dislocation Structures in Cyclically Deformed Nickel Single Crystals of Different Orientations, *Crystal Research and Technology* 17(6) (1982) 743-758.
- [262] Z. Michael, S. Stefan, Scaling properties of dislocation simulations in the similitude regime, *Modelling and Simulation in Materials Science and Engineering* 22(6) (2014) 065012.
- [263] E.F. Rauch, M. Véron, Automated crystal orientation and phase mapping in TEM, *Materials Characterization* 98(0) (2014) 1-9.
- [264] H. Mughrabi, Deformation-induced long-range internal stresses and lattice plane misorientations and the role of geometrically necessary dislocations, *Philosophical Magazine* 86(25-26) (2006) 4037-4054.
- [265] S. Xia, A. El-Azab, Computational modelling of mesoscale dislocation patterning and plastic deformation of single crystals, *Modelling and Simulation in Materials Science and Engineering* 23(5) (2015) 055009.
- [266] S.X. Xia, A. El-Azab, A preliminary investigation of dislocation cell structure formation in metals using continuum dislocation dynamics, *IOP Conference Series: Materials Science and Engineering* 89(1) (2015) 012053.
- [267] P.F. Rottmann, K.J. Hemker, Nanoscale elastic strain mapping of polycrystalline materials, *Materials Research Letters* 6(4) (2018) 249-254.
- [268] T.C. Pekin, C. Gammer, J. Ciston, A.M. Minor, C. Ophus, Optimizing disk registration algorithms for nanobeam electron diffraction strain mapping, *Ultramicroscopy* 176 (2017) 170-176.
- [269] D. Cooper, T. Denneulin, N. Bernier, A. Béch e, J.-L. Rouvi re, Strain mapping of semiconductor specimens with nm-scale resolution in a transmission electron microscope, *Micron* 80 (2016) 145-165.
- [270] T.C. Pekin, C. Gammer, J. Ciston, C. Ophus, A.M. Minor, In situ nanobeam electron diffraction strain mapping of planar slip in stainless steel, *Scripta Materialia* 146(Supplement C) (2018) 87-90.
- [271] S.I. Rao, D.M. Dimiduk, J.A. El-Awady, T.A. Parthasarathy, M.D. Uchic, C. Woodward, Atomistic simulations of cross-slip nucleation at screw dislocation intersections in face-centered cubic nickel, *Philosophical Magazine* 89(34-36) (2009) 3351-3369.
- [272] A.M. Hussein, S.I. Rao, M.D. Uchic, D.M. Dimiduk, J.A. El-Awady, Microstructurally based cross-slip mechanisms and their effects on dislocation microstructure evolution in fcc crystals, *Acta Materialia* 85(0) (2015) 180-190.

List of abbreviations

| | |
|----------|--|
| ACOM | Automated Crystallographic Orientation Mapping |
| AFM | Atomic Force Microscopy |
| ANF | Annular Dark Field |
| BF | Bright Field |
| CPU | Central Processing Units |
| CRSS | Critical Resolved Shear Stress |
| CSL | Coincident Site Lattice |
| CSS | Cyclic Stress-Strain |
| CTB | Coherent Twin Boundary |
| DD | Dislocation Dynamics |
| DF | Dark Field |
| DP | Diffraction Pattern |
| DSC | Displacement Shift Complete |
| EBSD | Electron Backscatter Diffraction |
| ECCI | Electron Channelling Contrast Imaging |
| ED | Electron Diffraction |
| EDS | Energy Dispersive X-Ray Spectroscopy |
| EDX | Energy Dispersive X-Ray Spectroscopy |
| E-stress | Engineering Stress |
| FCC | Face Centre Cubic |
| FE | Friedel–Escaig |
| FIB | Focused Ion Beam |
| FL | Fleischer |
| F-R | Frank-Read |
| Ga | Gallium |
| GB | Grain Boundary |
| GIS | Gas Injection System |
| GND | Geometrically Necessary Dislocations |
| HAAD | High-Angle Annular Dark Field |
| HCF | High-Cycle Fatigue |
| HRTEM | High Resolution Transmission Electron Microscopy |

| | |
|------|---|
| LCF | Low-Cycle Fatigue |
| MEMS | Micro-Electro-Mechanical System |
| NEMS | Nano-Electro-Mechanical System |
| Ni | Nickel |
| PSB | Persistent Slip Bands |
| Pt | Platinum |
| PTP | Push-To-Pull |
| RSS | Resolved Shear Stress |
| SAD | Selected-Area Diffraction |
| SAED | Selected-Area Electron Diffraction |
| SAS | Single Arm Sources |
| SE | Secondary Electrons |
| SEM | Scanning Electron Microscopy |
| SF | Stacking Fault |
| SFE | Stacking Fault Energy |
| SPM | Scanning Probe Microscopy |
| SSD | Statistically Stored Dislocations |
| ST | Slip Trace |
| STEM | Scanning Transmission Electron Microscopy |
| TB | Twin Boundary |
| TEM | Transmission Electron Microscopy |

Appendix

MATLAB script for Image Cross-Correlation:

```

%% Main body of the script.
clear all
clc
close all
%% Browse for the AVI movie file
[FileName,PathName,FilterIndex] = uigetfile({'*.avi';'*.*'},'Load an AVI file');
xyloObj = VideoReader(strcat(PathName,FileName));
vidframeRate=xyloObj.FrameRate;
vidWidth = xyloObj.Width;
vidHeight = xyloObj.Height;
global nFrames
nFrames = xyloObj.NumberOfFrames;
videtime = xyloObj.duration;

%% getting some information from the user about the vertical distance of the PTP gap and also the frame rate of the movie
prompt = {'Enter PTP GAP distance(nm):','Enter movie framerate: ex. 5'};
dlg_title = 'Input';
num_lines = 1;
def = {'1',num2str(vidframeRate)};
answer = inputdlg(prompt,dlg_title,num_lines,def);
pxsize2=str2double(answer(1));
frateuser=str2double(answer(2));
frate=1/vidframeRate;

%% Pre-allocating movie structure.
mov(1:nFrames) = struct('cdata', zeros(vidHeight, vidWidth, 3, 'uint8'),'colormap', []);
k = 1;
%% Reading the frames.
for i=1:nFrames
h=waitbar(i/nFrames);
mov(i).cdata = read(xyloObj, i);
end
close(h);
clear h i

%% indicating the pixel size, the used is asked to rectangle in in which its height is equal to the the vertical distance of the PTP gap.
firstfrm=mov(1).cdata;
imshow(firstfrm,[]);
clc
recttop =abs(getrect)
pxsize = pxsize2/recttop(3)
close all;

%% Converting the frames to black and white mode. By adjusting the amount of threshold you can modify the quality of conversion.
J=mov(1).cdata;
imshow(J)
threshold=0.7
JJJ= im2bw(J,threshold);
imshow(JJJ)

%% this part can be used to see if B-W conversion works properly in all the frames of the movie.
for k = 1 :(nFrames/20)
    LL= im2bw(mov(k*20).cdata,threshold);
    imshow(LL)
    pause(0.01);
end
close all
clear LL

%% in the case the sample is not really vertical; this part can be used in order to correct the imaging condition.

RotOfMovie=5; % the amount of the rotation,
gggg = imrotate(mov(1).cdata,RotOfMovie,'bilinear');
imshow(gggg)
for k = 1 : nFrames

```

Appendix

```
h=waitbar(k/nFrames)
mov(k).cdata = imrotate(mov(k).cdata, RotOfMovie, 'bilinear');
end

%% in this part user is asked to determine the distance counting should be done in how many locations and then asked to select the location
by an rectangle.

%% the number of areas for measuring the distances
prompt = {'Number of the Area (1 or 2):'};
dlg_title = 'Input';
num_lines = 1;
def = {'1'};
answer = inputdlg(prompt,dlg_title,num_lines,def);
Arenumber=str2double(answer);

%% in the case cropping is needed, this part can be used,
J=mov(1).cdata;
imshow(J)
croptop =abs(getrect)
% getrec =[xmin ymin width height]
I2 = imcrop(J,croptop);
imshow(I2)

%% in this part the user is asked to select the areas for distance measuring.
JJJ= im2bw(I2,threshold);
imshow(JJJ)
for k = 1 :Arenumber
    recttop =abs(getrect)
    % getrec =[xmin ymin width height]
    if k==1
        XRange1= [recttop(1); recttop(1)+recttop(3)]
        hold on;
        plot(XRange1(1), 1,'r','MarkerSize',20)
        plot(XRange1(2), 1,'r','MarkerSize',20)
        end
    if k==2
        XRange2= [recttop(1); recttop(1)+recttop(3)]
        hold on;
        plot(XRange2(1), 1,'r','MarkerSize',20)
        plot(XRange2(2), 1,'r','MarkerSize',20)
        end
end
pause(1);
close all;

%%this part does cross correlation, the cropping and counting the pixels in each frame.
for k=1:nFrames
    h=waitbar(k/nFrames);
    K=imcrop(mov(k).cdata,croptop);
    KKK= im2bw(K,threshold);
    intK=sum(KKK,1);
    int=intK-intJ;
    if Arenumber==1
        intensity=int(XRange1(1):XRange1(2));
    end
    if Arenumber==2
        intensity=[int(XRange1(1):XRange1(2)) int(XRange2(1):XRange2(2))];
    end
    M(k) = mean(intensity);
    MM(k)= mode(intensity);
    MMM(k)=median(intensity);
end
close all

%% measuring the distance and saving in the excel file:
clear topxcor
gg = waitbar(0,'Cross Correlation...');
for i= 1:(nFrames)
    waitbar(i/nFrames)
    topxcor(i,1)=i*frate;% time
    topxcor(i,2)=M(i).* pxsiz;% y movement (main)
    topxcor(i,3)=0;% x movement
end
close(gg)
totalXcorY=topxcor(:,2);%+botxcor(:,1);
```

```

totalXcorX=topxcor(:,3);%+botxcor(:,2);
totalXtime=topxcor(:,2);% time of each frame
totalXload=topxcor(:,2);% load related to each frame
figure;
subplot(121);plot(totalXcorX);
subplot(122);plot(totalXcorY);
title('Displacement(px) vs Time(sec)')
[filename,PathName,FilterIndex] = uigetfile({'*.xlsx','*.*'},'Load an EXCEL file');
sheet = 1;
subsetA = xlsread(filename,sheet);
Times=subsetA(:,3);
Depthnm=subsetA(:,1);
LoadN=subsetA(:,2);
ss=size(Times);
org=zeros(ss(1),6);
org(:,1)=Times;
org(:,2)= Depthnm;
org(:,3)=LoadN;
a =ss(1);
b =size(topxcor(:,1));
c = a/b(1);
for i= 1:b(1)
    org((round (i*c)),4)= topxcor(i,1);% new time
    org((round (i*c)),5)= topxcor(i,2);% new displacement
    org((round (i*c)),6)= topxcor(i,2);% new displacement
end
for i= 1:(b(1))
    q=1;
    totalXtime(i)= frate*i;
    totalXload(i)= org((round (i*c)),3);
    for j=(round ((i-1)*c)+1):(round (i*c)-1)
        if i==1
            org(j,5)= ((org((round (i*c)),5))/(round(c)))*q ;
            q=q+1;
        else
            org(j,5)= ((org((round (i*c)),5)-org((round ((i-1)*c)),5))/(round(c)))*q + org(round ((i-1)*c),5);
            q=q+1;
        end
    end
    org((round (i*c)),5)= topxcor(i,2);% new displacement
end
filename2 = strcat('C1',filename);
xlswrite(filename2,[ ; org]);
filename = strcat('C2',filename);
org2(:,1)=totalXtime;
org2(:,2)=totalXcorX;
org2(:,3)=totalXcorY;
org2(:,4)=totalXload;
xlswrite(filename,[ ; org2]);

```

List of scientific contributions

Journal articles related to the PhD work

- **Samaeeaghmiyoni**, V., Idrissi, H., Groten, J., Schwaiger, R., Schryvers, D., “Quantitative in-situ TEM nanotensile testing of single crystal Ni facilitated by a new sample preparation approach”, *Micron* 94, 66-73.,
- **Samaee**, V., Gatti, R., Devincere, B., Pardoen, T., Schryvers, D., Idrissi, H., “Dislocation driven nanosample plasticity: new insights from quantitative in-situ TEM tensile testing”, *Scientific Reports* 8(1) (2018) 12012.
- **Samaee**, V., Groten, J., Idrissi, H., Sandfeld, S., Pardoen, T., Schwaiger, R., Schryvers, D., “Dislocation microstructure in cyclically deformed Ni micropillars: new insights from transmission electron microscopy”, (submitting process),
- **Samaee**, V., Pardoen, T., Schryvers, D., Idrissi, H., “Experimental investigation of dislocations – coherent twin boundary interactions by quantitative in-situ TEM tensile Testing, (under preparation),

Journal articles NOT related to the PhD work

- Lumbeeck, G., Idrissi, H., Amin-Ahmadi, B., Favache, A., Delmelle, R., **Samaee**, V., Proost, J., Pardoen, T., Schryvers, D., “Effect of hydriding induced defects on the small-scale plasticity mechanisms in nanocrystalline palladium thin films”, *Journal of Applied Physics*, submitted.
- Guzzinati, G., Altantzis, T., Batuk, M., De Backer, A., Lumbeeck, G., **Samaee**, V., Batuk, D., Idrissi, H., Hadermann, J., Van Aert, S., Schryvers, D., Verbeeck, J., Bals, S., “Recent Advances in Transmission Electron Microscopy for Materials Science at the EMAT Lab of the University of Antwerp”, *Materials* 11, 1304,
- H. Goodarzy, A. Akbarzadeh, V. **Samaee**,” Effect of route of ECAP on properties of aluminum plate samples”, 4th National Conference of Metals and Materials Forming, MATFORM’87, Sharif University of Technology, 3-4 Dec. 2008 - Tehran, Iran.

Conference contributions

- V. **Samaeeaghmiyoni**, H. Idrissi, D. Schryvers. “Nanomechanics of dislocations and interfaces revisited with new dedicated in-situ TEM tensile method”, Nanobruecken2018, Feb. 2018, Erlangen, De. (oral presentation),

- V. **Samaeeaghmiyoni**, H. Idrissi, D. Schryvers. “In-situ TEM Investigation of Plasticity/Fatigue Mechanisms of Single and Bi-Crystal Ni Samples by Using Micro/Nano-Mechanical Testing”, Microscopy Conference, August 2017, Lausanne, Ch. (oral presentation),
- V. **Samaeeaghmiyoni**, J. Groten, H. Idrissi, R. Schwaiger, D. Schryvers. “Using ex situ and in situ SEM/TEM micro/nano-mechanical testing to investigate plasticity/fatigue mechanisms at interfaces in Ni”, GDRi MECANO, May. 2017, Toulouse, Fr. (oral presentation),
- V. **Samaeeaghmiyoni**, J. Groten, H. Idrissi, R. Schwaiger, D. Schryvers. “Quantified In-situ TEM Tensile Test Experiments on Ni thin films prepared by new optimised techniques”, Material Research Society (MRS), Apr. 2017, Phoenix, AZ, USA. (oral presentation),
- V. **Samaeeaghmiyoni**, J. Groten, H. Idrissi, R. Schwaiger, D. Schryvers. “Using In situ SEM Fatigue Test and Advanced Ex situ TEM Techniques to Investigate Fatigue Mechanisms in Single and Bi-crystal Nickel Micropillars ”, Material Research Society (MRS), Apr. 2017, Phoenix, AZ, USA. (oral presentation),
- V. **Samaeeaghmiyoni**, H. Idrissi, R. Schwaiger, D. Schryvers. “Quantified In-situ TEM Tensile Test Experiments on Ni thin films prepared by new optimized techniques”, Nanobruecken2017, Apr. 2017, Manchester, UK. (oral presentation),
- V. **Samaeeaghmiyoni**, J. Groten, H. Idrissi, R. Schwaiger, D. Schryvers. “Using ex situ and in situ SEM/TEM micro/nano-mechanical testing to investigate plasticity/fatigue mechanisms at interfaces in Ni”, MMM2016, Oct. 2016, Dijon, Fr. (oral presentation),
- V. **Samaeeaghmiyoni**, J. Groten, H. Idrissi, R. Schwaiger, D. Schryvers. “Using ex situ and in situ SEM/TEM micro/nano-mechanical testing to investigate plasticity/fatigue mechanisms at interfaces in Ni”, the 16th European Electron Microscopy Congress, Aug.-Sep. 2016, Lyon, Fr. (oral presentation),
- V. **Samaeeaghmiyoni**, H. Idrissi, and D. Schryvers, “Sample Preparation Method for in-situ TEM Tensile Test of Pure Nickel”, International Workshop on Advanced and In-situ Microscopies of Functional Nanomaterials and Devices, Jul. 2015, Hamburg, De. (poster presentation).

Acknowledgment

Bringing a Ph.D. thesis up to its end is obviously an important personal challenge. But it cannot be properly carried out without the scientific, technical and human contribution of numerous people, who I wish to warmly acknowledge here.

Foremost, I would like to express my sincere gratitude to my advisors Prof. Dominique Schryvers and Prof. Hosni Idrissi for giving me the opportunity to start my PhD studies at world-class EMAT research group. I also thank them for their continuous support of my PhD study and research, for their patience, motivation, enthusiasm, and immense knowledge. Their guidance helped me in all the time of research and writing of this thesis. I could not have imagined having better advisors for my PhD study.

Besides my advisors, I would like to thank the rest of my jury members: Prof. R. Schwaiger, Prof. T. Pardoen, Prof. B. Partoens, and Prof. J. Hadermann for their encouragement, insightful comments, and useful questions.

I would also like to cordially thank Prof. R. Schwaiger and Dr. J. Groten from KIT, Prof. S. Sandfeld from TU Bergakademie Freiberg, Prof. B. Devincere and Dr. R. Gatti from CNRS-ONERA, and Prof. T. Pardoen from UCL for providing the materials and the samples, for performing simulations and for fruitful scientific discussions.

I want to express my great gratitude to my colleagues in EMAT, especially to Hamed, Behnam, Gunnar, Saeid, Stijn, Armand, Liesbet, and Tine for their help and support during the process of researching and writing this thesis.

Financial support from the Flemish (FWO) and German Research Foundation (DFG) through the European M-ERA.NET project “FaSS” (Fatigue Simulation near Surfaces) under the grant numbers GA.014.13 N and SCHW855/5-1, respectively, is gratefully acknowledged. I also acknowledges the FWO research project G012012N “Understanding nanocrystalline mechanical behaviour from structural investigations”.

Finally, and most importantly, I must express my very profound gratitude to my mother, my family, and my girlfriend, Ykje, for providing me with unfailing support and continuous encouragement throughout my education. Thank you.